The Low-Energy and Large-Scale Frontier of Dual-Phase Xenon Time Projection Chambers for Dark Matter Search

---

Dissertation

zur

Erlangung der naturwissenschaftlichen Doktorwürde
(Dr. sc. nat.)

vorgelegt der

Mathematisch-naturwissenschaftlichen Fakultät

der

Universität Zürich

von

Kevin Thieme

aus der

Bundesrepublik Deutschland

Promotionskommission

Prof. Dr. Laura Baudis (Vorsitz)
Prof. Dr. Marc Schumann
Prof. Dr. Nicola Serra
Dr. Patricia Sanchez-Lucas

Zürich, 2022

Abstract

Astrophysical and cosmological evidence indicates the presence of dark matter in the universe, which is more than five times as abundant as baryonic matter by mass. Its particle nature, however, is unknown to date. One of the most promising particle candidates is the weakly interacting massive particle (WIMP). The most successful direct detection experiments deploy liquid noble gas targets in dual-phase (liquid/gas) time projection chambers (TPCs). In particular, detectors using xenon as target are widely deployed in dark matter and other rare event searches.

The DARWIN (DARk matter WImp search with liquid xenoN) observatory is a proposed next-generation detector involving 50 t (40 t active) of liquid xenon (LXe) in a 2.6 m × 2.6 m (height × diameter) TPC. It will explore the entire experimentally accessible parameter space for WIMP masses above 5 GeV/c^2 down to the irreducible background from coherent elastic neutrino-nucleus interactions. DARWIN will also be searching for various other rare interactions such as the neutrinoless double beta decay and low-energy solar neutrinos. The construction of DARWIN involves a series of technological challenges and design choices which are addressed in a rich R&D programme. In this thesis, we focus on silicon photomultipliers (SiPMs) as potential photosensor candidates for DARWIN, low-energy interactions in LXe required for the modelling of the response of LXe detectors and the direct demonstration of the detector principle at the full DARWIN scale.

For the first time, a small dual-phase xenon TPC, Xurich II, was equipped with a top array of SiPMs for light and charge readout. We describe the instrument, as well as the data processing and the event position reconstruction, and obtain a horizontal spatial resolution of $\sim$ 1.5 mm, limited only by the detector geometry. The SiPM performance is evaluated *in situ* and the detector is characterised with internal gaseous ^{37}Ar and ^{83m}Kr calibration sources. We detail the production of ^{37}Ar as well as its introduction into the gas system. The observed light and charge yields are compared to predictions of the Noble Element Simulation Technique (NEST) v2.3.0 for electronic recoil (ER) energies of $2.82 - 41.56$ keV and additionally at 0.27 keV for charge-only.

Conclusions on the interacting particle in LXe rely on a precise reconstruction of the deposited energy which requires aforementioned calibrations of the energy scale of the detector. However, a microscopic calibration, i.e. the translation from the number of excitation quanta into deposited energy, also necessitates good knowledge of the energy required to produce single scintillation photons or ionisation electrons in LXe. The sum of these excitation quanta is directly proportional to the deposited energy in the target. The proportionality constant is the mean excitation energy and is commonly known as W-value. We present a measurement of the W-value with ER interactions in Xurich II. Our result is based on the ^{37}Ar and ^{83m}Kr calibration data and single electron events. We obtain a value of $W = 11.5\,^{+0.2}_{-0.3}\,(\text{syst.})$ eV, with negligible statistical uncertainty, which is lower than previously measured at these energies. If further confirmed, our result will be relevant for modelling the absolute response of LXe detectors to particle interactions.

We designed and built a full-scale vertical demonstrator, Xenoscope, with the main goal of achieving electron drift over a 2.6 m distance. The following mechanical, cryogenic and gas handling subsystems of the facility are described in detail: the horizontal cryostat levelling system with a precision of 60 µm/m, the heat exchanger system with a minimum mean efficiency of 97.3 % for a gas flow range of $20 - 80$ slpm, the filtration and safety gas system, and two independent gas and liquid xenon recovery and storage systems which allow for average xenon recovery speeds of at least 3.3 kg/h and 19.1 kg/h, respectively. In a first commissioning run, the cryogenic components were benchmarked, demonstrating reliable and continuous operation over 40 days.

Acknowledgements

I never ran a marathon, but I imagine it to have very much in common with a Ph.D. It is an ambitious far goal that you set yourself and that can only be achieved by your own constantly high efforts. And it's all over in the moment you stop as you can be supported but not carried through. In my case, it was a one year training period, during which I learned and tried, followed by a three year run, during which I progressed and of which writing this thesis was only the final spurt.

Thinking I know how to run, or at least in theory, I arrived in the running group in November 2017. The training period is about learning the basics of a runner's life, trying to increase the distance and about failing. This phase is for finding the correct approach or technique fitting to the runner. However, no matter how well the runner performs, not a single metre that they ran during the training counts towards the actual marathon. All you take away is experience. And just as the most I have seen, I struggled a little during this phase with finding the right track, how to tackle the challenge and sometimes with the training method. This phase felt unsatisfactory and like lost time but in retrospect it was necessary. Nobody can run a marathon without practising. In this period, maybe more than later, it is the coach who forms the runner, by criticism or motivation but surely by the best of support. And it depends on the ability of the coach to judge how steep the slope of progression can be. It was my coach giving me the right track, the ^{37}Ar calibration, that fit to my profile. This was the point when the actual marathon started. The run itself was a balancing act between being too precise and thus, not coming forward, and going too fast and getting exhausted too much. It was also a constant fight with myself to keep the motivation high. However, even having completed the training, no runner will not make it to the finish on themself. Their success highly depends on the environment which strengthens their endurance, performance and willpower. And indeed, my coach was there encouraging from the sideline: asking to push for good split times, evaluating my performance at steep sectors, making sure I pace myself but do not rest before the finish line, and steadily increasing the intervals of advice. But my coach was also always one to lend a sympathetic ear and cheered me up when it was most needed: I remember her saying in a confident tone "It's physics, it will work!" when I desperately could not see the event rate increase right after the introduction of the ^{37}Ar source into Xurich II. But there are also others: I ran enough in my life to know that nothing pushes you forward more than other runners aiming for the same goal and going at the same pace or even a little faster. To keep you focused on the next metre only, and distract you from thinking about how many are left, there are supporters at the side of the track. Not knowing the details that you and your coach share and worry about, they unconditionally motivate, set you in a good mood and let you feel their trust and backing. And finally, from time to time, only a cold drink can push you a little further. After all, I made it to the finish. I am grateful for everyone and everything that helped me to achieve this.

Most notably I would like to thank my coach, Prof. Dr. Laura Baudis, to select me for her squad, her trust, advise and support, and for her own hard work that allowed me to perform my Ph.D. under such comfortable conditions. She gave me demanding tasks but all the freedom to approach them with my own technique, and created an environment that let me grow as a person and researcher. This allowed me to stay on my personal runner's high for the last two years during which I made most the distance.

Moreover, I would like to express my gratitude to Dr. Patricia Sanchez-Lucas who was the hard-working assistant coach that would run at your side most of the marathon. No matter how much she fought with her own tasks, she invested time to help and gave excellent advice. She also took time

to proofread this thesis, for which I thank her greatly. I really enjoyed working with her and would like to thank her for the daily fun we had in the office. For the future, I wish her the best of luck for her own career.

I profited a lot from the appreciated comments and questions of my external committee member Prof. Dr. Marc Schumann that I received in our regular meetings. His view from outside complemented perfectly the feedback from my group and made me rethink and rework my doing. I thank him for making me thereby progress further.

I also thank Prof. Dr. Nicola Serra who joined my Ph.D. committee a little bit later. I highly appreciate his encouraging feedback and the open discussions that we had about my future career.

Additionally and notably, I would like to thank my fellow Frédéric Girard with whom I spend most of my work time. We planned, designed, assembled, machined, laughed, swore and drank together – and the result could really be worse. I thank him for being a good friend, for all the help we shared and for bringing so much joy to the group. I will miss playing with liquid nitrogen and finding water with him, and I wish him all the best for the finish.

I would particularly like to thank my friend and former colleague Dr. Adam Brown who was there for me since the very first coffee break. His knowledgeable input and efficient way of solving problems have helped me not only once. I really enjoyed his sense of humour, the time we spend at bars (as long as it was not for drinking "Gueuze"), the skiing trips and bringing back the XENON1T TPC from LNGS. The last year after he graduated and left the group, became indeed a little more monotonous and I hope we will stay in contact.

I also thank Dr. Julien Wulf with whom I overlapped one and a half years. He introduced me to the existing hard- and software and to the group habits. I profited a lot from his work and we had a fun time.

Many thanks also to my office mate Yanina Biondi who helped me multiple times with computer issues and physics questions. With her little anecdotes, she oftentimes brought joy to our workaday life and I liked sharing my Ph.D. run with her – despite our little clashes. I also wish her all the power that it needs for the finish.

Huge thanks also to Reto Maier and the team of the mechanical workshop of the Department of Physics. Such a big hardware project would not have been possible without the active and committed technical support of Chris Albrecht, Silvio Scherr, Bruno Lussi, Marcel Schaffner and Brandon Markwalder and their incredible machining expertise.

I furthermore thank David Wolf and Daniel Florin from the electronics workshop who helped me to clear many electrical hurdles.

Moreover, I thank my B.Sc. student Stefan Hochrein for his good input to the Xurich II processing framework. His careful way of working helped me to improve the processor by fixing a lot of bugs.

I also would like to thank Dr. Alexander Kish and Dr. Francesco Piastra for the kind introduction to Xurich II at the beginning of my Ph.D. Furthermore, I thank Dr. Alessandro Manfredini for the great teamwork and his open-minded way of approaching challenges.

I thank the whole group, and in particular Giovanni Volta, Ricardo Peres, Dr. Chiara Capelli and Dr. Roman Hiller, for the enjoyable fun time and the friendly atmosphere. Many thanks also to Michelle Galloway who gave me the key tip for my next career step.

Special thanks also to my beloved fiancée Dr. Nastassia Grimm who initially encouraged me to apply for this position. She did not only back me and bear all the emotions I brought home, but she also helped me with the involved mathematics like with the combinatorics for the SiPM DPE analysis. I very much enjoyed the time we spend in Zurich studying for our Ph.Ds. Now, I am excitedly looking forward to our next step in Geneva and awaiting eagerly to marry her.

Finally, I am deeply grateful for the unconditional support of my parents throughout my doctorate. They made this step possible by giving me the opportunity to study at ETH Zurich. Coming home always meant leaving all the trouble behind which was needed more than once.

Preface

The nature of dark matter remains one of the biggest mysteries of modern physics, which scientists have tried to unravel during the past decades in a global hunt with various direct detection techniques. The most sensitive detector type for the promising WIMP dark matter candidate is the dual-phase noble element TPC. The XENON [1], LUX [2], PandaX [3] and DarkSide [4] collaborations have set world-leading exclusion limits to WIMP interactions using xenon and argon as targets. New results with larger and more sensitive detectors are underway in the near future [5–9]. This doctoral thesis stands at the forefront of the low-energy and large scale frontier of the dual-phase xenon TPC detector technology to push its sensitivity even further. It is structured as follows: We outline the evidence for dark matter and its known properties and introduce potential candidates as well as the principle of direct WIMP detection in Chapter 1. Note that we keep the focus on particle dark matter. We also provide a brief review of past and ongoing direct detection experiments. Chapter 2 focuses on xenon as detector medium and discusses its properties that make it an ideal WIMP target. We discuss particle interactions in LXe and how these can be recorded in dual-phase TPCs. Then we turn our discussion towards the DARWIN observatory [8] which is a next-generation dual-phase xenon TPC and likely the ultimate evolution in size and sensitivity of this detector technology. This thesis presents cutting edge R&D on novel silicon photosensors in a dual-phase TPC and xenon physics with keV-scale calibration sources (the low-energy frontier) and the development of a vertical full-scale prototype platform for DARWIN (the large-scale frontier). In Chapter 4 we present a new TPC detector concept, Xurich II, equipped with novel SiPMs, enlarge upon the data acquisition (DAQ) and processing and characterise the performance of the photosensors. In Chapter 5 we show the ability of Xurich II to detect low-energy decays of an ^{37}Ar source. This low-energy source is only recently deployed in LXe TPCs [10–12]. This chapter is complemented by the analysis of ^{83m}Kr calibration data in Appendix A. These decay events are used to calibrate the low-energy response of the detector. Based on this calibration data and single electron events, we present a new measurement of the mean electronic excitation energy of LXe in Chapter 6. Chapter 7 introduces the vertical DARWIN demonstrator Xenoscope and discusses the design and performance of dedicated mechanical, cryogenic and gas handling subsystems in detail. These are: a horizontal fine-levelling system for the detector cryostat, a high-efficiency heat exchanger system, and two separate gas and liquid xenon recovery and storage systems. Appendix B shows a design calculation of the safety relief valve for the high-pressure vessel BoX (Ball of Xenon) which is the main component of the liquid recovery system.

As mentioned, this doctoral project was performed within the context of the global experimental effort to detect dark matter. Thus, standing on the shoulders of giants, a good fraction of the presented work is based on prior efforts of others or was a subproject of a larger team effort and published abreast with closely related work of my colleagues. Below, I summarise my contribution to the content of each chapter and delimit my own work of which most was published in scientific journals. The respective references are listed below. Naturally, the content of this thesis shows a verbatim overlap with the very articles.

Chapter 1 and 2 These introductory chapters review the wide literature on the topic.

Chapter 3 This chapter presents work of the DARWIN collaboration. The overview was published in a similar form as conference proceeding to ICRC 2021:

[I] Kevin Thieme, *DARWIN – a next-generation liquid xenon observatory for dark matter and neutrino physics*, in *Proceedings of 37th International Cosmic Ray Conference PoS(ICRC2021)*, vol. 395, p. 548, 2021.

Chapter 4 In this chapter, I describe the upgraded Xurich II setup with SiPMs, the DAQ, the processing stages and the measured characteristics of the SiPMs in the detector. The design of the TPC, the cryogenics, gas handling and readout electronics setup is the work of former group members and was published in Reference [13]. The prospects of the SiPM top array and its design, in particular of the preamplifier board, is the work of Julien Wulf [14]. Together with others, I was involved in the assembly work of the upgrade. The DAQ software was written by Julien Wulf and adopted for zero length encoding (ZLE) by Frédéric Girard [15]. The processing framework in its current configuration is my work and based on Julien Wulf's raw data processor [14] that I optimised, adopted for ZLE data and upgraded for TPC event building. The script to merge the output files of the analog-to-digital converter modules was written by Alessandro Manfredini. The position reconstruction algorithms, I developed together with my Bachelor student Stefan Hochrein. All the rest of the presented work is solely my own. Most of this chapter was published in

[II] L. Baudis, Y. Biondi, M. Galloway, F. Girard, S. Hochrein, S. Reichard, P. Sanchez Lucas, K. Thieme and J. Wulf, *The first dual-phase xenon TPC equipped with silicon photomultipliers and characterisation with ^{37}Ar*, Eur. Phys. J. C **80** (2020) 477, [arXiv:2003.01731]

of which I am one of two corresponding authors. Sections 4.3.4 and 4.3.5 were published as part of

[III] Laura Baudis, Patricia Sanchez-Lucas and Kevin Thieme, *A measurement of the mean electronic excitation energy of liquid xenon*, Eur. Phys. J. C **81** (2021) 1060, [arXiv:2109.07151]

of which I am the corresponding author. The presented light simulation in Xurich II is based on Julien Wulf's code [14] but was significantly refined in the geometry and materials for the SiPMs and the TPC. For instance, the cuts on the quartz window corners, and chamfers and fillets on the polytetrafluoroethylene reflector were added as well as the larger top diameter of the TPC correctly implemented. Furthermore, I adopted the xenon and material parameters from the DARWIN Monte Carlo code [16], added or updated parameters and properties like the total reflection on quartz.

Chapter 5 Here, I show the production of the ^{37}Ar source, the design of the source introduction setup and the data analysis. The fundamental idea of the ampule breaking mechanism of the source introduction system goes back to Christopher Hils [17]. An earlier version of Figure 5.20, left, that shows the comparison of the light and charge yields at 968 V/cm to predictions of NEST [18] was generated together with Yanina Biondi. All other described work in this chapter is my own. Except for the ^{37}Ar L- and M-shell analysis, this work was presented in Publication [II].

Chapter 6 In this chapter, I show a measurement of the mean electronic excitation energy in LXe based on low-keV calibration data with internal ^{37}Ar and ^{83m}Kr sources and single electron events. The detection and tagging efficiencies were provided by Patricia Sanchez-Lucas. For the analysis, I used the charge and light yields from ^{83m}Kr calibration data that was not analysed by myself, see the comment below on Appendix A. Apart from that, all presented work is my own. This work was presented in Publication [III].

Chapter 7 Here, I describe the design and construction work for the vertical DARWIN demonstrator Xenoscope and present commissioning data. All subsystems described in detail, i.e. the cryostat levelling mechanism, the heat exchanger system, the filtration and safety gas system and both recovery and storage systems were designed, acquired, assembled, commissioned and some smaller parts of them also machined by myself. I always worked together with Frédéric Girard who build most of the remaining mechanical, cryogenic and gas handling systems including the support structure, the

cooling tower, the cryostat and the purification gas system. We provided each other input during design phases and shared help during assemblies. The xenon compressor pressures in Figure 7.6, left, were acquired by him as well [15]. The design, the construction and the commissioning data were published in

[IV] L. Baudis, Y. Biondi, M. Galloway, F. Girard, A. Manfredini, N. McFadden, R Peres, P. Sanchez Lucas and K. Thieme, *Design and construction of Xenoscope – a full-scale vertical demonstrator for the DARWIN observatory*, J. Instrum. **16** (2021) P08052, [arXiv:2105.13829]

of which I am one of three corresponding authors. I was also responsible for the approval and registration of the BoX pressure vessel assembly of the liquid recuperation system. The Swiss Safety Center AG [19] certified the conformity of the assembly. It was registered as pressure device at Suva [20] and will be inspected by the pressure vessel inspectorate of the SVTI [21]. My work included also the organisation of the registration of the levelling mechanism as utility model at the German Patent and Trade Mark Office. At the time of writing a patent at the Swiss Federal Institute of Intellectual Property is being filed. Moreover, I performed preliminary finite element analysis simulations to confirm the structural integrity of the inner frame that supports the cryostat and was responsible for the communication to the consulting engineers of Helbling Technik AG [22] that provided feedback on the top flange and the inner vessel of the cryostat.

Appendix A The ^{83m}Kr analysis was performed by Stefan Hochrein as Bachelor's project under my supervision [23]. I base my analysis on data that was reanalysed by Patricia Sanchez-Lucas after changes in the raw data processing. The shown figures, however, were produced by myself. This work was also part of Publication [II].

Appendix B This part was developed during the approval process of BoX with the Swiss Safety Center AG and is my own work.

Contents

List of Figures

List of Tables

Chapter 1

Particle Dark Matter

Compelling astrophysical and cosmological observations suggest the existence of a stable, massive, non-baryonic and non-luminous matter component in the universe, moving at non-relativistic speed, that interacts gravitationally with baryonic matter. Often attributed to the astronomer Fritz Zwicky, this additional component is referred to as dark matter (originally in German: "dunkle (kalte) Materie") since 1933 [24]. However, already at the beginning of the 20th century in 1906, Henri Poincaré used the French term "matière obscure" in response to Lord Kelvin's earlier work on the velocity dispersion of the stars in the Milky Way [25]. From the motion of the stars, Kelvin estimated the mass of the galaxy and found a discrepancy to the visible mass [26]. The astronomers Jacobus Kapteyn in 1922 [27] and Jan Oort in 1932 [28] were also hypothesising the existence of dark matter from stellar motions in the Milky Way before Zwicky. Modern surveys imply that of the total energy content in the universe, the known *normal* baryonic matter only constitutes 5.0 %, while the dark matter accounts for 26.5 %. The remaining 68.5 % is attributed to dark energy that is causative for the accelerated expansion of the universe [29]. Over the past decades, the dark matter puzzle has become one of the most intriguing mysteries of modern physics and led to a tremendous theoretical and experimental effort as to the composition of dark matter. In particular, the search for particle dark matter has received considerable interest. Hypothesising that dark matter has a particle nature, none of the known particles of the standard model of particle physics (SM) could prove to be a valid candidate. Thus, the need for one or more new dark matter particles beyond the standard model (BSM) emerged.

This chapter is structured as follows: In Section 1.1 we summarise the astrophysical and cosmological evidence that implies the existence of dark matter. This leads to a set of known properties of dark matter that we outline in Section 1.2. In Section 1.3, we provide an overview of the potential dark matter candidates. While we focus on particle dark matter candidates, in particular on the well motivated weakly interacting massive particles (WIMPs), we also briefly mention alternative hypothetical solutions to the long-standing dark matter problem. Finally, we discuss the principle of direct WIMP dark matter detection in Section 1.4 and review the different experimental approaches and efforts.

1.1 Evidence for Dark Matter

To date dark matter has not been identified, and its nature still remains unravelled. However, a number of compelling observations from the dynamics of galaxies and galaxy clusters, gravitational lensing and relic photons from the early universe have made scientists believe in its existence.

The astronomer Fritz Zwicky was among the first who claimed the existence of dark matter in 1933 [24]. Studying the velocity dispersion of extragalactic nebulae in the Coma cluster, he found a discrepancy between the mass estimated from the luminosities of the galaxies and the gravitational mass in the viral theorem that relates the time-averaged kinetic and potential energy of the galaxies:

$$\overline{E}_{\text{kin}} = -\frac{1}{2}\overline{E}_{\text{pot}} \quad . \tag{1.1}$$

To resolve the discrepancy, he proposed the existence of an additional non-luminous matter component but overestimated its abundance by roughly a factor 75 compared to today's measurements. Zwicky's dark matter hypothesis was met with disapproval for a long time.

Only in 1970 the astronomers Vera Rubin and Kent Ford reported another strong evidence for dark matter [30], supported by parallel work of the astronomer Ken Freeman [31]. They performed precise measurements of the rotation speed $v(r)$ of stars and interstellar gas in disc galaxies as a function of radius r from the gravitational centre of the galaxy, cf. Figure 1.1, left. Classically, we expect the following rotation speed for a matter distribution $M(r)$:

$$v(r) = \sqrt{\frac{GM(r)}{r}} \quad , \tag{1.2}$$

where G is the gravitational constant. If the luminous mass is mostly concentrated below a certain radius R and the mass density is negligible in the outer region beyond R, we would expect the speed to increase below R, depending on the distribution $M(r)$, and to fall like $v(r) \propto 1/\sqrt{r}$ for $r > R$. However, Rubin and Ford observed that the luminous matter was actually moving at constant speed far beyond R. These observations can be explained by the presence of an additional non-luminous matter component that yields in total $M(r) \propto r$ at $r > R$, the dark matter halo. In the following years, optical and radio observations of several spiral and lenticular galaxies showed flat rotation curves at large radii [32–39].

Unlike the kinetic approach of Zwicky, modern studies of galaxy clusters mostly compare the distributions of baryonic matter and the total matter. The former is typically determined from the electromagnetic signal, while the latter can be determined from gravitational lensing phenomena of luminous objects in the background. Well-known examples of colliding or merging clusters that provide strong evidence for dark matter are the Bullet Cluster (1E 0657-558) [40] and the Pandora's Cluster (Abell 2744) [41] that show a clear separation of the hot and colliding intergalactic gas of baryonic matter and dark matter that interacts only gravitationally.

Besides these astrophysical observations, strong cosmological evidence is provided by the cosmic microwave background (CMB), which allows for a precise quantitative measurement of the dark matter density. The CMB, accidentally discovered by the radio astronomers Arno Allan Penzias and Robert Woodrow Wilson in 1965 [42], is a relic electromagnetic radiation that was emitted after the recombination epoch during photon decoupling $\sim 380\,000$ years after the Big Bang. The recombination epoch describes the time when the universe had cooled down enough by expansion, to $\sim 3000\,\mathrm{K}$ such that neutral hydrogen atoms were able to form from protons and electrons. As a result, the universe became transparent for photons. From that moment on, the photons propagated almost freely unlike before recombination, when photons had scattered off charged particles in the hot plasma. These photons have been travelling through the universe ever since while undergoing redshift due to the expansion of space. Today they are observable in the microwave region of the electromagnetic spectrum as an almost perfect black-body radiation with a temperature of $(2.7255 \pm 0.0006)\,\mathrm{K}$ [43] and a power spectrum which has only little anisotropies in the range $10 - 76\,\mu\mathrm{K}$ depending on the angular scale [44]. These temperature fluctuations, discovered by the COBE experiment in 1992 [45], come from acoustic oscillations in the hot plasma in the early universe and are responsible for the formation of the large-scale structures of the galaxy distribution. Measurements of the power spectrum of the fluctuations yield the relic densities of baryonic matter and dark matter, as well as of dark energy. The COBE [46], WMAP [47, 48] and Planck [29, 49] spacecrafts have measured the anisotropies of the CMB with increasing and remarkable precision which allows to constrain dark matter theories quantitatively. The CMB measurements are well in agreement with the ΛCDM model[1], the standard model of cosmology. Recent measurements of the Planck spacecraft yield a dark matter relic density

[1] Λ denotes the cosmological constant that parametrises dark energy and CDM is the abbreviation of cold dark matter which indicates dark matter that moves at non-relativistic speeds.

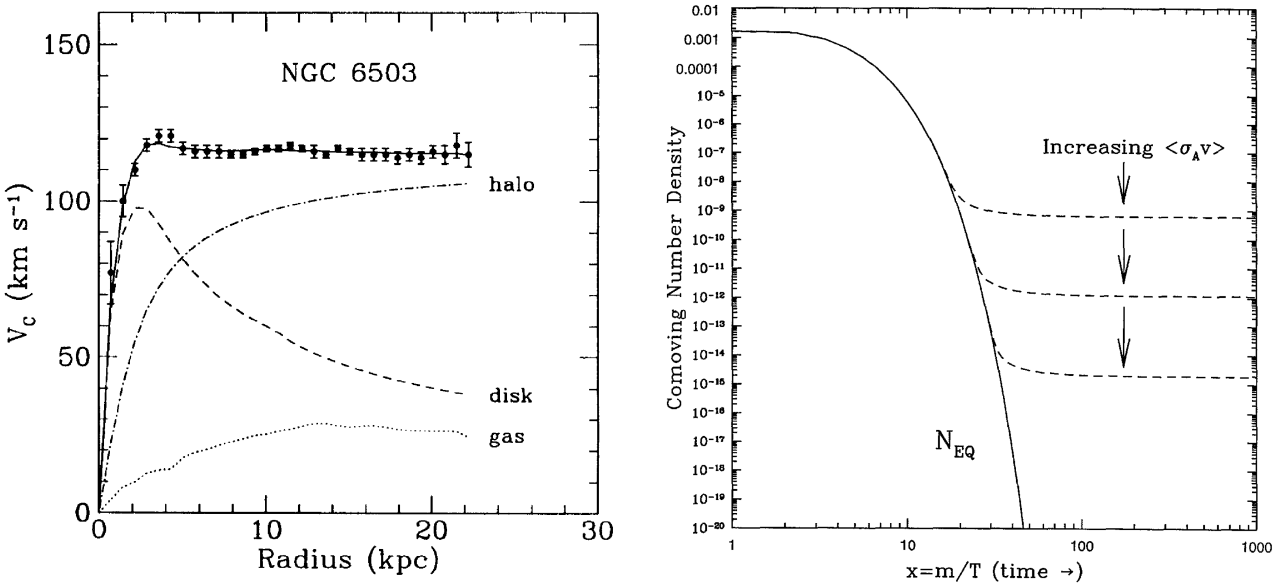

Figure 1.1: Left: Rotation speed curve data of the spiral galaxy NGC 6503 as function of distance from the galactic centre. The dashed curve is the expected velocity profile of the galactic disk based on the visible luminous mass. The dotted curve is the contribution of the interstellar gas. The dash-dot curve is the required dark matter contribution to match observation. The resulting dark-halo fit to the data is shown as solid curve. Figure from Reference [50], a similar figure was originally published in Reference [36]. **Right:** Comoving, i.e. expansion-corrected, WIMP number density as a function of WIMP mass m over temperature T (proportional to the time since the Big Bang) from the epoch of thermal equilibrium to the time of the WIMP decoupling, the freeze-out. The left-over relic WIMP density depends on the product of the thermally averaged total WIMP annihilation cross-section and the relative velocity $\langle\sigma_A v\rangle$. Figure from Reference [51].

of $\Omega_c h^2 = 0.120 \pm 0.001$ which is 5.4 times the baryonic matter density [29]. The density parameter Ω_c is normalised by the critical density $\rho_{\text{crit.}} = 3H^2/(8\pi G)$ of the Friedmann universe and $h = H_0/100\,\text{kms}^{-1}\text{Mpc}^{-1}$ is the dimensionless Hubble constant. The Hubble constant H_0 is today's value of the Hubble parameter H which describes the expansion of the universe.

1.2 Dark Matter Properties

The observations mentioned above have fixed the basic properties of dark matter, that can be summarised as *dissipationless, collisionless, cold, stable, fluid and classical* [52]. *Dissipationless* refers to its optical darkness. That is to say, dark matter interacts at most very weakly via the electromagnetic force and thus, cannot cool by radiating energy electromagnetically and, as a result, dark matter does not collapse towards a common centre unlike baryonic matter. This implies that it has no or very small electric charge, electric or magnetic dipole moments, or that it has such a high mass that it barely loses energy by bremsstrahlung. *Collisionless* means that dark matter does not interact non-gravitationally with baryonic matter, or at least not with high cross-sections. If so, dark matter could transfer linear and angular momentum which would result in collapsing small spherical dark matter objects in contrast to observations that suggest ellipsoidal halos with a substantial flattening [53,54]. Collisionless dark matter can well explain the formation of large scale structures. However, self-interacting dark matter is a possible solution to the core-vs-cusp problem as it erases small structures [55]. Observations indicate that dark matter halos of dwarf galaxies feature a constant density profile at the centre (core) unlike simulations that include only dark matter which favour a sharp density rise at small radii (cusp) for collisionless dark matter [56]. *Cold* refers to the non-relativistic speed of the dark matter at the time of decoupling, necessary for the formation of the structures ob-

served today. Alternatively, warm dark matter (WDM) can be considered with properties in between cold and hot dark matter [57]. Such WDM particles with $\mathcal{O}(1\,\mathrm{keV})$ masses were relativistic at the time of decoupling and slowed down to non-relativistic speeds during the radiation dominated era. The higher speed of the particles suppresses the formation of small scale structures and reduces the phase space density compared to CDM. Since dark matter was produced in the early universe and it is still observable today, it must be *stable* on time scales longer than the age of the universe with a lower bound of 160 Gy [58]. *Fluid* means that dark matter cannot have a mass granularity higher than $10^3 - 10^4\,\mathrm{M}_\odot$ [59–62]. Discrete dark matter induces a time-dependent gravitational potential that disrupts galaxy and cluster structures and induces noise in the power spectrum of dark matter density fluctuations. Microlensing surveys constrain the upper mass range further to the solar mass range. Objects between $10^{-7} - 10^{1}\,\mathrm{M}_\odot$ do not make up more than $\sim 20\,\%$ of the dark matter in the Milky Way halo [63,64]. The requirement that dark matter is sufficiently *classical* refers to constrains that can be set on the dark matter mass based on typical length scales ($\mathcal{O}(1\,\mathrm{kpc})$), mass densities ($\mathcal{O}(1\,\mathrm{GeV}/(\mathrm{c}^2 \cdot \mathrm{cm}^3))$) and velocity dispersions ($\mathcal{O}(100\,\mathrm{km/s})$) of galaxies and the requirement that dark matter must be confined within. For bosonic dark matter a lower mass bound of $\sim 10^{-22}\,\mathrm{eV/c^2}$ can be derived from the confinement requirement of the de Broglie wavelength in galaxies [65]. From the maximum phase space density, a lower mass bound of $\sim 25\,\mathrm{eV/c^2}$ can be derived for fermionic dark matter [66].

1.3 Dark Matter Candidates

Different possible solutions have been proposed to explain the astrophysical and cosmological observations outlined in Section 1.1. The landscape of dark matter candidates ranges over an enormous mass range of 90 orders of magnitude from fuzzy cold dark matter at $10^{-22}\,\mathrm{eV/c^2}$ to primordial black holes with a few tens of solar masses. This section can by no means be a comprehensive essay of all of these candidates but provides a concise overview of the most popular candidates or classes.

Figure 1.2 shows the rich landscape of particle dark matter theories that predict particles which can be potential dark matter candidates. The SM however, is nowhere to be found in the figure. As noted already at the beginning of this chapter, it cannot provide a candidate that constitutes the dark matter or at least not all of it. The only known neutral, massive, stable and very weakly interacting particle is the neutrino. Analogue to the CMB, the relic cosmic neutrino background (CNB) would be a plausible source of neutrinos constituting the dark matter. However, since neutrinos, unlike the CMB photons, decoupled already $\sim 1\,\mathrm{s}$ after the Big Bang due to their weak interaction strength, they are at relativistic speeds. Such *hot dark matter* is incompatible with the observed structures in the universe [67]. In addition, limits on the neutrino mass imply that the total relic density is not sufficient to be the dominant dark matter contributor [68]. This requires the introduction of one or several new BSM particles to explain the dark matter evidence. As can be inferred from Figure 1.2, the set of particle dark matter candidates forms the proverbial *particle zoo* as outlined below.

1.3.1 Weakly Interacting Massive Particles

A well-motivated class of dark matter candidates are the weakly interacting massive particles (WIMPs), that are the focus of this thesis and that have received a considerable experimental attention over the past two decades, see Section 1.4.3. WIMPs include any non-baryonic weakly-interacting particles in the mass range $\mathcal{O}(2\,\mathrm{GeV/c^2})$ to $\mathcal{O}(100\,\mathrm{TeV/c^2})$.

A widely-believed and robust production mechanism of WIMPs is referred to as *freeze-out*, able to explain the observed dark matter density [70]. In the early universe, the number densities of SM and WIMP particles were in approximate thermal equilibrium, i.e. production and annihilation rates, in particular those of WIMPs were equal, see Figure 1.1, right. However, as the universe cooled

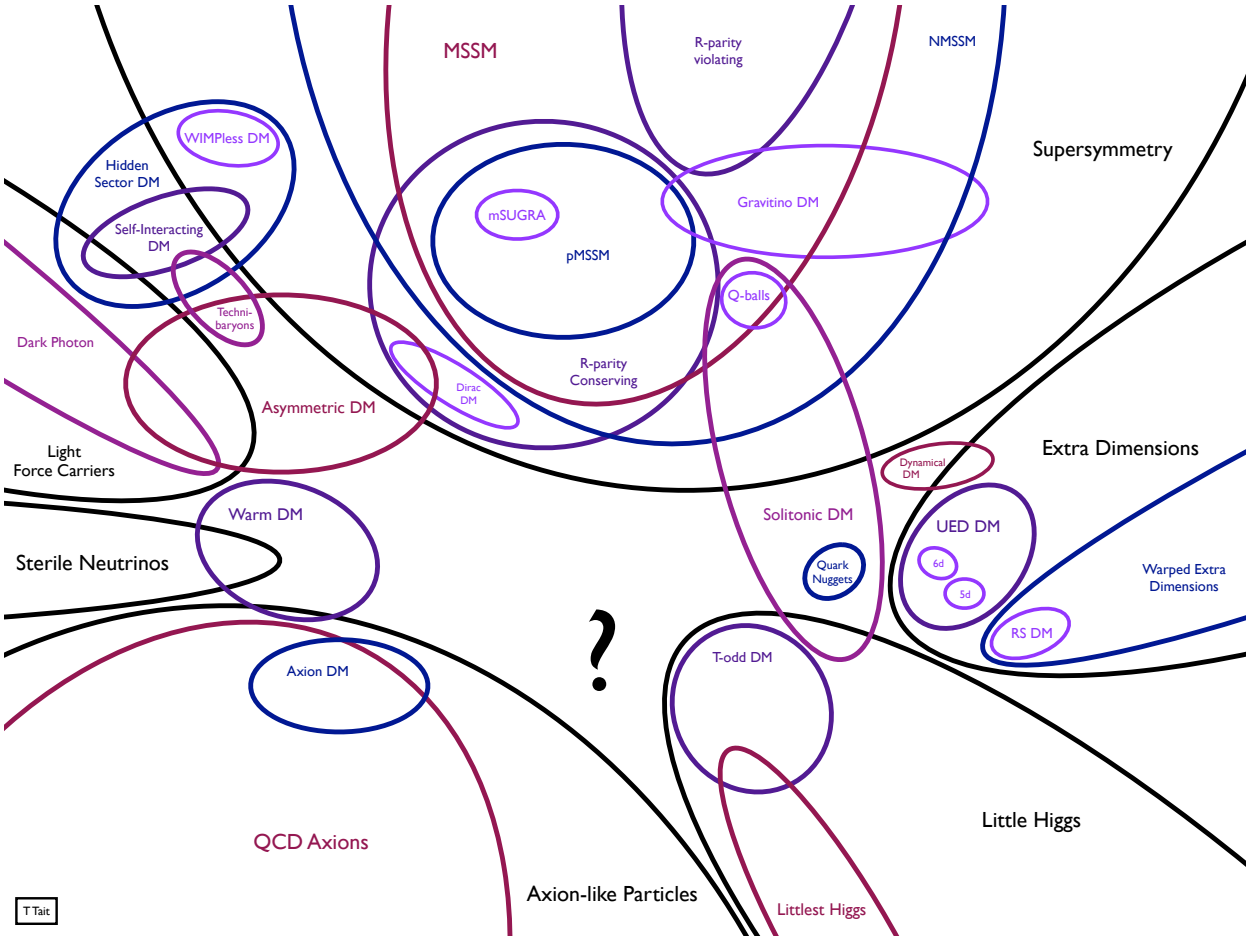

Figure 1.2: The landscape of candidate particle dark matter (DM) theories. Figure from Tim M. P. Tait [69].

by expansion and the thermal energy $k_{\mathrm{B}}T$ got smaller than the WIMP energy corresponding to its rest mass $m_\chi c^2$, the WIMP production rate fell below the WIMP annihilation rate $\Gamma_A = n_\chi \langle \sigma_A v \rangle$, decreasing the WIMP number density n_χ exponentially. We denote the product of the thermally averaged total WIMP annihilation cross-section and the relative velocity by $\langle \sigma_A v \rangle$. When the Hubble expansion rate H of the universe increased above the WIMP annihilation rate, the WIMP number density fell out of equilibrium with the thermal plasma. At the scale of weak interactions, this freeze-out happened at $m_\chi / T \approx 20 - 30\ k_{\mathrm{B}}/c^2$. Normalised by comoving volume to make it expansion-independent, the WIMP density remained constant ever since. The observed dark matter density that we mentioned in the previous section is related to the annihilation cross-section by [70, 71]

$$\Omega_{\mathrm{c}} h^2 = \frac{m_\chi n_\chi}{\rho_{\mathrm{crit}}} h^2 \approx \frac{3 \times 10^{-27}\,\mathrm{cm^3 s^{-1}}}{\langle \sigma_A v \rangle} \quad . \tag{1.3}$$

See Reference [72] for a more precise study of the relic abundance. It is called the *WIMP miracle* that a particle that interacts with the typical strength of the weak scale and that has a mass in the range of the electroweak scale, can reproduce the observed relic dark matter density. However, Equation 1.3 can actually be satisfied for a wide range of mass values and annihilation coupling constants g since $\sigma_A \propto g^4 / m_\chi^2$, which led to criticism of the WIMP miracle [73, 74].

Alternative production mechanisms have been proposed for cases in which the product $\langle \sigma_A v \rangle$ is either too high or too low to generate directly the correct relic dark matter abundance [71]. In

particular, the so-called *freeze-in* mechanism has been considered for feebly interacting massive particles (FIMPs) [75]. In this scenario, the initial dark matter abundance was negligible. FIMPs have such a low annihilation cross-section that they never reached thermal equilibrium in the early universe. Thus, they were almost decoupled from the plasma. Still, they were feebly produced from decays and collisions of SM particles, slowly increasing their abundance. As the thermal energy $k_\mathrm{B}T$ of the plasma fell below the energy corresponding to the rest mass $m_\chi c^2$ of the FIMPs, FIMPs could be produced most efficiently for renormalisable interactions, i.e. for those involving combinations of field operators with low enough dimension. At even lower temperatures, the production rate was exponentially suppressed and the dark matter density stayed constant. This freeze-in happened at $m_\chi/T \approx 2-5\ k_\mathrm{B}/c^2$. Unlike in the freeze-out mechanism in which the dark matter particles diverged away from thermal equilibrium, they converged towards equilibrium in the freeze-in mechanism. Another mechanism includes a freeze-out with a subsequent decay to lighter particles, the so-called superWIMPs [76].

The possible mass range of WIMPs can be constrained as follows. The Lee-Weinberg bound [77] constrains the lower end of the range to $\mathcal{O}(2\,\mathrm{GeV/c^2})$. For a weak interaction with the Z-boson as mediator, we have $\sigma_A \propto m_\chi^2/M_\mathrm{Z}^4$. The lower the mass of the WIMP, the lower the annihilation cross-section and thus, the earlier the freeze-out of the WIMP. This leads to a higher relic abundance at a higher temperature. A lower bound of $\mathcal{O}(2\,\mathrm{GeV/c^2})$ can be derived to attain the curvature of the universe and avoid overclosing. The upper limit of $\mathcal{O}(100\,\mathrm{TeV/c^2})$ is a partial-wave unitarity bound that sets a maximum possible annihilation cross-section and thus a minimum possible relic abundance [78].

WIMPs emerge from a variety of BSM theories. The most popular ones in Figure 1.2 can be identified as R-parity conserving supersymmetry (SUSY) [70], universal extra dimension (UED) theories with KK-parity [79] and T-odd parity little Higgs theories [80]. The lightest particles predicted by these theories are stable due to parity conservation and can be shown to be viable WIMP candidates. The minimal supersymmetric extension to the standard model (MSSM) for instance, which provides in particular a natural solution to the hierarchy problem, involves a lightest supersymmetric particle (LSP) such as the lightest neutralino which is stable due to R-parity conservation. The respective particle candidates of the other two theory classes are the lightest Kaluza-Klein particle (LKP) and the lightest T-odd particle (LTP).

1.3.2 Other Particle Candidates

As mentioned at the beginning of this section, there is a large number of particle candidates of which the addressed WIMPs, FIMPs and super-WIMPs classify only a few. Another popular dark matter candidate is the axion [81], that emerges from the spontaneous breaking of the Peccei–Quinn symmetry [82] and was found to solve the strong CP (charge conjugation parity) problem [83, 84]. Axions are classified as ultralight dark matter ($< \mathcal{O}(1\,\mathrm{eV/c^2})$) and belong to the axion-like particles (ALPs), a more general set of dark matter candidates. Light dark matter candidates ($< \mathcal{O}(1\,\mathrm{GeV/c^2})$) involve for instance the hidden-sector particles sterile neutrinos [85] and dark photons [86]. Located above the WIMP mass range are WIMPzillas ($10^{12} - 10^{16}\,\mathrm{GeV/c^2}$) [87] and composite dark matter like Q-balls [88]. For a more complete overview of the field, we suggest to consult the wide literature [68, 89, 90].

1.3.3 Non-Particle Candidates

Albeit this chapter is on particle dark matter, for completeness we end this section with a brief review of alternative hypotheses. Non-particle explanations can be classified into two categories: macroscopic dark objects and modified gravity (MOG). Since any type of stable and non-relativistic matter that predominantly or even exclusively interacts via the gravitational force could explain the

dark matter phenomena, there is a priori no necessity to introduce a new particle. Such theories include massive astrophysical compact halo objects (MACHOs) such as (primoridal) black holes, neutron stars or brown dwarfs and macroscopic (Macros) dark matter [91]. Microlensing surveys of stars in the Magellanic Clouds have shown that only a fraction of the dark matter halo of the Milky Way can be made of MACHOs [63, 92]. These results depend however on the used halo model and an all-MACHO halo cannot be rejected [93].

MOG theories are designed to explain the gravitational anomalies by modifications of the gravitational theory that are required at large scales. An early example of such theories was introduced by the physicist Mordehai Milgrom in 1983 [94]. Modified Newtonian dynamics (MOND) was created to explain the galaxy rotation curves by a modification of Newton's laws. The observations could be explained if the gravitational force on stars at large radii from the galactic centre was inversely linearly, instead of quadratic, proportional to the radius. A relativistic extension of MOND was developed by the theoretical physicist Jacob Bekenstein in 2004 [95]. As a relativistic theory, Tensor–Vector–Scalar gravity (TeVeS) allows for gravitational lensing like general relativity. However, while MOG theories can be adjusted to explain certain phenomena like the galaxy rotation curves, they have difficulties to consistently explain all the dark matter evidence. For instance, MOG theories are challenged by galaxy collisions, where a clear offset of the gravitational and luminous centre is observed, by the CMB power spectrum and structure formation. Comparisons of the propagation speed of electromagnetic and gravitational waves also disfavour many MOG theories [96]. Furthermore, the observation of a galaxy that does not seem to contain dark matter at all, disfavours MOG theories due to universality of the laws of nature [97].

1.4 Direct Dark Matter Detection

1.4.1 Detection Approaches

We addressed the astrophysical and cosmological evidence for dark matter in Section 1.1. Technically, we have thus detected dark matter by its gravitational interaction, assuming that our theory of gravity is sufficiently precise. If dark matter has a particle nature and if it was in equilibrium with SM particles at some point in time, we would expect additional non-gravitational interactions with SM particles such as illustrated in Figure 1.3, left. A record of such interactions is what the hunt for dark matter is about and what dark matter detection commonly refers to. The observation of such interactions would allow physicists to constrain or even measure the properties of the dark matter particle(s). If the properties would be set in such way that the particle(s) could explain all of the gravitationally observed phenomena, it would be fair to claim that dark matter was *found*. More likely, however, is that non-gravitational detections would open a new chapter in particle physics and demand new or modified models that in turn would predict the existence of other particle species. Figure 1.3, left, shows three different approaches to search for non-gravitational interactions: production, indirect detection and direct detection. At sufficiently high energies, dark matter particles could be produced from SM particles in particle colliders such as the Large Hadron Collider (LHC) [98]. A collision topology involving a dark matter particle would then be seen as a missing conserved quantity in the detector, such as missing transverse energy or momentum. A drawback of this approach is that a new particle, if produced, must by no means be stable or the one constituting the dark matter. The inverse process of dark matter production is annihilation. The observation of the annihilation products is referred to as indirect detection. Such products could be gamma rays, neutrinos, electron-positron pairs or proton-antiproton pairs and could be observed with space- or ground-based particle detectors and telescopes. The highest flux of annihilation products is expected from regions with a high dark matter density like the centres of galaxies. Examples of indirect detection experiments are the Fermi Gamma-ray Space Telescope [99], HESS [100], CTA [101] and IceCube [102], see Reference [103] for

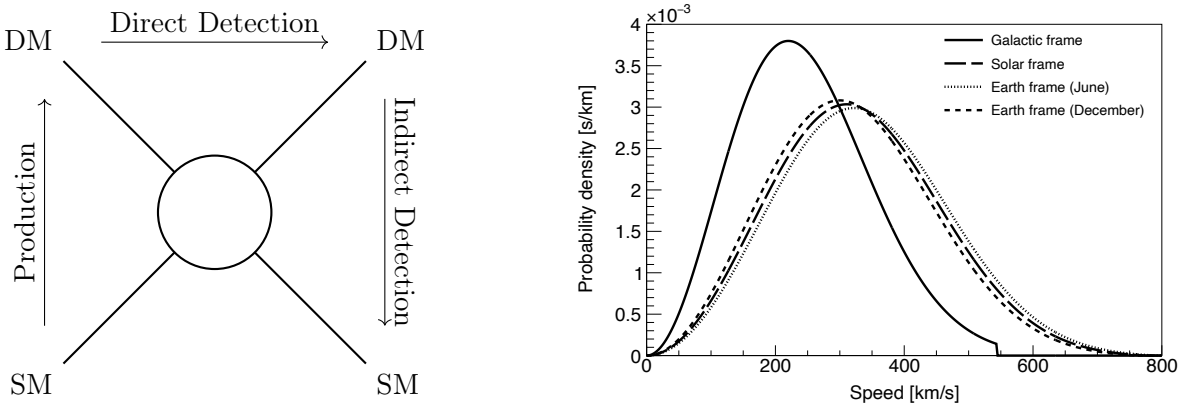

Figure 1.3: Left: Schematical Feynman diagram to illustrate the three possible interaction directions of standard model (SM) and dark matter (DM) particles, assuming the latter feature additional non-gravitational interactions. The arrows indicate the direction of time. Dark matter particles can be produced from SM particles at particle colliders. Its production would be visible as a collision topology with a missing conserved quantity such as missing transverse energy or momentum. Dark matter particles can be directly detected when scattering off target SM particles, leaving a recoil signature in a particle detector such as the TPCs discussed in the next chapter. Dark matter particles can annihilate and produce SM particles such as gamma-ray photons or neutrinos that can be detected by space-based particle detectors or ground-based Cherenkov telescopes. **Right:** Normalised dark matter Maxwell-Boltzmann speed distribution of the standard halo model in the galactic, solar and earth reference frames. The truncation due to the escape velocity is clearly visible in the galactic rest frame. We used $v_{\mathrm{esc}} = 544\,\mathrm{km/s}$, $v_0 = 220\,\mathrm{km/s}$, $v_\odot = 232\,\mathrm{km/s}$ and $\Delta v_E = 15\,\mathrm{km/s}$ as parameters, see text.

a review. However, the challenge for indirect searches is to distinguish the potential dark matter annihilation signals from other astrophysical processes. It is considered a direct detection when a dark matter particle of the Milky Way halo scatters off a SM particle in a particle detector. As these interactions are expected to be extremely rare, the background in such detectors must be mitigated and well-known. A particular detector technology for direct detection, the dual-phase time projection chamber (TPC), is the focus of this thesis. Preferably, dark matter particles are seen in more than one of the outlined approaches for complementary searches.

1.4.2 Elastic Nuclear Scattering

Here, we present the general detection idea of direct searches. Suppose dark matter scatters off an atomic target, the interaction can either be with the atomic electrons or with the nucleus, producing an electronic (ER) or nuclear recoil (NR), respectively. Electrically neutral WIMPs with masses above $\mathcal{O}(1\,\mathrm{GeV/c^2})$ would be preferably scattering off the atomic nuclei. For simplicity we treat here only elastic recoils, i.e. the nucleus will not be left in an excited state after the interaction.

For a simple illustration of the direct detection principle, it is enough to assume the idealised standard halo model [104] for our Milky Way. The standard halo is an isotropic, isothermal sphere with a density profile $\rho(r) \propto r^{-2}$, corresponding to the expected dark matter distribution that we derived in Section 1.1 to obtain a flat rotation curve at large radii. The average local density in our solar system is $\rho_0 = 0.3\,\mathrm{GeV/(c^2 \cdot cm^3)}$ [105]. The dark matter velocity $v = \|\vec{v}\|$ follows a Maxwell-Boltzmann distribution [106]. In the galactic rest frame, we have

$$f(v) = \begin{cases} \frac{1}{N_{\mathrm{esc}}} \left(\frac{3}{2\pi\sigma_v^2}\right)^{\frac{3}{2}} \exp\left(-\frac{3v^2}{2\sigma_v^2}\right) & , v < v_{\mathrm{esc}} \\ 0 & , v \geq v_{\mathrm{esc}} \end{cases} , \tag{1.4}$$

where $\sigma_v = \sqrt{3/2} v_0$ is the one-dimensional velocity dispersion, related to the most probable circular

speed v_0 whose standard value is 220 km/s. As shown in Figure 1.3, right, the distribution has a cutoff at the escape velocity $v_{\mathrm{esc}} = 544\,\mathrm{km/s}$ of the Milky Way. The normalisation

$$N_{\mathrm{esc}} = \mathrm{erf}\,(\frac{v_{\mathrm{esc}}}{v_0}) - \frac{2v_{\mathrm{esc}}}{\sqrt{\pi}v_0}\exp\left(-\left(\frac{v_{\mathrm{esc}}}{v_0}\right)^2\right) \tag{1.5}$$

accounts for the truncation due to the cutoff. However, an observer in the earth's rest frame would observe a Galilean-boosted velocity distribution. Assuming circular orbits, the solar system is moving with a speed of $v_\odot = 232\,\mathrm{km/s}$ [107]. Moreover, this speed is modulated with an amplitude of $\Delta v_E = 15\,\mathrm{km/s}$ [108] over the course of a year due to the earth's revolution around the Sun. The boosted speed distributions are also shown in Figure 1.3, right. One can additionally also consider the speed modulation due to the rotation of the earth. This speed however is less than 0.5 km/s, depends on the position on the earth's surface and is thus neglected here. These effects, of course, together with the ellipticity of the orbits, lead generally to a three-dimensional time- and direction-dependent velocity distribution. However, most direct detection techniques are not directionally sensitive and a measurement of a time-modulation of dark matter signals requires a decent rate. We thus treat the simplest case in the following, that exploits the energy-dependence of the signal and assume the directional and temporal dependencies to be integrated out. We refer to Reference [109] and references therein for more information, which we loosely follow for the subsequent discussion.

A potential dark matter signal in a direct detection experiment would be visible as an excess in the recoil spectrum. This would allow to constrain the mass and interaction cross-section of the WIMP given the astrophysical input of the dark matter halo. WIMPs of mass m_χ propagating at a speed v would lead to a total rate of

$$R = N n_\chi \langle \sigma_{\chi N} v \rangle \tag{1.6}$$

in a detector with N target nuclei for an elastic WIMP-nucleus scattering cross-section $\sigma_{\chi N}$. For a number density $n_\chi = \rho_0/m_\chi$, the differential recoil energy (E_R) event rate, normalised by the target mass Nm_N, where m_N is the mass of a single target nucleus, is

$$\frac{\mathrm{d}R}{\mathrm{d}E_R} = \frac{\rho_0}{m_\chi m_N}\int\limits_{v_{\mathrm{min}}}^{v_{\mathrm{esc}}} \frac{\mathrm{d}\sigma_{\chi N}(E_R, v)}{\mathrm{d}E_R} f(v) v\,\mathrm{d}^3 v \quad . \tag{1.7}$$

We show the differential rate in Figure 1.4 for various noble gas and semiconductor targets at a fixed WIMP mass and for xenon at different WIMP masses. The minimum WIMP speed v_{min} that is required to produce a recoil can be calculated from the non-relativistic kinematics of a back-to-back scattering:

$$v_{\mathrm{min}} = \sqrt{\frac{E_{R,\,\mathrm{max}} m_N}{2\mu_{\chi N}^2}} \quad , \tag{1.8}$$

where we defined the reduced mass of the system WIMP-nucleus as:

$$\mu_{\chi N} \coloneqq \frac{m_\chi m_N}{m_\chi + m_N} \quad . \tag{1.9}$$

One can distinguish spin-independent (SI) and spin-dependent (SD) interactions of the WIMP with the nuclei and thus, split the expression for the cross-section in these two components,

$$\frac{\mathrm{d}\sigma_{\chi N}}{\mathrm{d}E_R} = \frac{m_N}{2v^2\mu_{\chi N}^2}\left(\sigma_0^{\mathrm{SI}} F_{\mathrm{SI}}^2(E_R) + \sigma_0^{\mathrm{SD}} F_{\mathrm{SD}}^2(E_R)\right) \quad , \tag{1.10}$$

where we included the nuclear form factors $F_{\mathrm{SI,SD}}$ for each mode. These form factors account for the fact that the nucleus has a substructure which can be resolved at high momentum transfers when

the de Broglie wavelength of the mediator gets comparable to the size of the nucleus. Larger nuclei can be resolved at lower momentum transfer. This reduces the cross-section already at lower recoil energies, as can be seen for xenon in Figure 1.4, left. With σ_0^{SI} and σ_0^{SD} we denote the cross-sections of the two modes at zero momentum transfer. For spin-independent interactions and at low momentum transfers, however, the WIMP interacts with the nucleus as a whole and the scattering amplitudes of all nucleons (Z protons and $(A-Z)$ neutrons) add coherently. At zero-momentum transfer, we can write the total spin-independent cross-section in terms of the couplings to protons and neutrons, f_{p^+,n^0}:

$$\sigma_0^{\mathrm{SI}} = \frac{4\hbar^2 c^2}{\pi} \mu_{\chi N}^2 \left(Z f_{p^+} + (A-Z) f_{n^0} \right)^2 \quad . \tag{1.11}$$

Usually, the coupling strengths of protons and neutrons are assumed equal, $f_{p^+} = f_{n^0}$, and the latter expression takes the form

$$\sigma_0^{\mathrm{SI}} = A^2 \frac{\mu_{\chi N}^2}{\mu_{\chi n}^2} \sigma_{\chi n} \quad , \tag{1.12}$$

where $\sigma_{\chi n}$ is the WIMP-nucleon cross-section and $\mu_{\chi n}$ is the reduced WIMP-nucleon mass. This expression shows that it is preferable to have targets with a high nuclear mass for spin-independent dark matter searches. The A^2-dependence is even enhanced to an approximate A^4-dependence at very high WIMP masses. For $m_\chi \gg m_{N,n}$, we have $\mu_{\chi N,\chi n} \approx m_{N,n}$ and thus $\lim_{m_\chi \to \infty} \sigma_0^{\mathrm{SI}} = A^4 \sigma_{\chi n}$ with $m_N \approx A m_n$. Please note, that we state this dependence for the cross-section at zero-momentum transfer and that the total cross-section is subject to the form factor, see Equation 1.10.

For spin-dependent interactions, only unpaired nucleons, which have a non-zero net spin, contribute significantly to the cross-section. Thus, only isotopes with an odd number of protons or neutrons are sensitive to such interactions and there is no A^2-dependence in the cross-section. The spin-dependent cross-section in terms of the effective couplings a_{p^+,n^0} can be written [109]

$$\sigma_0^{\mathrm{SD}} = \frac{32}{\pi} \mu_{\chi N}^2 G_{\mathrm{F}}^2 \left(a_{p^+} \langle S^{p^+} \rangle + a_{n^0} \langle S^{n^0} \rangle \right)^2 \frac{J+1}{J} \quad , \tag{1.13}$$

where G_{F} is the Fermi coupling constant, J is the total nuclear spin and $\langle S^{p^+,n^0} \rangle$ are the expectation values of the nuclear spin state due to the proton and neutron groups.

We note that the presented modelling of WIMP-nucleus interactions with spin-independent and spin-dependent contributions is only approximate. More detailed calculations use a non-relativistic effective field theory with 14 operators of which the discussed spin-independent and spin-dependent interactions, although dominant, are only represented by two [110–113]. This approach reflects the composite nature in detail, going beyond the description of the form factors that attempt to model the finite spatial extend of the spin and charge densities [109].

1.4.3 Direct Detection Experiments

In the final section of this particle dark matter introduction, we review briefly the different existing experimental approaches of direct detection [116,117], before we focus on a certain detector technology in the next chapter and for the rest of the thesis. As discussed in the previous section, a dark matter particle that scatters in the detector target leads to a recoil energy. This energy can be transformed into a signal that can be read out. In Figure 1.5, we show the three signal channels of which one or a combination of several are exploited by direct detection experiments: heat or phonons, charge and light. It is advantageous to read more than one channel or ideally all three. This allows for ER/NR discrimination, a low energy threshold and good energy resolution. In the following, we guide the reader through Figure 1.5 with concrete example experiments that belong to the signal channel categories. The spin-independent WIMP-nucleon limits set by selected former or ongoing experiments together with projected sensitivities of upcoming detectors are shown in Figure 1.6.

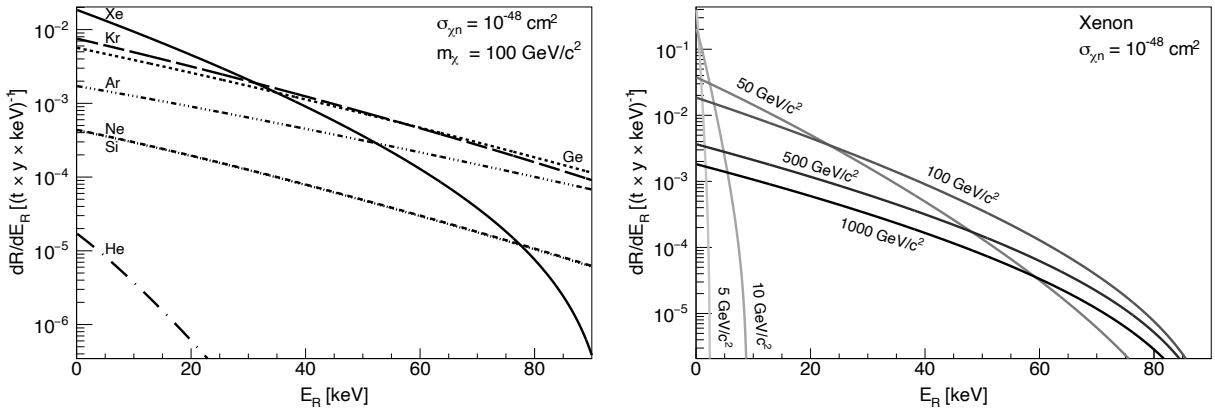

Figure 1.4: Expected differential spin-independent scattering rates of WIMPs with target nuclei versus recoil energy for a WIMP-nucleon cross-section of $\sigma_{\chi n} = 10^{-48}\,\mathrm{cm}^2$. The calculations are based on the standard halo model and the Helm form factor [114] with the parametrisation from Reference [115]. **Left:** At a WIMP mass of $m_\chi = 100\,\mathrm{GeV/c^2}$ for noble gas and semiconductor targets. Due to the similar mean atomic mass, the curves for neon and silicon are overlapping. The scattering rates are generally higher for targets with higher atomic mass. However, the form factor of xenon leads to a pole in the spectrum at $E_R \sim 94\,\mathrm{keV}$ which highly suppresses the rate at high recoil energies. At this momentum transfer, the contributions of the nucleons cancel one another out [115]. In particular, the scattering rate of xenon gets lower than the one for argon above $E_R \sim 52\,\mathrm{keV}$. **Right:** For xenon at different WIMP masses. The rate is generally reduced for higher WIMP masses as the number density is reduced. However, the spectra for higher mass WIMPs extend to higher recoil energies limited by the escape velocity.

The category of experiments measuring heat or phonons can be divided into two main approaches: cryogenic bolometers or calorimeters, and bubble chambers using superheated fluids. Experiments with the former approach use crystals that are kept close to absolute zero and detect tiny temperature increases from particle interactions within the crystal. An example experiment was CRESST [118] which used sapphire crystals (Al_2O_3) with a total mass of 262 g held at $\sim$ 15 mK and tungsten transition edge thermometers. Cryogenic bolometers have typical energy thresholds of $\sim$ 1 keV [119]. Bubble chambers on the other hand use a superheated liquid that is held in a metastable state. Energy depositions from particle interactions induce phase transitions that lead to the formation of bubbles and their extension to macroscopic size. These bubbles can be detected by optical imaging and by their acoustic signal. The energy threshold is tunable by pressure and temperature changes and is typically also $\sim$ 1 keV. Above a few keV energy threshold, bubble chambers are insensitive to ER background [120]. A drawback of this technique is that the recompression of the fluid after bubble formation leads to a significant downtime. An example experiment was PICO-60 using 36.8 kg of CF_3I [121] or 52.2 kg C_3F_8 [122] and its predecessor PICO-2L with 2.91 kg C_3F_8 [123] (upcoming are PICO-40L and PICO-500 [124]). Natural fluorine only contains the stable isotope ^{19}F which is very sensitive to spin-dependent WIMP-proton interactions due to its high spin enhancement factor [125]. For this reason, bubble chambers with fluorine targets are the leading technology in the search for such interactions. The earlier PICASSO experiment used 32 droplet detectors with in total 3 kg of C_4F_{10} [126]. To overcome the challenge of long downtimes of conventional bubble chambers, such droplet detectors disperse the target in polymerised water-based gels. Particle interactions can turn only one droplet inactive at a time and recompression is thus needed rarely. While this technique allows for duty cycles of almost 100 %, it is at the cost of target mass and background [127].

By additionally exploiting the charge or light channel, cryogenic bolometers and bubble chambers can increase their potential for particle discrimination and reduce their energy threshold. A well-known example of a cryogenic bolometer with charge readout is SuperCDMS. While SuperCDMS deployed 600 g germanium at $\sim$ 50 mK [128], its predecessor CDMS II used 230 g germanium and

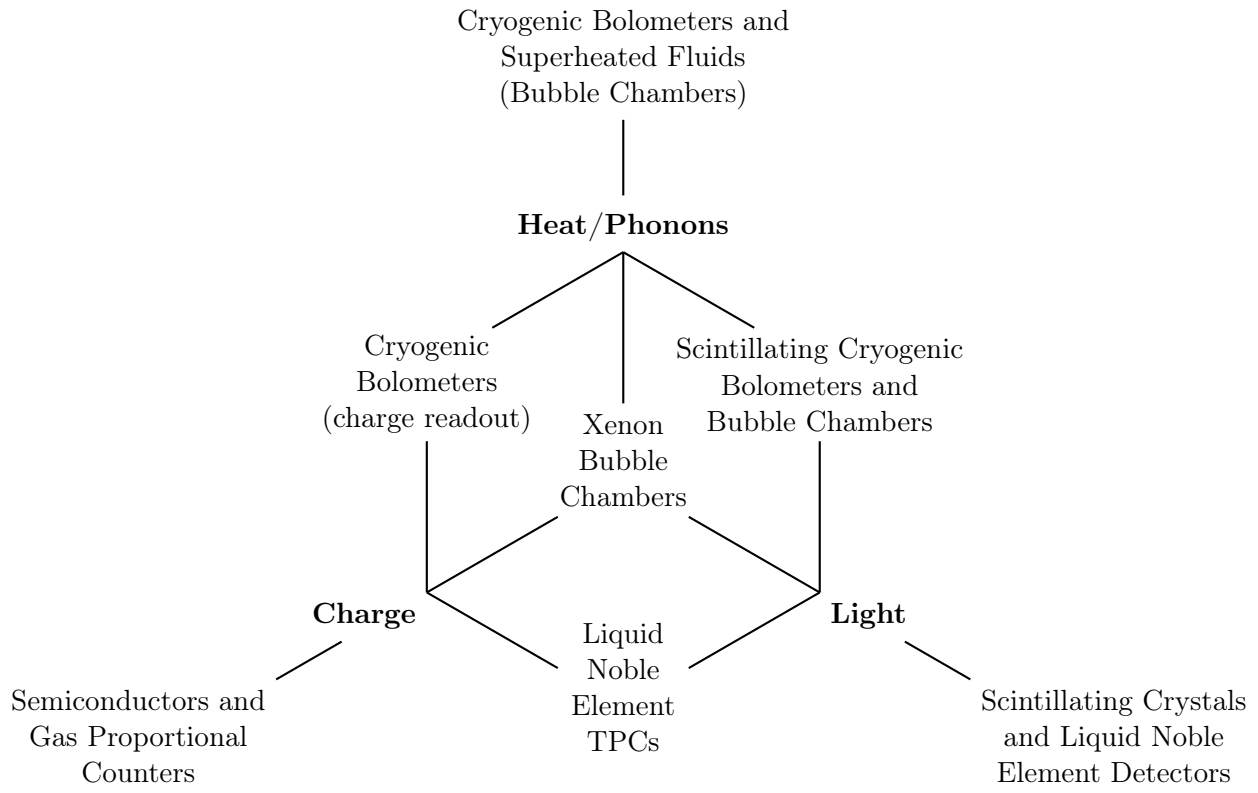

Figure 1.5: Signal channels of direct detection experiments and associated detector technologies.

100 g silicon [129]. The detectors are equipped with tungsten transition edge sensors as phonon detectors. Electric fields within the superconductors allow for an additional charge readout from the drift of electron holes and electrons. Further examples include the CDEX [130, 131] and EDELWEISS experiments [132–134] that use germanium crystals. These detectors have good sensitivities to low-mass WIMPs due to their typically low energy threshold of $\mathcal{O}(10 - 100\,\mathrm{eV})$. An example of a scintillating cryogenic bolometer experiment is CRESST-III [135] (and its predecessor CRESST-II [136]) which uses a $CaWO_4$ crystal. In addition to the phonon readout of CRESST-I, the setup contains a photo-sensitive silicon-on-sapphire wafer that is coupled to another transition edge sensor and allows to read the light signal. The same technique is exploited by the COSINUS experiment with NaI crystals held at $\sim 10\,\mathrm{mK}$ [137]. Scintillating cryogenic bolometers can reach energy thresholds of $\mathcal{O}(10\,\mathrm{eV})$ [135]. Scintillating bubble chambers additionally exploit the light channel. The SBC experiment [138, 139] uses xenon-doped liquid argon as superheated fluid and detects the argon scintillation light, wavelength-shifted by the xenon dopant, with silicon photosensors. Xenon bubble chambers are also investigated [140]. Achievable energy thresholds are reduced compared to traditional bubble chambers and estimated to be $\mathcal{O}(10 - 100\,\mathrm{eV})$. Bubble chambers exploiting all three channels – heat, light and charge – are object of current R&D efforts [141].

The category of experiments measuring only charge can also be divided into two main approaches: semiconductors and gas proportional counters. A prime example of the first kind is DAMIC [145] which uses seven 6 g silicon charge-coupled devices (CCDs). Like discussed before for the cryogenic bolometers with charge readout, electron holes and electrons produced by particle interactions can be drifted to the surface by an electric field. A high pixel density allows for a precise two-dimensional position reconstruction. The third dimension can be inferred from lateral charge diffusion during the drift. The energy threshold of such devices is set by the band gap of the semiconductor and hence typically in the order of $\mathcal{O}(1\,\mathrm{eV})$, with analysis thresholds of $\mathcal{O}(10\,\mathrm{eV})$ [145]. This makes semicon-

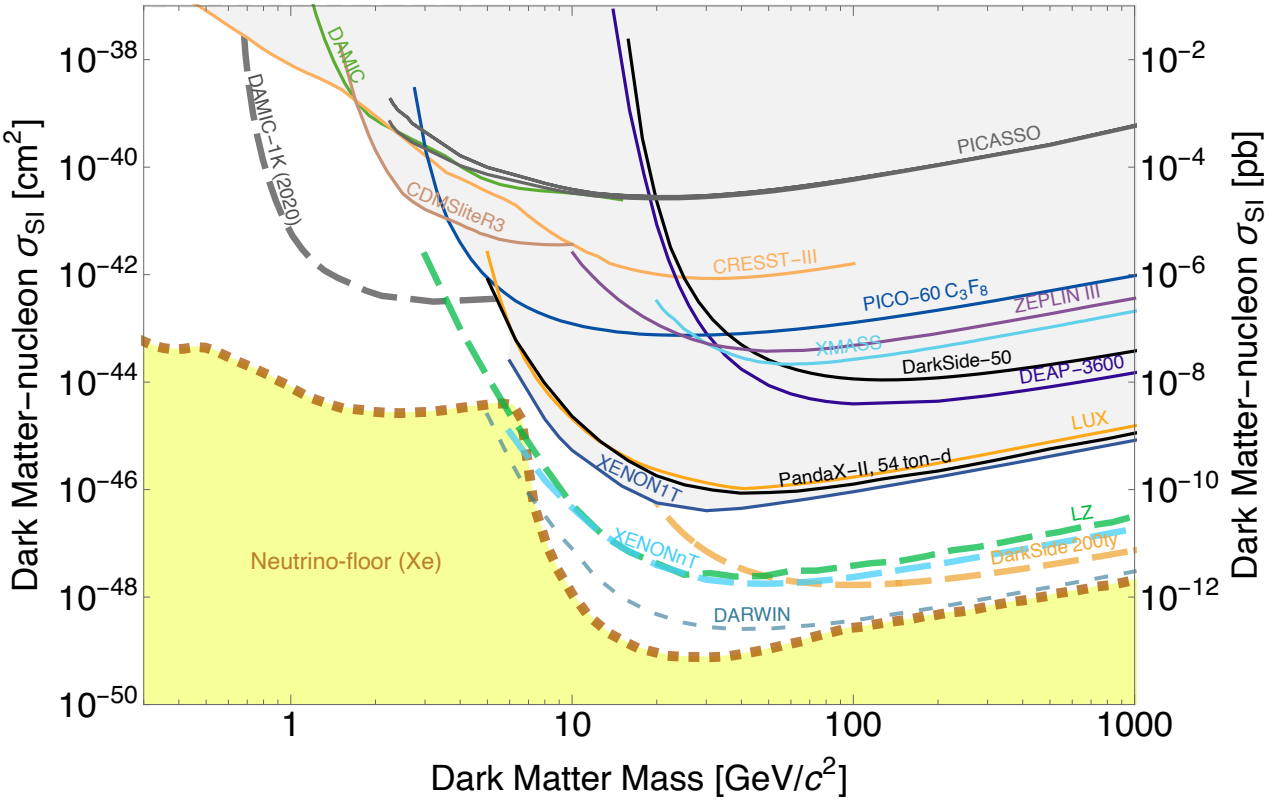

Figure 1.6: Past and present spin-independent exclusion limits on the WIMP-nucleon cross-section together with the projected sensitivities of the current generation experiments XENONnT and LZ. DARWIN will push these sensitivities by another order of magnitude and ultimately reach the xenon *neutrino floor* [142], or more recently referred to as *neutrino fog* [143]. Figure created with the Dark Matter Limit Plotter v5.16 [144].

ductor detectors very sensitive to low-mass WIMPs. Other example experiments are CoGeNT [146], which employs a 443 g germanium detector, and the silicon CCD experiment SENSEI [147]. Gas proportional counters include NEWS-G that operated a 60 cm prototype spherical proportional counter with neon and methane [148] and DRIFT-IId, a negative-ion TPC with a gas mixture of CS_2, CF_4 and O_2 [149]. Such detectors drift the charge produced in the gas targets towards a readout electrode and allow for position reconstruction.

The only-light channel distinguishes two detector types: scintillating crystals and liquid noble element detectors. A well-known example of a detector of the first type is DAMA/LIBRA, the successor of DAMA/NaI, which uses NaI(Tl) crystals with a mass of 242.5 kg read out with photomultiplier tubes. The experiment claims a $12.9\,\sigma$ evidence for a modulating dark matter signal, originating from the earth's motion around the Sun [150], cf. discussion in Section 1.4.2. This detection claim is in strong tension with observations of other experiments such as the ones shown in Figure 1.6. The experiments COSINE-100 [151], ANAIS-112 [152] and KIMS [153] with 106 kg, 112.5 kg and 17.4 kg of NaI(Tl), respectively, use the same technology as DAMA/LIBRA for a direct model-independent test of the claim. The results of these experiments tend to disfavour the measurements of DAMA/LIBRA but so far lack exposure for a robust rejection. Liquid noble element detectors reading scintillation light include DEAP-3600 [154] which uses 3.3 t of argon and XMASS [155] which uses 832 kg of xenon. An older example single-phase detector was ZEPLIN I with a 5 kg active xenon mass [156]. Detectors of this category have typical energy thresholds of $\mathcal{O}(1\,\mathrm{keV})$.

The final category are liquid noble element TPCs that simultaneously exploit the charge and the

light signal. The charge readout can either be performed directly with charge collecting electrodes in single phase or via proportional scintillation in dual-phase TPCs. The latter is discussed in detail in the next chapter. These detectors have typical energy thresholds of $\mathcal{O}(1\,\mathrm{keV})$, a strong ER/NR discrimination power and are scalable to great sizes. Present and current dual-phase TPCs using xenon include the experiments XENON10/100/1T/nT [1, 5, 157, 158] that grew from 14 kg to 5.9 t active mass, ZEPLIN II/III [159, 160], LUX [2], LUX-ZEPLIN [161] with active masses from 12 kg to 7.0 t and PandaX-I/II/4T [3,7,162,163] with active masses from 37 kg to 4 t. The next-generation detector DARWIN [8] is the motivation for this thesis and is discussed in detail in Chapter 3. Examples for dual-phase TPCs using argon are DarkSide-50 [4] and the future DarkSide-20k [9] with active masses of 46 kg and 23 t as well as WARP [164] and ArDM [165]. The dual-phase TPC detector technology is the topic of the next chapter with a focus on the noble gas xenon as detector medium. However, simultaneous readout of charge and light signals is not only possible in two-phase detectors but also in single phase. The charge can then either be read out by proportional scintillation light produced in the high-field regions around thin wires [166] or by the drift-induced charge on electrodes. The latter is not exploited as detector technology for dark matter searches due to its high threshold on the charge signal. It can however be used for other purposes like in EXO-200 and nEXO for the search for the neutrinoless double beta decay in xenon [167, 168] or like in MicroBooNE as argon neutrino beam detector [169].

Chapter 2

Dual-Phase Xenon Time Projection Chambers

Xenon is widely used as both sensitive target and radiation source in time projection chambers (TPCs) for various rare event searches. These include e.g. searches for neutrinoless double beta decay [16, 167, 170–172], the extremely rare decay of ^{124}Xe via double electron capture [173, 174], the measurement of low-energy solar neutrinos [175] and searches for solar axions, axion-like particles and dark photons [176–178]. Xenon is furthermore successfully deployed in the search for WIMP dark matter in the GeV/c^2 to TeV/c^2 mass range. In particular, TPCs operated in dual-phase mode with liquid xenon (LXe) at the bottom and a gaseous xenon (GXe) layer at the top are among the leading technologies in the past, present and near-future hunt for WIMPs [1, 2, 5, 7, 8, 161, 179].

This chapter is structured as follows: In Section 2.1, we present the key properties of xenon that make it an ideal detector medium for rare particle interactions. We present the microphysics of a particle interaction in LXe in Section 2.2 and the subsequent response of LXe detectors in Section 2.3. Finally, in Section 2.4, we explain the working principle of dual-phase xenon TPCs and discuss common challenges of this detector technology.

2.1 Xenon as Sensitive Target and Radiation Source

In this section we summarise the relevant properties of xenon as detector medium and motivate its use as dark matter target and source of rare nuclear decays. A comprehensive review of that topic can be found in Reference [180] and a list of the most important physical properties is provided in Table 2.1.

Xenon was discovered by the British chemists William Ramsay and Morris Travers in 1898 [181] and was named after the ancient greek word for stranger or foreigner, $\xi\acute{\epsilon}\nu o\varsigma$, referring to its low abundance of 0.09 ppm in air. Later in 1904, William Ramsay was awarded with the Noble Price in Chemistry "in recognition of his services in the discovery of the inert gaseous elements in air, and his determination of their place in the periodic system" [182].

2.1.1 Atomic and Nuclear Properties

Xenon is the noble element with the highest atomic number of $Z = 54$ with stable isotopes and is found in period 5, group 18 in the periodic table. As a noble gas, xenon has a full valence electron shell with the electron configuration $1\,s^2\,2\,s^2\,2\,p^6\,3\,s^2\,3\,p^6\,3\,d^{10}\,4\,s^2\,4\,p^6\,4\,d^{10}\,5\,s^2\,5\,p^6$. Noble gases are generally chemically inert. Heavy and large noble gas atoms, however, have lower ionisation energies because their nucleus is shielded by the inner electrons. This allows for the formation of typically unstable noble gas compounds with electronegative elements. Among all noble gases, most of such noble gas compounds like fluorides and oxides are known for xenon.

In Table 2.1, we provide a list with the naturally occurring xenon isotopes and their relative abundances. Of those, all isotopes are either long-lived or stable. ^{126}Xe and ^{134}Xe are suspected of

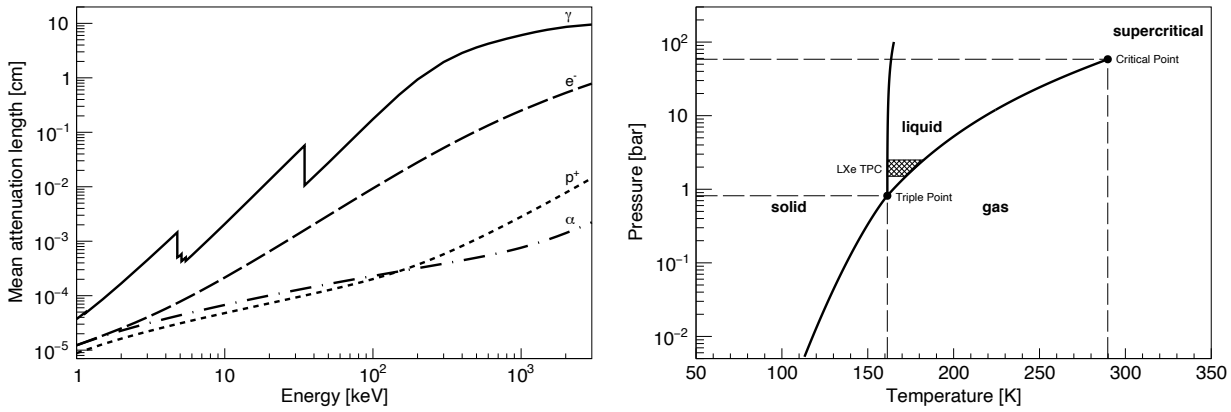

Figure 2.1: Left: Mean attenuation length of photons (γ), electrons (e^-), protons (p^+) and alpha particles (α) in LXe in the $\mathcal{O}(1\,\text{keV})$ to $\mathcal{O}(1\,\text{MeV})$ energy range. Data from Reference [188, 189]. **Right:** Phase diagram of xenon. The shaded region represents the typical operating regime of the LXe in TPCs. Saturation curve data from Reference [190].

undergoing double beta decay with long half-lives which has not been observed yet. The two long-lived isotopes ^{124}Xe and ^{136}Xe are interesting physics channels on their own but contribute to the ER background of the search for elastic WIMP scattering at low recoil energies [175]. The isotope ^{124}Xe undergoes a double electron capture which was observed for the first time in the XENON1T experiment [173]. The isotope ^{136}Xe decays via two-neutrino double beta decay and is used as a source in experiments searching for the hypothetical neutrinoless double beta decay, a lepton number violating process. The half-lives of the other xenon isotopes that can be anthropologically, radiogenically or cosmogenically produced range from $\mathcal{O}(1\,\mu\text{s})$ to $\mathcal{O}(10\,\text{d})$. Of these, ^{127}Xe is the isotope with the highest half-life of 36.4 d and decays via electron capture [183].

As we saw in Chapter 1, Equation 1.12, the spin-independent WIMP-nucleus cross-section is proportional to the square of the atomic mass number. Thus, the high mean atomic mass of natural xenon of 131.293 g/mol makes it an ideal target. In particular, it has a strongly enhanced expected WIMP-nucleus interaction rate compared to lighter noble element targets, see Section 2.1.4. The isotopes ^{129}Xe and ^{131}Xe with a total isotopic abundance of $\sim 47.6\,\%$ have an odd number of nucleons. The unpaired neutrons result in a non-zero total nuclear angular momentum and thus allow for spin-dependent WIMP interactions [184, 185].

The high mean atomic mass of natural xenon and the high mass density (cf. Section 2.1.2) of LXe equips it with a great stopping power for ambient radiation. In Figure 2.1, left, we show the mean attenuation length for various particles and see that even gamma rays with $\mathcal{O}(1\,\text{MeV})$ energies are stopped within a few centimetres. Thus, ambient radiation from materials can be shielded very effectively and will get absorbed in the outermost layer of the detector volume. By the definition of central detector regions, i.e. the fiducialisation, one can exploit this self-shielding power of xenon to reduce the material-induced background significantly. At higher energies that are reached e.g. with particle beams, the typical length scales are: The nuclear interaction length, i.e. the mean distance covered by a hadronic particle before undergoing an inelastic nuclear interaction, is 58.29 cm for a 200 GeV neutron and widely independent of the particle momentum at these energies. The radiation length of LXe for electromagnetically-interacting particles at high energies is 2.872 cm [186]. This is both the mean length after which high-energy electrons have lost all but $1/e$ of their energy by bremsstrahlung and 7/9 of the mean free path for pair-production by a high-energy photon [187].

2.1.2 Thermodynamic Properties

If not noted otherwise, all thermodynamic properties listed below are based on the National Institute of Standards and Technology (NIST) Chemistry WebBook and references therein [191]. In Figure 2.1, right, we show the phase diagram of xenon. At standard pressure (1013.25 hPa), the density of xenon is 5.898 kg/m^3 at 273.15 K, and its boiling and melting points are 165.05 K and 161.40 K, respectively. The corresponding enthalpies of vaporisation and fusion are 95.587 kJ/kg and 17.48 kJ/kg, respectively [190]. Noble gases with a lower atomic mass have significantly lower melting and boiling points. Argon for instance condenses at 87.30 K. The moderately high condensation temperature of xenon, facilitates its efficient liquefaction by means of liquid nitrogen (LN_2) or cryocoolers using helium. The typical working pressure in dual-phase xenon TPCs is ~ 2 bar. At this pressure, the boiling and melting points of xenon are 177.88 K and 161.43 K, respectively. Between these temperatures, xenon is in liquid state with densities in the range $2854.7 - 2966.6\,\mathrm{kg/m^3}$ which allows for the construction of high mass detectors with a fairly small form factor. The triple point is at 161.38 K and 0.816 bar and the critical point is at 289.74 K and 58.42 bar with a critical density of $1100\,\mathrm{kg/m^3}$.

Cryogenic distillation allows to separate xenon from residual noble gases that contain radioactive isotopes such as krypton that consists to a small fraction of ^{85}Kr, and ^{222}Rn that is emanated from the detector materials [192–194]. Furthermore, xenon can be purified from electronegative impurities such as oxygen, nitrogen and water. To that end, one deploys hot metal getters that typically use zirconium to catch electronegativities in GXe and liquid purification systems that use e.g. copper to form copper oxide.

2.1.3 Optical Properties

LXe scintillates in the vacuum-ultraviolet (VUV) range with a peak centred at $175 - 178$ nm wavelength [195, 196]. As we shall see in later chapters, light at this wavelength can be detected with commercially available photosensors. The production mechanism of the scintillation light is discussed in detail in Section 2.3. The VUV light yield of LXe at zero electric field and 122 keV is 63 photons/keV [197], granting good energy resolution and a low energy threshold. However, note that this yield is highly energy and field dependent. An important feature of LXe is that it is transparent to its own scintillation light and thus, it can be exploited for the detection of particle interactions. The mechanism through which transparency is made possible is explained in Section 2.2. The mean attenuation length for light at 178 nm is (364 ± 18) mm at (170 ± 1) K [198]. Apart from emitting light in the VUV region, GXe is known to emit significantly in the infrared (IR) range [199–203]: it features a strong line at a wavelength of 1300 nm with a VUV-comparable zero-field light yield of (21 ± 3) photons/keV[1] at 2 bar, measured with α-particles at 4.3 MeV [205]. At high pressures, the IR spectrum of GXe is red-shifted and broadened [206, 207]. LXe features a different IR scintillation spectrum which emits mostly below 1200 nm but with a very poor yield [204].

2.1.4 Other Noble Elements

Besides xenon, argon is the only other noble element which is successfully deployed as a target for WIMP searches [4, 9, 154, 165, 212]. Compared to xenon, however, argon is expected to have a roughly tenfold decreased WIMP-nucleus scattering rate at $\mathcal{O}(1\,\mathrm{keV})$ recoil energy, see Figure 1.4, left. Due to its high mean mass number, xenon yields higher expected scattering rates than all other noble element targets at low recoil energies. As discussed in Section 2.1.1, xenon only contains stable or long-lived isotopes. Atmospheric argon on the other hand contains the cosmogenically activated isotope ^{39}Ar at a mass concentration of $(8.0 \pm 0.6) \times 10^{-16}$ that undergoes a beta-decay with a half-life

[1] This is only a lower limit measured at $700 - 1600$ nm but can be assumed to be the true value considering Reference [204].

Property	Value	Note/Condition	Ref.
Atomic and Nuclear			
Atomic number	54		
Mean atomic mass	131.293 g/mol		[208]
Natural isotopes (abundance)	^{124}Xe (0.095 %)	ECEC, $(1.8 \pm 0.6)\,10^{22}$ y	[173]
	^{126}Xe (0.089 %)	observationally stable	[183]
	^{128}Xe (1.910 %)	stable	[183]
	^{129}Xe (26.401 %)	stable	[183]
	^{130}Xe (4.071 %)	stable	[183]
	^{131}Xe (21.232 %)	stable	[183]
	^{132}Xe (26.909 %)	stable	[183]
	^{134}Xe (10.436 %)	observationally stable	[183]
	^{136}Xe (8.857 %)	$\beta^-\beta^-$, $(2.165 \pm 0.075)\,10^{21}$ y	[209]
LXe nuclear interaction length	58.29 cm	for a 200 GeV neutron	[186]
LXe radiation length	2.872 cm		[186]
Thermodynamic			
Boiling point	165.05 K	at 1013.25 hPa	[191]
	177.88 K	at 2 bar	[191]
Melting point	161.40 K	at 1013.25 hPa	[191]
	161.43 K	at 2 bar	[191]
Triple point	161.38 K, 0.816 bar		[191]
Critical point	289.74 K, 58.42 bar		[191]
Enthalpy of vaporisation	95.587 kJ/kg	at 1013.25 hPa	[190]
	92.505 kJ/kg	at 2 bar	[191]
Enthalpy of fusion	17.48 kJ/kg	at 1013.25 hPa	[190]
GXe heat capacity (isobaric)	1.6067×10^{-1} kJ/(kg · K)	at 1013.25 hPa, 273.15 K	[191]
	1.6303×10^{-1} kJ/(kg · K)	at 2 bar, 273.15 K	[191]
GXe heat capacity (isochoric)	9.5651×10^{-2} kJ/(kg · K)	at 1013.25 hPa, 273.15 K	[191]
	1.6303×10^{-1} kJ/(kg · K)	at 2 bar, 273.15 K	[191]
LXe heat capacity (isobaric)	3.3929×10^{-1} kJ/(kg · K)	at 1013.25 hPa, 165.05 K	[191]
	3.4380×10^{-1} kJ/(kg · K)	at 2 bar, 177.88 K	[191]
LXe heat capacity (isochoric)	1.6612×10^{-1} kJ/(kg · K)	at 1013.25 hPa, 165.05 K	[191]
	1.5999×10^{-1} kJ/(kg · K)	at 2 bar, 177.88 K	[191]
Density	5.898 kg/m^3	at 1013.25 hPa, 273.15 K	[191]
	2854.7 − 2966.6 kg/m^3	at 2 bar, 161.43 − 177.88 K	[191]
Optical			
LXe scintillation wavelength	(174.8 ± 0.2) nm	at 168 − 169 K, 1.10 − 1.17 bar	[196]
	178.0 nm	at 160 K	[195]
LXe refractive index	1.69 ± 0.02	at (170 ± 1) K, 178 nm	[198]
LXe attenuation length (Rayleigh scattering [210])	(364 ± 18) mm	at (170 ± 1) K, 178 nm	[198]
Electrical			
Dielectric constant	1.85		[211]

Table 2.1: Summary of the physical properties of xenon.

of 268 y and an endpoint at 565 keV. For that reason, the DarkSide-50 experiment deploys argon from an underground source [4]. For the next-generation detector DarkSide-20k, a 350 m tall distillation column is being built to further isotopically deplete the underground argon from ^{39}Ar [213]. One of the biggest advantages of argon over xenon is the possibility to use pulse-shape discrimination (PSD) to distinguish ER and NR interaction. We come back to that point in the next section when we discuss the production of scintillation light in LXe. Liquid argon scintillation light has a wavelength of 128 nm. While the scintillation light of xenon can be directly detected with photosensors, the argon scintillation light is below the sensitivity range of ordinary sensors. For this reason, wavelength-shifting materials like tetraphenyl butadiene are used that shift the wavelength to the visible region. In order to overcome the complication of the use of wavelength shifters in the detector design, the use of a $1 - 1000$ ppm level doping of argon with xenon is studied [214]. While preserving good PSD power [215, 216], the wavelength of the xenon-argon mixture is as high as the one of xenon [217], enhancing the photon yield [218, 219].

The WIMP-nucleon scattering rates in helium and neon are highly suppressed due to their low atomic mass number, see Figure 1.4, left. However, both are very radiopure targets with no long-lived isotopes. The experimental challenges when using liquid helium and neon [220–223] are their low boiling points of 4.23 K and 27.10 K (at 1013.25 hPa) [191], respectively, their low liquid scintillation wavelengths in the extreme ultraviolet range at around 80 nm [224–226] and the fact that much larger detectors are needed to reach comparable sensitivities to detectors using argon or xenon. However, proposals for detectors with these light noble gases as target for rare event searches were put forward [227–231].

2.2 Particle Interaction in Liquid Xenon

As discussed in Chapter 1, Section 1.4.2, a particle interacting within LXe can either transfer its energy to the atomic electrons or to the nucleus, producing an ER or NR, respectively. In practise, the former process involves electrons, muons or photons that interact electromagnetically. However, also weak interactions of neutrinos with the atomic electrons can be considered. Moreover, ER would be the channel for hypothetical interactions of solar axions or ALPs. The NR process on the other hand involves weak interactions of typically neutral particles like neutrons with the nuclei. Neutrinos for instance undergo coherent elastic neutrino nucleus scattering (CEνNS). Nuclear recoil interactions are also the ones expected for WIMPs.

A particle that deposits energy in LXe yields scintillation photons (see Section 2.1.3), ionisation electrons and heat via atomic motion, see centre of Figure 2.2. We collectively refer to scintillation and ionisation as excitation in this work. The scintillation light is composed of direct scintillation of the xenon atoms,

$$\mathrm{Xe}^* + 2\mathrm{Xe} \rightarrow \mathrm{Xe}_2^* + \mathrm{Xe} \rightarrow 3\mathrm{Xe} + \gamma \quad , \tag{2.1}$$

and light from the recombination of xenon ions with electrons,

$$\mathrm{Xe}^+ + \mathrm{Xe} \rightarrow \mathrm{Xe}_2^+ \quad , \tag{2.2}$$

$$\mathrm{Xe}_2^+ + e^- \rightarrow \mathrm{Xe}^{**} + \mathrm{Xe} \rightarrow \mathrm{Xe}^* + \mathrm{Xe} + \mathrm{heat} \quad , \tag{2.3}$$

$$\mathrm{Xe}^* + 2\mathrm{Xe} \rightarrow \mathrm{Xe}_2^* + \mathrm{Xe} \rightarrow 3\mathrm{Xe} + \gamma \quad . \tag{2.4}$$

Herein, we call an excited xenon atom Xe* a xenon exciton, Xe_2^* an excited dimer or excimer and $\mathrm{Xe}_2{}^+$ a diatomic xenon ion. In both mechanisms, scintillation light is produced by de-excitation of xenon dimers that form from xenon excitons and xenon atoms in less than a picosecond after excitation. The scintillation light has two components resulting from the two states of the excimers. They can be either in a spin-singlet $^1\Sigma_u^+$ or spin-triplet state $^3\Sigma_u^+$ which have decay times of (2.2 ± 0.3) ns and (27 ± 1) ns to the ground state $^1\Sigma_g^+$, respectively, measured with relativistic electrons at an electric

field of 4 kV/cm [232]. The spin singlet and triplet states of the excimers refer to the total spin number, $s = 0$ or $s = 1$, of the excited Rydberg electron and the angular momentum due to the molecular orbit. A spin singlet has one spin component (spin quantum number: $m_s = 0$) and a spin triplet has three components (spin quantum number: $m_s = -1,\ 0,\ +1$). The decay times are different since the decay from the singlet state is an allowed radiative transition, while the direct decay from the triplet state to the ground state is forbidden by selection rules and is instead mediated by mixing with the $^1\Pi_u$ state through spin-orbit coupling. The wavelength of the scintillation light emitted by an excimer is redshifted compared to the one of the light that would result from a direct de-excitation of excitons. For this reason, the production of VUV photons by the decay of excimers rather than directly from excitons makes LXe transparent to its own scintillation light. Different particle types produce different ratios of singlet and triplet state excimers and thus show different scintillation pulse decay shapes. The single/triplet ratio, scaled with the singlet/triplet decay times, was measured to be 0.27 for NR and 0.04 for ER interactions [233]. In principle, PSD can thus be used to distinguish ER from NR interactions. However, given the temporal resolution of current photosensors and readout electronics, PSD in LXe is experimentally difficult to access due to the short time separation of the two components. Unlike LXe, liquid argon does feature a long separation of the singlet and triplet decay times that are (6 ± 2) ns and (1590 ± 100) ns, respectively [234]. This allows for a very effective PSD of ER and NR interactions [235]. The ionisation electrons that do not undergo the recombination process can be drifted away from the interaction site by an electric field of $\mathcal{O}(100\,\mathrm{V/cm})$ with a typical drift speed of $\mathcal{O}(1\,\mathrm{mm/\mu s})$ [236] and then be detected separately. The drift speed is weakly field-dependent and saturates at high field strengths. We show an electron drift speed measurement in Xurich II in Chapter 4, Section 4.2.4. The xenon ions quickly combine with xenon atoms to form diatomic xenon ions. These only drift very slowly with a speed of $\mathcal{O}(0.1\,\mathrm{mm/s})$ [237]. However the charge drifts via the transport of electron holes among the atoms with a speed of $\mathcal{O}(1\,\mathrm{mm/s})$ [238]. Due to energy conservation, the size of the signals from scintillation and ionisation are anti-correlated [239,240]. The recombination fraction and thus the energy distribution between these is dependent on the potential presence of an outer electric field. The recombination probability decreases with increasing electric field strength as the electrons are getting pulled away from the interaction site where the ions are. Furthermore, the recombination process depends on the type and energy of the interaction which affect the charge distribution. This is because NR interactions typically feature a higher linear energy transfer (LET) than ER interactions. The LET describes the density of electron-ion pairs produced along the particle track. At high LET, the ions and electrons are in close proximity which enhances the recombination probability and thus the scintillation yield of NR interactions.

At low interaction energies like the ones interesting for the WIMP search ($\mathcal{O}(1 - 10\,\mathrm{keV})$), the atom, i.e. the nucleus and the electrons, as a whole recoils. However, the possibility that the electrons are left behind the nucleus for some time after the NR recoil is also being considered. The so-called Migdal effect results in additional scintillation and ionisation [241, 242].

Heat is produced in three different ways. First, heat is produced by the initial interaction, which leads to a motion of the recoiling nucleus that then elastically collides with other nuclei. While this effect is negligible for ER, it is significant for NR interactions. When the energy of these collisions is lower than the electronic excitation threshold, it is finally converted to heat. This reduces the overall excitation in NR interactions compared to ER interactions [243]. This quenching is described by the energy-dependent Lindhard factor $\mathcal{L}$ [244, 245]. Second, heat is produced during the relaxation of the doubly-excited exciton Xe^{**} in the recombination process, see Equation 2.3. Third, heat can be produced for high LET events, such as from alpha decays, by biexcitonic or Penning quenching [246, 247]. In this process, two excitons combine:

$$\mathrm{Xe}^* + \mathrm{Xe}^* \rightarrow \mathrm{Xe}^+ + e^- + \mathrm{Xe} + \mathrm{heat} \quad . \tag{2.5}$$

While two separate excitons yield two scintillation photons, this process only yields one excitation

quantum. Depending on whether recombination takes place or not, the biexcitonic quenching results in a scintillation photon or an ionisation electron.

The microphysics of noble element interactions is implemented in the software package Noble Element Simulation Technique (NEST) [18] that models the scintillation and ionisation yields of particle interactions of different energies and different electric fields. We use it in Chapters 5 and 6 to compare the yields seen with calibration data in a small dual-phase xenon TPC to this model.

2.3 Response of Liquid Xenon Detectors

We denote the number of scintillation photons, produced directly or by recombination, by n_γ, and the number of ionisation electrons, that do not recombine, by n_{e^-}. The sum of these quanta, produced in an ER interaction, is linearly related to the deposited energy E by the constant work function W [243]:

$$E = (n_\gamma + n_{\mathrm{e}^-})W \quad . \tag{2.6}$$

This is the combined scintillation and ionisation energy scale of ER interactions. The W-value can be regarded as the average energy needed to produce a single free quantum in LXe and the above expression as its defining equation. It determines the underlying recombination-independent energy scale in a LXe detector that detects both scintillation light and ionisation charge. Note that we implicitly assume here that every recombining electron-ion pair leads to the production of one photon. For an NR interaction, we have to include quenching by the energy-dependent Lindhard factor $\mathcal{L}$:

$$E = \mathcal{L}^{-1}(n_\gamma + n_{\mathrm{e}^-})W \quad . \tag{2.7}$$

Since the ratio of the number of excitons over the number of ions is larger for NR than for ER interactions and less energy is needed to produce an exciton than an electron-ion pair, W would be lower for NR interactions. However, this difference can formally be absorbed in the Lindhard factor, yielding the same W-value for ER and for NR interactions [243]. The widely employed numerical value of W is $(13.7 \pm 0.2)\,\mathrm{eV}$ [243]. In Chapter 6, we provide a new measurement of W with the Xurich II TPC.

Given the scintillation signal (S1) and ionisation signal (S2) (see Section 2.4), we can define the detector-specific gains $g1$ for scintillation and $g2$ for ionisation as

$$g1 \coloneqq \mathrm{S1}/n_\gamma \quad \text{and} \quad g2 \coloneqq \mathrm{S2}/n_{\mathrm{e}^-} \tag{2.8}$$

and rewrite Equation 2.6 as

$$E = \left(\frac{\mathrm{S1}}{g1} + \frac{\mathrm{S2}}{g2}\right) W \quad . \tag{2.9}$$

The gains $g1$ and $g2$ describe the detector response to the excitation quanta, for photosensors typically in PE/γ and PE/e^- (PE – photoelectron). The response includes the light and charge collection and photosensor detection efficiencies and a potential S2-amplification process. The use of these detector gains to characterise the detector response justifies the definition of the W-value as mean excitation energy. The inequality of the work functions for scintillation and ionisation are absorbed by $g1$ and $g2$.

We have already used the terminology scintillation, light or photon yield (LY) and ionisation, charge or electron yield (QY). These are intrinsic properties of the LXe and can be defined as $\mathrm{LY} = \mathrm{S1}/(E \cdot g1)$ and $\mathrm{QY} = \mathrm{S2}/(E \cdot g2)$. They feature units of number of quanta per energy deposited. However, as the reader will notice, we also call the expressions $\mathrm{S1}/E$ and $\mathrm{S2}/E$, with units of PE per energy deposited, the light and the charge yield. By doing so, we mean the yields of the detector and LXe combined as these are not corrected for the detector gains $g1$ and $g2$. It is clear from the context to which one we refer.

2.4 Working Principle of Dual-Phase Xenon TPCs

A dual-phase xenon TPC is a detector for particle interactions with a low $\mathcal{O}(1\,\mathrm{keV})$ energy threshold. By exploiting the scintillation and ionisation signals that are produced in LXe, it allows for a three-dimensional reconstruction of the interaction site, a measurement of the recoil energy and the classification of the particle type in NR or ER. Both signals are detected as light. Heat that is produced during a particle interaction cannot be detected. A dual-phase TPC is placed inside a cryostat that is partially filled with LXe and that features a GXe layer on top of the LXe. The detector consists of a field-cage that allows for the application of vertical electric fields in the liquid and at the liquid-gas interface. It also features photosensors sensitive to the VUV-scintillation light of xenon. Typically dual-phase TPCs feature a rotational symmetry around the vertical axis or are even of cylindrical shape. This optimises the light collection efficiency, the electric field uniformity and the volume to surface ratio, and also facilitates the event position reconstruction. In Figure 2.2 we show a schematic of the main detector components and its working principle. The field-cage includes three transparent electrodes: a negatively biased cathode at the bottom, a gate at ground potential located below the liquid surface and a positively biased anode in the gas above the liquid surface. This yields an external electric drift field $\vec{E}_\mathrm{d}$ of typically $\mathcal{O}(100\,\mathrm{V/cm})$ in the liquid and an external electric extraction field $\vec{E}_\mathrm{e}$ of typically $\mathcal{O}(1-10\,\mathrm{kV/cm})$ at the liquid-gas interface. The effective electric fields are reduced due to the dielectric polarisation of the xenon. While this effect is negligible for GXe, LXe has a relative permittivity of 1.85, see Table 2.1. Hence, the effective extraction field is almost twice as high in GXe than in LXe. If the field-cage was only defined by the parallel electrodes, that are finite in size, the resulting electric field would feature field-inhomogeneities towards the outside of the TPC volume. For that reason, equidistant field-shaping rings surround the active volume and provide a linear electrical potential drop along the vertical direction, in practise realised by a resistor chain connecting gate and cathode via the field-shaping rings. This field-cage configuration provides a homogeneous drift field up to very large radii. Two photosensor arrays, one below the cathode in LXe and one above the anode in GXe detect the scintillation light. Additional screening electrodes directly below (above) the top (bottom) photosensor array can be used to protect the photosensors from the high electric fields produced by the anode (cathode) [5]. To increase the light-collection efficiency, the inner surfaces of TPCs are typically highly reflective to the VUV light. Typically, one uses polished polytetrafluoroethylene (PTFE) which has a reflectance close to unity [248, 249].

Particle interactions in the LXe target of a dual-phase TPC are detected by the prompt scintillation light S1 and a delayed scintillation signal S2 which is proportional to the charge signal. The latter is produced from electroluminescence caused by the ionisation electrons that are drifted upwards, extracted into the gaseous phase and accelerated by the vertical electric fields. Collisions of these electrons with atoms in the gas phase yields scintillation light proportional to the extracted charge. Multiple collisions lead to a signal amplification which results in a much larger relative S2 light signal compared to the S1. Thus, both scintillation S1 (light) and ionisation S2 (charge) signals can be observed by photosensors sensitive to the VUV scintillation light. As mentioned above, heat that is produced by the atomic motion during the interaction cannot be exploited by dual-phase TPCs. The twofold signal topology distinguishes the strength of a dual-phase TPC and allows for fiducialisation and background discrimination. The vertical position or depth of the interaction vertex can be reconstructed from the time difference of the occurrence of the S1 and S2 signals, the drift time, knowing the drift speed at the particular drift field. The horizontal position can be inferred from the localised light distribution or hit pattern of the S2 light detected by the top photosensors. The interaction energy is reconstructed from the combined S1 and S2 signals and their ratio serves as a discriminator for the type of interaction as NR and ER interactions feature different yields, see Section 2.3. Depending on the size of the detector and the granularity of the photosensors, the event position resolution is typically in the range $\mathcal{O}(1-10\,\mathrm{mm})$ [250, 251] and is affected by the

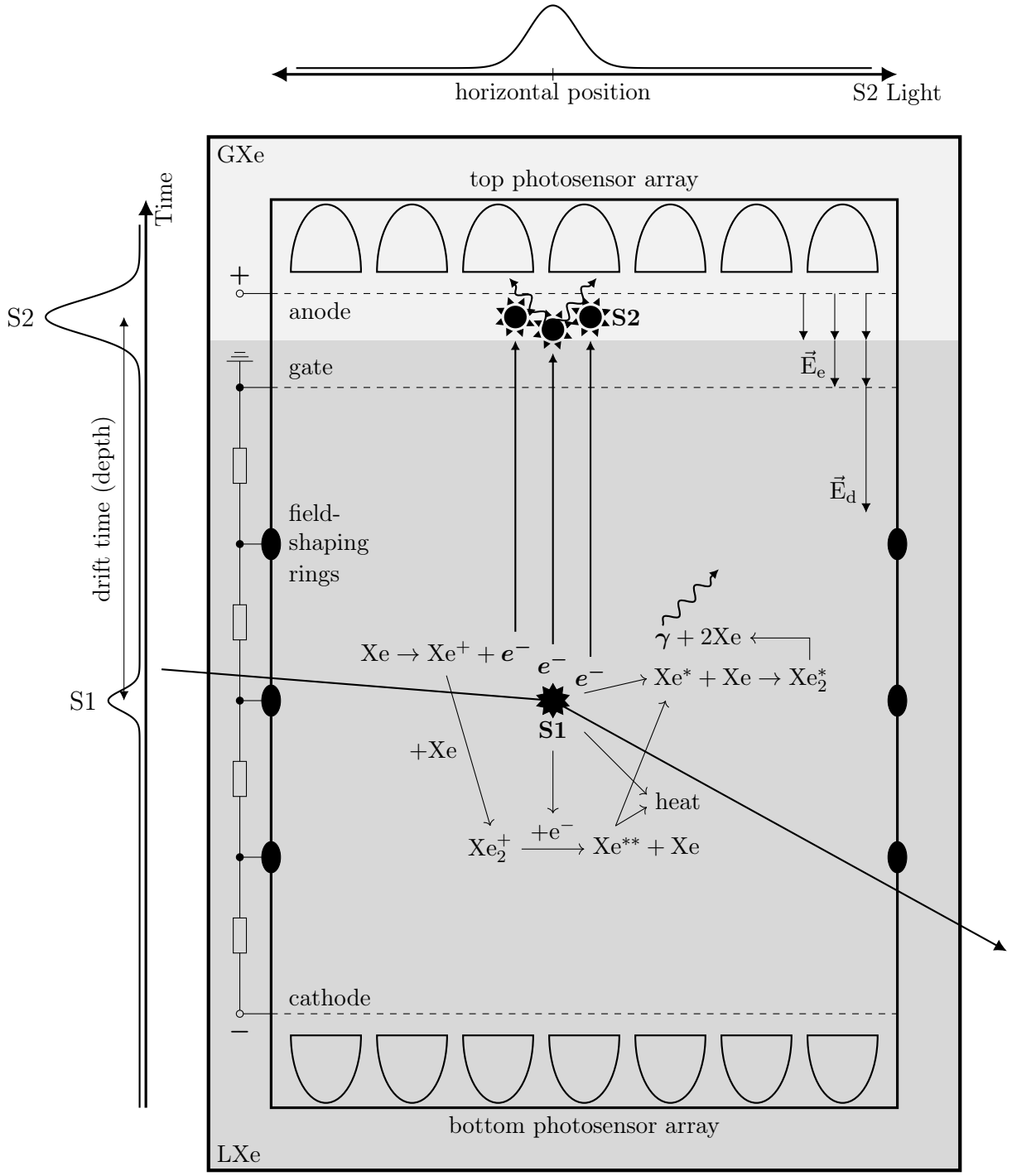

Figure 2.2: Schematic of the dual-phase TPC working principle. A particle that deposits energy in LXe yields scintillation photons in the VUV-range, ionisation electrons and heat via atomic motion, where only the former two processes are detectable with dual-phase TPCs. Photosensors detect the prompt scintillation light (S1) which is composed of direct scintillation of the xenon atoms and light from the recombination of xenon ions with electrons. In both mechanisms, scintillation light is produced by de-excitation of xenon dimers that form from xenon excitons and xenon atoms. Electrons that do not recombine are vertically drifted and extracted to the gas phase, by means of an electric drift $\vec{E}_d$ and extraction field $\vec{E}_e$, where they collide with xenon atoms. In this process, a secondary proportional scintillation signal (S2) is produced by electroluminescence which is also detected by photosensors. The interaction site can be reconstructed in the vertical dimension by means of the drift time, i.e. the time delay between the S1 and S2 signal, and in the horizontal plane by means of the S2 light distribution.

transversal and longitudinal diffusion of the electron cloud during the drift [252]. This resolution is not sufficient to reconstruct tracks in LXe that would give directional information of the incoming particle. Directionality, however, can be exploited with high-pressure GXe TPCs with great potential for direct dark matter search [253].

Besides all the discussed strengths of the dual-phase TPC technology, it also features some challenges. The free electrons can e.g. attach to electronegative impurities in the LXe during their drift. In this case the signal from the electrons is lost as they do not contribute to the S2 signal. This process is quantified by the *free electron lifetime* which is inversely proportional to the concentration of such impurities in the LXe. The free electron lifetime is the average time after which the number of initial electrons has fallen by factor e. In a TPC, it can be measured as decay constant of an exponential fit of the S2 signal versus drift time. A high free electron lifetime, which can be achieved by purification from electronegative impurities, is required for a good energy resolution, a low energy threshold and a good position reconstruction. Besides this, a strong homogeneous and vertical electric drift field is required. Only then the horizontal event position can be retained and absorption of the electrons on the TPC walls can be avoided. Among other mechanisms this can lead to an accumulation of charge on the PTFE that in turn distorts the electric field [254]. A strong extraction field is necessary to avoid the accumulation of charge under the liquid surface that can eventually lead to a high rate of single electrons that are extracted with some delay [255]. The electron lifetime and the electric fields are important parameters for a high ionisation gain $g2$. Of similar importance is a high detection efficiency of the scintillation light, parametrised by $g1$. This can be achieved with highly reflective TPC surfaces, highly transparent electrodes and a good photosensor coverage, increasing the light collection efficiency. In addition, the photosensor itself must feature a good photon detection efficiency. Since dual-phase TPCs are insensitive to the heat deposited in the target during a particle interaction, their energy threshold restricts the sensitivity to WIMPs with masses below $\mathcal{O}(1\,\mathrm{GeV/c^2})$, see Figure 1.6. Some of these points, especially a high light collection efficiency and strong electric fields are increasingly challenging to achieve when scaling up the detector technology to lengths scales of $\mathcal{O}(1\,\mathrm{m})$ and target masses of $\mathcal{O}(10\,\mathrm{t})$. This is the case for the DARWIN observatory that we introduce in the next chapter.

Chapter 3

The DARWIN Observatory

Building upon the experience and know-how of the XENON Dark Matter Project [256] on the construction of dual-phase xenon TPCs for dark matter search, the proposed DARWIN (DARk matter WImp search with liquid xenoN) observatory [8, 257] can be regarded the ultimate evolution of this detector technology. Involving an active xenon mass of 40 t (50 t total), the primary goal of the observatory is to explore the entire experimentally accessible parameter space for WIMP masses above $5\,\mathrm{GeV/c^2}$, down to the irreducible *neutrino floor*[1] [142], see Figure 1.6.

The DARWIN project is a world-wide team effort of currently almost 200 researchers from 34 institutions. After the XENONnT [5] and LUX-ZEPLIN (LZ) [161] experiments are finished, the XENON/DARWIN and LZ collaborations will unite their experience to form a new and stronger collaboration with the common goal to build a single multi-tonne xenon observatory. This was defined in a memorandum of understanding, signed by 104 senior researchers on 6 July 2021.

This chapter is structured as follows: We introduce the baseline detector design in Section 3.1 and discuss its potential science reach and relevant backgrounds in Section 3.2. The ongoing R&D efforts towards the final detector design is covered in Section 3.3.

3.1 Conceptual design

In its baseline design presented in References [8, 16], DARWIN features a cylindrical TPC of both height and diameter of 2.6 m filled with an active xenon mass of 40 t (50 t total). The active region is surrounded by highly reflective PTFE walls, made of 24 panels, see Figure 3.1. The drift region is defined in the vertical direction by a bottom cathode and a gate under the liquid surface that provide a drift field of $\mathcal{O}(100\,\mathrm{V/cm})$. To ensure the uniformity of the electric field, 92 equidistant field-shaping rings from oxygen-free high-conductivity copper surround the detector volume. These are interconnected by a resistor chain to account for a linear potential change between the cathode and the gate. An extraction field of $\mathcal{O}(1\,\mathrm{kV/cm})$ is created between the gate and the top anode at the liquid/gas interface. Additional screening meshes protect the top and bottom photosensor arrays from high electric fields. They provide light and charge (also detected by light) readout and allow for position and energy reconstruction of interactions in the active volume. Past and present LXe dark matter experiments use VUV-sensitive photomultiplier tubes (PMTs) as photosensors that are up to 3 in in diameter [6, 7, 258–263] and that are optimised for low levels of radioactivity [264, 265]. In the baseline scenario, the two photosensor arrays of a DARWIN-sized detector would be instrumented by $\sim$ 1800 R11410 3-inch PMTs from Hamamatsu Photonics K.K. In addition to this traditional solution, alternative novel photosensors are under study, see Section 3.3. The TPC is housed by a low-background double-walled titanium cryostat of which both vessels are reinforced by circumferential stiffening rings that allow to reduce the wall thicknesses and thus the material budget of the cryostat. The cryostat is surrounded by a neutron veto and a water Cherenkov detector to shield effectively from environmental radioactivity and from cosmic rays whose flux is highly suppressed by locating the

[1] More recently referred to as *neutrino fog* [143] to emphasise that it is not a hard boundary.

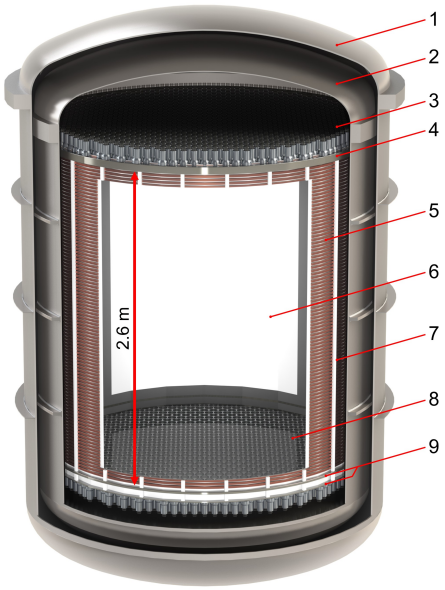

Figure 3.1: Rendering of a possible realisation of the DARWIN TPC equipped with 3-inch PMTs inside the cryostat. This is a simplified geometry as it is used for the Monte-Carlo simulation of the material-induced background. **Legend:** 1 – Outer vessel, 2 – Inner vessel, 3 – Top photosensor array, 4 – Top electrodes, 5 – Field-shaping rings, 6 – PTFE reflector panels, 7 – PTFE support structure, 8 – Bottom photosensor array, 9 – Bottom electrodes.

facility in a deep underground laboratory. The sensitivity studies below consider the overburden of the Laboratori Nazionali del Gran Sasso (LNGS) as baseline. In 2019, a letter of intend was submitted to LNGS in which the DARWIN collaboration proposed to place the detector in this underground lab. Subsequently. the collaboration was invited to submit a conceptual design report.

3.2 Sensitivity and Backgrounds

As we shall see below, DARWIN's high target mass, low energy threshold and ultra-low ER- and NR-induced background level will allow it to reach not only an unprecedented WIMP-sensitivity at low NR energies ($\mathcal{O}(1-10\,\mathrm{keV})$) as primary goal but also to search for a variety of other rare processes [8]. Of those we present the neutrinoless double beta decay at high ER energies ($\sim 2.5\,\mathrm{MeV}$) and the observation of solar neutrinos at low ER energies ($\mathcal{O}(1-100\,\mathrm{keV})$).

3.2.1 WIMP dark matter

As shown in Reference [266], the projected spin-independent WIMP sensitivity of DARWIN with an NR energy threshold of 5 keV for a 200 t × y exposure of a 30 t fiducial mass reaches $2.5 \times 10^{-49}\,\mathrm{cm}^2$ for WIMPs with a mass of $40\,\mathrm{GeV/c}^2$, see in Figure 1.6. This estimate is based on a series of background assumptions, see Figure 3.2. Among those are a low concentration of 0.1 ppt $^{\mathrm{nat}}$Kr and 0.1 µBq/kg ^{222}Rn in the liquid target. While a concentration of 0.03 ppt for $^{\mathrm{nat}}$Kr has already been achieved by the XENON collaboration in a cryogenic distillation test [267], the assumed ^{222}Rn concentration is an order of magnitude lower than targeted by current experiments. Important other ER backgrounds to the WIMP search are γ-rays from detector and cryostat materials, low-energy (pp, ^{7}Be) solar neutrino scattering on electrons and the two-neutrino double beta decay ($2\nu\beta\beta$) of ^{136}Xe. The sensitivity study in Reference [266] assumes in particular, that the cryostat is made from copper. Cosmogenic or radiogenic neutrons and CEνNS with solar (mostly ^{8}B) and atmospheric neutrinos present relevant

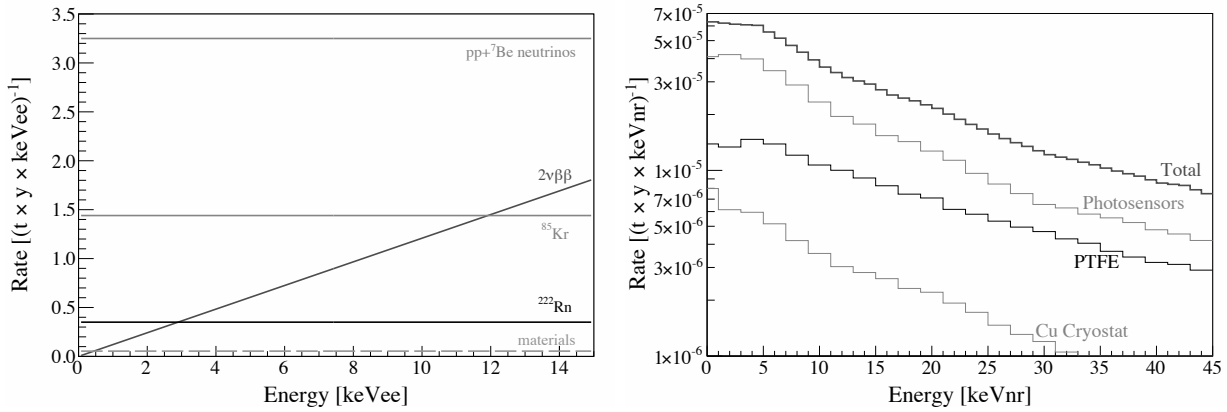

Figure 3.2: Differential background energy spectra with infinite energy resolution. Figures from Reference [266]. **Left:** ER background with no ER rejection applied. **Right:** NR background from detector materials at 100 % NR acceptance.

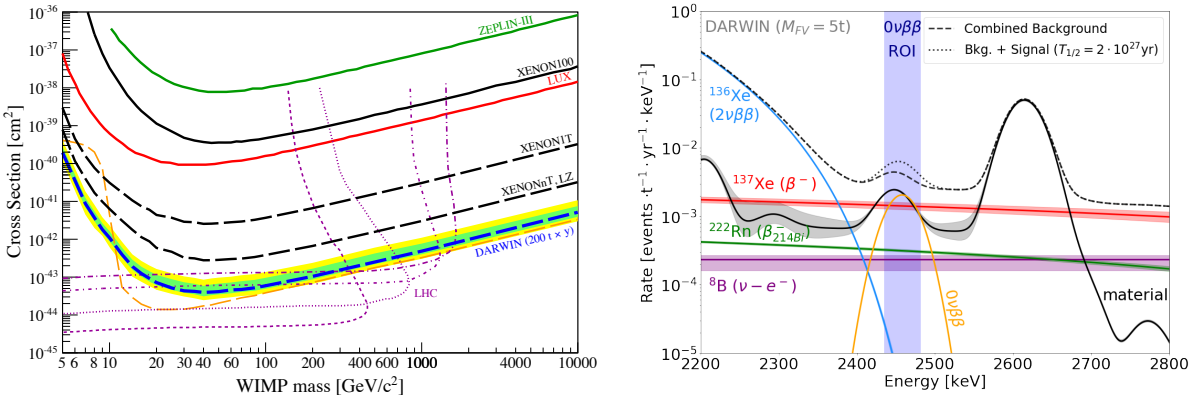

Figure 3.3: Left: Past and present spin-dependent exclusion limits on the WIMP-neutron cross-section together with the projected sensitivities for XENONnT, LZ and DARWIN in comparison with the high-luminosity 14 TeV LHC. Figure from Reference [8]. **Right:** ER background spectrum around the $0\nu\beta\beta$ region of interest for an optimised 5 t fiducial volume together with a hypothetical signal corresponding to $T^{0\nu}_{1/2} = 2 \times 10^{27}$ y. Shown are $\pm 1\sigma$ uncertainty bands. Figure from Reference [16].

NR background sources, that all leave a WIMP-like signal in the detector. Representing an irreducible background, the latter ultimately limits the sensitivity of this detector technology. The other named backgrounds can be mitigated by cryogenic distillation, target purification, a careful material selection and screening, fiducialisation, a neutron veto, and a water Cherenkov detector and shielding. The quoted sensitivity relies on an assumed ER background-rejection level of 99.98 % at an NR-acceptance of 30 % achieved by a uniform and high light and charge yield. This level of ER/NR discrimination has already been achieved in ZEPLIN-III [160]. In addition, DARWIN will complement measurements of the high-luminosity 14 TeV LHC for spin-dependent WIMP-nucleon interactions and even probe the phase space above 1 TeV/c^2 WIMP mass, beyond the reach of the LHC [266], see Figure 3.3, left.

3.2.2 Neutrinoless double beta decay

As noted in Table 2.1, natural xenon contains the isotope ^{136}Xe at an abundance of 8.857 %, which corresponds to an active mass of $\sim$ 3.5 t inside DARWIN even without enrichment. This isotope is a candidate for the hypothetical neutrinoless double beta ($0\nu\beta\beta$) decay with an endpoint of the beta spectrum at $Q_{\beta\beta} = 2458$ keV. This energy region is subject to a number of backgrounds, see

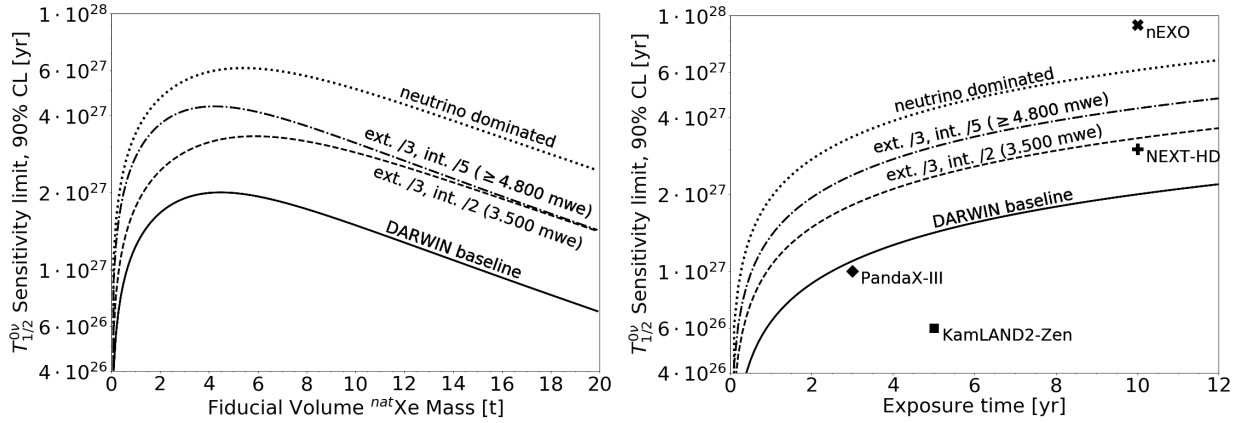

Figure 3.4: Median $0\nu\beta\beta$ half-life sensitivity of DARWIN at 90 % CL. Shown are the results for the conservative baseline scenario and several more optimistic scenarios with reduced external (ext.) and internal (int.) backgrounds at different laboratory depths. Figures from Reference [16]. **Left:** As function of fiducial mass for 10 y exposure time. **Right:** As function of exposure time for an optimised 5 t fiducial mass in comparison to future $0\nu\beta\beta$ experiments.

Figure 3.3, right. Besides those that are also relevant for the WIMP search like the uranium and thorium chains of the materials, ^{222}Rn, ^{8}B solar neutrinos and the standard $2\nu\beta\beta$, this search is in particular influenced by β^--decays from ^{137}Xe produced by capture of thermalised cosmogenic neutrons on ^{136}Xe inside the xenon target. For an optimised fiducial mass of 5 t (see Figure 3.4, left, for the optimisation) and incorporating background uncertainties, a $0\nu\beta\beta$ half-life sensitivity of $T^{0\nu}_{1/2} = 2.4 \times 10^{27}$ y (90 % CL) was calculated from a profile-likelihood analysis for the baseline scenario with 3σ discovery potential of 1.1×10^{27} y after an exposure of 10 y. This makes DARWIN competitive to dedicated $0\nu\beta\beta$ near-future experiments, see Figure 3.4, right. The result corresponds to an effective Majorana mass of $m_{\beta\beta} = 18 - 46$ meV and, hence, enables DARWIN to cover the inverted hierarchy mass region, see Figure 3.5. Inverted hierarchy refers to the ordering of the neutrino mass eigenstates in which the third mass eigenstate is the lightest, followed by the first and the second. Normal hierarchy is the natural ordering with the first, second and third mass eigenstate in increasing mass order. A discussion of the Monte Carlo (MC) background simulations, the sensitivity study and a comparison to near-future $0\nu\beta\beta$ experiments can be found in Reference [16].

3.2.3 Solar neutrinos

While being a background to the aforementioned studies, elastic scattering of solar neutrinos off target electrons is an interesting science channel on its own [268]. A detailed study on the matter can be found in Reference [175]. Besides the background from the uranium and thorium chains in the detector and cryostat materials, the most significant backgrounds for the detection of low-energy solar neutrinos come from internal ^{222}Rn, see Figure 3.6. The study assumes a concentration of 2 ppq $^{\text{nat}}$Kr and 0.1 µBq/kg ^{222}Rn in the target. This $^{\text{nat}}$Kr concentration is an order of magnitude lower than currently achieved [267]. However, even at the current level, it has only little effect on flux, electroweak mixing angle and electron neutrino survival probability measurements. In addition, the double beta decay of ^{136}Xe presents a background which can be mitigated by depletion to the disadvantage of the $0\nu\beta\beta$ prospects.

Based on the signal and background models, DARWIN's sensitivity to the solar neutrino flux component can be assessed with a multivariate spectral fit of all signal and background components [175]. The study shows that DARWIN can provide a high-precision measurement of the solar neutrino flux. In particular, with a 30 t fiducial mass it would reach the 10 % (2.7 %) precision on the *pp* (^{7}Be) neu-

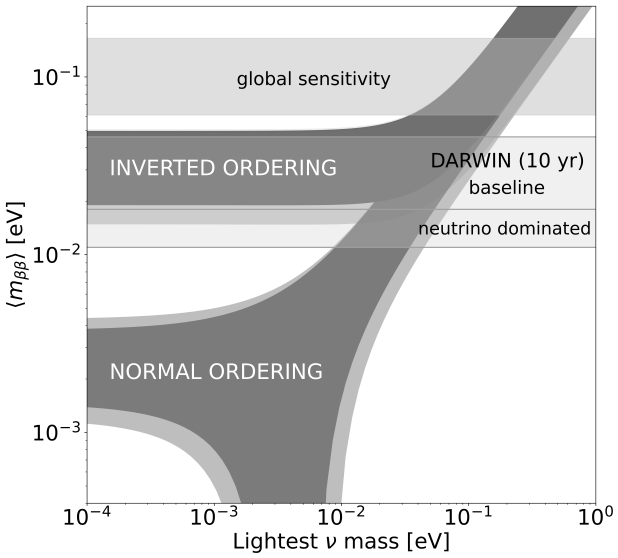

Figure 3.5: Effective Majorana mass versus lightest neutrino mass. DARWIN covers the inverted ordering region of the neutrino Majorana mass for a 50 t × y exposure. Figure from Reference [16].

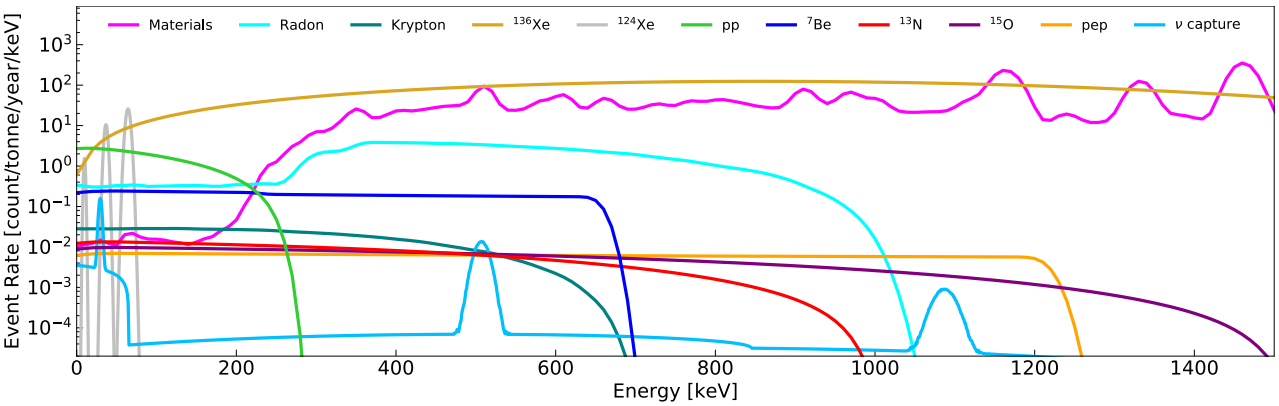

Figure 3.6: ER background spectrum for a 30 t fiducial mass together with the recoil spectra of five solar neutrino components from the high-metallicity model. Figure from Reference [175].

trino flux currently set by Borexino [269] with 1 t × y (60 t × y) exposure and reach a precision of 0.15 % (1 %) at 300 t × y, see Figure 3.7. These high-precision measurements would allow DARWIN to constrain the uncertainties of the neutrino-inferred solar luminosity to 0.2 % and to determine the electroweak mixing angle $\sin^2\theta_W$ and the electron-type neutrino survival probability $P_{\nu_e \to \nu_e}$ at yet unprobed low energies (< 200 keV) with a precision of 5.1 % and 4.0 % (for a natural xenon target), respectively (see Figure 3.8). The ^{13}N and ^{15}O neutrinos are within reach as well. Sensitivity to the *pep* component and of the neutrino capture process on ^{131}Xe, however, requires depletion from ^{136}Xe of the xenon target. Moreover, depletion would allow DARWIN to probe the metallicity of the Sun and help to distinguish high- and low-metallicity models up to the theoretical uncertainties. These high-precision flux measurements also allow to measure the neutrino mixing angle $\sin^2\theta_{13}$, with the potential to exclude $\sin^2\theta_{13} = 0$ close to the 3σ level [270], and to improve the sensitivity to sterile neutrino mixing [271].

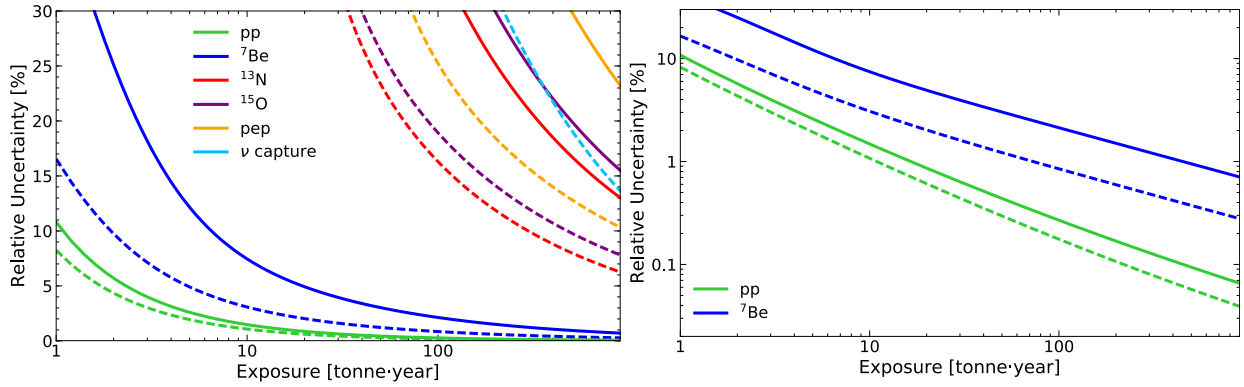

Figure 3.7: Relative uncertainty on the flux of the solar neutrino components versus exposure with a detail view in logarithmic scale shown in the right panel. Figure from Reference [175].

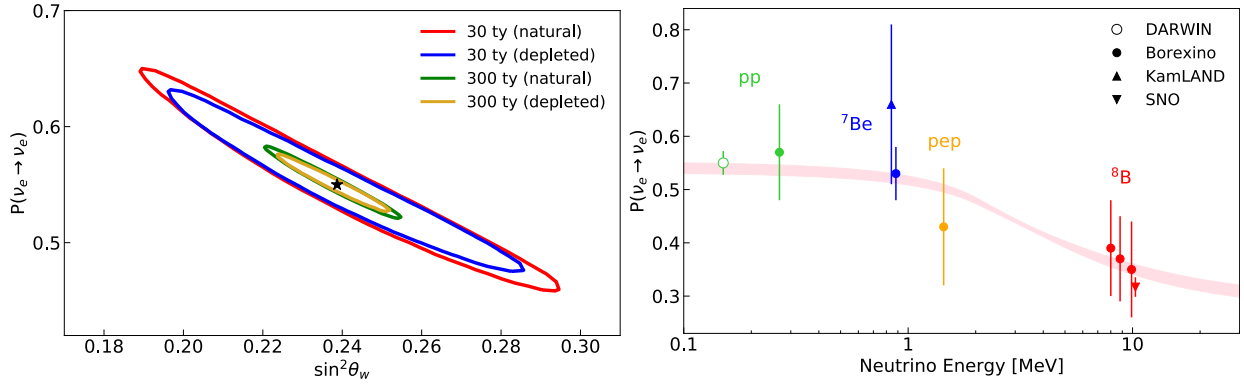

Figure 3.8: Left: 68 % confidence regions on the weak mixing angle and the electron neutrino survival probability. Figure from Reference [175]. **Right:** Electron neutrino survival probability versus neutrino energy under the high-metallicity model. The band represents the 1σ band of the theoretical prediction. Figure from Reference [175].

3.2.4 Other Physics Channels

DARWIN is a unique platform to study various other channels. Among those are searches for solar axions, and for galactic axion-like particles and dark photons as light dark matter candidates [8]. Other neutrino channels include the observation of CEνNS with solar ^{8}B neutrinos and neutrinos from galactic supernovae [272]. DARWIN will also be able to probe diffuse supernova neutrinos of all flavours via CEνNS [273]. For a recent review on the dark matter and neutrino physics reach of a DARWIN-like detector, see Reference [274].

3.3 Research and Development Efforts

To build a DARWIN-sized detector and meet the design goals and background requirements, a series of R&D challenges have to be addressed and various key technologies to be tested. This is the motivation for the topics of all subsequent chapters. One of the major development and testing campaigns in the collaboration is the identification of alternative photosensors and readout schemes to the above mentioned 3-inch PMTs in the baseline design. The most prominent candidates are silicon photomultipliers (SiPMs) [251, 275–277]. In Chapter 4 we show the first implementation of SiPMs in a dual-phase xenon TPC and demonstrate its performance in Chapter 5 and 6 at low energies. Considered photosensor alternatives of the DARWIN collaboration include digital SiPMs [278], hybrid photosensors like ABALONE [279] and vacuum silicon photomultiplier tubes [280,281], but also other

PMT models and novel ideas like bubble-assisted liquid hole multipliers [282]. The choice of the photosensor type and their placement inside the TPC is guided by optical simulations with the goal of maximising the light collection [283].

To prove the working principle of the detector technology at theses scales, to test equipment and instrumentation and to probe LXe properties under DARWIN-like conditions, two full-scale DARWIN demonstrators have been constructed. Xenoscope at the University of Zurich (UZH) is a full-height facility that was built to demonstrate the electron drift over a distance of 2.6 m and to address the liquid xenon purity requirements [284]. Other objectives of Xenoscope are the high-voltage feed to the cathode as well as measurements of electron cloud diffusion and optical properties of xenon. A general description of Xenoscope and the design, construction and commissioning of selected subsystems is the topic of Chapter 7. Pancake, located at the University of Freiburg, is a full-diameter facility. Its primary goal is the study of the mechanical and electrical behaviour of the electrodes and the testing of detector materials under cryogenic conditions to address e.g. the uniformity of the S2-amplification and the shrinkage of the detector components.

Considerations on the detector design include, but are not limited to, the development of single phase liquid detectors [285] (cf. Reference [166]), hermetic TPCs [286] and novel radon mitigation techniques [287–291].

Chapter 4

The Xurich II TPC with Silicon Photomultipliers

In the previous chapter, we have seen that PMTs are widely deployed as photosensors in dual-phase xenon TPCs for dark matter search. However, they are among the dominant sources of ER and NR backgrounds, and they limit the horizontal position resolution, correlated to their size, and thus the power to distinguish single and multiple interactions. As outlined, the backgrounds in DARWIN need to be reduced further compared to current-generation experiments. For this reason, one considers the use of SiPMs for one or both photosensor arrays.

To demonstrate that SiPMs are viable alternative photosensors, we have built the first dual-phase xenon TPC equipped with a top photosensor array containing 16 SiPM channels read out individually [251]. The characterisation of the detector by means of calibration, i.e. the determination of its charge and light response parameters, was performed with two internal sources: ^{37}Ar and ^{83m}Kr. These allow us to investigate ER interactions at low energies with monoenergetic peaks. ^{37}Ar provides independent energy lines at 0.27 keV and 2.82 keV from L- and K-shell electron capture processes [292], respectively, see Chapter 5. ^{83m}Kr offers two energy lines at 32.15 keV and 9.41 keV from an isometric transition, see Appendix A. The two lines, following shortly after one another, are the result of an intermediate decay state with a half-life of 155.1 ns [293]. If they are not resolved separately at short delay times, due to detection or data processing limitations, or if they are purposely merged in the data analysis, we observe the combined energy of 41.56 keV.

This chapter is structured as follows: We describe the detector and the data acquisition (DAQ) system in Section 4.1, detail the processing tools in Section 4.2 and evaluate the SiPM characteristics and performance in Section 4.3. Section 4.4 summarises this chapter.

4.1 Setup, Operating Conditions and Data Acquisition

The subsequently described TPC is an upgrade of the Xurich II setup [13] operated at UZH. The upgrade concerned the replacement of the top PMT with an array of SiPMs and their read-out electronics.

The detector is placed inside a vacuum-insulated stainless steel vessel which is coupled to a liquid nitrogen bath via a copper cold finger. The TPC drift region is defined by a 31 mm × 31 mm (diameter × height) cylindrical PTFE shell with a cathode mesh at the bottom and a gate mesh at the top, shown in Figure 4.1. The anode is placed 4 mm above the gate. The liquid surface was kept in the middle of the two top electrodes, at $\sim$ 2 mm above the gate for the presented data in Chapters 5 and 6, optimised for S2-amplification. Seven copper field-shaping rings, separated by PTFE spacers and connected via a resistor chain, ensure a uniform drift field, which is maintained between the negatively biased cathode and the gate at ground potential. By varying the cathode voltage, we can acquire data at different drift fields. For the ^{37}Ar source, we acquired data in the

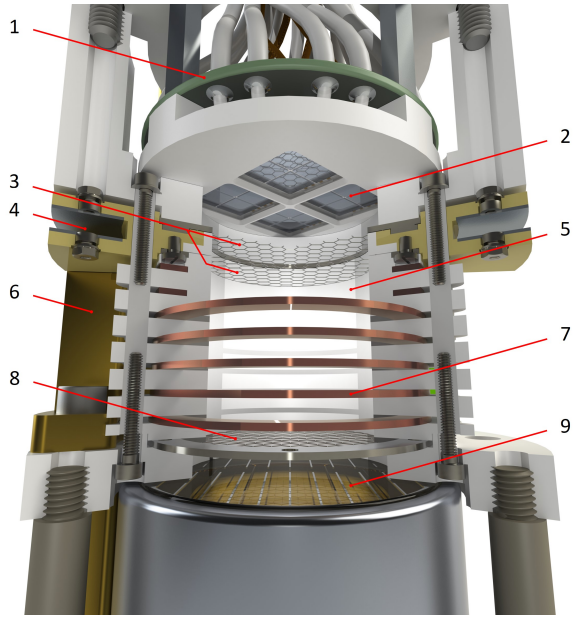

Figure 4.1: Rendering of the upgraded Xurich II TPC. The active LXe is contained within a PTFE cylinder and surrounded by copper field-shaping rings. A 2-inch PMT is placed in the liquid, and an array of 16 SiPMs is placed in the gaseous phase at the top. For the sake of visualisation, two field-shaping rings have been cut. **Legend:** 1 – PCB with ×10 pre-amplifier, 2 – SiPM array, 3 – Anode and gate mesh, 4 – Level meters, 5 – PTFE reflector wall, 6 – Weir for liquid level control, 7 – Copper field-shaping rings, 8 – Cathode, 9 – PMT.

range $80-968\,\mathrm{V/cm}$ while we probed the interval $484-968\,\mathrm{V/cm}$ for $^{83\mathrm{m}}$Kr[1]. The electron extraction field is created between the gate and the positively biased anode and was kept constant at $10\,\mathrm{kV/cm}$ ($5.4\,\mathrm{kV/cm}$) in the gas (liquid) phase by setting the anode to a nominal voltage of $+4\,\mathrm{kV}$.

The xenon is continuously purified of electronegative impurities by circulating the gas phase through a hot metal getter, an integral part of the gas handling system. The gas system features a source chamber which allows for the introduction of $^{83\mathrm{m}}$Kr from the decay of ^{83}Rb with $T_{1/2} = (86.2 \pm 0.1)\,\mathrm{d}$ [13, 293]. With an additional gas mixing setup, described in Section 5.1, that can be connected in parallel to the ^{83}Rb source chamber, we also deploy a gaseous ^{37}Ar source.

The S1 and S2 signals are detected by a single 2-inch diameter PMT (R6041-06 MOD, Hamamatsu Photonics K.K.), placed in the liquid phase at the bottom of the TPC, and sixteen $6 \times 6\,\mathrm{mm}^2$ VUV4 SiPMs (2×2 array of S13371, Hamamatsu Photonics K.K.) placed in the gas phase. The PMT was biased with $-940\,\mathrm{V}$, while the SiPMs were biased with $51.5\,\mathrm{V}$. To install the SiPMs in the TPC, a PTFE holder which exactly replaced the area occupied by the former top PMT was designed and built. The SiPMs were arranged in the holder to maximise the light collection efficiency (LCE) as studied in MC simulations [14]. The distance from the surface of the SiPMs to the anode is $5\,\mathrm{mm}$, optimised to obtain good position resolution.

The new configuration of the TPC requires 17 readout channels, 15 more than in the previous design. To handle this number of cables in the small detector, we installed a new CF-40 feedthrough for 20 double-shielded coaxial signal cables (RG 196) for the photosensors and 7 Kapton® insulated wires for voltage biasing. To independently read out the 16 SiPM channels, a printed circuit board (PCB) was designed. Each SiPM, on its cathode side, is connected in series with a $10\,\mathrm{k\Omega}$ resistor to the bias voltage to limit the current and avoid possible damage to the device. On its anode side, each SiPM

[1] We also acquired ^{37}Ar data at $1000\,\mathrm{V/cm}$, and $^{83\mathrm{m}}$Kr data at $194\,\mathrm{V/cm}$ and $323\,\mathrm{V/cm}$ but do not use these data sets for the analysis presented here due to their low statistics. However, we do show a drift speed measurement up to $1000\,\mathrm{V/cm}$ in Table 4.1 based on ^{37}Ar data.

is grounded with a 50 Ω resistor and coupled to a custom-made ×10 voltage amplifier circuit [14]. The main component of the circuit is the ultra-low noise, non-inverting voltage feedback operational amplifier OPA847 from Texas Instruments Incorporated [294]. This amplifier has a nominal gain of 20 when connected to an open circuit at the output and is able to reduce the electronic pick-up noise to a negligible level. It operates from direct current to 250 MHz and has a 50 Ω output impedance that matches the input impedance of the ADC (analog-to-digital converter). These two resistances form a voltage divider at the amplifier output. Because of this loading effect, the effective final signal amplification with a 50 Ω load from the ADC is tenfold. The heat dissipation of the entire amplifier board is ~ 3 W, whereas it was negligible for the former 2-inch PMT base. This additional heat load can safely be handled by the cooling system of the detector.

The detector was operated such that the GXe was kept at a pressure of 2.0 bar and the LXe was slightly below its boiling point at 177 K. Under these conditions, LXe has a density of 2861 kg/m^3 [191]. The detector was kept in this state during the calibration runs and the thermodynamical parameters only varied slightly over the data taking periods: The pressure and LXe temperature range was 0.05 bar and 0.4 K, respectively. The gas recirculation flow through the hot metal getter was stable within $0.5 - 0.6$ slpm (slpm – standard litre per minute).

The signal sizes are energy dependent, thus deploying different calibration sources requires an adjustment of the settings in the DAQ. The S1 signals of the ^{37}Ar lines, for instance, are much smaller than those of the ^{83m}Kr lines and can even be missed by the trigger or absent in the waveform. At the high end in signal size, the PMT channel could, if not limited in voltage, saturate the electronics with S2 signals from ^{83m}Kr. Below, we discuss the DAQ settings and the deployed hardware in detail.

We show a schematic of the DAQ of Xurich II in Figure 4.2. The raw data is digitised by three 8-channel CAEN S.p.A. V1724 [295] modules connected in daisy chain, each with a 100 MHz sampling rate (10 ns samples) and 14-bit resolution at 2.25 V dynamic range. The daisy-chained data is then sent via a CAEN V2718 VME (Versa Module Europa) to PCI (Peripheral Component Interconnect) optical link bridge to a PC (personal computer). The pre-amplified SiPM signals are fed directly to the Flash ADCs. The PMT signal is attenuated by a factor of 10 for the ^{83m}Kr data, while not attenuated for ^{37}Ar, then sent to the digitisers. After passing through a CAEN 625 fan-in/fan-out module the trigger is generated by a CAEN N840 leading edge discriminator based on the PMT signal. For ^{83m}Kr, we require the attenuated PMT signal to exceed 2 mV, which corresponds to a peak with integrated charge of $> 15 - 21$ PE. For ^{37}Ar, we trigger on 7 mV of the raw PMT signal corresponding to $> 4 - 5$ PE. Only for the data at 80 V/cm drift field we use 6 mV. The event window for the ^{83m}Kr data was chosen to be 40 µs with 30 µs post-trigger time, which is sufficiently large to contain the S2 even for the lowest field of 194 V/cm when triggered on the S1. Triggers on ^{83m}Kr S2 signals are expected to be rare and are removed in the analysis phase to avoid a bias of events towards the upper half of the TPC. For ^{37}Ar, the event window was chosen to be 60 µs with the trigger placed in the middle at 30 µs to contain the entire waveform, regardless of whether the trigger was issued by an S1 or S2. The maximum observed drift time at the lowest applied field of 80 V/cm from the cathode to the liquid surface is ~ 22 µs, cf. Section 4.2.4.

Depending on the user settings, entire waveforms can be written to disk or, to save memory, only the samples exceeding a certain threshold (henceforth referred to as *good* as distinguished from *skipped*) by means of zero length encoding (ZLE), as shown in Figure 4.3. The first half of the ^{83m}Kr data was taken without ZLE while the rest, including the ^{37}Ar data, was acquired with ZLE. The ZLE threshold for ^{83m}Kr, which only comes into play if a trigger is issued, was chosen to be 15 bins (~ 2.06 mV at ADC input) for the PMT channel and 10 bins (~ 1.37 mV at ADC input) for the SiPM channels. To catch the S1s of ^{37}Ar at the single PE level, we have chosen 20 bins (~ 2.75 mV at ADC input) for the PMT channel and 6 bins (~ 0.82 mV at ADC input) for the SiPM channels as ZLE thresholds. These values were determined empirically and, in the case of ^{37}Ar, set just above the baseline. In addition to the over-threshold samples, a certain number of backward- and forward-

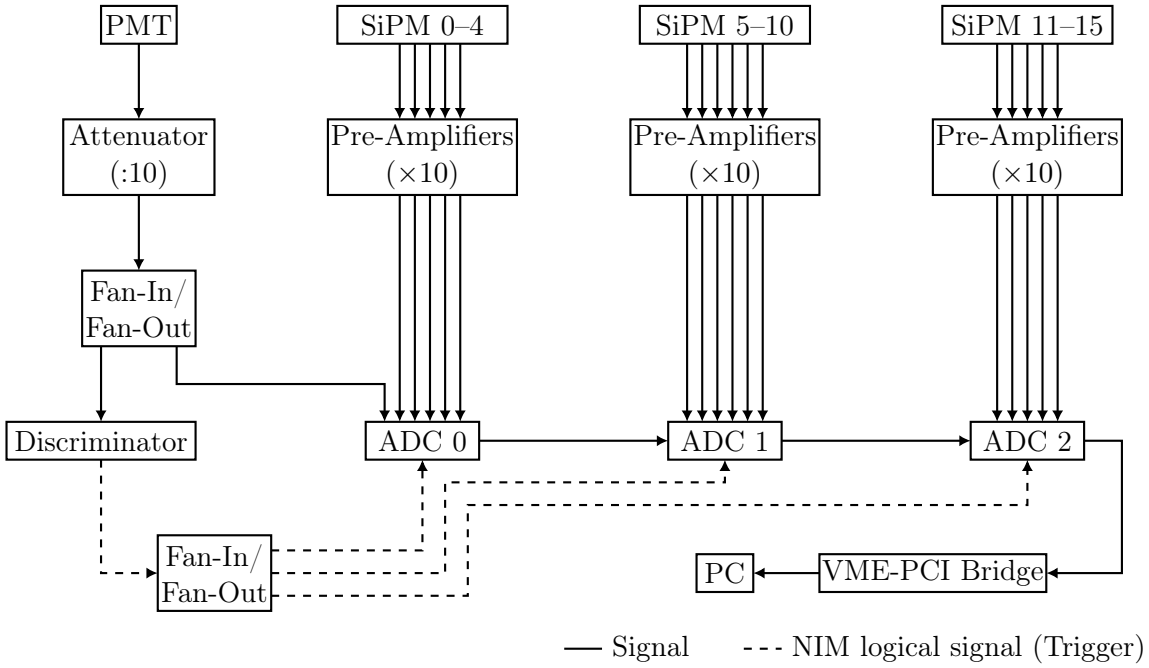

Figure 4.2: Schematic of the Xurich II DAQ. The attenuator on the PMT signal was used for ^{83m}Kr data taking only. The ADC boards are triggered by a NIM (Nuclear Instrumentation Modul) logical signal generated by a leading edge discriminator based on the PMT signal.

samples can be specified to include the rise and the tail of the peak. To keep timing information, the counts of good samples and skipped samples are recorded as so-called *control words* [296]. We recorded 150 (200) backward-samples and 150 (100) forward-samples for ^{83m}Kr (^{37}Ar). For these DAQ settings, a data set of 500000 events recorded with ZLE typically occupies ~ 6 GB of disk space. Thus, the amount of data at DAQ rates of $\mathcal{O}(10\,\text{Hz})$ can be handled with standard equipment and saved on hard disks.

4.2 Data Processing

The upgrade of Xurich II made the development of a new raw data processor necessary, as the one described in References [13, 297] was not designed for the large number of channels, nor was it for ZLE or the new photosensor type. In fact, it used a χ^2 filter on the S1 peak shape tailored to PMT signals. For this reason, a more general framework for an arbitrary number of photosensor channels of more generic type for both, ZLE and normal waveforms, was developed in C++ and ROOT [298].

The data processing consists of three stages. The first is devoted to event alignment and merging of the data files from the three ADC modules into one. The second stage is the main raw data processing of the waveforms on an event-by-event basis. It retrieves basic information about the peaks in the individual channels, identifies pulses as coincidences of these peaks and classifies their pulse type (S1/S2/noise). The third step is the post-processing tailored to the analysis phase: Events are built by combining S1s and S2s based on measured charges and physical drift times. Geometry or drift time related corrections are applied later in the analysis, as discussed in Chapter 5, Section 5.2. We detail on these three stages below.

4.2.1 Pre-Processing

The first stage ensures the correct matching of the events recorded by the three ADC modules by means of a comparison of the trigger time tag changes among triggers. Misalignment among the modules can be caused by an incorrectly propagated busy state. However, an efficient offline realigning-algorithm typically restores 99.9 % of the raw events. Once all the events are aligned, events of one data set are merged into one ROOT file.

4.2.2 Main Processing

Prior to the actual processing, in the ZLE case, the waveforms are reconstructed from the control words. The second stage starts with the baseline calculation of the raw waveforms and the inversion of the negative PMT signal. For the non-ZLE traces, the mean of the first 50 samples is subtracted from the whole trace. In the ZLE case, we account for baseline shifts by calculating the baseline for each good-region individually based on the first half of the backward-samples, shown in Figure 4.3. This is of particular importance to detect very small S1 signals that are hidden in the recovery region of high-charge background signals. For two consecutive good-regions, i.e. overlapping forward-samples of the previous and backward-samples of the following good-region, the baseline is taken within the $[60, 90]$ % interval between the two adjacent over-threshold regions.

The threshold for peak-detection (not to be confused with the ZLE threshold for the DAQ) was chosen to be two standard deviations, 2σ, of the baseline distribution around zero. The peak integration limits are dynamically defined based on the following criteria on the variation of the baseline: The left edge of the first peak in the waveform (non-ZLE) or good-region[2] (ZLE) is the first sample that is outside $\pm 1\sigma$ around the baseline with a relative difference of more than 1σ to the following. The condition for the right edge, and accordingly for both boundaries of all following peaks of the respective region, is weaker due to possible baseline shifts and large fluctuations. Necessary for the peak integration to stop is that the waveform is again below the peak-detection threshold. Sufficient is one of the following: if the waveform is back to the $\pm 1\sigma$ region, if it exceeds the threshold again[3] or if the sum of at least five consecutive samples, each closer than 2σ to the next, is less than 2σ. This ensures that the integration is terminated as soon as the waveform is flat again even if it underwent a large baseline shift. Integration windows smaller than 3 samples are discarded for noise suppression.

The processor can, to a certain extent, distinguish multiple peaks that overlap. This is necessary to resolve the event topology of ^{83m}Kr with two S2 signals arriving shortly after one another (see Appendix A) and is helpful to separate afterpulses[4] from the main peak. To reduce the sensitivity to random fluctuations, the method requires over-threshold regions of at least 6 samples. We split two peaks based on their moving average of order of 4 samples (order 2 samples for over-threshold regions ≤ 25 samples) whenever both have fallen below half of their individual maximum value. Thus, for a Gaussian-shaped peak almost 90 % of its charge is integrated when cut on one side. In Chapter 6, we use a data-driven approach to quantify this leakage for actual ^{83m}Kr waveforms. The moving average limits the algorithm to a minimum peak separation of 40 ns or 20 ns, respectively. This time-scale is sufficiently short to split even close S1 signals efficiently and is irrelevant for S2 signals for which the requirement of the contained charge dominates.

After a peak is found, separated from others and its integration window fixed, the peak properties are extracted. The area is determined from the summed bin content of each sample, the peak position is defined as the position of the maximum sample. We also determine the width of the peak which

[2] For consecutive good-regions this applies to the first one.

[3] In that case the peaks are split in the local minimum between the last and next over-threshold sample.

[4] Afterpulses are small correlated signals that, within a certain time period, follow a larger signal and that are due to a delayed charge amplification. This effect is known for PMTs [263] and SiPMs [14].

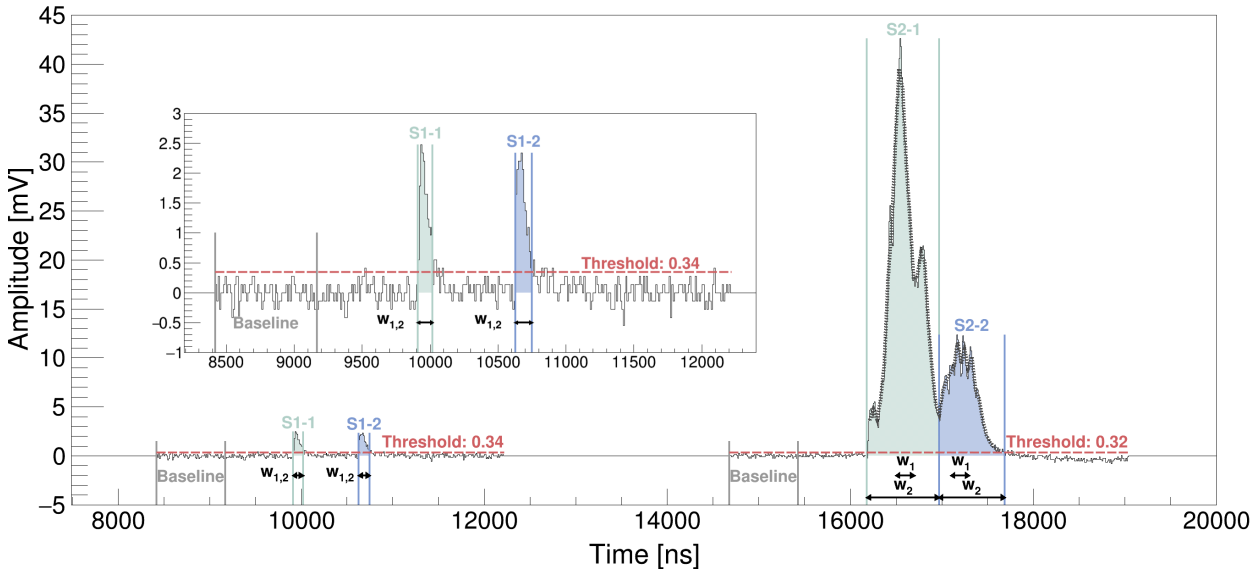

Figure 4.3: Recorded SiPM waveform of a ^{83m}Kr event acquired with ZLE. For visualisation, we present the relevant region of the 40 µs DAQ window of an event from a SiPM channel located at an outer corner of the array that exhibits small S2 signals for events in the horizontal center of the TPC. The peaks are located in two good-regions surrounded by 150 backward- and forward-samples with skipped-regions in between. The integration windows are shaded and enclosed by lines. The baseline, from which the threshold is defined, is calculated individually for each good-region. While for disjointed good-regions, like here, it is based on the first half of the backward-samples, for two consecutive good-regions, the baseline is calculated within the $[60, 90]$ % interval between the two adjacent over-threshold regions. The S2 signals are overlaid with the moving average on which the splitting algorithm is based. While it splits the two S2s because they have both fallen below half of their individual maximum value, it is insensitive to the visible fluctuations of the S2 light. The widths w_1, w_2 used for the filters are limited to the integration window and, hence, are equal for the S1 signals. In the zoom, it is visible that over-threshold regions below 3 samples are not integrated.

serves as discriminator for the S1- and S2-identification. S1 and S2 signals are distinguished by width-based filters, where the filters at the ith bin are defined as:

$$S1_i := \sum_{j=i-\frac{w_1}{2}}^{i+\frac{w_1}{2}} A_j \quad \text{and} \quad S2_i := \sum_{j=i-\frac{w_2}{2}}^{i+\frac{w_2}{2}} A_j - S1_i \quad . \tag{4.1}$$

A_j is the baseline-subtracted signal at the jth bin and w_1, w_2 are the two widths. While a maximum summation width of $w_1 = 20$ samples contains the entire S1, w_2 was chosen to be maximum 100 samples. The sums are bounded by the peak integration window to guarantee that it is not summed over a distinct close-by peak. Both filters are evaluated at bin i being the centre of the full width at half maximum of the peak to account for their asymmetric shape. The S2-filter will be zero for an isolated S1-like signal and much larger for an S2. We choose the ratio $S2/S1$ as discriminator and identify a peak with S2 if this ratio is > 0.2, i.e. if $> 20\,\%$ more charge is contained within w_2 than within w_1. This reveals the importance of good S1-splitting as we rely on the fact that S1s are contained inside w_1. Unlike the previous processor [13, 297] which applied these filters on the whole waveform to define the S1 and S2 search regions, here, we apply them on already detected peaks.

For the event building stage, it is essential to form physical pulses from the detected peaks. We define a pulse as a set of peaks of at least two channels in time coincidence. The coincidence window is different for S1 and S2 signals and set based on the classification of the PMT peak: We use ±4 samples (±20 samples) for an S1 (S2) signal around the median sample(s) of a certain accumulation of peaks.

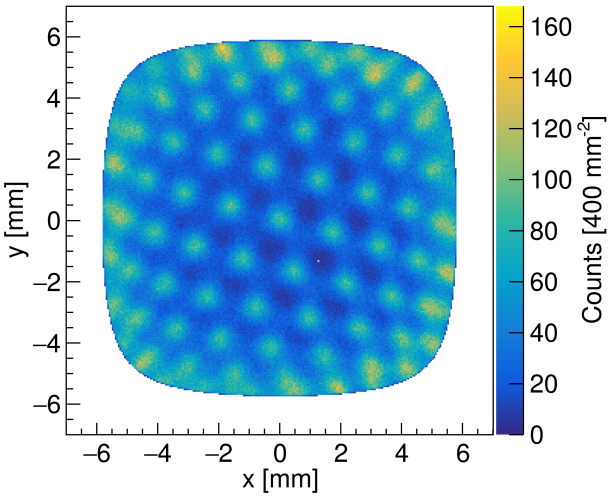

Figure 4.4: Uncorrected (x, y)-positions from ^{37}Ar K-shell capture data. While the performance of the horizontal position reconstruction with the centre-of-gravity algorithm is very good in the middle of the TPC, it features a square-shaped bias towards the TPC boundary.

To be distinct, accumulations are defined by a separation of > 8 samples. These medians are biased by the slightly different peak rise time of SiPMs that constitute the majority of the channels. For this reason, even if outside of the tighter coincidence window, a PMT peak in an accumulation region is counted to the pulse. To keep the information from the peak-splitting and not deteriorate the minimum splitting distance, we allow at most one PMT peak per pulse[5].

4.2.3 Post-Processing

The post-processing script creates high-level variables based on the described output of the main processing. Sufficient for the examined calibration sources, it selects the two highest-charge S1s and S2s of an event with the corresponding peak properties from those pulses in which the PMT was involved. In addition, it stores the photosensor gains, reconstructs the (x, y)-position of each event and calculates the drift times from the delay between the S1 and S2 signals. We require a positive and physical drift time, i.e. the S1 must happen before the corresponding S2 and their distance must not exceed a maximum value. To reduce the contribution of high-energetic events and ensure correct S1-S2-pairing, we remove saturated signals just below the maximum input voltage of the limiting fan-in/fan-out module of 1.6 V at 11 600 ADC bins or higher. The calculation of higher-level variables and the conversion from ADC bins to PE are performed at the analysis stage.

4.2.4 Position Reconstruction and Fiducial Volume

The top photosensor array allows for the reconstruction of the (x, y)-position of interactions. We use a simple centre-of-gravity algorithm to determine the (x, y)-position of an event from the light distribution among the photosensors caused by the largest S2 signal. We denote the physical position of the ith SiPM in the array by $(X, Y)_i$, with the origin of the coordinate system being the centre-of-gravity of the array. We then obtain the (uncorrected) event position in x from a geometry- and

[5]Split peaks of pure SiPM pulses could get merged into the same pulse but are rejected in the post-processing phase.

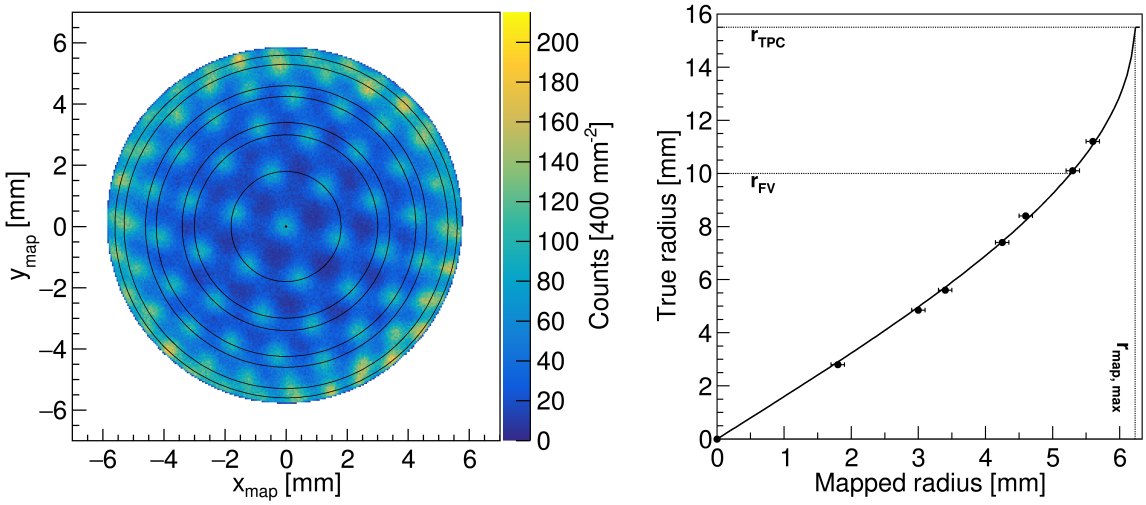

Figure 4.5: Left: Reconstructed (x, y)-positions from ^{37}Ar K-shell capture data. To obtain the corrected positions, the mapped radii of the black circles intercepting the dots are compared to the true positions of the gate mesh junctions in the right figure. **Right:** Projection function (Equation 4.4) between mapped and true radius with an approximately linear region below 10 mm defining the fiducial radius. The data points are the mapped radii of the circles from the left figure. The span of the error bars covers the radius of the high event-density region of a typical dot.

gain-weighted sum of the integrated S2 charge of each sensor[6],

$$x = \frac{1}{Q_{\mathrm{S2}}^{\mathrm{tot}}} \sum_{i=1}^{16} X_i \cdot \frac{Q_{\mathrm{S2}}^{i}}{g_i} \quad , \tag{4.2}$$

where the normalisation $Q_{\mathrm{S2}}^{\mathrm{tot}} \coloneqq \sum_{i=1}^{16} Q_{\mathrm{S2}}^{i}/g_i$ is the total collected S2 charge in the top array with the gain g_i of the ith SiPM channel. While this approach neglects the fact that the light intensity follows an inverse-square law with the distance from the light production site, we find that the algorithm is an adequate choice for our small-scale TPC and leads to excellent reconstruction in the TPC centre. Because of the square arrangement of the SiPMs and the nature of the centre-of-gravity approach, the resulting positions will not represent the actual circular cross-section of the TPC. In fact, while the reconstruction in the TPC centre is very good, events at the TPC boundary feature a square-shaped bias, see Figure 4.4. For this reason, the square is scaled down to unit side length with a constant, $x_{\mathrm{scal}} = x/c$, and then mapped onto a unit circle that is scaled back,

$$x_{\mathrm{map}} = c \cdot x_{\mathrm{scal}} \cdot \sqrt{1 - \frac{y_{\mathrm{scal}}^2}{2}} \quad . \tag{4.3}$$

While these mapped positions are centred around the origin of the coordinate system due to the gain correction in Equation 4.2, they still feature a radial bias because of the solid angle seen by the individual photosensors, see Figure 4.5, left. Using a data-driven approach, we correct for this effect by comparing the radial positions of the spots visible in the (x, y)-distribution with the true radii on which the gate mesh junctions are located, see Figure 4.5, right. Up to a radius of ~ 10 mm from the TPC centre, the correction function is fairly linear, i.e. the correction can be performed with a scaling factor, whereas for larger radii it diverges. This can be described by a projection of a sphere

[6] The reconstruction is performed analogously for the y-position.

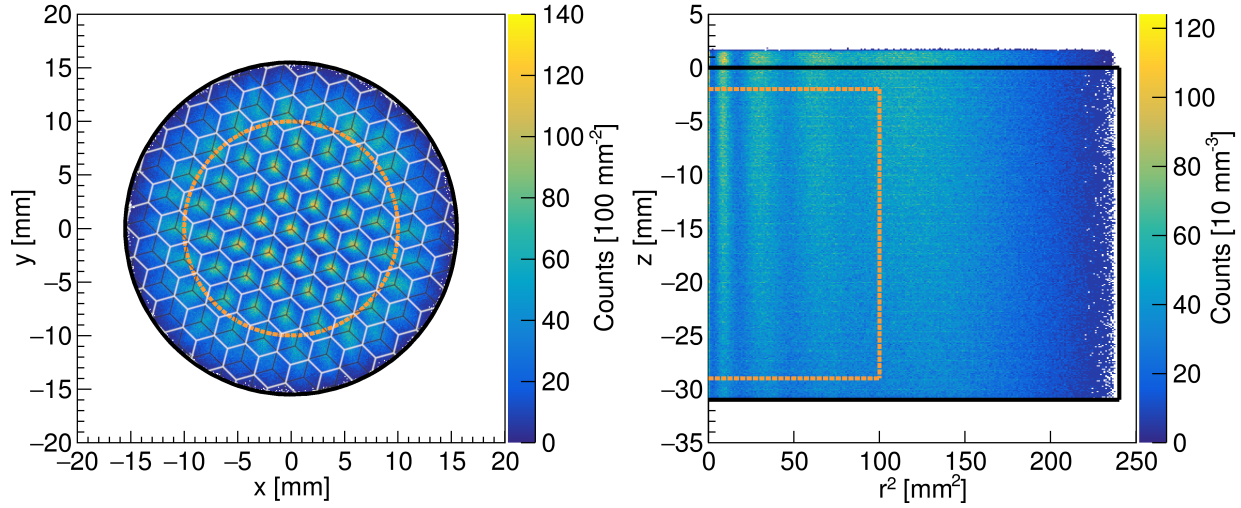

Figure 4.6: Event distribution from ^{37}Ar K-shell capture data. The boundaries of the detector and fiducial volume are represented by solid black and dashed orange lines, respectively. **Left:** Corrected x-y distribution with hexagonal gate (black) and anode (white) mesh. **Right:** r^2-z distribution. The $\sim 2\,\mathrm{mm}$ liquid level above the gate is visible.

onto a plane as:

$$x_{\mathrm{corr}} = \frac{d_{\mathrm{TPC}}}{r_{\mathrm{map}}} \cdot \left(\frac{1}{2} - \frac{1}{\pi} \cdot \arccos \frac{r_{\mathrm{map}}}{r_{\mathrm{map,\,max}}} \right) \cdot x_{\mathrm{map}} \quad , \tag{4.4}$$

where $r_{\mathrm{map}} = \sqrt{x_{\mathrm{map}}^2 + y_{\mathrm{map}}^2}$ is the mapped radius of the interaction site with $r_{\mathrm{map,\,max}}$ being the boundary of the TPC after the mapping and $d_{\mathrm{TPC}} = 2r_{\mathrm{TPC}} = 31\,\mathrm{mm}$ the true diameter of the TPC, see Figure 4.5, right. The linear region of this projection defines our radial fiducial volume cut to be $r < r_{\mathrm{FV}} = 10\,\mathrm{mm}$.

In Figure 4.6, left, we show the resulting (x, y)-distribution from ^{37}Ar data overlaid by the drawing of the meshes. The spots occur due to focusing of drifting electrons to the high-field regions around the junctions of the grounded hexagonal gate mesh. This limits the accuracy of the (x, y) event position reconstruction to roughly half the distance between the junctions, which is $\sim 1.5\,\mathrm{mm}$.

The z-position of an interaction is obtained from the time difference between the S1 and S2 signals. We extract the electron drift speed for a given electric field from the clearly visible position of the cathode and the gate in the drift time histogram, see Figure 4.7, and their spatial separation. The procedure, together with a drift speed measurement at different fields in Xurich II in the former configuration with two PMTs, are detailed in Reference [13]. The drift speeds that we find here are in agreement with former measurements [236, 297] and are in the range $1.5 - 2.0\,\mathrm{mm/\mu s}$, see Table 4.1.

To avoid high and potentially non-uniform electric field regions around the electrodes, we select only events within $z \in [-29, -2]\,\mathrm{mm}$, where $0\,\mathrm{mm}$ is the position of the gate and $-31\,\mathrm{mm}$ is the position of the cathode. The fiducial region defined by these boundaries is shown in Figure 4.6 and contains a xenon mass of $\sim 24.5\,\mathrm{g}$. We find for the homogeneously distributed ^{37}Ar events that a fraction of 34.9 % passes the radial fiducial volume cut. The number of events is reduced by another 62.8 % to 13.0 % after a subsequent application of the fiducial volume depth.

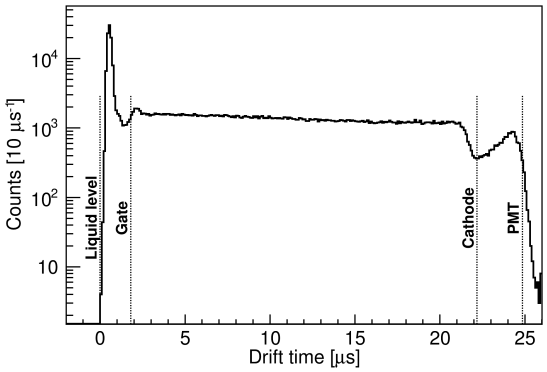

Figure 4.7: Drift time histogram from ^{37}Ar K-shell capture data at 80 V/cm drift field with the marked positions of the liquid level, gate, cathode and PMT. Unlike at high drift fields, we can see events below the cathode because the negative bias voltage of the PMT is, in absolute terms, higher than the cathode voltage. This allows electrons to drift upwards into the region between the PMT and the cathode.

Drift Field [V/cm]	**Drift Speed** [mm/µs]
80	1.52 ± 0.03
100	1.59 ± 0.03
200	1.63 ± 0.03
400	1.75 ± 0.03
600	1.83 ± 0.03
800	1.90 ± 0.04
968	1.96 ± 0.04
1000	1.96 ± 0.04

Table 4.1: Determined electron drift speeds for different electric fields at 177 K.

4.3 Photosensor Characteristics and Performance

4.3.1 Photosensor Working Principle

To facilitate the understanding of the subsequent photosensor characteristics, in particular those of the SiPMs on which we focus, we briefly outline the working principles of the discussed photosensors in a conceptional manner. In Figure 4.8, we show a schematic of a PMT. A generic PMT is a vacuum tube housing a photosensitive electrode, the photocathode, at a certain constant electric potential, several dynode stages, in this case four, at increasing potential and a readout anode at the highest potential. The potential drops can for example be realised with a resistor chain. A photon impacting onto the photocathode with an energy higher than the work function of the cathode material yields a primary electron ($\equiv$ 1 PE) by external photoelectric effect with a quantum efficiency (QE). The primary electron is accelerated to the first dynode stage. Focusing electrodes can be used to increase the collection efficiency (CE) of the primary electron to reach the first dynode, where it knocks more electrons out of the dynode. These secondary electrons are accelerated to the next dynode, where this process repeats. This leads over several dynode stages to an electron multiplication producing an anode current. With this method single photons can be detected. Within the linear regime of the PMT, the integrated anode current is proportional to the number of detected photons. We call the product of QE and CE the photon detection efficiency (PDE) of the PMT.

A SiPM uses a comparable electron multiplication method to detect photons but uses a silicon

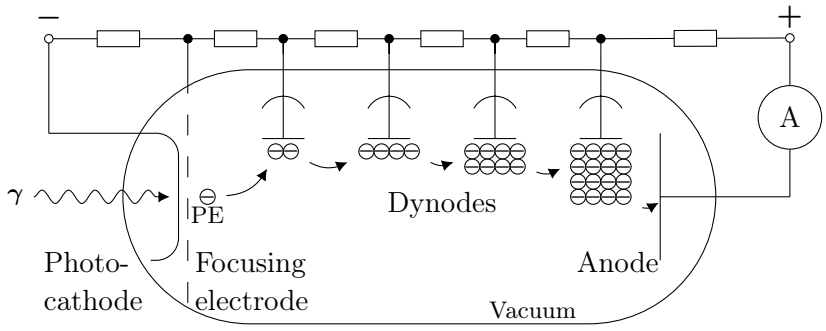

Figure 4.8: Schematic of the PMT working principle.

lattice and internal photoelectric effect instead. In Figure 4.9, we show a schematic of the working principle of a SiPM. A SiPM consists of a high number of parallelly-connected microscopic cells or pixels of a typical side length of $\mathcal{O}(10\,\mu\text{m})$. Each cell consists of a single avalanche photodiode (APD) and a quenching resistor (R_q). An APD is a p-n junction (highly doped p^+ and n^+) with an additional p^+ implant just below the n^+ layer [299]. When reversely-biased with an externally applied voltage, the p^+ implant creates a region of high electric field towards the n^+ sheet and a region of low electric field towards the p^+-doped substrate. These two regions are separated by a moderate electric field region, the π layer. The band gap of silicon sets the photon detection threshold to $> 1.1\,\text{eV}$. The energy of a photon which is absorbed in the bulk π layer ionises the silicon crystal, yielding an electron-hole pair. The electron and the hole drift in the electric field towards the n^+ and p^+ side, respectively. In the region of high electric field, the electron gains sufficient energy to create other electron-hole pairs by impact ionisation, whose electrons create in turn more electron-hole pairs. This self-sustaining avalanche process amplifies the integrated photocurrent of the initial drifting single electron to a measurable signal and increases exponentially with time. The photocurrent in a cell is limited by the quenching resistor in series to the APD as follows: In order for the APD to be sensitive, it is operated, reversely biased, above the breakdown voltage which sets the APD in the so-called *Geiger mode*. The breakdown voltage is the bias voltage above which the creation rate of electron-hole pairs in the high-field avalanche region is greater than the collection rate of the charge carriers in the silicon lattice of the low-field ends. The difference of the used bias and the breakdown voltage is known as overvoltage. The voltage drop over the quenching resistor is the higher, the higher the photocurrent due to the avalanche process is, lowering the voltage on the APD to the breakdown. This stabilises the photocurrent and finally halts the avalanche. After the current vanished, the APD is set back into Geiger mode by the bias voltage. The resulting signal has a sharp rise due to the avalanche process and a slow recovery tail due to the recharge of the cells. The recharge time depends on the quenching resistance, the internal capacitance and resistance of the cells and the number of fired cells. An important property of APDs is that they count photons binary, i.e. the output signal is the same for one or several photons that get absorbed at the same time and excess photons onto cells thus stay undetected. The light detection and linearity of SiPMs, that consist of typically several thousand cells, thus relies on the assumption that more light to be detected, i.e. a higher number of photons, is also spread over a larger area on the SiPM. The SiPM is ultimately operated outside of its dynamic regime when the number of impacting photons is equal to the number of cells. However, all cells of a SiPM operate independently of each other and stay sensitive and charged while another cell is triggered.

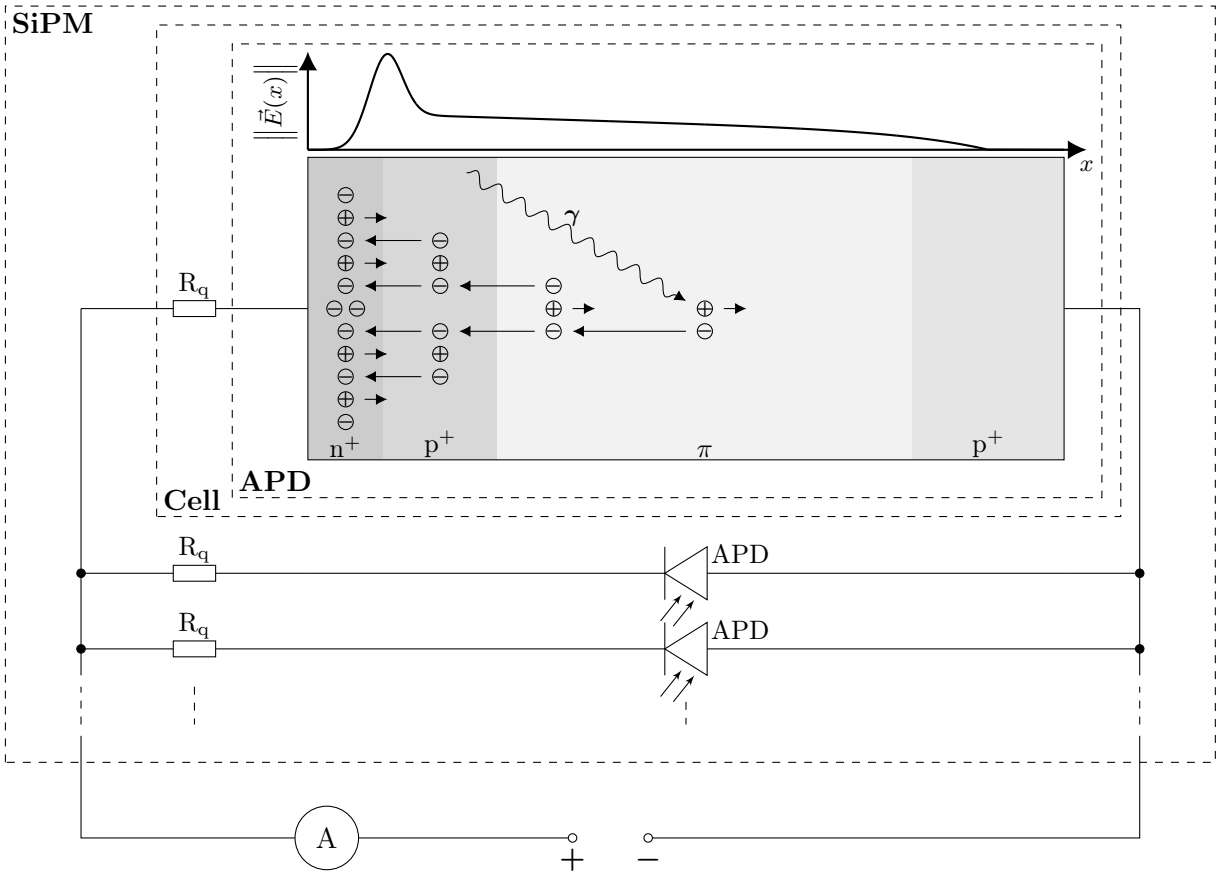

Figure 4.9: Schematic of the SiPM working principle.

4.3.2 Photosensor Gain

The photosensor gain describes the internal signal amplification factor of the photosensor. As we discussed above, in the case of a PMT, the primary electron from an incident photon on the photocathode is multiplied over several dynode stages. The gain is given by the ratio of the number of electrons at the last dynode stage or anode and the number of initial electrons. The same definition is applied to SiPMs, where instead of discrete dynode stages the gain is due to the electron avalanche in the electric field of the cells.

In Xurich II the gain of the photosensors was monitored and calibrated about once a week during data taking periods. The calibration was performed with light from an external blue light-emitting diode (LED) as described in Reference [13]. The gain values are calculated following the model-independent approach proposed in Reference [300]. The SiPMs showed a stable gain during the entire data taking period. In Figure 4.10, left, we present the stability of the averaged SiPM gain.

In addition, the gain of the SiPMs is found to be uniform across the array, with small variations of $< 6\,\%$ among channels (see Figure 4.11, left). The signals of the channels are however scaled individually with their mean gain. In Figure 4.11, left, we see that channel 5 shows a gain which is $\sim 3\,\%$ lower than the mean, attributed to a higher temperature in that corner of the amplifier board. Since all SiPM channels were operated at the same constant bias voltage, a higher temperature reduces the overvoltage and thus, the gain [275]. We also observe that the channels 1 and 3 have a gain which is $\sim 3\,\%$ higher than the mean. However, as we shall see below, this is the only metric for which these two channels stand out.

The error-weighted SiPM mean gain over the data-taking period is $(3.12 \pm 0.01) \times 10^6$ at a bias

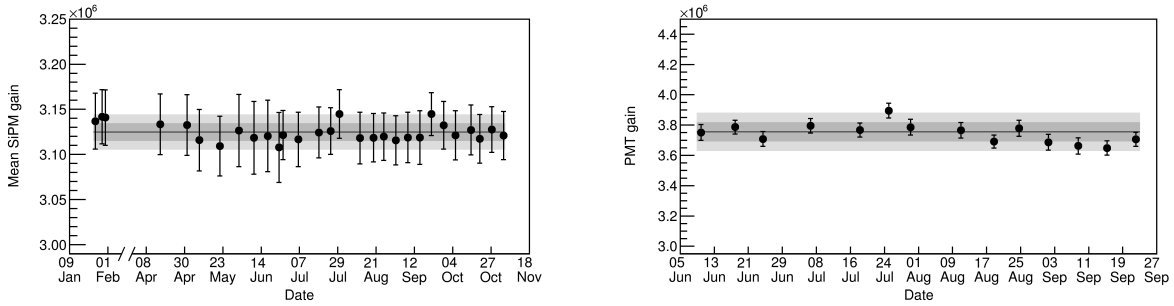

Figure 4.10: Longterm stability of the photosensor gains. We show the $\pm 1\sigma$ and $\pm 2\sigma$ uncertainty bands around the means. **Left:** Error-weighted mean gain of the 16 SiPM channels over the entire data taking period in 2019. We measured $(3.12 \pm 0.01) \times 10^6$ as average. Data with ^{83m}Kr (^{37}Ar) was acquired before (after) the time-axis break. **Right:** PMT gain during the ^{37}Ar data taking period. We measured $(3.76 \pm 0.06) \times 10^6$ as average.

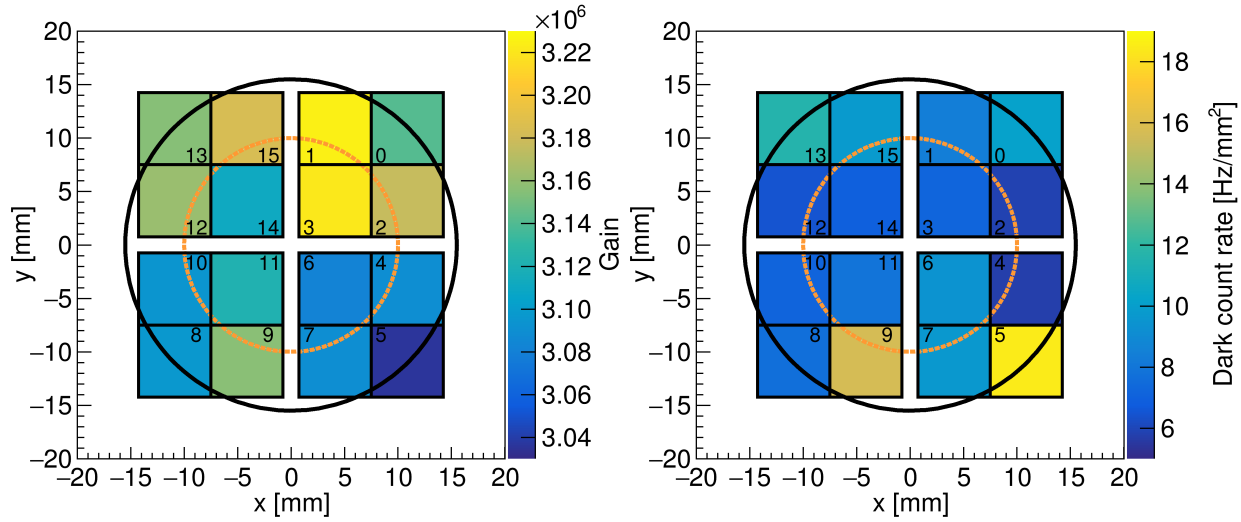

Figure 4.11: Left: Mean gains of the SiPM channels, measured during operation with xenon in dual-phase mode. **Right:** Dark count rates in the SiPM channels, measured with nitrogen gas at $\sim 190\,\mathrm{K}$. **Both:** The detector and fiducial circumferences are represented by a solid black and dashed orange circle.

voltage of 51.5 V. For the bottom PMT, the measured gain during the ^{37}Ar data taking phase is $(3.76 \pm 0.06) \times 10^6$ at an operating voltage of $-940\,\mathrm{V}$, see Figure 4.10, right. The given uncertainties correspond to the standard deviation of the time averaged gains.

4.3.3 SiPM Dark Count Rate

The dark count rate of a photosensor is its uncorrelated thermal noise rate, in the absence of external light. In the case of SiPMs this is due to imperfections in the silicon structure. In Xurich II, the dark count rate was measured based on scintillation-free data acquired with nitrogen gas in the TPC under very similar thermodynamic conditions to those observed when using xenon. To this end, the DAQ was set up in such a way that the investigated SiPM channel triggered all three ADC boards when its waveform exceeded the baseline, i.e. while only that one SiPM channel issued triggers, all SiPM channels were recorded. The dark count spectrum of channel 5 is shown in Figure 4.12.

The number of dark count events is defined as the integral of the spectrum above a threshold of 0.5 PE. Located in the gas phase at $\sim 190\,\mathrm{K}$, the SiPMs have shown an error-weighted mean

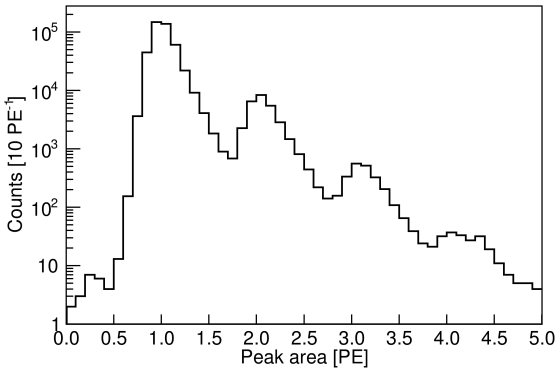

Figure 4.12: Dark count spectrum of a single SiPM channel (channel 5) with single PE resolution.

dark count rate of $(8.05 \pm 0.03)\,\mathrm{Hz/mm^2}$ at a bias voltage of 51.5 V, which is consistent with an extrapolation of the data shown in Reference [275]. In Figure 4.11, right, we show the distribution of the dark count rates of the individual channels. The dark count rate in channel 5 is increased by more than a factor two compared to average. This confirms the hypothesis that this SiPM was slightly warmer than the rest of the array since the dark count rate of SiPMs features an exponential temperature dependence at constant over-voltage while it is only linearly dependent on the over-voltage at constant temperature [275]. The dark count rate of the PMT was not measured. However, PMTs typically feature a rate which is one to two orders of magnitude lower than the one of SiPMs at comparable gain and LXe temperature. Reference [301] shows for example that the dark count rate of a R6041-506 MOD PMT from Hamamatsu Photonics K.K., similar to the model used here, is $0.01 - 0.6\,\mathrm{Hz/mm^2}$ in the temperature range $87 - 300\,\mathrm{K}$, at comparable bias voltage.

4.3.4 SiPM Crosstalk

Another characteristic of photosensors is their crosstalk among neighbouring channels, i.e. their correlated noise, which enhances the light signal. In the case of SiPMs, we can distinguish two types of crosstalk: internal crosstalk among neighbouring cells within a single sensor and external crosstalk among different sensors in close proximity. The former is due to photons, either primary or secondary from the avalanche process, that cross the boundary of the cell and trigger an avalanche in a nearby cell. This effect can be reduced by the use of optically opaque trenches that separate the cells. The standard way to quantify the internal crosstalk is to calculate the probability that a dark count event, in the absence of external light, triggers more than one avalanche resulting in a signal with $> 1\,\mathrm{PE}$. Note that this definition relies on the assumption that the dark count rate and the number of cells in the investigated sensor is low enough such that the probability of a random coincident dark count of two cells, for a given trigger time window, is negligible. This is the case for the deployed SiPMs [302]. The crosstalk probability of a given channel is calculated from spectra like in Figure 4.12 as the ratio of the integrated events above 1.5 PE threshold and the total number of dark count events above 0.5 PE threshold [275]. We obtain an error-weighted mean internal crosstalk probability of $(8.63 \pm 0.03)\,\%$ over the SiPM array. This internal crosstalk probability is roughly by a factor 4 higher than expected from the measurements in Reference [275] where the maximum measured crosstalk probability is $< 7\,\%$ at the highest investigated over-voltage of 7 V. We comment on this point in the next section where we present an independent measurement method of the internal crosstalk probability based on data from the ^{37}Ar calibration run. In Figure 4.13, left, we show the distribution of the internal crosstalk probability values over the array and see that channel 5 again shows a slightly lower value. While the crosstalk probability is constant with temperature for a fixed

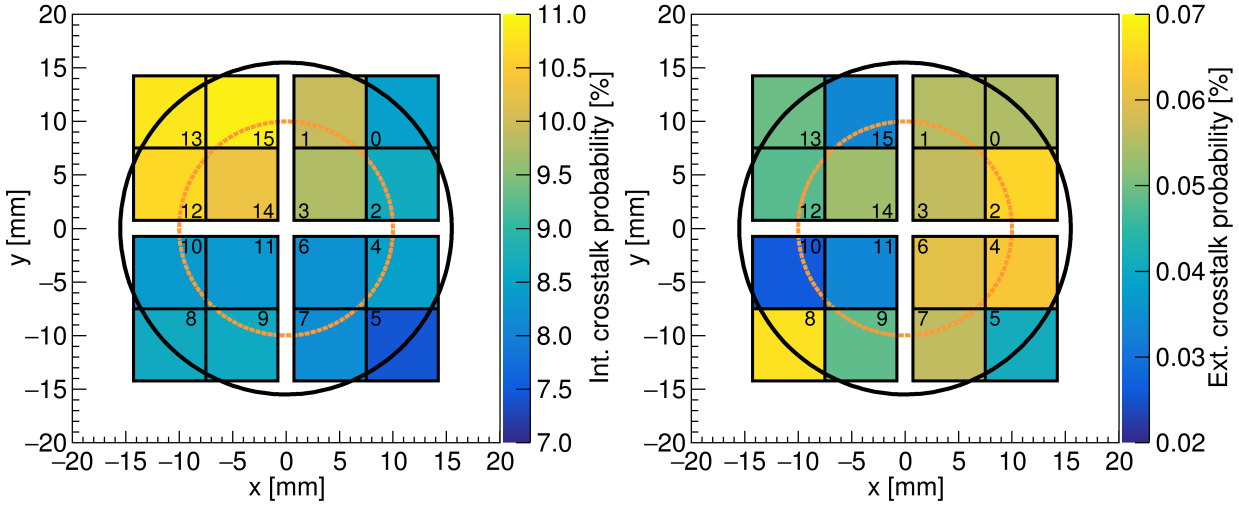

Figure 4.13: Crosstalk probabilities of the SiPM channels, measured with nitrogen gas at $\sim 190\,\mathrm{K}$. The detector and fiducial circumferences are represented by a solid black and dashed orange circle. Note the different colour-scales on the probability axes. **Left:** Internal crosstalk among neighbouring cells. **Right:** External crosstalk among neighbouring SiPM channels.

over-voltage, it increases with increasing over-voltage [275]. Since the breakdown voltage increases with higher temperatures, the over-voltage decreases for a fixed bias-voltage. Thus, the behaviour of channel 5 can again be understood as a temperature effect. In addition, the sensors in the second quadrant (channels $12-15$) feature an internal crosstalk probability higher than average. This could be attributed to an internal difference of this SiPM quad-module as a temperature dependence can be excluded based on the other discussed metrics.

Besides the internal crosstalk, SiPMs are known to feature an external crosstalk capability among different sensors [303]. Photons produced during electron avalanches can, instead of travelling to another cell, escape the sensor and eventually reach another one where they trigger a secondary avalanche. Such an effect must be estimated *in situ* as it is geometry-dependent. For this, we can again use the acquired dark count data. For a certain channel that issued the trigger, we can search for coincident events in other channels on which we did not trigger. Since dark counts of different sensors are uncorrelated, the external crosstalk probability can be estimated from correlated events of a few PE in size. We obtain an error-weighted mean effective external crosstalk probability of a SiPM in the top photosensor array of $(0.05 \pm 0.01)\,\%$. This result is corrected by the probability that a given sensor is in uncorrelated coincidence with any other sensor of the array within the examined trigger time window of 40 ns. We measured this accidental probability to be $0.02\,\%$ from coincidences outside of the trigger window, in agreement with expectation for the mean dark count rate shown in Section 4.3.3. In Figure 4.13, right, we show the external crosstalk probabilities of all channels in the array. Unlike the internal crosstalk probability, the external one is not enhanced for the channels in the second quadrant. We do not expect the estimated external crosstalk probability among SiPM channels to change to a significant value, compared to the internal one, when the TPC is operated with xenon in dual-phase mode. During operation with LXe, an external SiPM crosstalk recorded by the PMT would be visible as a small coincident S1-only signal in the PMT and a SiPM channel. However, we did not observe any event of this kind e.g. during the ^{37}Ar calibration at $968\,\mathrm{V/cm}$ drift field.

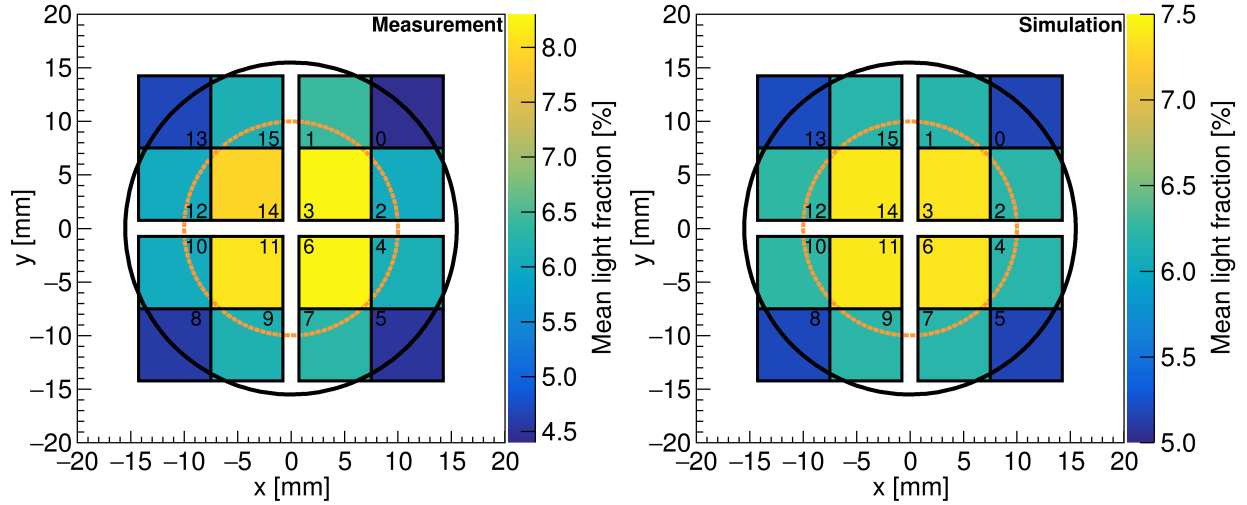

Figure 4.14: Mean S2 light fractions of the SiPM channels for events within the fiducial radius which is represented by the dashed orange circle. The TPC circumference is represented by the solid black circle. **Left:** Measurement with SE data. **Right:** Simulation with Geant4 [307].

4.3.5 SiPM Double Photoelectron Emission

Double photoelectron emission (DPE), i.e. the emission of two primary electrons originating from a single photon impacting the photocathode, is well-known for PMTs [304–306]. In contrast, the working principle of SiPMs disfavours the existence of such an external enhancement effect. The output of a single cell is independent of the excess number of impacting photons and thus, light detection with SiPMs relies on the fact that, within their linear regime, the signal size is proportional to the number of triggered cells. The only known effect that increases the light signal of an isolated SiPM is the internal crosstalk among neighbouring cells. As we saw above, the internal crosstalk probability is usually determined from dark counts inside the cells which provides a good source of single PEs. However, below, we study data from external illumination of the sensors and outline a combinatorial approach which is independent of the origin of the enhancement effect. We base this analysis on single electron (SE) extraction data. We shall see more about the SE event population in the Chapters 5 and 6. For the sake of this section it is enough to know that it is caused by a quantised, one-by-one, extraction of electrons to the gas phase, causing small S2 signals in the top array which are only a few PE in size.

We aim to determine the probability q that a 2 PE signal originates from one initial incoming photon onto the photocathode. We assume that q is universal to all channels. Given a fiducial radius, let $\{p_i\}_{i=0,\dots,15}$ be the set of mean light fractions of the 16 SiPMs for homogeneously distributed SE events. Furthermore, we denote the number of recorded hits in sensor i by k_i. For good statistics in the SE population, we consider events with 3 detected hits and we call the total number of these events $N^{3\mathrm{h}}$. Then, we can distinguish three cases[7]:

I. $k_i = 3,\ k_j = 0 \quad \forall j \neq i$. This signal can be produced by 3, 2 or 1 initial photons. The latter process is next-to-next-to-leading order and thus highly suppressed. However, we discard this first case as no such events were recorded, for it is a highly improbable event topology, and it is thus not accessible here. Note, that this is not due to the twofold coincidence requirement of the event building because additional PMT-triggers are allowed.

[7] A two-channel coincidence requirement for event building is based on narrow coincidence time windows, see Section 4.2. This reduces the contribution of randomly-coinciding dark counts to a negligible level.

II. $k_i = 2$, $k_l = 1$, $k_j = 0 \quad \forall j \neq l \neq i$. This signal can be produced by 3 or 2 initial photons. We expect the following number of events with 2 hits in one and 1 hit in another sensor:

$$N^{\mathrm{II}} = \begin{cases} N^{3\mathrm{h}} \cdot 3 \sum_{i=0}^{15} p_i^2 (1 - p_i), \ q = 0 \\ N_{3\,\gamma} \cdot 3 \sum_{i=0}^{15} p_i^2 (1 - p_i) + N_{2\,\gamma}^{2\mathrm{s}} \cdot 2q(1 - q), \ q > 0 \end{cases} \quad . \tag{4.5}$$

Here, $N_{3\,\gamma}$ denotes the number of events with 3 initial photons that are all detected and $N_{2\,\gamma}^{2\mathrm{s}}$ is the number of events with 2 initial photons that are both detected by two different sensors. If $N^{2\mathrm{h},\,2\mathrm{s}}$ is the number of events with total 2 hits in 2 sensors, i.e. one in each, we can identify

$$N_{2\,\gamma}^{2\mathrm{s}} = \frac{N^{2\mathrm{h},\,2\mathrm{s}}}{(1 - q)^2} \quad . \tag{4.6}$$

III. $k_i = k_l = k_m = 1$, $k_j = 0 \quad \forall j \neq l \neq m \neq i$. This signal can only be produced by 3 initial photons. We expect the following number of events with 3 hits in three sensors, i.e. one in each:

$$N^{\mathrm{III}} = \begin{cases} N^{3\mathrm{h}} \cdot \sum_{i=0}^{15} \sum_{j \neq i} p_i p_j (1 - p_i - p_j), \ q = 0 \\ N_{3\,\gamma} \cdot \sum_{i=0}^{15} \sum_{j \neq i} p_i p_j (1 - p_i - p_j), \ q > 0 \end{cases} \quad . \tag{4.7}$$

Combining the Equations 4.5, 4.6 and 4.7 for $q > 0$, we obtain

$$q = \frac{\tilde{N}}{2N^{2\mathrm{h},\,2\mathrm{s}} + \tilde{N}} \quad , \tag{4.8}$$

$$\tilde{N} \coloneqq N^{\mathrm{II}} - N^{\mathrm{III}} \frac{3 \sum_{i=0}^{15} p_i^2 (1 - p_i)}{\sum_{i=0}^{15} \sum_{j \neq i} p_i p_j (1 - p_i - p_j)} \quad . \tag{4.9}$$

The following mean light collection fractions of the sensors can be deduced from SE data for a 10 mm fiducial radius (see Figure 4.14, left): 4.6 % (corner sensors), 6.2 % (edge sensors), 8.0 % (middle sensors). Those match well our light simulations with the Geant4 particle physics simulation kit [307], see Figure 4.14, right, yielding 5.2 % (corner sensors), 6.2 % (edge sensors), 7.4 % (middle sensors). The little differences between measurement and simulation for the middle and corner sensors can be understood as systematics from the parametrisation of the xenon and the TPC materials, see Tables 2.1 and 4.2. The TPC geometry in Geant4 is a detailed copy of the CAD (computer-aided design) drawing, cf. Figure 4.15, with only a few simplifications, see caption of Table 4.2. The simulated light collection fractions of the sensors were determined with 10^5 events originating from a homogeneous and mono-energetic particle source with a fiducial volume of $r = 10$ mm. To this end, electrons with an energy of 2 keV were shot along the positive z-direction inside the amplification region between liquid level and anode. A scan of several slices in the amplification region showed that the light collection in each sensor does not depend significantly on the depth of interaction. Hence, the precise position of the production of the electroluminescence and the interplay of acceleration in the electric field (which is different in the gas than in the liquid due to the difference in the dielectric constants) and energy loss can be neglected within the 2 mm gap. Furthermore, as we are interested in the mean light seen by the sensors, the initial energy or the initial number of photons per event does not matter. A 2 keV electron caused on average 66 photon hits in the top array. The total

Material	Component	Parameter [unit]	Value	Ref.
PTFE	TPC wall,	Refractive index	1.60	[249]
	SiPM reflector	Reflectivity (LXe/GXe) [%]	99/80	[248, 308]
Quartz	SiPM and PMT window,	Refractive index	1.60	[309]
	SiPM casing	Absorption length [mm]	143	[310]
Silicon	SiPM photo-	Refractive index	1.0	[311, 312]
	sensitive area	Reflectivity [%]	25	[313, 314]
		Absorption length [nm]	6.4	[315, 316]
Stainless steel	Cathode/Gate and anode	Absorption length [mm]	1.62/1.38	
		Reflectivity [%]	0.02/0.02	

Table 4.2: Optical material properties used for the light simulation with Geant4. The SiPM casing was modelled with quartz although it is made of a white ceramic. Since GXe is optically less dense, light incident on the casing is lost to the outside of the TPC. The electrodes were modelled as homogeneous disks for simplicity. Their absorption lengths correspond to 94 % (cathode) and 93 % (gate and anode) transparency of the meshes at a thickness of 0.1 mm. The reflectivity of stainless steel is assumed to be 30 % which is scaled with the transparency to obtain the mean reflectivity of the electrode disks. The refractive index of the disks match the ones of LXe (cathode and gate) and GXe (anode). For LXe (GXe) we assumed a Rayleigh scattering length of 0.36 m (100 m) and an absorption length of 50 m (100 m) (cf. Reference [308]).

number of simulated events was sufficiently high. The differences of the light fraction among sensors with the same geometrical probability are very little and stable.

We obtain the counts N^{II}, N^{III} and $N^{2\mathrm{h},\,2\mathrm{s}}$ from integrals of the respective regions in the SE spectra under two-and threefold coincidence requirements, see Figure 4.16. The data selection of the SE population is detailed in Chapter 6. In summary, this yields $q = (2.2 \pm 0.1)\,\%$, with Poissonian uncertainty. The crosstalk probability of the VUV4 S13371 SiPMs was measured to be 2.1 % at 4 V overvoltage and 3.3 % at 5 V overvoltage, and is widely constant with temperature [275]. We operated the SiPMs in Xurich II at 51.5 V which corresponds to 5 V overvoltage at a temperature of 190 K measured in the gas phase. However, due to the heat dissipation of the pre-amplifiers of ~ 3 W, the temperature at the sensors is expected to be slightly higher. In fact, the overvoltage is reduced by 1 V below 220 K. In this regard, the determined probability q is well within the range of the expected crosstalk and we do not see an excess that points towards an external SiPM DPE effect. Moreover, we can conclude that the crosstalk determination based on dark counts inside the cells is well-motivated as the result does not change when using an external source of single scintillation photons. However, while the result here is well in agreement with the measurement of the internal crosstalk probability in Reference [275], it is by a factor 4 lower than the one obtained from dark count data measured in nitrogen gas, see Section 4.3.4. Note that there we defined the internal crosstalk probability as the ratio of events above 1.5 PE and above 0.5 PE, while the calculated q here is the probability that a single primary electron produces a 2 PE signal. However, because crosstalks with > 2 PE are higher order processes, this does not explain the discrepancy. In fact, using an upper integration threshold of 2.5 PE in the internal crosstalk calculation yields an only marginally lower probability of $(8.10 \pm 0.02)\,\%$. It is furthermore unlikely that the discrepancy is due to a temperature difference between the measurements with nitrogen and xenon. The crosstalk probability is fairly independent of the temperature at a fixed overvoltage. In addition, the overvoltage at a fixed bias voltage does not depend strongly enough on temperature to create such a difference in crosstalk for reasonable temperature offsets [275]. A temperature of ~ 140 K during the nitrogen measurement, instead of the nominal 190 K, would be needed to reach $\sim 8\,\%$ crosstalk probability. This is however impossible as the dark count rate measured in nitrogen gas and presented in Section 4.3.3 is well compatible

Figure 4.15: Visualisation of the Geant4 SiPM top array geometry as seen from the TPC volume. The electrodes are suppressed. Note that in this view the corner SiPMs are almost completely visible unlike what is expected from e.g. Figure 4.14. This is simply due to the parallax effect of the point-like camera used for the visualisation.

with a temperature of $\sim$ 190 K [275]. The detector was not opened between the ^{37}Ar calibration run from which the SE population was used here and the measurement in nitrogen. It thus remains unclear why the crosstalk probability differs between the measurements. This makes apparent that temperature sensors close to the SiPMs, preferably on the PCB, would be advantageous for future applications. For its compatibility with the dedicated measurements in Reference [275], we use the *in situ* measurement in xenon with SE presented here for the estimation of the systematic uncertainties in Chapter 6.

4.4 Summary and Conclusion

In this chapter we have described the first dual-phase xenon TPC with a SiPM photosensor top array. We have discussed the operating conditions, the readout and the DAQ as well as the data processing procedure which are relevant for the subsequent data analysis chapters. We have particularly focused on the reconstruction of the horizontal event positions with a centre-of-gravity algorithm. The resolution of this reconstruction is $\sim$ 1.5 mm, limited by the electrode mesh geometry, not by the capability of the SiPMs. We have also provided a measurement of the electron drift speed in LXe at various drift fields. Moreover, focusing on the SiPMs, we have evaluated the photosensor performance in the TPC in terms of the gain, the dark count rate, and the internal and external crosstalk probability. We have also studied a potential DPE effect of SiPMs, finding no evidence beyond the internal crosstalk effect.

Xurich II provides the proof of principle for the use of SiPMs in dual-phase xenon TPCs on the small scale. Due to their size, SiPMs provide the possibility for a very good position reconstruction resolution which is essential to distinguish single from multiple scatter interactions and important for the background discrimination at the TPC boundaries. As we shall see in the next chapters, the single photoelectron resolution of SiPMs is advantageous at low energies compared to PMTs. However, although not limiting the performance here due to the relatively low number of channels and the possibility to trigger on the bottom PMT, the dark count rate is a challenge when using

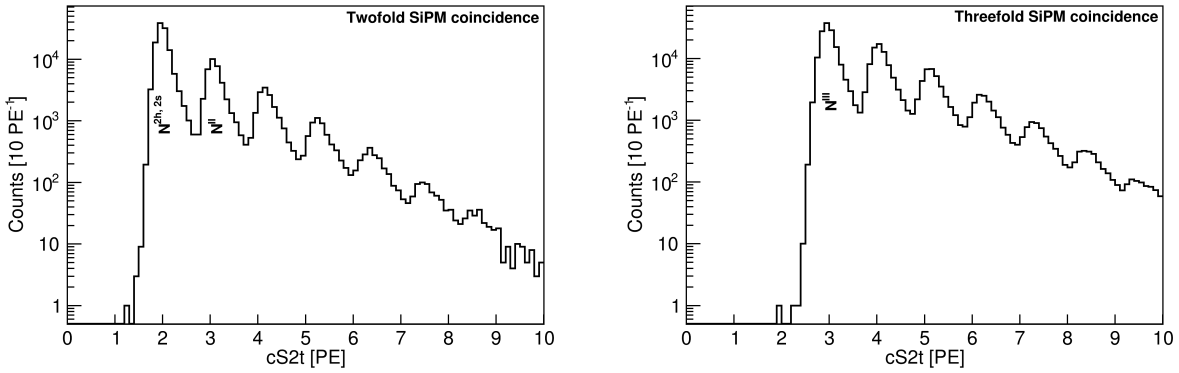

Figure 4.16: SE spectra of the summed top SiPM array signal. **Left:** With exactly two SiPM channels in coincidence. **Right:** With exactly three SiPM channels in coincidence.

SiPMs in tonne-scale LXe detectors to detect low energy events. A sophisticated readout scheme has to be developed to limit the rate of accidental coincidence events, due to SiPM dark counts, and the amount of recorded data [15]. In parallel, SiPMs with lower dark count rates need to be developed. While the lower temperature of liquid argon reduces the SiPM dark count rate significantly and allows the use of SiPMs e.g. in DarkSide-20k [9], it remains a challenge for LXe detectors. Further R&D is needed to develop cryogenic low-background electronics for the SiPM signal amplification with low power dissipation. This is particularly important when SiPMs are used in the liquid phase.

Chapter 5

Calibration of the Xurich II TPC with an ^{37}Ar Source

The performance of the upgraded Xurich II detector was characterised with the low-keV internal gaseous source ^{37}Ar [251]. To deploy the source, a stand-alone setup to introduce it into the xenon recirculation loop was designed and connected to the gas system of the detector.

This chapter is structured as follows: We describe the production and insertion of the ^{37}Ar calibration source in Section 5.1 and show the analysis of the different calibration lines of the source in Section 5.2. We present and discuss the calibration results in Section 5.3 and summarise this chapter in Section 5.4.

5.1 ^{37}Ar Calibration Source

The ^{37}Ar isotope decays with a half-life of $T_{1/2} = (35.01 \pm 0.02)\,\mathrm{d}$ via electron capture into stable ^{37}Cl, with a Q-value of $(813.9 \pm 0.2)\,\mathrm{keV}$ [317]:

$$e^- + {}^{37}\mathrm{Ar} \rightarrow {}^{37}\mathrm{Cl} + \nu_e \quad . \tag{5.1}$$

Depending on the inner atomic shell from which the electron is captured, 2.8224 keV, 0.2702 keV and 0.0175 keV X-rays and Auger electrons are released (K-, L-, and M-shell, respectively). See Table 5.1 for the corresponding branching ratios. These mono-energetic lines with uniformly distributed events in the TPC can be used for calibrations down to low ER energies [10, 11, 318–321]. Note that ^{37}Ar can also represent a serious concern for dark matter searches at low-keV energies [176, 322, 323] if not actively removed by cryogenic distillation [324].

Decay Mode	**Energy Release** [keV]	**Branching Ratio** [%]
K-shell capture	2.8224	90.2
L-shell capture	0.2702	8.9
M-shell capture	0.0175	0.9

Table 5.1: Energy release and branching ratios of the decay modes of ^{37}Ar [292].

5.1.1 Source Production

The isotope ^{37}Ar can be produced by thermal neutron capture of $^{40}\mathrm{Ca}(\mathrm{n},\alpha)$ or $^{36}\mathrm{Ar}(\mathrm{n},\gamma)$. Exploiting the former process involves baking of the calcium target at high temperatures to emanate ^{37}Ar. Due to this practical complication and for its high capture cross-section of $\sim 5\,\mathrm{b}$, we produced the ^{37}Ar source by thermal neutron activation of the gaseous ^{36}Ar:

$$^{36}\mathrm{Ar} + n \rightarrow {}^{37}\mathrm{Ar} + \gamma \quad . \tag{5.2}$$

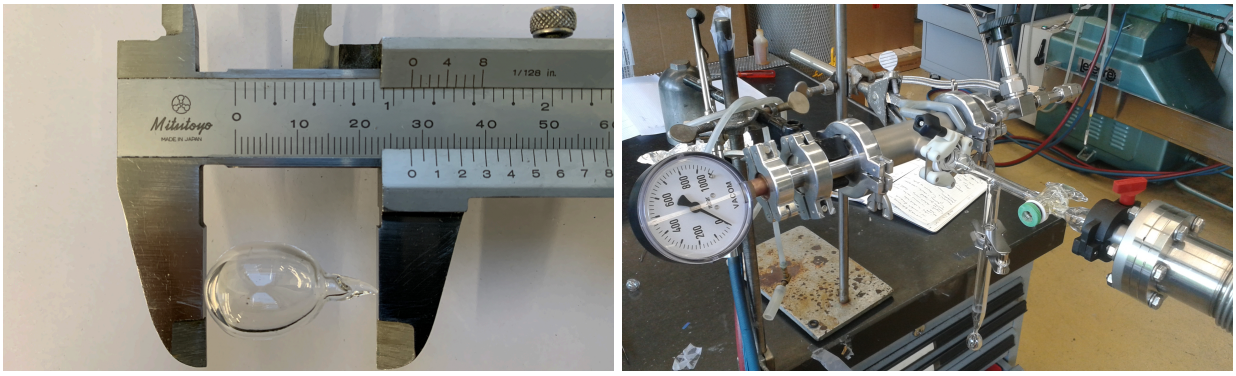

Figure 5.1: Left: Photograph of a filled argon quartz glass ampule. **Right:** Photograph of the filling setup. Vacuum pump and vacuum gauge connected on the front right. Pressure read on the left. Gas bottle connected on the back right. Glass ampule located at the lower end of the glass tube at the bottom.

Natural argon gas has a low ^{36}Ar abundance of 0.334 % [183]. However, it is sufficiently high to generate a source with a decent ^{37}Ar activity of $\mathcal{O}(10\,\mathrm{keV})$ fairly easily as we shall see below. In collaboration with the glassblowing facility at UZH, we filled fused quartz glass ampules with natural argon 6.0 (purity $\geq$ 99.9999 %), see Figure 5.1, left. The use of pure silicon dioxide was required in order to reduce the activation of other nuclei. The ampules were initially emptied to $\sim 10^{-6}$ mbar and then filled to the desired pressure, melted off the quartz glass tube and sealed, see Figure 5.1, right. For the sealing process to work, the inner argon pressure must not exceed atmospheric pressure. We filled the ampules at a pressure of 0.8 bar or 0.9 bar, corresponding to 2.3 mg and 2.7 mg of argon respectively.

To make sure that the filling procedure worked and that no contaminants were introduced into the filling, the content of a non-activated ampule was checked with a residual gas analyser (RGA), model Prisma™ 80 from Pfeiffer Vacuum GmbH [325]. To this end, the ampule was placed in the source introduction setup described in the next section. We show the mass-to-charge ratio spectrum before and after breaking the ampule in Figure 5.2. The offset of the two spectra by more than one order of magnitude is due to different total pressures during the measurements. In order to reach the low operating pressure of $< 10^{-4}$ mbar of the RGA after breaking the ampule, the amount of sample gas in the vacuum chamber was reduced in several steps. For this, a small chamber containing the sample gas, was opened to an evacuated larger one. Then both chambers were isolated again and the larger one was evacuated. Multiple iterations of this procedure allowed to reach a pressure at which the RGA is operational. From the spectrum, we can identify the following main contaminants: Besides the standard contaminants air, water and hydrogen and their fragments, we have CO_2, CO, methane, ethane and other organic components as well as ethanol. While the latter is due to cleaning procedures, the others are likely combustion residues and natural gas components from the ampule sealing process. However, these were already present in the background spectrum and did not increase relative to the other peaks after the ampule was opened. Thus, these were deposited either on the surface of the ampule, which was however thoroughly cleaned before the test, or on the surface of the vacuum chamber itself. A background spectrum of the latter without the ampule was not acquired. However, based on the RGA test, we can exclude that the flame of the torch gets in contact with the interior and confirm that the ampule was properly sealed, containing natural argon. Helium from the atmosphere can diffuse quickly through quartz glass. The diffusion coefficient is $\sim 10^{-12}\,\mathrm{s^{-1}Pa^{-1}}$ at room temperature [326], i.e. roughly 1 % of the atmospheric helium pressure inside the ampules would be reached after one day. Gas permeation typically decreases very fast with decreasing temperature. For this reason, the ampules were stored at $\sim 4\,^{\circ}\mathrm{C}$ before activation and, in addition, located in an argon-pressurised stainless-steel tube.

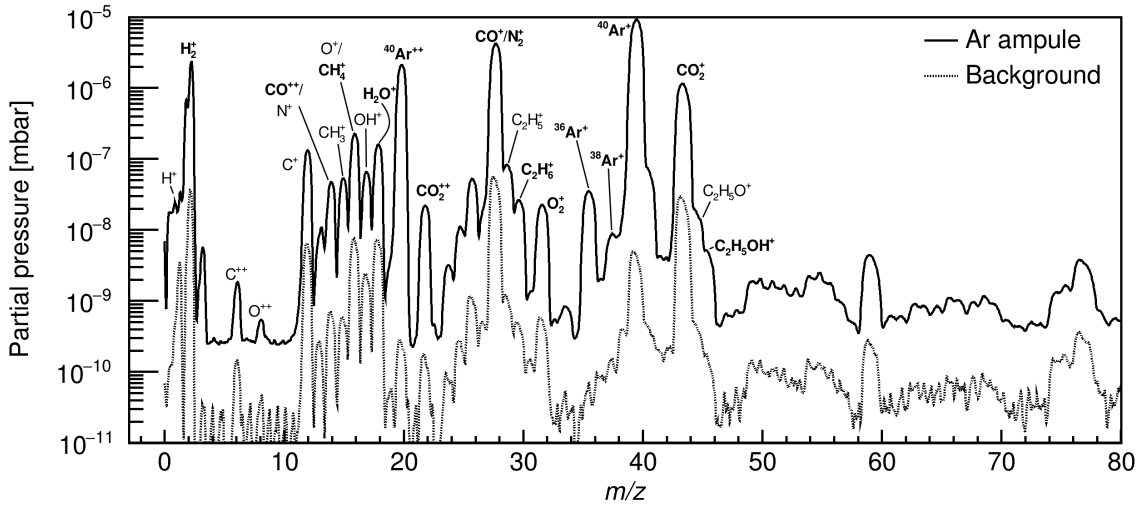

Figure 5.2: RGA spectrum before and after breaking the ampule. The most relevant peaks are labelled, parent ions in bold and fragments in regular thickness. The entire spectrum raised after breaking the ampule due to different total pressures during the measurements. However, only the argon peaks increased relative to the others. The peak at $m/z\,3$ is most likely due to an offset He^+ contribution. The peaks between $m/z\,22$ and $m/z\,26$, and above $m/z\,46$ are from organic molecules.

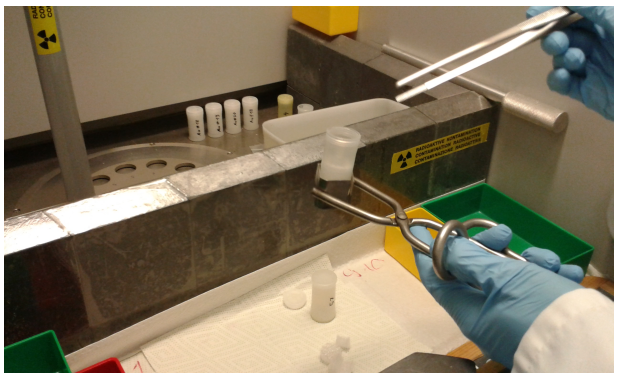

Figure 5.3: Photograph of the preparation of an argon sample for activation at SINQ, PSI.

The activation took place between the 4th and 7th December 2018 at the Swiss Spallation Neutron Source (SINQ) at Paul Scherrer Institute (PSI), Villigen (Switzerland), providing a thermal neutron flux of $\sim 10^{13}\,\mathrm{cm^{-2}s^{-1}}$. A total of four fused quartz ampules were each activated for an irradiation time of 3.75 hours. The samples were placed in polyethylene capsules and surrounded with packaging foam as protection as they undergo some stress during the transport to the neutron source in a pneumatic pipe system, see Figure 5.3. Analytically, we expect an initial ^{37}Ar activity between $19-22\,\mathrm{kBq}$ per ampule. However, the activity cannot be measured directly because the low energetic radiation cannot penetrate the quartz glass.

The use of natural argon gives rise to the activation of two other relevant isotopes: ^{39}Ar from ^{38}Ar and ^{41}Ar from ^{40}Ar. Of less relevance are ^{43}Ar from ^{42}Ar, of which only traces are present in natural argon, and ^{42}Ar itself from secondary activation of ^{41}Ar [183].

As the natural abundance of ^{38}Ar is more than five times lower than the one of ^{36}Ar and its cross-section for thermal neutrons is more than six times lower, we expect to have produced ^{39}Ar with an activity lower than $0.23\,\mathrm{Bq}$ per ampule. It decays with a half-life of $268\,\mathrm{y}$ into its stable daughter ^{39}K solely via beta decay with an endpoint of $565\,\mathrm{keV}$ [327].

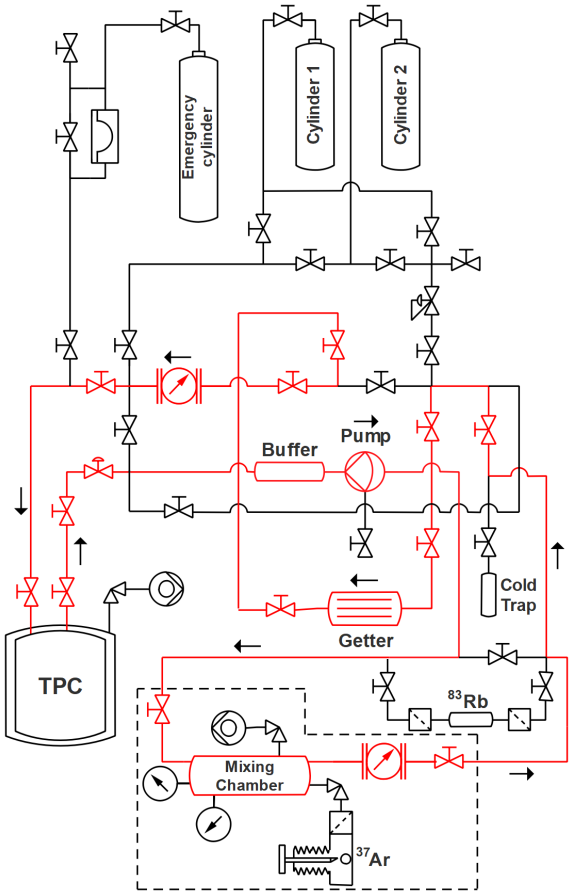

Figure 5.4: Piping and instrumentation diagram (P&ID) of the gas system of Xurich II and the added ^{37}Ar setup (framed with a dashed line). The gas recirculation path to introduce the source into the xenon flow is indicated in red.

The high abundance of 99.6 % of ^{40}Ar yields a high activity of ^{41}Ar shortly after the irradiation. This required that the activation happened in two steps with a minimum cool-down time of 24 hours in between. ^{41}Ar decays into stable ^{41}K with a half-life of 109.6 min [328]. Hence, its activity decreased below 1 Bq after 2 days and was negligible after $\sim$ 160 days[1] when the source was introduced into the detector. Similarly, if ^{43}Ar ($T_{1/2}$ = 5.4 min) had been produced, it would have been negligible after a short time as the subsequent decay of its daughter isotope ^{43}K into stable ^{43}Ca takes place with a half-life of 22.3 h [329]. The secondary activation of ^{41}Ar to ^{42}Ar ($T_{1/2}$ = 32.9 y), which decays via ^{42}K into stable ^{42}Ca [330], is negligible as well since the initial activity can be estimated to be $\sim$ 50 µBq.

5.1.2 Source Introduction Setup and Mixing Procedure

To introduce the ^{37}Ar source into the Xurich II TPC, the quartz ampules must be placed and broken inside the gas system. We designed and built a dedicated system that contains a mixing chamber and an ampule breaking mechanism. We refer to Figure 5.4 for a schematic view and to Figure 5.5 for pictures of the setup. The fragile ampule is firmly held in place by a custom-made holder welded onto a CF-40 blank mounted on one of the sides of a CF-tee. By actuating a guillotine through

[1] The source was introduced with some delay after the activation due to maintenance work between the ^{83m}Kr and ^{37}Ar data taking runs.

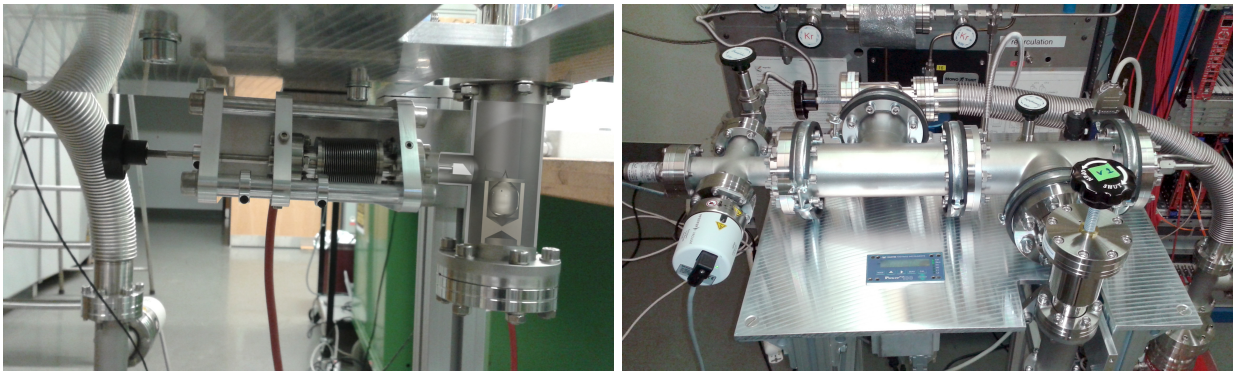

Figure 5.5: Photographs of the ^{37}Ar calibration setup. **Left:** Ampule chamber with crushing mechanism, overlaid by a rendering of the interior. **Right:** Mixing chamber with pressure and vacuum gauges and flowmeter, connected to the gas system of Xurich II. The gas flows from the left to the right. The ampule chamber, front right, and a vacuum pump, bottom right, are connected via angle valves to the mixing chamber.

a vacuum bellow, the neck of the ampule can be cut off in vacuum. Due to the volume ratios of the ampule and mixing chamber, $\sim 94\,\%$ of the argon is transferred through a filter when the angle valve to the evacuated mixing chamber is opened. After isolating the ampule chamber again, xenon from a gas bottle can be added, cf. Figure 5.4, until the TPC working pressure of $\sim 2\,\mathrm{bar}$ is reached. Bypassing the recirculation flow through the mixing chamber and integrating the flow, the introduced ^{37}Ar activity can be estimated. The argon gas of multiple ampules can be injected by stopping the recirculation, isolating the TPC and recuperating the xenon/argon mixture remaining in the gas system into a cold trap cooled by liquid nitrogen. After inserting a new ampule, the gas system can be evacuated from a port on the mixing chamber. The use of the cold trap ensures that the amount of xenon and, hence, the pressure and liquid level remain unchanged during ampule changes. For the data described in the subsequent sections, three ampules with an estimated total activity of 2.7 kBq were broken mid-May 2019 to release the activated argon into the xenon.

The system used here is similar to the one described in Reference [17] which was deployed in XENON1T at the end of its lifetime [12]. The main difference is the use of higher activity source ampules ($\sim 100\,\mathrm{kBq}$) produced from enriched ^{36}Ar. This necessitates a dosing procedure to control the introduced activity. In contrast to the approach of integrating the gas flow described here, one made use of dosing volumes and controlled the introduced gas flow by their volume ratios. The major goal of this test was to the demonstration of the efficient removal of ^{37}Ar via cryogenic distillation [324].

5.2 Calibration Data

The data used for the calibration was acquired between late-May and early-July 2019 while a long-term measurement campaign lasted until mid-October 2019 with the aim to determine the ^{37}Ar half-life. Because of the low ^{37}Ar signal rate in the detector volume, $\mathcal{O}(10\,\mathrm{Hz})$, we expect a negligible pile-up rate for a DAQ window of $60\,\mu\mathrm{s}$. This includes pile-up with background events with a rate of the same order of magnitude. In this section, we describe the data selection, the applied quality cuts and the signal corrections for all three ^{37}Ar lines, cf. Table 5.1. While for the K-shell capture line at 2.82 keV we require correctly paired S1 and S2 events, we perform an S2-only analysis for the L-shell and M-shell capture lines at 0.27 keV and 0.0175 keV, respectively. We apply a series of data selection cuts that are common to all three lines: As described in Chapter 4, Section 4.2.3, the post-processing step accounts for physical drift times and removes saturated signals from e.g. cosmic muons or gamma rays from materials. In addition, we apply the fiducial volume cut described in Chapter 4, Section 4.2.4, to remove wall and gas events, regions with an inhomogeneous electric field, and those

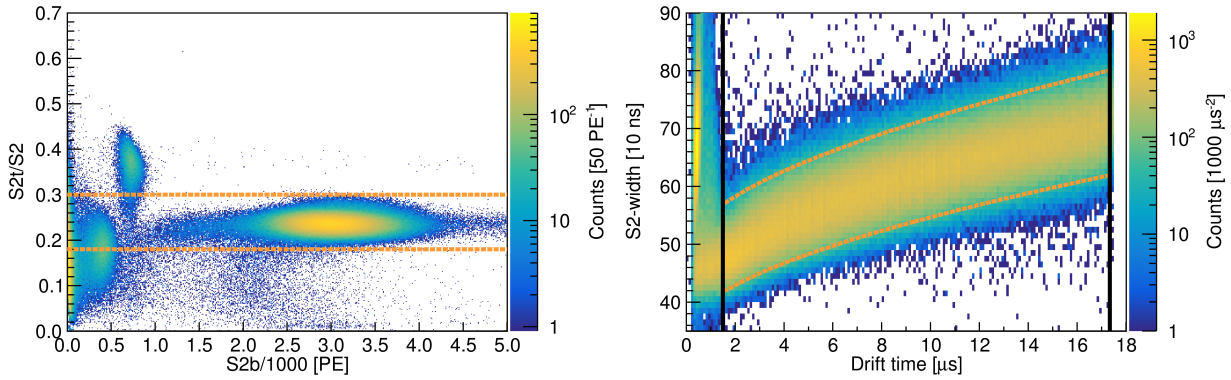

Figure 5.6: Data quality cuts for the K-shell capture line. The accepted region is enclosed by the dashed orange lines. **Left:** AFT cut to remove gas events with a fraction of $0.3 - 0.5$. Besides the K-shell population on the right we also select parts of the L-shell below S2b = 600 PE and the SE event population in the low PE-region that are both mostly located in S2-only space. These are removed by an energy cut. **Right:** S2-width cut to remove accidental coincidences and remaining gas events, see text. The drift region defined by the cathode and the gate are marked by solid black lines.

outside of the linear region of the (x, y)-position reconstruction algorithm. Note that for the S2-only analysis for the two lower energy lines, drift time related cuts are not accessible and thus we only constrain the selected (x, y)-position. Furthermore, we select only single S2s, for we do not expect multiple scatters from a single ^{37}Ar decay. The data quality cuts and corrections were developed for each of the seven analysed drift fields separately. Here, we present the ones for the data sets acquired at 968 V/cm which feature the highest statistics.

5.2.1 K-Shell Capture Line

Data Selection and Quality Cuts

To ensure a correct S1-S2-matching, we require the S2 signal to contain more charge than the S1. To effectively remove events in the gas phase that yield a large S2 in the top array compared to the total S2, we apply an area fraction top (AFT) cut as shown in Figure 5.6, left. Note that we refer with b to the PMT channel (bottom) and with t to the combined SiPM channels (top). To remove the lower energy lines from the analysis, we apply a cut on the energy, namely in the centre of the 5σ boundaries of the L- and the K-shell populations in the total S1+S2-space, see Figure 5.7. This also removes the remaining gas events that leaked into the acceptance region of the AFT cut, cf. Figure 5.6, left. Since accidental coincidences have by definition a random drift time, they can be effectively removed with a cut on a variable with a strong drift time dependence. The longitudinal diffusion of the electron cloud during the drift leads to such a dependence of the S2-width, as shown in Figure 5.6, right. We see that the S2-width increases with the depth of the interaction in the TPC. Higher electric fields allow for higher drift speeds that reduce the effect of diffusion [331]. The S2-width distribution follows an empirical function with three parameters $P0$, $P1$ and $P2$:

$$\mathrm{S2-width}(t_{\mathrm{drift}}) = P_0 + P_1 \cdot t_{\mathrm{drift}} + \sqrt{P_2 \cdot t_{\mathrm{drift}}} \quad . \tag{5.3}$$

Here, the width corresponds to the full width at tenth maximum. The upper and lower cuts are defined as follows: The histogram is sliced in drift time bins, and the fit is performed through the 97.7 % and 2.3 % quantiles of those bins. We thus select the $\pm 2\sigma$ region around the mean. In Table 5.2, we provide a summary of the event survival fraction after each cut. A fraction of 43.1 % of the recorded non-saturated events within the fiducial volume that generate an S2 signal pass all data quality cuts.

Cut	Abs. Survival Fraction [%]	Rel. Survival Fraction [%]
Single scatter	52.5	52.5
S1 < S2	50.8	96.7
AFT	46.7	92.0
Energy	45.3	97.1
S2-width	43.1	95.1

Table 5.2: Survival fraction of non-saturated events within the fiducial volume that generate an S2 signal after each data selection and quality cut for the ^{37}Ar K-shell analysis. We show the absolute survival fractions in order of the applied cuts and the relative survival fractions compared to the preceding cut.

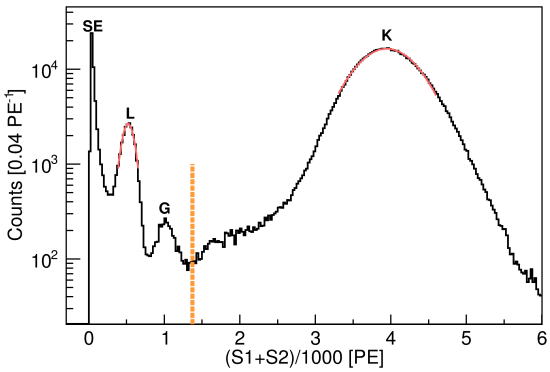

Figure 5.7: Energy cut in total S1+S2-space to separate the K-shell population from the SE, L-shell and the remaining gas events (G).

Corrections

All the subsequently described corrections are performed on data within the fiducial volume only. For simplicity, we do not apply (x, y)-dependent corrections. As a result of the attachment of the drifting free electrons to electronegative impurities in LXe, the S2 charge degrades with drift time. In Chapter 2, Section 2.4, we introduced the free electron lifetime τ_e, defined as the decay constant in an exponential decay law, as a measure of the LXe purity and to quantify this charge loss. Being a property of the LXe, the drift time dependence of the S2 signal of any channel can be used to correct for this systematic effect. We base our correction on the bottom PMT as it collects more S2 light than the top array. To this end, we fit the 50 % quantiles of the 2-dimensional S2b versus drift time histogram with an exponentially decreasing function, see Figure 5.8, left. We thus obtain the corrected S2 charge by multiplying with its inverse, i.e. we scale according to the S2 at zero drift time:

$$\mathrm{cS2} = \mathrm{S2} \cdot e^{t_{\mathrm{drift}}/\tau_e} \quad . \tag{5.4}$$

The stable detector conditions during the data acquisition period resulted in an electron lifetime of $85 - 187\,\mu s$, for a maximum drift time of $\sim 22\,\mu s$ at $80\,V/cm$, without showing any abrupt changes. While we correct for the electron lifetime on a daily basis, in Figure 5.8, left, we show for simplicity the combined data at $968\,V/cm$ drift field with an averaged electron lifetime.

The LCE in the top and bottom photosensors depends on the geometry, and the optical properties of the TPC surfaces and the LXe. While the production of the S2 light is very localised, the collected S1 light varies with the depth of the event. We use a data-driven approach and fit the 50 % quantiles of the 2-dimensional S1b versus drift time histogram with a 4th order polynomial, as shown in Figure 5.8, right. The corrected signal cS1b is obtained by scaling around the drift time corresponding to the

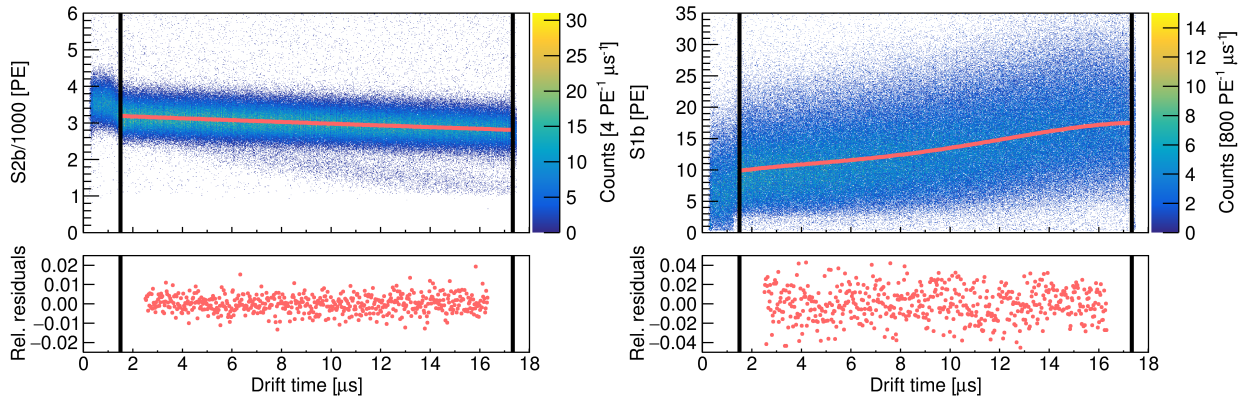

Figure 5.8: Corrections for systematic detector effects. The drift region defined by the cathode and the gate is marked by solid black lines. **Left:** Electron lifetime correction fit with relative residuals. The electron lifetime from the combined data at 968 V/cm is (124.2 ± 0.7) µs. The error is the error on the fit parameter and purely statistical. **Right:** S1b correction fit with relative residuals.

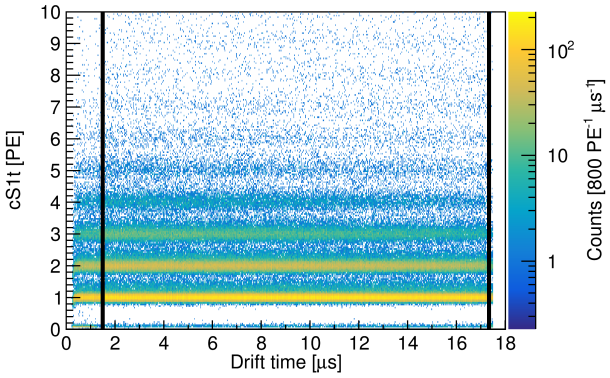

Figure 5.9: Corrected S1t versus drift time histogram with the single-PE band structure.

centre of the TPC. Thanks to the excellent single PE resolution of SiPMs, the S1t histogram features a band-like structure, as visible in Figure 5.9. Since the small light signal seen by the SiPMs does not show any drift time dependency within a single band, no data-based drift time dependent correction could be performed for S1t. Because of this discreteness, we would need to know which events changed to the next lower band after a certain drift time. However, these bands help us to fix the charge scale in PE. To that end, Gaussian fits on the seven lowest bands are performed in the S1t histogram and then linearly mapped onto the expected charge in PE, see Figure 5.10. Figure 5.9 shows the corrected result. The same scaling is applied to the S2t signal.

Population of the K-Shell Capture Events

After applying the described corrections, we show in Figure 5.11 the isolated populations from the 2.82 keV line of ^{37}Ar in total S2- versus total S1-space and in S2t- versus total S1-space at 968 V/cm. At this drift field, the mean of the population is located at S1 $= (14.04 \pm 0.01\,(\text{stat.})\,^{+0.28}_{-0.78}\,(\text{syst.}))$ PE and S1 $= (4459.7 \pm 0.7\,(\text{stat.})\,^{+63.7}_{-85.7}\,(\text{syst.}))$ PE. These means are not corrected for photosensor effects such as crosstalk or DPE. The statistical error is the one of the fitting procedure. The systematical errors are discussed in detail in the next chapter. One of them is due to the fact that the two-dimensional distributions feature a slight asymmetry (skewness) which was also observed elsewhere [10, 332]. This is due to DAQ and processing efficiencies, the low light level and charge loss, and can be modelled with

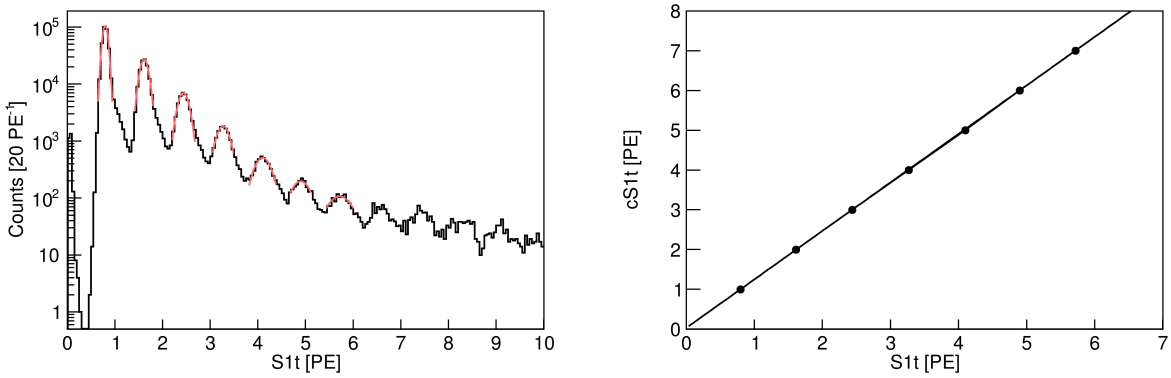

Figure 5.10: Scaling of the S1t signal to true PE-units. This correction is also applied to the S2t signal. **Left:** Gaussian fits of the PE-bands. **Right:** Linear correction fit.

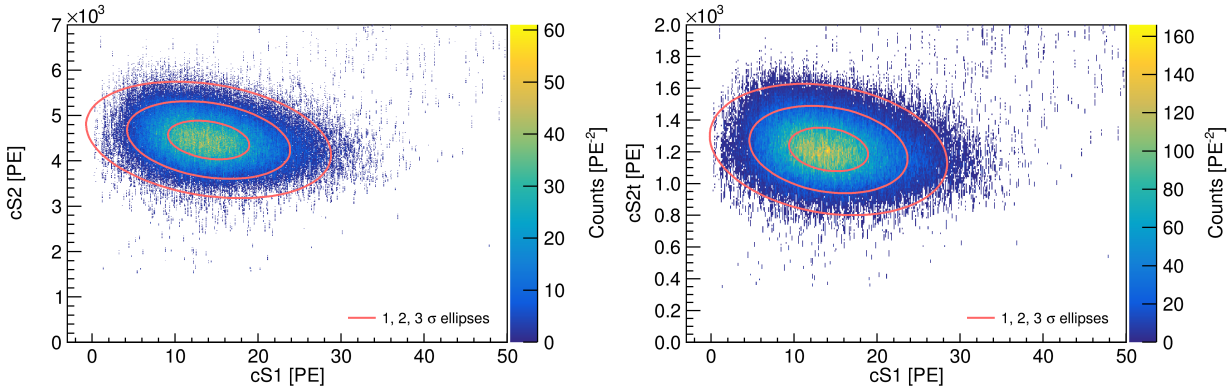

Figure 5.11: 2.82 keV line of ^{37}Ar without DPE/crosstalk correction. The charge and light anti-correlation is moderated at this low energy. The data was acquired at a drift field of 968 V/cm. The ellipses show the 1, 2, 3σ regions of the distribution. **Left:** Total S2- versus total S1-space. **Right:** S2t- versus total S1-space. At this energy, the SiPM top array collects roughly one quarter of the total detected S2 light.

skew-Gaussians [333]. However, we use for simplicity standard Gaussians as fit functions and provide a more detailed error estimation on the position of the mean in the next chapter. The anti-correlation between ionisation and scintillation signals is evident, however less pronounced at the low energy of ^{37}Ar, compared to higher energies, cf. Appendix A due to the small S1 signals. Comparing the mean of the two ellipses in Figure 5.11, we can deduce that 27 % of the total detected S2 light is collected by the SiPM top array at 2.82 keV. As we saw in Figure 4.6, the K-shell events are homogeneously distributed in the detector volume.

5.2.2 L-Shell Capture Line

Data Selection and Quality Cuts

We show the top fraction of the low-S2 region in Figure 5.12, left. Similarly to the K-shell selection, we apply an AFT cut to remove gas events and to cut on the band at S2t/S2 = 0.1. To separate the L-shell line from the K-shell, we revert the energy cut mentioned above and accept events below the mark in Figure 5.7. However, these populations are different in the signal topology. We perform an S2-only analysis here as S1 and S2 signals are randomly paired due to the low or vanishing light yield at such low energies [332, 334]. Because of this, we can demand a single lone-S2 topology, i.e. events with just one S2 and no S1 signal in the waveform. This cleans up the selection from

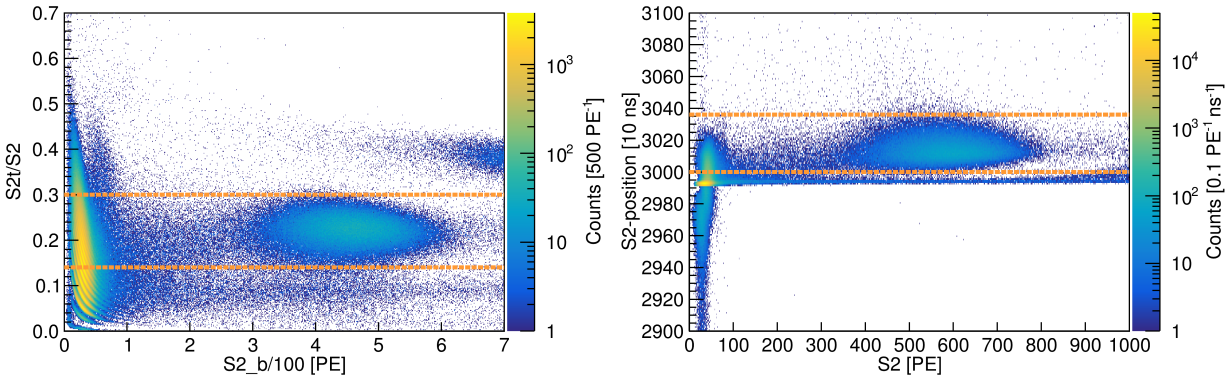

Figure 5.12: Data quality cuts for the L-shell capture line. The accepted region is enclosed by the dashed orange lines. **Left:** AFT cut to remove gas events and the band at S2t/S2 = 0.1. Besides the L-shell event population we also partially select the SE event population in the low PE-region. This population is suppressed by the trigger position and S2-width cut and removed by the S2-height cut. **Right:** Trigger position cut to remove the band at 30 µs and to highly suppress the SE event population.

Cut	**Abs. Survival Fraction** [%]	**Rel. Survival Fraction** [%]
Single scatter	64.2	64.2
Lone-S2	42.6	66.3
AFT	29.9	70.2
Trigger position	5.2	17.5
Energy	3.1	58.3
S2-width	2.4	78.6
S2-height	2.2	91.8

Table 5.3: Survival fraction of non-saturated events within the fiducial radius that generate an S2 signal after each data selection and quality cut for the ^{37}Ar L-shell analysis. We show the absolute survival fractions in order of the applied cuts and the relative survival fractions compared to the preceding cut.

noisy events and pile-up. If not triggered on noise, we can thus also demand that the trigger was issued on the S2 signal of interest. We apply a cut on the trigger position in the waveform in the time window $[0, +360]$ ns around the trigger, see Figure 5.12, right. Due to the S2-only topology, we cannot apply drift time based cuts like the drift time dependent S2-width cut developed above for the K-shell population. In fact, the S2-width is not a good discriminator against the SE event population because they are overlapping in S2-width space, see Figure 5.13, left. However, just like the AFT and the trigger position cut, it very effectively removes the band of events with similar energy but at lower constant width of ~ 250 ns and further cleans up the selection. We require the width to be within the range $[350, 1000]$ ns. The separation to the SE event population is achieved with a cut on the signal amplitude, i.e. we demand the S2-height to be > 200 ADC, see Figure 5.13, right. While the application of the radial fiducial volume cut is straightforward, the depth of an interaction is not directly accessible due to the lack of an S1 signal. While the S2-width does give some information on the drift time and, hence, on the depth, cf. Figure 5.6, right, it is too imprecise to be used as a measure for fiducialisation. Given the width of its distribution, the S2-width does not vary enough over the short drift length. In Table 5.3, we provide a summary of the event survival fraction after each cut. A fraction of 2.2 % of the recorded non-saturated events within the fiducial radius that generate an S2 signal pass all data quality cuts.

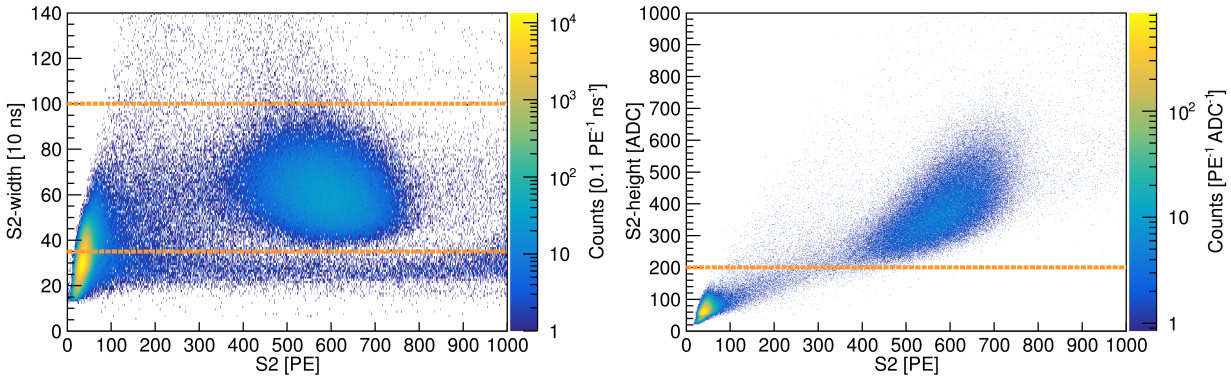

Figure 5.13: Data quality cuts for the L-shell capture line. **Left:** S2-width cut to clean the selection from e.g. gas events. Just like the AFT and the trigger position cut, it also removes effectively the band at $\sim 250\,\mathrm{ns}$ width. The accepted region is enclosed by the dashed orange lines. **Right:** S2-height cut to separate the L-shell and the SE event populations. The accepted region is above the dashed orange line.

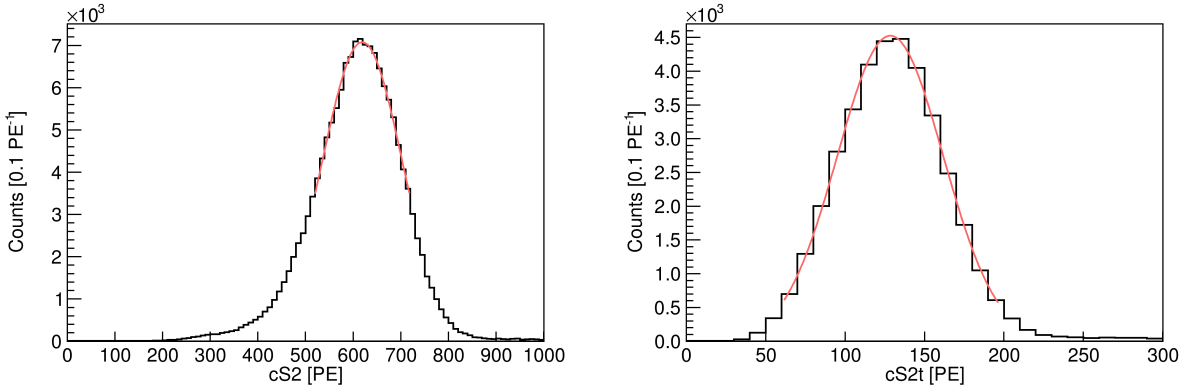

Figure 5.14: 0.27 keV line of ^{37}Ar in S2-only space without DPE/crosstalk correction. The data was acquired at a drift field of 968 V/cm. **Left:** Total S2 signal. **Right:** S2t signal. At this energy, the SiPM top array collects roughly one fifth of the total detected S2 light.

Corrections

Due to the lack of information on the depth of interactions, an electron lifetime correction cannot be applied. This is however not critical as the high and stable electron lifetime, see Section 5.2.1, ensures that the uncorrected S2-mean will only be reduced by some percent. The S2t signal is scaled to the true PE units according to the correction developed for the K-shell event population.

Population of the L-Shell Capture Events

We show in Figure 5.14 the isolated population from the 0.27 keV line of ^{37}Ar in total and top S2-space at 968 V/cm. At this drift field, the mean of the population is located at S2 = (619.1 ± 0.4) PE, obtained with a Gaussian fit. This mean is not corrected for photosensor effects such as crosstalk or DPE. The slight asymmetry of the peaks is due to the charge loss towards lower energy which is a consequence of the lack of drift time information. Comparing the mean of the two distributions, we can deduce that 21 % of the total detected S2 light is collected by the SiPM top array at 0.27 keV. This top collection fraction is lower than for the K-shell population. We come back to that point in the next chapter. The selected events are homogeneously distributed in x-y-space, see Figure 5.15.

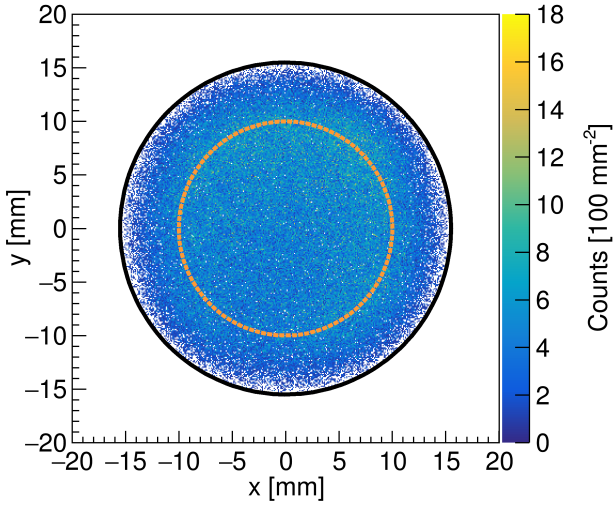

Figure 5.15: x-y event distribution from ^{37}Ar L-shell capture data. The boundaries of the detector and fiducial volume are represented by solid black and dashed orange lines, respectively. Unlike for the K-shell there are no spots visible due to the lower number of events.

5.2.3 M-Shell Capture Line

The M-shell capture releases an energy of 17.5 eV, close to the mean excitation energy of the xenon atom, see Chapter 6. In fact, we expect on average 1.3 quanta from that interaction using the literature W-value of 13.7 eV [243]. At such low energies, it is unlikely that the decay energy is released in the form of scintillation photons for a significant number of decays. However, the fact that we require a 2-sensor coincidence for event building, meant to reduce the sensitivity to dark count events, would highly suppress the detection of photons. Detected as S2 signal however, such an interaction causes a single or double electron extraction signal. Given the ionisation gain $g2 = 37.05\,\mathrm{PE/e^-}$ of Xurich II[2], whose derivation we shall see in Section 5.3.1, this corresponds on average to S2 = 47 PE. Extrapolating from the S2 signal of the L-shell line, cf. Section 5.2.2, we expect the M-shell capture line at ~ 40 PE in S2. However the discrete nature of the process would yield an S2 signal of 37 PE or 74 PE. The extraction of the M-shell line is complicated by the fact that it shares the same signature of the very abundant SE event population and indeed, the relative abundance between the SE and the L-shell event populations is far too high to be caused by the argon only. Even if the M-shell line is contained inside the population, it is overshadowed by SE events of a different origin. In order to isolate the M-shell, we need to make use of the known properties of SEs and electron trains: This population in dual-phase TPCs is well-known but its origin not yet fully understood. Single electrons can originate from a delayed extraction to the gas phase due to an imperfect electron extraction, from trapped charge on the TPC surfaces or from electron emission at the cathode [335]. Other production mechanisms involve stimulation by the VUV-scintillation light, such as photodetachment from impurities or photoelectric effect on metal surfaces [336, 337]. The References [336–342] observe a temporal correlation to high-energy depositions as well as a dependence on the concentration of electronegative impurities in the LXe. The latter property cannot be exploited for our purpose. The electron lifetime during ^{37}Ar data taking was stable and higher than 100 µs and the number of SE events is not reduced by selecting the cleanest data sets. However, the time-correlation of electron trains and high energy depositions in the detector can be exploited. Single electrons tend to occur in high quantities after high-energy events within the order of milliseconds. This is the topic of the

[2]This value is not corrected for S2-detection and tagging efficiencies or photosensor systematics, cf. Chapter 6, Section 6.2.1.

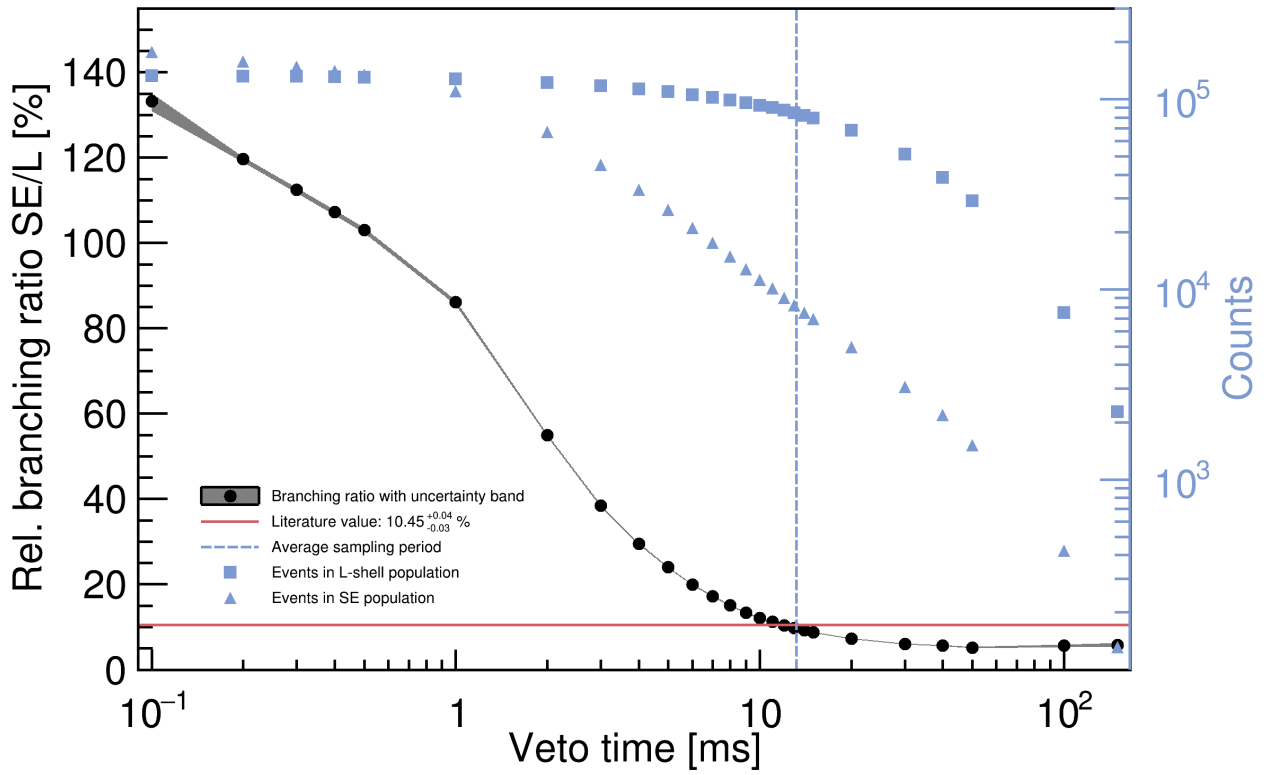

Figure 5.16: Relative abundance of the SE and L-shell event populations as a function of veto time, see text.

next section.

Data Selection and Quality Cuts

In order to exploit the time-correlation of electron trains with preceding events and the random occurrence of the M-shell events, we apply a time veto after any event. This approach relies on the assumption that the SE event population only consists of time-correlated events, i.e. delayed electrons from other interactions, and the M-shell signal. We assume that no other isotope releases a signal in that region nor that there is another source of time-uncorrelated SEs. We evaluate afterwards if this assumption is justified. In Figure 5.16 we can see that after ~ 15 ms veto time the relative branching ratio of the SE and the L-shell event populations converges to a plateau. This plateau is only a few percent below and roughly at half of the expected ratio of 10.5 %. The error band of the constant branching ratio of $5 - 6$ % gets wider for larger veto times. This is due to the fact that the statistics is diminished by the time veto. After 13 ms we are in the regime of the mean event separation based on the inverse of the trigger rate. Therefore at veto times > 13 ms, even time-uncorrelated events start to get removed very effectively by the time veto cut. Note that we apply the veto cut after any event, disregarding its type. The reason for this choice is that it allows us to cut SE events that follow closely one after another with relatively low veto times, and thus to reach a plateau in the branching ratio at all, while preserving a good acceptance of time-uncorrelated events.

The branching ratio is calculated as the ratio of the number of events located $<$ cS2 $= 90$ PE, which corresponds to roughly $2.5 \cdot g2$, and the number of events contained in the $\pm 3\sigma$ region around the L-shell event population. We expect these integration intervals to be conservative and to contain the vast majority of the relevant events. In Figure 5.17 we show the populations after 40 ms veto

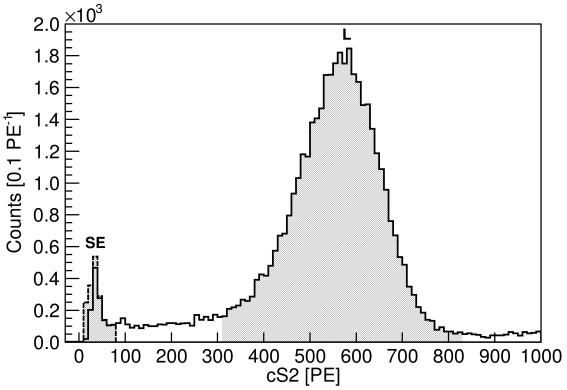

Figure 5.17: SE and L-shell event populations after a veto time of 40 ms. The dashed SE histogram includes the DAQ and processing efficiencies that are discussed in Chapter 6, Section 6.3.3.

time when the plateau is reached. The efficiencies for detection in the DAQ and the S2-tagging in the processing are lower in the SE regime, see Chapter 6, Section 6.3.3. Hence, the SE event population is corrected for these efficiencies, see the dashed histogram in Figure 5.17. We stop correcting below 5 % efficiency to avoid division by small numbers. We do not see a double electron peak, although based on our discussion above, it is expected to contain roughly 30 % as many events as the SE electron peak if due to M-shell decays. The over-fluctuation at ~ 100 PE is too high in energy to be identified with the double electron extraction peak.

To select the two populations at equal acceptance, we applied, qualitatively, the same cuts as described in the previous section for the L-shell event population except for the AFT and the S2-height cut. To include the SE event population at full acceptance, we modified the trigger position cut to $[-100, +360]$ ns and the width cut to $[110, 1000]$ ns.

Although efficiency-corrected, we observe that the converged branching ratio of the SE and L-shell event populations is lower than expected from the literature. A possible explanation is that events which show charge loss are at least partially integrated for the L-shell event population while completely lost for the SE event population. On the other hand, we can exclude that the twofold coincidence requirement in the event building stage reduces the number of reconstructed events significantly due to a missing hit in the SiPM channels. Light simulations with Geant4 show that only in one permille of the cases none of the photons hit the SiPM array. This estimation is based on the simulation framework described in Chapter 4, Section 4.3.5. Unknown to the author, for lack of literature, is the efficiency to excite a xenon atom at 17.5 eV, if scintillation photons are still released at such low energies and if so, what the relative fraction of scintillation and ionisation quanta is.

Corrections

Just as for the L-shell S2-only analysis, we cannot apply an electron lifetime correction. The S2t signal is scaled to the true PE units according to the correction developed for the K-shell event population.

Population of the Single Electron Events

In Figure 5.17, we show the SE population after a veto time of 40 ms. However, the population was selected as it is time-uncorrelated to other events and for its abundance which is close to expectation. We present the evolution of the relative branching ratio with the L-shell event population in Section 5.3.4 and show that the selected set of events contains additional SE events from another time-uncorrelated source, irreducible to the M-shell events.

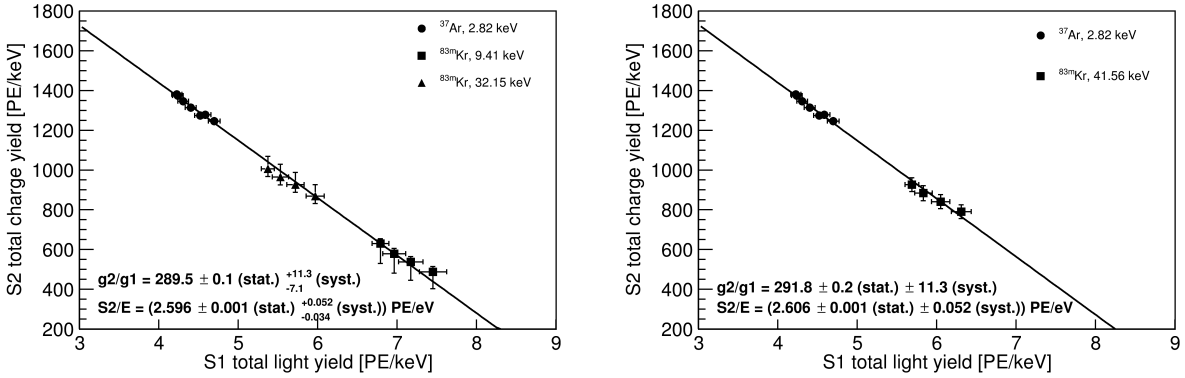

Figure 5.18: Anti-correlated charge versus light yield of ^{37}Ar and ^{83m}Kr with linear fit at various drift fields in the range $80 - 968$ V/cm for ^{37}Ar and $484 - 968$ V/cm for ^{83m}Kr. The axis intersections yield the detector-specific gains $g1$ and $g2$ from the combined energy scale. The yields are corrected for DPE/crosstalk of the photosensors, see next chapter. **Left:** Including the split 9.41 keV and 32.15 keV ^{83m}Kr lines with asymmetric error bars from the splitting routine. **Right:** Including the merged 41.56 keV line.

5.3 Calibration Results

5.3.1 Yields, Detector Response and Energy Resolution

From the mean of the K-shell capture distribution, Figure 5.11, left, we deduce a light yield of $(4.973 \pm 0.01\,(\text{stat.})^{+0.10}_{-0.28}\,(\text{syst.}))$ PE/keV and a charge yield of $(1580.1 \pm 0.3\,(\text{stat.})^{+22.6}_{-30.4}\,(\text{syst.}))$ PE/keV by normalising to a decay energy of 2.82 keV at 968 V/cm drift field.

Calculating the total light and charge yield for data at different drift fields yields an anti-correlation plot in charge versus light yield space, to which we refer as *Doke plot* [239], shown in Figure 5.18. The light and charge yield measurements of the K-shell line from ^{37}Ar and two lines from ^{83m}Kr (see Appendix A) feature a clear anti-correlated linear dependence. The ^{37}Ar points are less spread than those from ^{83m}Kr because the drift field dependence of the charge and light yield decreases rapidly below ~ 10 keV ER energy [334]. The errors include statistical uncertainties, as well as systematic uncertainties which we detail in the next chapter. These include for example photosensor gain uncertainties and a bias introduced by the peak-splitting method described in Chapter 4, Section 4.2.2. The latter is the origin of the asymmetric vertical error bars assigned to ^{83m}Kr. The larger 32.15 keV S2 signal features a systematic bias towards lower charge yield as its charge is integrated for the smaller 9.41 keV S2 signal. This however, is not the case for the ^{83m}Kr S1 signals as the S1-delay time is sufficiently long to provide complete separation in S1 for any split S2 signal, see Appendix A. We come back to this discussion in the next chapter.

The detector-specific gains $g1$ and $g2$ as defined in Equation 2.8, Chapter 2, can be calculated from the combined energy scale, Equation 2.9, using a literature value for $W = (13.7 \pm 0.2)$ eV [243]. From the axis intersections of the linear regression in Figure 5.18, left, we obtain $g1 = \left(0.123\,^{+0.004}_{-0.005}\,(\text{syst.})\right)$ PE/γ and $g2 = \left(35.6\,^{+0.9}_{-0.7}\,(\text{syst.})\right)$ PE/e$^-$. We use the fit from the split 9.41 keV and 32.15 keV lines for its lower parameter errors than compared to the fit with the 41.56 keV line of ^{83m}Kr. The statistical error is not quoted separately because it is subdominant to the systematical one. The asymmetry of the error region is due to the above mentioned ^{83m}Kr-S2-splitting. Note that this plot includes yields that are corrected for crosstalk or DPE systematics. In the next chapter, we examine the properties of the Doke plot in more detail and turn around the procedure to derive the W-value with an independent measurement of $g2$.

The charge yield at 0.27 keV from the L-shell line is $(2291 \pm 1\,(\text{stat.}) \pm 31\,(\text{syst.}))$ PE/keV. Because of the S2-only character of the signal, we cannot have a measurement of the light yield at this energy.

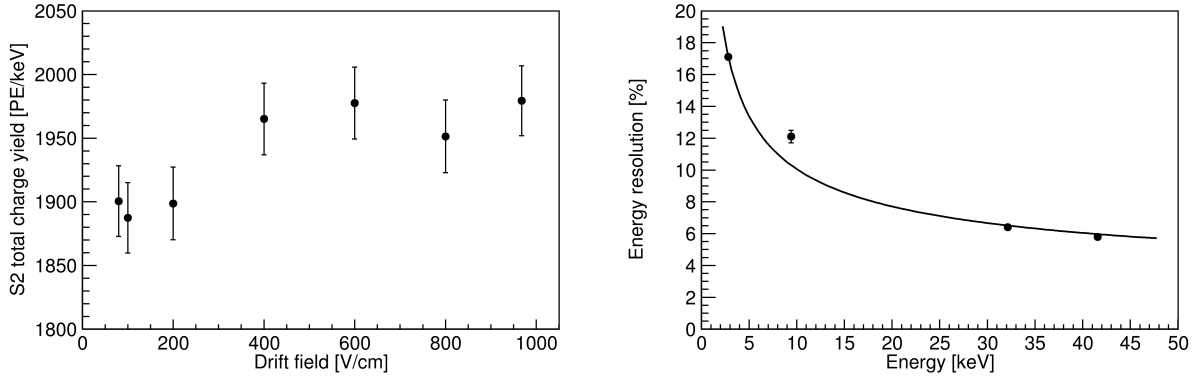

Figure 5.19: Left: Dependence of the charge yield of the L-shell line at 0.27 keV on the electric drift field. The yields are corrected for DPE/crosstalk of the photosensors, see next chapter. The error bars include the photosensor gain uncertainties. **Right:** Energy-dependence of the energy resolution of Xurich II at the ^{37}Ar K-shell and the ^{83m}Kr calibration lines. The error bars are partially smaller than the markers and include statistical and systematical uncertainties. The slightly larger error bars on the data point at 9.41 keV is due to higher uncertainties on the S2 signal from the splitting algorithm. See text for details on the fit function.

However, similar to the Doke plot, we can represent the dependence of the S2 signal on the drift field, see Figure 5.19, left. We observe a slight anti-correlation but due to the non-corrected drift time dependence of the S2 signal, the data points do not lie on a straight line. The charge yield axis of this plot can be viewed as the continuation of the space in Figure 5.18 towards higher charge yields.

The combined energy resolution σ_E/E from S1 and S2 signals of the 2.82 keV ^{37}Ar line is (17.1 ± 0.1) % at 968 V/cm and stays, as expected for the combined energy scale, constant down to 600 V/cm. Below this value, the resolution degrades slowly to (18.1 ± 0.1) % at the lowest measured field. For comparison, we show in Figure 5.19, right, the energy resolution also at the energies of the ^{83m}Kr calibration lines. For instance, the resolution at 32.15 keV is (6.4 ± 0.2) % which is consistent with the one measured with the TPC with two PMTs [13]. The fit curve in Figure 5.19, right, follows the two-parameter function

$$\frac{\sigma_E}{E} = \frac{P_0}{\sqrt{E}} + P_1 \tag{5.5}$$

as used in Reference [343]. Although being of S2-only type, we find for the 0.27 keV line a good energy resolution of (13.5 ± 0.2) % at 968 V/cm. At lower drift fields the resolution varies in the range $12.9 - 16.2$ % without showing a conclusive trend.

5.3.2 NEST Comparison

The yields of all lines at 968 V/cm are compared to the NEST v2.3.0 [344] model predictions in Figure 5.20, left. Both charge and light yield at 32.15 keV and 41.56 keV agree well with the prediction for ^{83m}Kr and the gamma model. However unlike the good agreement at these energies, we find a lower charge and higher light yield than predicted at lower energies. Significant is the deviation at 9.41 keV from both the NEST ^{83m}Kr and the gamma model. While the yields of ^{37}Ar at 2.82 keV are only a few percent off from the gamma and beta models, our measurement of the charge yield at 0.27 keV is far below the predicted band at this energy. A similar discrepancy at 0.27 keV, although with higher uncertainties involved, was observed in Reference [10]. In Figure 5.20, right, we show the comparison for ^{37}Ar at the lowest field of 80 V/cm and find a better agreement at 2.82 keV but a similar behaviour at 0.27 keV. In Appendix A, Figure A.4, we provide the comparison for the ^{83m}Kr yields at 484 V/cm.

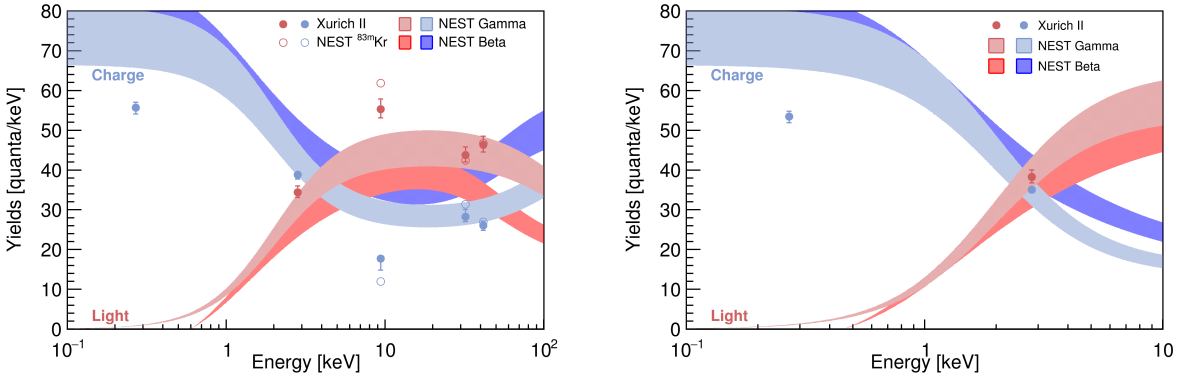

Figure 5.20: Comparison of the obtained charge (blue) and light (red) yields from the ^{37}Ar and ^{83m}Kr lines to the NEST v2.3.0 [344] gamma, beta and ^{83m}Kr models. The uncertainty bands reflect the typical ±10 % intrinsic systematical uncertainty of NEST [345]. **Left:** ^{37}Ar and ^{83m}Kr yields at 968 V/cm drift field. **Right:** ^{37}Ar yields at 80 V/cm drift field.

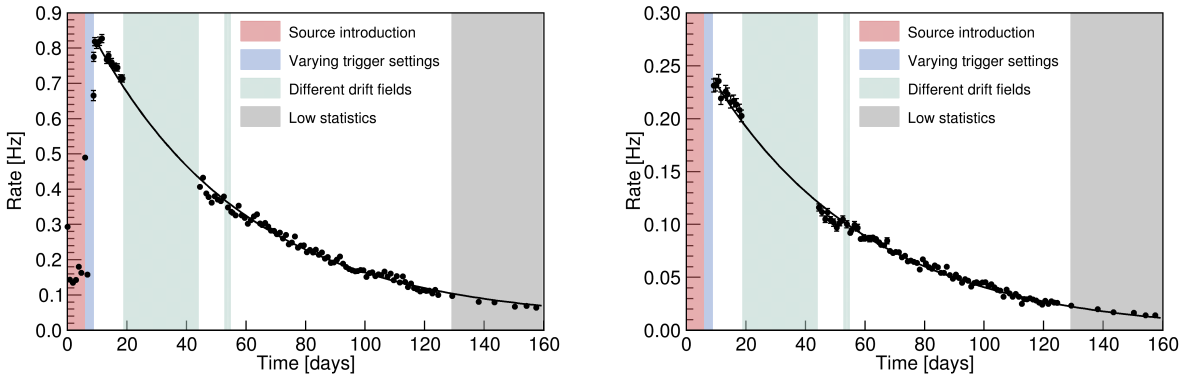

Figure 5.21: Activity evolution of the ^{37}Ar calibration lines over more than 4 half-lives with a one-day binning starting from the time at which the first ampule was broken. The fits were performed on 968 V/cm data only, because at other drift fields the data features systematic deviations caused by the varying efficiency of the applied data-driven cuts and corrections. The shaded regions are excluded from the fit. The errors on the individual data points are Poisson-like. **Left:** For the 2.82 keV line we obtain a half-life of (35.7 ± 0.4) d. **Right:** For the 0.27 keV line we obtain a half-life of (36.6 ± 0.7) d.

5.3.3 Half-Life

Data with the ^{37}Ar source was acquired stably with fixed trigger settings over a period of 149 days, which corresponds to more than 4 half-lives. Selecting the data as described in Section 5.2.1 in daily slices, we show in Figure 5.21, left, the evolution of the activity of the 2.82 keV line. For simplicity, we assume that all the systematics and applied cuts are stable over the time of the measurement. The exponential fit yields a half-life of (35.7 ± 0.4) d, where the most recent literature value is (35.011 ± 0.019) d from a weighted average of four measurements [317]. The given error is the error of the decay parameter of the least squares fit and does not include systematic uncertainties. However, within the scope of this work, we can be confident that we indeed selected events from ^{37}Ar decays.

In Figure 5.21, right, we show the evolution of the L-shell count rate over the period of data taking. We obtain a half-life of (36.6 ± 0.7) d, also close to the literature value. The shown rate is higher than expected from Figure 5.21, left, and the relative branching ratio from Table 5.1 simply due to the stricter data selection of the S1-S2 analysis of the K-shell event population.

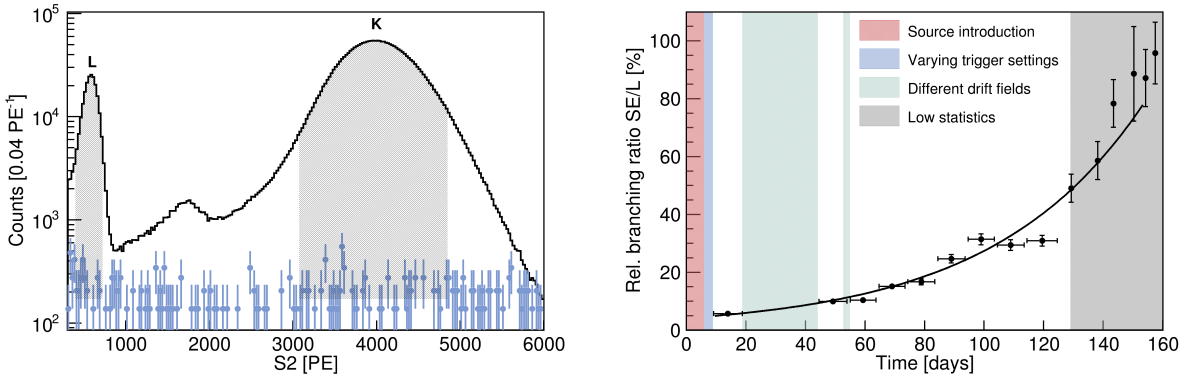

Figure 5.22: Left: L- and K-shell populations of ^{37}Ar. The shaded regions are used to calculate the relative branching ratio of the lines. The normalised background in blue is negligible. **Right:** Evolution of the branching ratio of the SE and L-shell event populations at 40 ms veto time.

5.3.4 Branching Ratios

As a consistency check, we calculate the branching ratio of the L-and K-shell populations. According to the literature it should be 9.9 %, cf Table 5.1. To this end we simply count the events within the $\pm 2\sigma$ regions of the populations, see Figure 5.22, left. As we shall see in the next chapter, the detection and S2-tagging efficiencies can fairly be assumed to be 100 % at the energies of these lines. Furthermore, only selection and quality cuts with the same expected acceptance for the two lines are applied, i.e. the fiducial volume radius and the AFT cut developed for the L-shell line. For a simple counting, we need to ensure that the background in the selected data sets for the energy region of interest is negligible. For the background estimation, we use three data sets with half a million events each that were acquired before the ^{37}Ar source was introduced. The trigger settings during for these were different, like for ^{83m}Kr data taking, however, allowed to trigger on signals of at least 21 PE in size, which is far below our region of interest. The normalised background is shown in blue in Figure 5.22, left, and is about two orders of magnitude lower than the peak count rate of the L- and K-shell populations. The population in the middle of the two ^{37}Ar lines are gas events. These are not removed here due to the small set of quality cuts. Here, we also assume that the pile-up event rate is negligible. This is certainly justified as the trigger rate was $\mathcal{O}(10\,\mathrm{Hz})$. We obtain a branching ratio of (8.6 ± 0.2) % at 968 V/cm drift field, close to the literature value. The reason for it to be lower by 13 % is most likely due to charge loss of the narrower L-shell which, because of its S2-only nature, is not corrected.

It is left to study the relative branching ratio of the S2-only event populations. This measure is more suited to understand if the SE event population indeed contains M-shell decay events than the time-evolution of its decay rate. Of course, if the selected SE event population was due to M-shell captures, we would expect it to decay over the period of the data acquisition, just like for the K- and L-shell, see Section 5.3.3. However, since the data selection involves a constant time veto, the efficiency with which we cut time-uncorrelated events decreases as the event separation, due to the decay, increases. For this reason, we observe the event rate to be roughly constant in time.

Suppose that besides the M-shell decay there is another unknown source of time-uncorrelated SE events whose rate, unlike the M-shell capture, is constant in time: $SE(t) = SE_0 = \text{const}$. In fact, the rate of that source is only assumed to be roughly constant over the period of data acquisition but could in principle have a long half-life. Then the time evolution of the branching ratio can be written as

$$\mathrm{BR}_{\mathrm{SE-L}}(t) = \frac{M(t) + SE_0}{L(t)} = \frac{M_0}{L_0} + \frac{SE_0}{L_0} e^{\frac{t \ln 2}{T_{1/2}}} \quad , \tag{5.6}$$

where M_0 and L_0 are the initial activities of the M- and L-shell at $t = 0$ and $T_{1/2}$ is the ^{37}Ar half-life. According to this simple model, we expect a constant branching ratio for $SE_0 = 0$ and otherwise an exponential rise. The corresponding plot with an exponential fit for a 40 ms veto time on both, the SE and the L-shell population, is shown in Figure 5.22, right. The data points are based on the summed rates with a ten-day binning and with higher statistics and more frequent data acquisition at the beginning than at the end. Fixing the half-life to the literature value, the exponential fit yields the parameters $M_0/L_0 = (0.8 \pm 0.7)\,\%$ and $SE_0/L_0 = (4.2 \pm 0.3)\,\%$. We expect a branching ratio of $M_0/L_0 = 10.1\,\%$, see Table 5.1. The branching ratio at $t = 0$ is the sum of M_0 and SE_0 and, thus the two parameters are correlated. This result favours the presence of another constant time-uncorrelated source of SE events and shows that the selected SE event population contains only very few M-shell events, if any. Such an additional source presents an irreducible background to the M-shell events. To keep decent statistics, the average separation of events does not allow us to apply longer veto times, cf. Figure 5.16. The identification of the M-shell events in the SE background would be facilitated if a very low-activity ^{37}Ar source was deployed. Less sensitive DAQ settings that reduce the content of noise events in the data sets, i.e. triggers on baseline fluctuations, would additionally improve the performance of the time veto cut. Additionally to the discussed properties of SE events, XENON1T observed a correlation of the (x, y)-position of SE events and preceding energy depositions [342]. This is attributed to the formation of negative impurity ions along the drift track of the primary interaction that release electrons by collisional electron detachment or photoionisation. Thus, if the SE events are primarily due to impurities, one could obtain a time veto with a higher acceptance for uncorrelated events by applying it only within a certain region around the horizontal position of the primary interaction. However, the small size of Xurich II, the relatively high event rate and the limitation of the horizontal position reconstruction resolution of SE events (see Chapter 6, Section 6.1.2) dampen the prospects for the development of a more efficient combined spatio-temporal veto.

5.4 Summary and Conclusion

In this chapter we have shown the characterisation of the Xurich II TPC with an internal ^{37}Ar calibration source. In particular, we have outlined the source production, and the source introduction setup and procedure. We have isolated the 2.82 keV K-shell line, exploiting the S1 and S2 signals, and the 0.27 keV L-shell line in an S2-only analysis. For this, we have developed cuts and corrections to improve the data quality. To confirm that the selected event populations can indeed be identified with the ^{37}Ar decay lines, we have checked their half-lives and relative branching ratios, showing good agreement with the literature. In addition, we have investigated the M-shell line by applying a time veto on the SE event population to separate the uncorrelated decay events from correlated SE background. However, the search has turned out to be inconclusive due to an additional irreducible background of uncorrelated SE events. Based on the isolated event populations, we have determined the light and charge yields at the respective energies and compared the latter to predictions from NEST. We have furthermore derived the detector response parameters from the combined energy scale, based on the ^{37}Ar and ^{83m}Kr lines at various drift fields, and have obtained: $g1 = \left(0.123\,^{+0.004}_{-0.005}\,(\text{syst.})\right)$ PE/γ and $g2 = \left(35.6\,^{+0.9}_{-0.7}\,(\text{syst.})\right)$ PE/e$^-$. In Appendix A we provide the analysis of data acquired with a ^{83m}Kr source.

^{37}Ar has great potential as low-keV calibration source for LXe detectors. It can be produced by thermal neutron capture on ^{36}Ar in either natural or isotopically enriched argon. The activity introduced into the detector can be dosed via the gas flow or dosing volumes. ^{37}Ar is mixed with the LXe, decays into stable chlorine and leads to homogeneously distributed events in the detector. However, its half-life of over one month makes an efficient cryogenic distillation necessary if used in dark matter detectors.

Chapter 6

Mean Electronic Excitation Energy of Liquid Xenon

We discussed in Chapter 2, Section 2.3, the response of LXe detectors to particle interactions and introduced the W-value as the average energy required to produce a single free quantum, either a photon or an electron, in LXe. The widely employed numerical value of W is (13.7 ± 0.2) eV measured at ~ 100 keV by E. Dahl [243] which we also used to calculate the detector gains of Xurich II in the previous chapter. However, a W-value of $(11.5 \pm 0.1\,(\text{stat.}) \pm 0.5\,(\text{syst.}))$ eV was measured in the EXO-200 experiment with various gamma sources at $\mathcal{O}(1\,\text{MeV})$ [346]. A list of other measurements of the W-value can be found in the same reference. The deviation of the EXO-200 value from former measurements motivated this study at keV-scale energies [347], deploying the internal ^{37}Ar and $^{83\text{m}}$Kr sources in Xurich II that we discussed in the preceding chapters.

This chapter is structured as follows: In Section 6.1 we outline the deployed experimental method and introduce briefly the data on which we base our analysis. In Section 6.2 we show the data analysis of the various inputs for the calculation of the W-value. The systematic uncertainties on the measurement and the applied data corrections are detailed in Section 6.3. We present the final result in Section 6.4 and discuss, interpret and summarise our findings in Section 6.5.

6.1 Experimental Approach

6.1.1 Measurement Principle

We rewrite Equation 2.6, Chapter 2, with the scintillation and ionisation gains defined in Equation 2.8, such that W reads

$$W = g2 \frac{E}{\frac{g2}{g1}\text{S1} + \text{S2}} \quad . \tag{6.1}$$

Thus, the W-value can be determined from the following inputs: an event population in S1-S2-space of a known calibration source yielding ERs at an energy E, an independent measurement of the ionisation gain parameter $g2$ and the (negative) slope $g2/g1$ of the first order polynomial in charge yield versus light yield space. As in the previous chapter, we refer to the latter representation of the anti-correlation of the S1 and S2 signals as *Doke plot* [239] and show a schematic in Figure 6.1, left.

Alternatively to this local approach, evaluated at a certain energy and scaled by the slope of the anti-correlation line in the Doke plot, we can extrapolate to S1 = 0, i.e. to the intercept with the charge yield axis, and obtain the global expression (see Figure 6.1, left)

$$W = g2 \left.\frac{E}{\text{S2}}\right|_{\text{S1}=0} \quad . \tag{6.2}$$

Besides the ionisation gain parameter $g2$, the only input here is the extrapolated (reciprocal) offset of the anti-correlation line at zero light yield. Both the ratio of gains $g2/g1$ as well as the offset S2/E at S1 = 0 require at least S1 and S2 data of a single energy line at two different electric drift fields or two

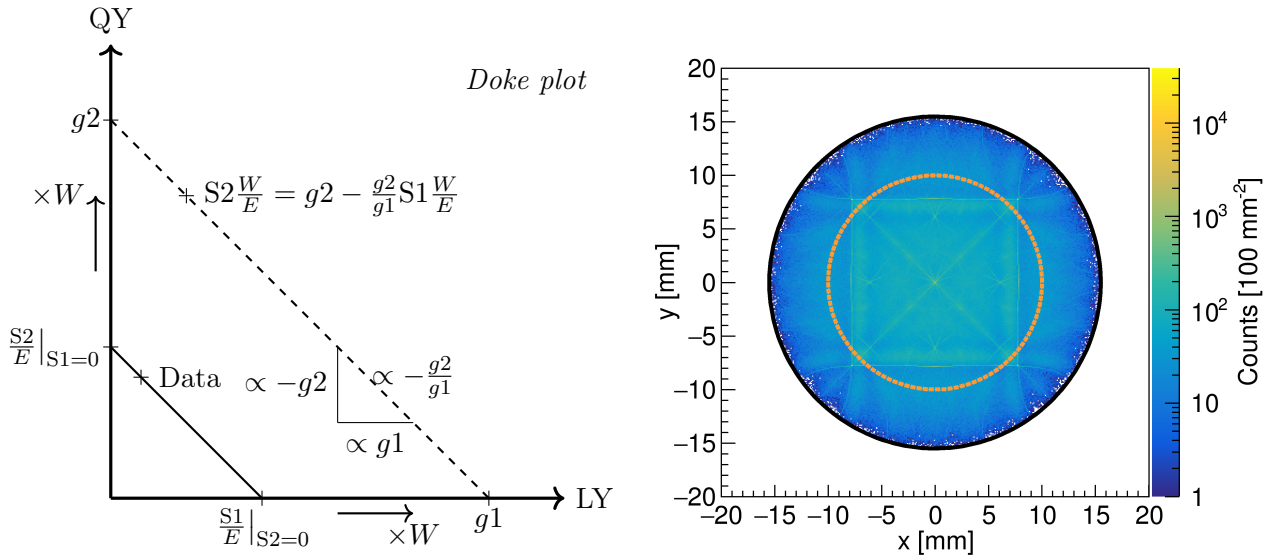

Figure 6.1: Left: Schematic of the *Doke plot* in charge yield (QY) versus light yield (LY) space for an interaction energy E. Measurements of the charge and light yield at different electric drift fields or interaction energies would yield the solid line. The dashed line, making the relation to the gain parameters $g1$ and $g2$ apparent, is obtained by a scaling of this space with W. While the local approach uses a point on the anti-correlation line and its (negative) slope $g2/g1$, the global one uses the (reciprocal) QY-axis intercept. Both require an independent measurement of the ionisation gain parameter $g2$. **Right:** x-y distribution of the SE event population. The boundaries of the detector and fiducial volume are represented by solid black and dashed orange lines, respectively. The discrete pattern is due to the use of a centre-of-gravity algorithm for the position reconstruction in the single photon regime.

different energy lines at one electric drift field. For more than two light and charge yield pairs, one performs a linear fit in the Doke plot whose accuracy depends on the separation in the S2/S1 ratio and on the yield errors.

Besides the parameters of the anti-correlation fit, both approaches require an independent measurement of the ionisation gain parameter $g2$ as input. To that end, we observe that for a SE that is extracted to the gas phase, we have $g2 = \mathrm{S2}$. Hence, a measurement of the SE event population with the S2 signal yields the ionisation gain parameter $g2$.

6.1.2 Data

We base our analysis on the high-statistics calibration data, discussed in Chapter 5 and Appendix A, in S1-S2-space from two different runs with internal ^{37}Ar and $^{83\mathrm{m}}$Kr sources. As mentioned in Section 6.1.1, the ionisation gain parameter $g2$ is determined based on the observed SE events with S2 signals only. These events occur at a high rate of $\sim$ 17 Hz in the detector volume and are homogeneously distributed in the horizontal plane. However, using the centre-of-gravity algorithm that we described in Section 4.2.4, Chapter 4, it is clear that SE events with e.g. only one photon in the top array are reconstructed at the centre of the hit photosensor, see Figure 6.1, right. This natural limitation of the position reconstruction in the single photon regime does however not affect the analysis. A systematical variation of the fiducial radius did not show any significant change of the bottom, top or total SE charge yield up to radii close to the TPC boundary.

In Section 5.2.3 of the previous chapter, we have discussed potential sources of the SE event population. In case of the deployed ^{37}Ar source, the M-shell electron capture process at 17.5 eV [292] could cause, based on the branching ratio with the K-shell, a small fraction of $\sim$ 0.5 % of this SE population. The origin of these electrons is however not relevant for the analysis here as they all

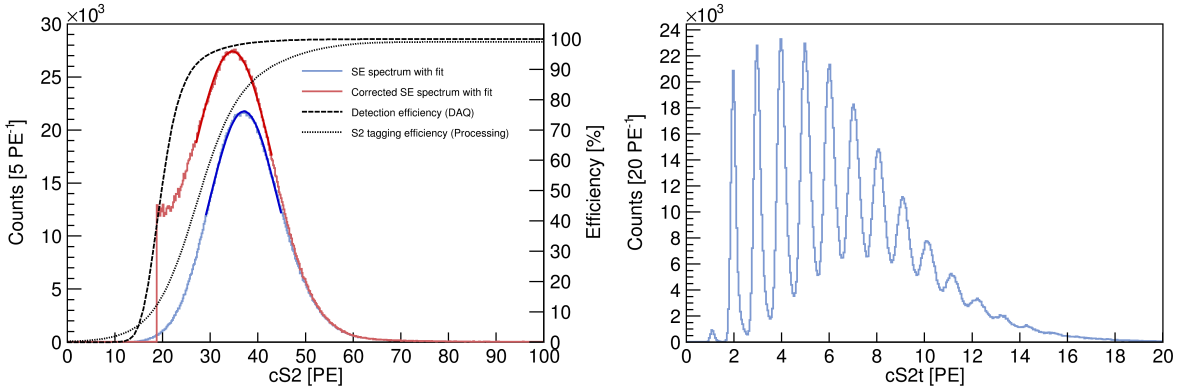

Figure 6.2: Total S2 population from SE extraction at 968 V/cm drift field without DPE/crosstalk correction. **Left:** Bare and efficiency-corrected S2 total spectrum with Gaussian fits together with the efficiency curves, see Section 6.3.3. The corrected (red) spectrum was cut on the left to avoid division by small efficiencies ($< 5\,\%$) that distort the distribution. **Right:** Bare S2t spectrum with single PE resolution. The PE-scale of the S2t signals is fixed by the centring of the peaks around the corresponding PE-tick mark using a linear correction function. We follow the same procedure for the S1t but base it on the 2.82 keV population of ^{37}Ar, cf. Chapter 5, Section 5.2.1.

share the same signal topology. We extract the SE population from the ^{37}Ar data sets since these were acquired with a low trigger threshold of $6-7$ mV on the PMT channel, cf. Section 4.1, Chapter 4. Because of the highly abundant one-by-one extraction of electrons at high $g2$[1], the SE event population is readily identified and isolated (cf. Figure 6.2).

6.2 Data Analysis

6.2.1 Single Electron Gain

To identify and isolate the SE event population, we apply the following data selection and quality criteria: a cut to remove saturated events, a single scatter cut on the PMT channel and a fiducial radius cut such as developed in Section 4.2.4, Chapter 4. In addition, we apply an S2-only cut, i.e. we remove events with an S1 signal in the PMT waveform. Furthermore, we require that the trigger was issued on the S2 signal, i.e. we keep events whose PMT S2 signal is located within a tight time window of $[-100, +130]$ ns around the trigger, see Figure 6.3, left. An S2-width cut of $[110, 550]$ ns further cleans up the population, see Figure 6.3, right. Compare also Figure 5.12, right, and Figure 5.13, left for a representation over total S2-space.

The mean of the Gaussian fit of the population is constant within the parameter uncertainty for the considered drift fields. We show the result for the 968 V/cm data sets in Figure 6.2. A Gaussian fit of the bare, i.e. non-corrected, spectrum yields $g2 = (37.05 \pm 0.01\,(\text{stat.}) \pm 0.50\,(\text{syst.}))\,\text{PE/e}^-$. Incorporating the DPE/crosstalk correction as well as the DAQ and processing efficiencies, discussed in Sections 6.3.2 and 6.3.3, we obtain $g2 = (29.84 \pm 0.01\,(\text{stat.}) \pm 0.40\,(\text{syst.}))\,\text{PE/e}^-$. While the DPE/crosstalk correction shifts the SE spectrum by $\sim 14\,\%$, the DAQ and processing efficiencies contribute by another $\sim 6\,\%$.

[1] Based on our calculation in Section 5.3.1, Chapter 5, we expect a high $g2$ of $28-37\,\text{PE/e}^-$ for an assumed W-value of $11-14$ eV.

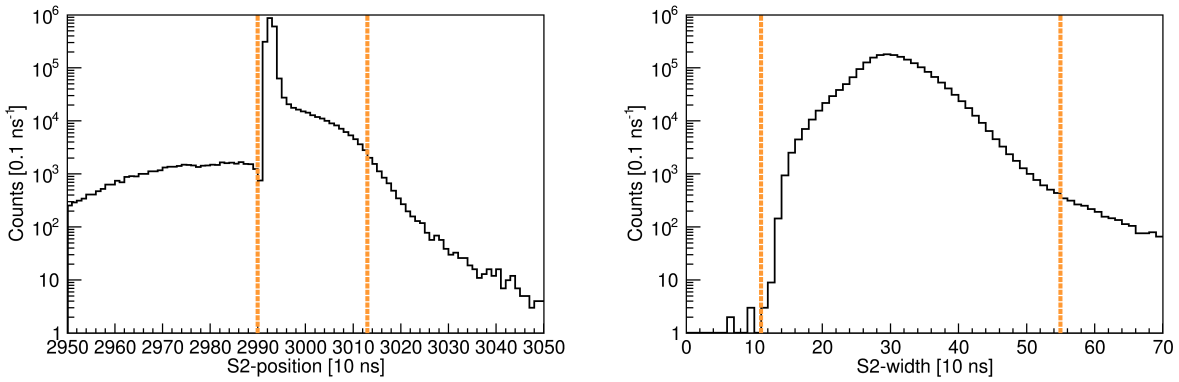

Figure 6.3: Data quality cuts for the SE event population. The accepted region is enclosed by the dashed orange lines. **Left:** Trigger position cut. **Right:** S2-width cut.

6.2.2 Anti-Correlation Fit Parameters

In Figure 5.18, Chapter 5, we show the means of the ^{37}Ar and ^{83m}Kr populations at the considered drift fields in charge versus light yield space. In the left plot, we show the fit with the split 32.15 keV and 9.41 keV lines and in the right one the merged 41.56 keV line. Although the 41.56 keV line is not subject to the effect of the peak-splitting routine, that is discussed in Section 6.3.3, it does not yield more precise results of the fit parameters on the anti-correlation line due to its smaller span in S1-S2-space. However, we find both fits to be compatible within errors. From the linear fit on the left of Figure 5.18 we obtain a (negative) slope of $g2/g1 = 289.5 \pm 0.1\,(\text{stat.})\,^{+11.3}_{-7.1}\,(\text{syst.})$ and a charge yield axis intercept of $\text{S2}/E = (2.596 \pm 0.001\,(\text{stat.})\,^{+0.052}_{-0.034}\,(\text{syst.}))\,\text{PE/eV}$. Using only the three ^{37}Ar and ^{83m}Kr data points at the fixed drift field of 968 V/cm yields compatible fit results with larger uncertainties: $g2/g1 = 302.8 \pm 0.4\,(\text{stat.})\,^{+36.7}_{-25.7}\,(\text{syst.})$ and $\text{S2}/E = (2.658 \pm 0.003\,(\text{stat.})\,^{+0.167}_{-0.124}\,(\text{syst.}))\,\text{PE/eV}$.

6.3 Systematic Uncertainties and Corrections

A determination of the absolute energy scale of a LXe detector requires a careful treatment of the systematic uncertainties and efficiencies that impact the result. Below, we discuss in detail both relevant sources and those that were identified to be negligible, as well as data corrections that were applied whenever possible. We provide a summary of all treated systematic effects and corrections in Table 6.1.

6.3.1 TPC Effects

Liquid Xenon Purity and TPC Geometry

We discussed in Section 5.2.1 of Chapter 5 that, for a given energy deposition, the size of the S1 and S2 signals depend on the vertical depth of the interaction in the TPC and thus, on the drift time. We thus apply corrections on the S1 and S2 signals as detailed above. Note that the SE S2 signal is not subject to any drift time dependence. The PE-scale of both S1 and S2t signals is fixed utilising the single PE resolution of the SiPMs, see Figure 6.2, right. However, such a correction is not accessible for the bottom signals due to the lack of single PE resolution of the PMT. To minimise geometry effects, ensure good performance of the position reconstruction algorithm, and to reduce the material-induced background and the effect of electric field distortions, we fiducialise our active volume like in the preceding chapters.

Electron Extraction Efficiency

The electron extraction efficiency from the liquid to the gas phase can be assumed to be $\sim 100\,\%$ at a gas (liquid) extraction field of 10 kV/cm (5.4 kV/cm). We base this assumption on various former measurements that applied different methods. Among these are early absolute measurements directly comparing the ionisation signal below and above the liquid surface [348,349]. In XENON100 a relative measurement was performed, comparing the recombination- and electron lifetime-corrected S2 signals of mono-energetic sources to the expected number of produced electrons [336]. XENON1T compared the $g2$ obtained from the anti-correlation fit of several mono-energetic sources (assuming a literature W-value) and the $g2$ from the lowest S2 signals [258]. However, more recent relative measurements imply that the extraction efficiency might only be $89-95\,\%$ at the extraction field of interest [211,255]. These were searching for saturation of the ratio of the S2 signals of mono-energetic calibration sources and the SE S2 at increasing extraction fields. As noted in Reference [211], such measurements are, however, highly subject to systematic uncertainties from the geometry of the extraction region. In Reference [255] the discrepancy to earlier relative measurements is attributed to scaling factors that arise when an independent determination of the number of initially produced electrons is lacking. In summary, the literature on this topic appears inconclusive and lacks a detailed unified explanation of the discrepancies between all the used methods. For this reason, we assume an electron extraction efficiency of 100 % in this study and consider the consequence of this effect on our analysis. While a lower extraction efficiency would only diminish the statistics of the SE population, it would reduce the charge yield of the calibration lines and thus, if disregarded, yield a higher W-value when determined via Equations 6.1 and 6.2. We further comment on the effect in Section 6.5.

Liquid Level

The ^{37}Ar and ^{83m}Kr calibrations were conducted in two separate runs with a complete xenon recovery and filling procedure in between. The levelling procedure gives rise to an uncertainty of the liquid-gas interface of $\pm 125\,\mu$m between the runs which is nominally kept in the middle of the gate and anode mesh. This uncertainty corresponds to one full revolution of the motion feedthrough whose resolution is defined by the major divisions of 25 µm. This in turn impacts the S2 signal amplification. A systematic study of this effect with ^{83m}Kr data shows that the levelling uncertainty corresponds to a maximum S2-uncertainty of 2.5 %, see Figure 6.4. This uncertainty is based on a linear interpolation between the data points at 1.5 mm and 2.125 mm liquid level. However, we only include this uncertainty in the ^{83m}Kr data points of the Doke plot (Figure 5.18, Chapter 5) where we use information of both runs for the anti-correlation fit, and assume the liquid level to be constant within the runs, due to stable thermodynamic conditions, and uniform in the horizontal plane.

6.3.2 Photosensor Effects

We note that Equations 6.1 and 6.2 are insensitive to an overall factor linear in $g1$, $g2$, S1, S2 that is constant in time, energy and common to the PMT and SiPMs. For instance, the result is insensitive to a scaling of the conversion from ADC bins to PE due to e.g. the read-out electronics as long as it concerns both top and bottom sensors. However, as we discuss in Section 6.5, the data shows a dependence of the relative light and charge yields of the top and bottom photosensors on the respective energy line, see Table 6.2. Therefore, we do expect an influence of the hybrid photosensor configuration from systematically different characteristics of PMTs and SiPMs. Two classes of such characteristics can be distinguished: time-dependent and time-constant ones. Photosensor gains can generally show a time-dependence, e.g. due to the aging of the photocathode [350]. Since we did not measure all input quantities for W at the same point in time, a systematic gain change could impact the result even though all of the input quantities in the Equations 6.1 and 6.2 scale with the gain in the same fashion. All other characteristics treated subsequently are expected to be constant

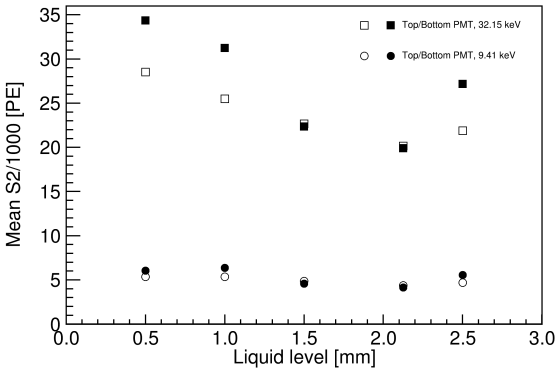

Figure 6.4: Mean of the S2 signal for the split ^{83m}Kr calibration lines versus LXe level above the gate. The scan was performed with the former configuration of Xurich II with two PMTs. The type and arrangement of the photosensors should however not impact the relative change of the S2-amplification with the liquid level.

in time as long as the thermodynamic conditions are unchanged. For the considered interactions the photosensors are operated in the linear regime of their dynamical range and thus, we expect the characteristics to be independent of the interaction energy.

Photosensor Gain

As discussed in Chapter 4, Section 4.3.2, the photosensor gains were determined weekly with an LED calibration and have shown to be stable in time. We measured a PMT gain of $(3.76 \pm 0.06) \times 10^6$. The error-weighted SiPM mean gain is $(3.12 \pm 0.01) \times 10^6$. The uncertainties on the gain measurements represent one standard deviation of the gain distributions of the photosensors which we use as an estimator for a systematic change over the period of data acquisition.

Double Photoelectron Emission and Crosstalk

We assume a typical DPE probability of $(20 \pm 5)\,\%$ for the R6041-06 MOD PMT and correct for it [304–306]. As we have shown in Chapter 4, Section 4.3.5, for the S13371 SiPMs, we do not see an excess with external scintillation light due to a DPE or DPE-mimicking effect beyond the internal crosstalk probability and conclude that the enhancement probability is $(2.2 \pm 0.1)\,\%$ for which we correct. Furthermore, we have seen in Section 4.3.4 that the external SiPM crosstalk effect can safely be neglected as it is subdominant to the internal one and no effect on the PMT is seen.

Photon Detection Efficiency

The manufacturer Hamamatsu Photonics K.K. claims for the VUV4 S13371 SiPMs a saturation PDE of 24 % at 175 nm and 25 °C operated at 4 V overvoltage without crosstalk and afterpulsing [351]. However, SiPM characterisations for the nEXO experiment imply a much lower saturation PDE of $9.9 - 17.6\,\%$, measured at $3.3 - 3.8$ V overvoltage and 233 K, that differs by 8 % among devices [313, 352]. We are operating the SiPMs at more than 4 V overvoltage, see Chapter 4. In view of these measurements, we can thus assume a typical PDE of 18 %. Hamamatsu Photonics K.K. provided us with the spectral response curve of the R6041-06 MOD PMT that shows a peak QE of $\sim 30\,\%$ at 175 nm. The MOD specification sets a minimum QE of 25 % at that wavelength as requirement. An independent measurement shows a QE of $\sim 28\,\%$ [353]. The electron collection efficiency of that PMT was specified with $\sim 70\,\%$ upon enquiry to the manufacturer. We can thus conclude that the typical PDE of that PMT is 20 %. Since the SiPMs and the PMT have similar typical PDEs with a percent-level difference, systematics from the PDE difference are negligible for this analysis.

Infrared Sensitivity

We have discussed the IR-scintillation of GXe and LXe in Section 2.1.3, Chapter 2 and concluded that GXe emits IR-light at a VUV-comparable yield while LXe scintillation light does not feature a high amount of IR radiation. For this reason, only the S2 light can contain a significant amount of IR radiation. However, both photosensor types are insensitive at these wavelengths and thus IR-scintillation does not contribute significantly to our signals. For the SiPMs, the band gap of silicon sets a sensitivity cutoff at $\sim 1100\,\mathrm{nm}$. According to the manufacturer, the PMT is insensitive beyond 1000 nm which is confirmed by the trend of the spectral response curve in Reference [354] that shows a vanishing QE for wavelengths above 650 nm.

Afterpulses

The typical time delay of afterpulses in PMTs is $> 0.5\,\mu\mathrm{s}$ and thus we can expect afterpulses to be split from the main pulse by the data processor even in the case of S2 signals [263]. The VUV4 SiPMs show secondary pulses, such as afterpulses and delayed crosstalk, in two clusters with delays of $10 - 100\,\mathrm{ns}$ and $> 1\,\mathrm{ms}$, measured at 163 K and 5.1 V overvoltage [352]. While pulses of the latter cluster are surely separated from both S1 and S2 signals, pulses of the former will usually not be resolved separately by the DAQ and the data processor. However, such events with indistinguishable afterpulses also contribute to the gain measurement. The used model-independent method to calculate the gain is only insensitive to separated and under-amplified pulses [300]. Therefore, we do not need to treat unresolved SiPM afterpulses with a very short delay separately because they are included in the SiPM gain.

6.3.3 Data Acquisition and Processing Effects

Detection and Tagging Efficiency

As mentioned, the DAQ settings during the ^{37}Ar calibration period allowed us to trigger on $6 - 7\,\mathrm{mV}$ PMT signals, see Section 4.1, Chapter 4. Naturally, the trigger efficiency of signals that have comparable or lower amplitudes is reduced which is particularly relevant for SE S2 signals. The translation from signal amplitude to signal charge depends on the signal type. We employ a data-driven approach for the SE population, using their amplitude-over-width ratio as discriminator to obtain a detection efficiency, as shown in Figure 6.2, left. To this end, we consider the fraction of SE peaks that did not issue a trigger in events in which a subsequent larger signal triggered. Based on the same discriminator, we obtain the tagging efficiency of the processor to correctly identify SE events as S2 signals, see the same figure. We correct the SE population for these efficiencies and assume that these are 100 % for larger signals.

Peak-Splitting Routine

In order to separate the distinct peaks of the 32.15 keV and the 9.41 keV line of $^{83\mathrm{m}}$Kr, the raw-data processor splits at the intermediate minimum whenever a moving average of the waveform has fallen below half of maximum values of both peaks. This algorithm was chosen for its simplicity and good performance as it avoids fitting and has no need for a waveform template. Assuming Gaussian shape, we estimated in Section 4.2.2, Chapter 4, that the typical leakage into the neighbouring peak, caused by the processor, is $\leq 10\,\%$.

We use a data-driven approach based on the actual shape of the photosensor signals to obtain a reliable estimate of the maximally possible leakage between the two peaks. To this end, we select a

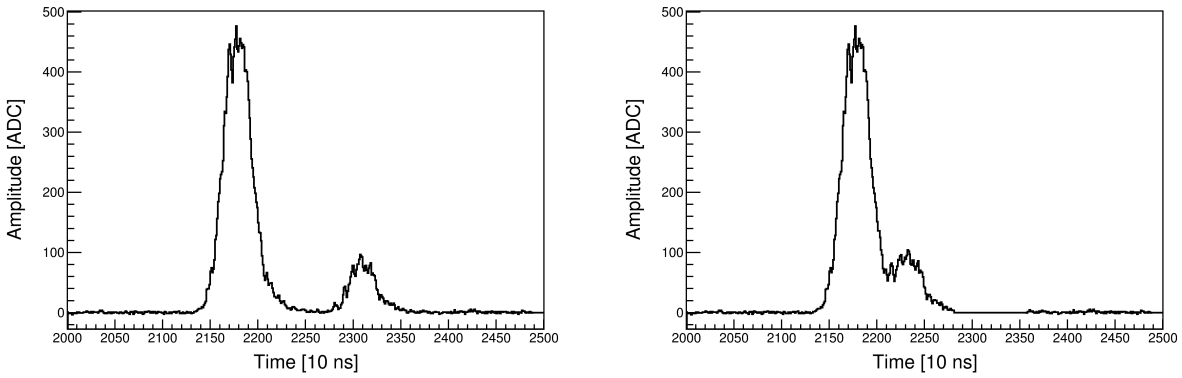

Figure 6.5: Data-driven approach to estimate the systematic error introduced by the peak-splitting algorithm. The smaller 9.41 keV S2 signal of a well-separated S2-pair is shifted towards the larger 32.15 keV S2 up to the point where the raw-data processor would still split two distinct peaks. Integration of the peaks yields the charge leakage between the peaks.

few hundred well-separated S2 signal pairs with a delay of at least 1.2 µs[2] and shift the small 9.41 keV S2 towards the large 32.15 keV S2 up to the point where splitting, according to the algorithm, is still just about possible, see Figure 6.5. Integration of the charge and comparison to the isolated peaks confirms the expectation that the leakage is directed from the large to the small S2 signal. The maximum errors of the PMT (SiPM) signals are $(-2.0 \pm 1.3)\,\%$ ($(-3.7 \pm 1.9)\,\%$) for the 32.15 keV line and $(+10.2 \pm 5.9)\,\%$ ($(+19.2 \pm 8.4)\,\%$) for the 9.41 keV line. A positive (negative) error indicates here that the S2 peak is reconstructed with a higher (lower) charge. Since a correction for any given S2-delay would be rather uncertain, we propagate these maximum errors.

We observe that the splitting algorithm only allows for a minimal ^{83m}Kr S2-delay of ~ 400 ns (see Figure A.2, left, in Appendix A) at which S1 signals, that feature widths in the range $60 - 140$ ns, are well-separated. The delay distribution peaks at ~ 700 ns and falls exponentially towards higher separation. At such large separations, no delay dependence of the S1 signals could be observed, unlike at shorter delays where corrections are needed [355].

Fitting Procedure

We have seen in the previous chapter, Section 5.2.1, that the 2.82 keV event distribution of ^{37}Ar in S1-S2-space features an asymmetric shape or skewness, see Figure 5.11. However, the shape of the distribution is of less relevance to the analysis for we only extract its mean. It is thus sufficient to use a standard Gaussian fit and instead estimate the uncertainty on the mean. To this end, and in addition to the standard fit parameter errors, we systematically varied the fit interval, including asymmetric intervals. This effect is more pronounced in the S1- than in the S2-direction and accounts for an S1-uncertainty of $^{+0.7}_{-4.1}\,\%$ and an S2-uncertainty of $^{+0.2}_{-0.7}\,\%$. In Reference [332] the larger S1 bias is explained by the fact that only upward S1 fluctuations above the S1 threshold are measured at such low light levels.

6.4 Result

We evaluate Equation 6.2 for the measurements of Section 6.2, considering the systematics and corrections of the previous section, and obtain $W = 11.5\,^{+0.2}_{-0.3}\,(\text{syst.})\,\text{eV}$. We do not quote a statistical

[2]The narrow ^{83m}Kr S2-width distribution is maximal at 0.6 µs, see Figure A.2, left, in Appendix A, and thus for delays > 1.2 µs, the waveform has basically fallen to baseline-level in between the peaks.

Systematic Effect	**Relevance and Treatment**
TPC Effects	
LXe purity (electron lifetime)	Drift time dependence of top and bottom S2 signals corrected
TPC geometry	Drift time dependence of bottom S1 signals corrected, active volume fiducialised in radius ($<$ 10 mm) and depth ($-[29, 2]$ mm)
Electron extraction efficiency	Assumed to be 100 %
Liquid level	Assumed constant within runs, maximum uncertainty of 2.5 % included in ^{83m}Kr data in Figure 5.18
Photosensor Effects	
Photosensor gain	Channels individually scaled for their mean gain, 1σ of gain distribution assumed as variation in time and included in result
DPE and crosstalk	Result corrected for PMT DPE of (20 ± 5) % and internal SiPM crosstalk of (2.2 ± 0.1) %, external SiPM crosstalk of (0.05 ± 0.01) % neglected
PDE	PMT/SiPM difference negligible
IR sensitivity	Negligible
Afterpulses	Irrelevant at high delays, included in SiPM gain if unresolved at $10 - 100$ ns
DAQ and Processing Effects	
Detection/tagging efficiency	Corrected for SE events, see Figure 6.2, left, assumed to be 100 % at higher energies
Peak-splitting routine	Relevant for ^{83m}Kr S2 signals, maximum uncertainty for PMT (SiPM) included in result: (-2.0 ± 1.3) % ((-3.7 ± 1.9) %) for 32.15 keV, $(+10.2 \pm 5.9)$ % ($(+19.2 \pm 8.4)$ %) for 9.41 keV
^{83m}Kr S1-delay dependence	Not observed
Fitting procedure	Parameter uncertainties included; for asymmetric 2.82 keV distribution, maximum uncertainty on S1 (S2) mean from systematic variation of fit intervals included in result: $^{+0.7}_{-4.1}$ % ($^{+0.2}_{-0.7}$ %)

Table 6.1: Summary of the considered systematic effects and applied corrections.

Energy [keV]	**LY Fraction** [%] **SiPMs / PMT**	**QY Fraction** [%] **SiPMs / PMT**
SE	– / –	18–19 / 81–82
2.82	10–11 / 89–90	25–27 / 73–75
9.41	7 / 93	20–21 / 79–80
32.15	7–8 / 92–93	31–32 / 68–69
41.56	7–8 / 92–93	29–30 / 70–71

Table 6.2: Fractions of the top SiPMs / bottom PMT sensors on the total light (LY) and charge yields (QY) for SE events, the 2.82 keV line of ^{37}Ar as well as the split 32.15 keV and 9.41 keV and the merged 41.56 keV line of ^{83m}Kr. The yields are independent of the drift field and the small variations among the measurements are represented by the displayed ranges.

uncertainty as it is subdominant compared to the systematic effects which are mainly due to the photosensor gain uncertainties, and the parameter errors of the anti-correlation fit. The latter come mostly from the liquid level uncertainty and the ^{83m}Kr-S2-splitting routine. The overall uncertainty is obtained from a propagation of the contributing uncertainties. The correlations of the inputs are maximal, however, these do not increase the final uncertainty much. Determining the W-value with the local approach using Equation 6.1 at any of the considered S1-S2-space populations of the calibration sources yields compatible results with mean values in the range $W = 11.1 - 11.6\,\mathrm{eV}$ with slightly higher errors due to the less direct nature of the approach.

6.5 Discussion and Conclusion

We observe slightly different relative light and charge yields of the top and bottom photosensors, depending on the selected event population, see Table 6.2. As there is no fundamental physical reason for such differences, we attribute these to systematic effects discussed in Section 6.3. For instance, the peak-splitting routine increases the charge yield of the 9.41 keV ^{83m}Kr line while it slightly reduces the one of the 32.15 keV line and leaves the light yield of both lines unchanged (see Section 6.3.3). The slightly higher relative PMT charge yield in SE events could be due to an unquantified systematic deficiency of our processing framework, leading to a higher (smaller) reconstructed charge in the single PE regime of the bottom (top) sensors. However, in lack of a thorough explanation of the deviations shown in Table 6.2, we would like to remark that a physical effect enhancing (reducing) the photosensor charge yield in the SE regime would increase (decrease) $g2$ and the resulting W-value. All photosensor effects were weighted with the relative yields in Table 6.2 when applied to the combined, top and bottom, signals. We note however, that the influence of the hybrid photosensor characteristics on the final result is suppressed by the fact that the weights are very similar and the effect would in particular vanish for equal weights, cf. discussion in Section 6.3.2.

As mentioned in Section 6.3.1, we did not consider an electron extraction deficiency in this study. We note however, that the resulting W-value would only be lower than the obtained one when correcting for an imperfect extraction efficiency. Because the incorporation of this systematic is a straightforward scaling of the charge yields of the ^{37}Ar and ^{83m}Kr lines and thus, of the W-value, we do not include the effect of a potential non-unity extraction efficiency in the lower error bound of the final result.

Albeit affected by various sources of systematics, our result features a competitive uncertainty range compared to former measurements. It is compatible with the W-value of $(11.5 \pm 0.1\,(\mathrm{stat.}) \pm 0.5\,(\mathrm{syst.}))\,\mathrm{eV}$ reported by the EXO-200 collaboration [346] at $\mathcal{O}(1\,\mathrm{MeV})$ energies which, thus, is reproducible at keV-scale energies. The EXO-200 experiment was a single-phase LXe detector with a wire charge readout. An external charge-injection allowed for an absolute calibration of the amplifier

on the readout plane. The uncertainty on the EXO-200 result is dominated by the calibrations of the light and charge response of the detector.

However, the W-value found here is lower than determined in other former measurements [239, 356]. In particular, it is incompatible with the established value measured by E. Dahl of (13.7 ± 0.2) eV [243] which was determined in a LXe detector of comparable size with 122 keV and 136 keV gamma rays from an external ^{57}Co source. The detector was operated in dual-phase and single-phase mode. For the latter, an amplifier on the anode allowed for a direct calibration of the charge yield used to measure the gain $g2$. The calibration of the amplifier was also the dominant source of uncertainty for the final result. In dual-phase mode, the detector was operated at the same extraction field as Xurich II and thus, the higher value found by E. Dahl cannot be explained by a lower electron extraction efficiency. The difference to our obtained value would stay constant for lower extraction efficiencies.

In order to check whether this discrepancy to former measurements is due to a higher observed absolute yield in the scintillation or ionisation channel, we can compare our result to predictions of NEST. From our measurements of $g2$ and $g2/g1$ in Section 6.2 we can calculate the corrected scintillation gain to be $g1 = 0.103\,^{+0.003}_{-0.004}\,\mathrm{PE}/\gamma$. Using the definitions of $g1$ and $g2$ (cf. Equation 2.8, Chapter 2), we obtain at 2.82 keV and 968 V/cm drift field on average the following number of excitation quanta from our measurements: $n_\gamma = 115.6$ and $n_{\mathrm{e}^-} = 130.4$. At this energy and drift field, and for the LXe density which corresponds to the operational conditions of Xurich II (cf. Chapter 4, Section 4.1), the NEST calculator [357] predicts absolute yields of $n_\gamma^{\mathrm{NEST}} = 85.8\,(71.1)$ and $n_{\mathrm{e}^-}^{\mathrm{NEST}} = 120.2\,(134.9)$, respectively, for the gamma (beta) model. Thus, the discrepancy is mostly seen in the scintillation channel and we observed S1 signals with a higher yield than predicted by NEST. Qualitatively, the same is seen at higher energies or lower drift fields. At the lowest field of 80 V/cm, we measured a mean of 128.6 photons and 117.7 electrons while NEST predicts 109.5 (93.8) photons and 96.5 (112.1) electrons for the gamma (beta) model. As expected, the detector response parameters that we calculated in Section 5.3.1, Chapter 5 with the literature W-value, compared to the ones found here with W as free parameter, are both simply scaled by the ratio of the W-values.

A change of the numerical value of W does not influence the translation from S1 and S2 signals into deposited energy when performing measurements relative to calibration lines. According to Equation 6.1 a lower W-value will generally reduce the microscopic detector response parameters $g1$ and $g2$ and thus, the absolute energy response to excitation quanta. As we have seen from the comparison with NEST, the rescaling will be mostly in the $g1$ value.

The Fano factor F accounts for the non-Poissonian nature of the intrinsic fluctuation of the number of quanta $n := n_\gamma + n_{\mathrm{e}^-}$ produced in an interaction [358–360]. At the recombination-independent combined scintillation and ionisation energy scale of ER interactions (cf. Equation 2.6, Chapter 2), we can write:

$$\sigma_n = \sqrt{Fn} \quad . \tag{6.3}$$

This expression is related to the (intrinsic) energy resolution of an ideal detector at energy E (Fano limit [180]):

$$\frac{\sigma_E}{E} = \frac{\sigma_n}{n} \quad . \tag{6.4}$$

Using Equation 2.6, Chapter 2, we obtain

$$\sigma_E = \sqrt{FEW} \quad . \tag{6.5}$$

Thus, for a measured energy resolution, the Fano factor can be determined based on W [361], and a lower value of W would imply a higher Fano factor.

Due to these implications, the deviation of the found W-value of almost 20 % from other low-energy measurements is important for modelling the response of LXe detectors and such measurements provide valuable input to e.g. NEST.

Chapter 7

Cryogenics and Mechanics for Xenoscope

As mentioned in Chapter 3, Section 3.3, the realisation of DARWIN requires the demonstration of a series of technologies at the 2.6 m drift scale. For this reason, we designed, built and commissioned Xenoscope, a full-scale vertical demonstrator [284]. The main goal of Xenoscope is to demonstrate directly, for the first time, an electron drift over a 2.6 m distance in a LXe. Other objectives are the measurement of the transverse and longitudinal diffusion of the electron cloud during the drift, leading to wider S2 signals in space and time, and the investigation of the optical parameters of LXe, such as the Rayleigh scattering length and the index of refraction. In addition, Xenoscope will be available to the entire DARWIN collaboration for full-scale tests of subsystems that will be installed in the future DARWIN experiment.

7.1 Overview of Xenoscope

Xenoscope, shown schematically in Figure 7.1, was constructed and assembled in the high-bay area of the assembly hall of the Department of Physics at UZH. The facility is designed to accommodate a full DARWIN-height TPC in a double-walled cylindrical stainless steel cryostat, capable to contain a maximum of 450 kg of LXe. The target operational mass is $350-400$ kg. The cryogenic system further consists of a cooling tower, a heat exchanger system and a liquid recuperation system. The cooling tower at the top of the cryostat houses a pulse tube refrigerator (PTR) that provides a constant cooling power to a copper cold head on which the xenon condenses. An electrical heater on the cold head controlled by a PID (proportional-integral-derivative) controller keeps it at a constant set temperature. The heat exchanger system allows for high recirculation rates of the xenon through a purification loop at room temperature at a minimal heat leakage. The liquid recuperation system allows to drain the xenon in liquid form into a pressure vessel that can store the full xenon inventory at room temperature. This system is complemented by a gas recuperation system into which gas xenon can be transferred by cryogenic pumping. The gas handling system can be divided into two parts: a main gas handling and purification system which allows for xenon filling from and recuperation to the storage systems, and for gas purification through a hot metal getter and a secondary safety and filtration gas system for automatic emergency recuperation and xenon filtration. The entire system is housed and supported by a structure which is constructed with extruded aluminium profiles. The structure has three main sections: the inner frame that sustains the cryostat, the outer frame that supports the inner frame laterally and provides a top platform for easy access and the stairs assembly. Additional structures support the heat exchanger system and the gas recovery and storage system.

The detector is constructed in three stages which also define the LXe purity measurement campaign. In the first stage, electrons, produced by the flash of a xenon lamp onto a photocathode, will be drifted in a 525 mm long purity monitor fully immersed in LXe. This detector only reads the drifting charge from the induced current in the electrodes at the bottom and at the top. The electron lifetime can be inferred from a comparison of the induced charges at the beginning and at the end of

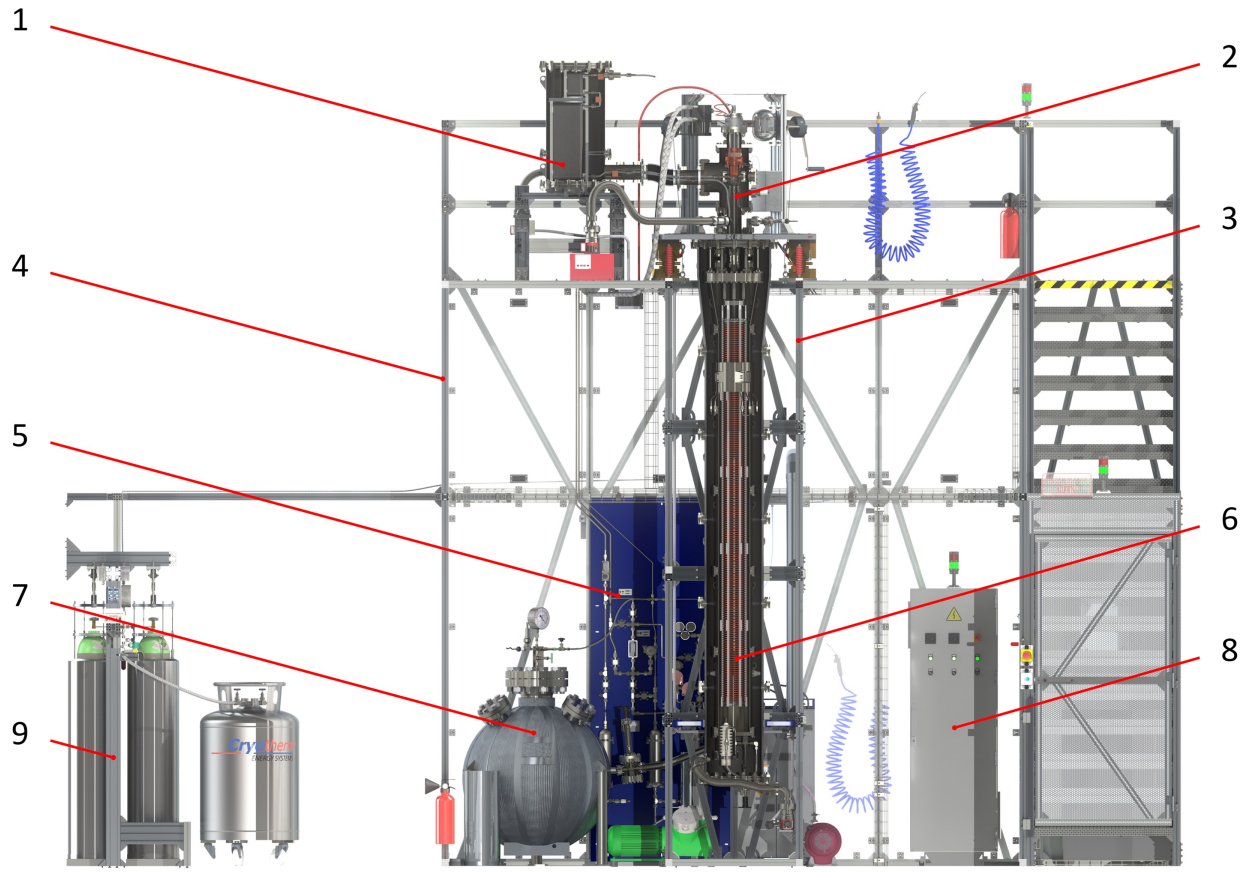

Figure 7.1: Schematic view of the full-scale vertical demonstrator Xenoscope with the 2.6 m TPC installed in the cryostat [284]. **Legend:** 1 – Heat exchangers, 2 – Cooling tower on top of levelling system, 3 – Inner frame, 4 – Outer frame, 5 – Purification gas panel, 6 – TPC inside double-walled cryostat, 7 – High-pressure storage vessel of liquid recovery system, 8 – Power distribution cabinet, 9 – Gas recovery and storage system.

the drift. In the second stage, the purity monitor will be extended to 1 m drift length and transformed into a dual-phase TPC by adding a liquid level control and an S2 signal amplification region. This will allow for the extraction of electrons from the liquid into the gaseous phase. An array of SiPMs will be placed at the top to detect the resulting proportional light signal. Finally the dual-phase TPC will be extended to its full length of 2.6 m.

In this chapter we discuss the following subsystems in detail: the cryostat levelling system in Section 7.2, the heat exchanger system in Section 7.3, the filtration and safety gas system in Section 7.4 and the two recuperation and storage systems 7.5. A complete overview of Xenoscope can be found in Reference [15], where all other mechanic, cryogenic and gas handling subsystems are addressed. Reference [362] contains the detector design of the purity monitor and the TPC phases.

7.2 Cryostat Levelling System

To ensure a uniform amplification of the ionisation signal in the TPC phases, as well as to prevent large radial forces onto the cryostat and its flanges, the xenon liquid-gas interface must be parallel to the gate and anode meshes. For this purpose, we engineered and commissioned a sophisticated fine adjustment levelling system. To protect this invention, it was registered as a utility model at the German Patent and Trade Mark Office. Reviews of the latter and the Swiss Federal Institute of

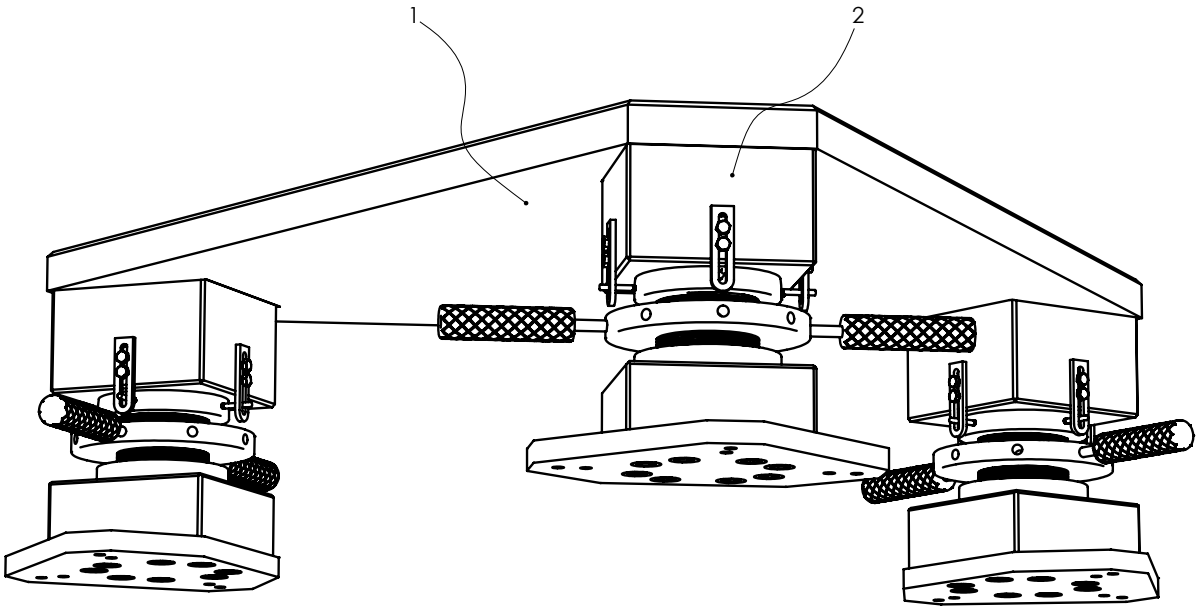

Figure 7.2: Tripod levelling assembly of Xenoscope. **Legend:** 1 – Top plate, 2 – Levelling leg. The drawing shows a simplified and modified version of the actual assembly from the utility model registration and does not contain e.g. the top flange and the cryostat.

Intellectual Property confirmed its novelty.

The top flange of the cryostat is bolted to the underside of a 40 mm aluminium-magnesium alloy triangular top plate supported symmetrically by three levelling legs that together constitute the levelling assembly, see Figure 7.2. The legs rest on three weight-bearing profiles of the inner frame. The full weight of the xenon-filled cryostat is $\sim 1.2\,\mathrm{t}$. The cryostat is placed in the centre of gravity of the equilateral triangle that the legs form. The legs and the top plate are decoupled by three 25 mm thick polyurethane vibration damping plates from BIBUS AG [363] to reduce the transmission of vibrations onto the detector, which can potentially be produced from instrumentation attached to the support structure. These dampers guarantee an isolation of $50 - 90\,\%$ for excitation frequencies in the range $25 - 50\,\mathrm{Hz}$ and $> 90\,\%$ for frequencies higher than 50 Hz [364]. The core of the levelling assembly are the levelling legs, shown in Figure 7.3. Each leg is composed by four major components: a central compression spring, a dual counter-rotating M92 fine thread screw and a hemispherical ball joint that are concentrically aligned, as well as a bottom fixation plate that permits lateral displacement.

The fine thread screw sits in a bottom block on one side and in the hemispherical dome of the ball joint on the other. The dome is mated with a corresponding cavity in the top block. This joint provides a maximum tilting angle of 5° between the central axes of the dome and the top block. A steel chain between the bottom and top block ensures that the top block does not lift off the dome. Two small orthogonal pins on the equator, positioned at an angle of 90° from each other, are guided by forks on the top block. This ensures that the dome does not rotate inside the cavity while the screw is turned. The spring is compressed between the top and bottom blocks, guided by an outer central tube and inner rods at both ends to prevent it from buckling. The bottom block is firmly bolted to the 10 mm thick stainless steel fixation plate, which is itself bolted on top of the inner frame of the support structure. While levelling, the fixation plate allows for a concentric displacement of the legs of $\pm 3\,\mathrm{mm}$.

The full weight of the filled cryostat rests on the three central springs of the legs, each with a spring constant of $100.8\,\mathrm{N/mm}$ and custom-made by Egli Federnfabrik AG [365]. The counter-rotating fine thread screws with a slope of 0.75 mm per turn make for an almost force-free fine adjustment, relieving

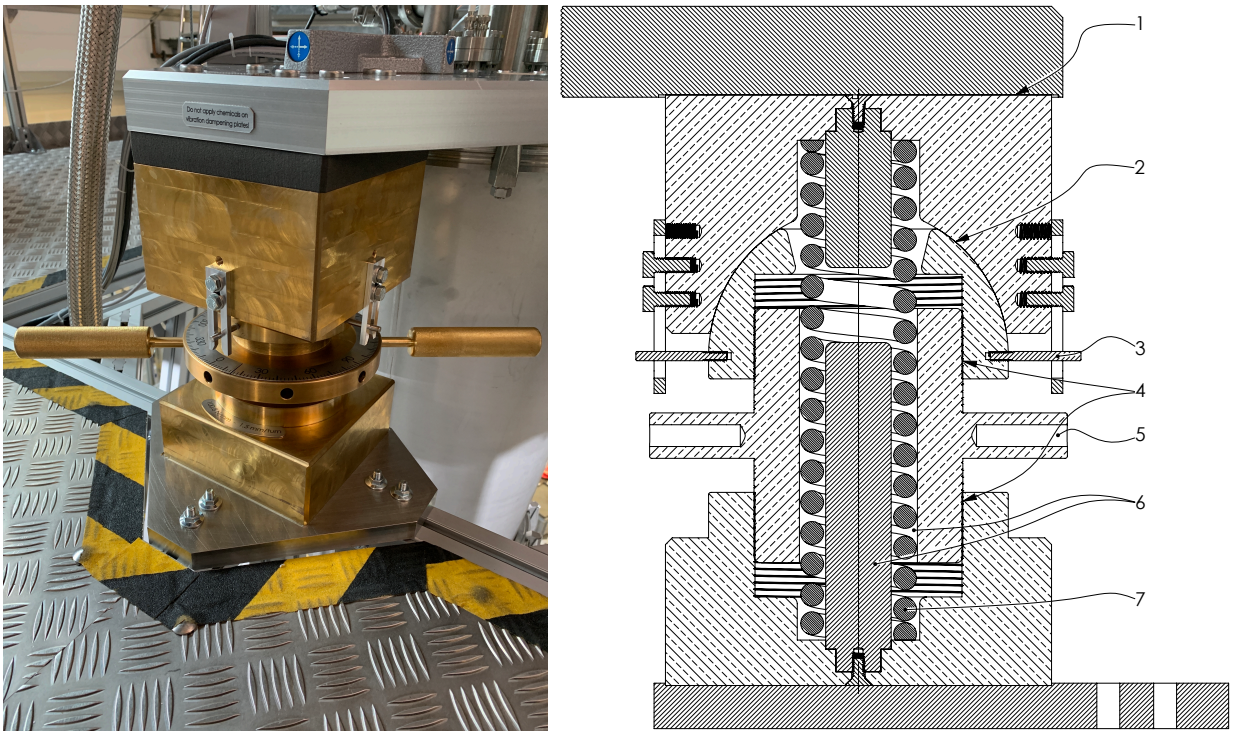

Figure 7.3: Levelling leg. **Left:** Photograph. **Right:** Cross-sectional view. **Legend:** 1 – Lateral bearing, 2 – Ball joint, 3 – Rotation and lifting lockout, 4 – Counter-rotating fine thread, 5 – Mechanical coupling for rotary motion, 6 – Inner rods and central tube, 7 – Compression spring. The drawing shows a modified version of the actual assembly from the utility model registration. For Xenoscope the lateral bearing was realised in between the bottom plate and the leg, and the lifting logout is realised by a steel chain.

with ease up to 80 kg from each spring. As the major load is carried by the springs, the fine thread stays functional at any time and is easy to turn by hand with short lever arms. Moreover, as the coupling of the bottom and top block is not rigid, and as almost the entire weight rests on the spring, we expect an additional vibration decoupling. The hemispherical joint, together with the concentric degree of freedom given by the fixture plate, allow for a fine horizontal levelling with a precision of $< 60\,\mu m/m$, and accordingly, a precise vertical levelling of the cryostat assembly. This precision corresponds to the ability of the operator to turn the fine thread screw in steps smaller than 1/32 of a full turn. The geometry of the legs and the configuration of the springs allow us to level masses up to ~ 700 kg per leg. The ball joint and the thread parts are made from brass, a soft metal, which ensures a smooth motion of the rotating and sliding components. As lubricant, a PTFE-based spray is applied.

The operational reliability was demonstrated in a controlled test on a single leg with a mass of 250 kg before installation, followed by the successful operation of the full assembly in place on the detector during the levelling procedure of the cryostat. The precision was confirmed with a cross-spirit level with a resolution of $50\,\mu m/m$. The cryostat could be levelled by hand in such a way that the divisions of the spirit level were sampled step by step in both dimensions.

7.3 Heat Exchanger System

In spite of the recent development of LXe recirculation and purification systems [366], the removal of impurities in the gas phase is still required. The growth of LXe detectors to multi-tonne scale and the resulting requirement to recirculate the GXe at high speeds have made the use of heat exchangers

indispensable [367–369]. Heat exchangers with high efficiencies minimise the heat leak from cold outgoing and warm incoming GXe and thus allow for the purification of high amounts of xenon in the gaseous phase in short time periods. This is necessary as the cooling power of commercially available PTRs is limited. For Xenoscope, we use an Iwatani Corporation PTR [370], model PC-150, rated to $\sim 200\,\mathrm{W}$ at 165 K. Based on this cooling power and the heat budget of the entire cryogenic system, we define the requirements on the heat exchanger system and derive the sizing parameters from a simple model that lead to the final realisation for the Xenoscope. Its performance is evaluated with data from the commissioning run of the facility. All gas properties used here and subsequently are based on Reference [191].

7.3.1 Heat Budget of the Cryogenic System

Three main contributions of heat transfer onto the cryogenic system can be identified: Thermal radiation onto all cold parts of the system is, due to its quartic temperature dependence, the dominant heat transfer process. Such radiative losses can be shielded efficiently with multi-layer insulation (MLI). However, reflection inefficiencies and imperfect coverage cause radiation input onto the cold parts. Another process of heat transfer is thermal conduction via connections between the cold inner and warm outer parts of the system. Such connections are indispensable for structural reasons or serve process-relevant purposes. They can be minimised in number and cross-section or decoupled by materials with a low heat conduction coefficient. Thermal convection and conduction by means of residual air between the cold inner and warm outer parts of the system can be assumed to be negligible due to the presence of a good insulation vacuum of $\mathcal{O}(10^{-6} - 10^{-5}\,\mathrm{mbar})$. Good vacuum is also required for a high efficiency of the MLI. However, when recirculating through the purification loop, a third main heat leak is given by the inefficiency of the heat exchange process. In order to set the design requirements for the heat exchanger system later, we need to define the allowable heat input onto the system caused by recirculation, based on the available cooling power and the other heat contributions.

We start with an estimation of the radiative heat input. To be conservative, we assume that all parts of the system which are cold during operation, i.e. the inner vessel, the cooling tower, the umbilical section and the heat exchangers, are at a temperature of 170 K and that the temperature in the laboratory is high at 303 K such that the temperature difference between cold inner and warm outer surfaces is $\Delta T := T_{\mathrm{out}} - T_{\mathrm{in}} = 133\,\mathrm{K}$. The radiation power onto the cold inner parts of the system can be estimated applying the Stefan-Boltzmann law on enclosed surfaces [371, 372]:

$$P_{\mathrm{rad}} = \frac{\sigma\left(T_{\mathrm{out}}^4 - T_{\mathrm{in}}^4\right)}{\frac{1-\varepsilon_{\mathrm{out}}}{\varepsilon_{\mathrm{out}} A_{\mathrm{out}}} + \frac{1-\varepsilon_{\mathrm{in}}}{\varepsilon_{\mathrm{in}} A_{\mathrm{in}}} + \frac{1}{A_{\mathrm{out}} F_{\mathrm{out}\to\mathrm{in}}}} \quad , \tag{7.1}$$

and using Kirchhoff's law of thermal radiation. Here, we denote emissivities by ε and surface areas by A, while σ is the Stefan-Boltzmann constant. We further denote the view factor from the outer to the inner surface, i.e. the fraction of radiation that is irradiated by the outer surface and that strikes the inner one, by $F_{\mathrm{out}\to\mathrm{in}}$. Since the inner surfaces are typically convex like the cylindrical inner vessel, we can approximate $F_{\mathrm{in}\to\mathrm{out}} = 1$. Applying the reciprocity relation of view factors, $A_{\mathrm{out}} F_{\mathrm{out}\to\mathrm{in}} = A_{\mathrm{in}} F_{\mathrm{in}\to\mathrm{out}}$, we can simplify Equation 7.1:

$$P_{\mathrm{rad}} = \frac{\sigma A_{\mathrm{in}}\left(T_{\mathrm{out}}^4 - T_{\mathrm{in}}^4\right)}{\frac{1-\varepsilon_{\mathrm{out}}}{\varepsilon_{\mathrm{out}}}\frac{A_{\mathrm{in}}}{A_{\mathrm{out}}} + \frac{1}{\varepsilon_{\mathrm{in}}}} \quad . \tag{7.2}$$

Note that the emissivity depends on the material, surface finish and the temperature. Metal surfaces typically feature an emissivity lower than 1, decreasing with temperature. However, to obtain a conservative estimate, we assume the outer surface to be a perfect black body with $\varepsilon_{\mathrm{out}} = 1$ in which case Equation 7.2 reduces to:

$$P_{\mathrm{rad}} = \sigma \varepsilon_{\mathrm{in}} A_{\mathrm{in}}\left(T_{\mathrm{out}}^4 - T_{\mathrm{in}}^4\right) \quad . \tag{7.3}$$

We can now use the parameter ε_{in} as measure of the mean inefficiency of the radiation shielding. By this we can accommodate for non-perfect coverage of the MLI, finite number of applied layers, potential direct thermal contact of MLI layers and non-perfect reflectivity of the surfaces. We assume conservatively $\varepsilon_{\text{in}} = 0.03$, see References [371, 373, 374] for studies on MLI efficiency. The inner cold surfaces can be estimated to be $< 6\,\text{m}^2$. This yields a maximum radiation input of $P_{\text{rad}} = 80\,\text{W}$.

We continue with the estimation of the heat input by thermal conduction. Most of the direct contacts of inner and outer surfaces, like on the heat exchanger holder or the cryostat centring arms at the bottom of the inner vessel, are decoupled by plastic of high thermal resistance. The only direct metal contacts of inner and outer surfaces are present at the top flange, necessary for suspension of the inner vessel or for process feedthroughs, and at the PTR cold head. The latter can be neglected as this is included in the net cooling power of the PTR. In addition but not intentional, MLI can conduct heat from inner to outer surfaces when in contact with both. We can estimate the total cross-section of the heat conducting surface to be $S = 50\,\text{cm}^2$. For a typical heat conduction length of 0.2 m between the inner and outer top flange and a thermal conductivity of $\lambda_{\text{SS}} = 16.3\,\text{W}/(\text{m}\cdot\text{K})$ for stainless steel (SS) [375], we obtain from

$$P_{\text{cond}} = \lambda_{\text{SS}} S \frac{\Delta T}{d} \tag{7.4}$$

a thermal conduction power input of $P_{\text{cond}} = 54\,\text{W}$.

In total, we obtain in this conservative scenario a cooling power of 134 W which is required for stable operation at zero recirculation flow. The heat dissipation of the internal instrumentation, from for instance photosensors and pre-amplifiers, is typically of the order of a few watt. Based on the available cooling power of 200 W and to keep an additional safety margin, we can thus conclude that a maximum of $\sim 50\,\text{W}$ of cooling power is available to compensate the loss due to recirculation.

7.3.2 Design Requirements

We determine the requirements on the heat exchanger system based on the maximum heat load of our application to justify the design choice presented in the next section. The goal is to supply the cryostat with purified xenon from the recirculation loop in liquid form. To this end, xenon gas at room temperature needs to be cooled down to its boiling point and liquefied. As the LXe in the cryostat is typically kept at its boiling point or only slightly below, there is no need for sub-cooling the supplied liquid.

We consider a closed loop system, i.e. the mass flow through the supply and the return line are equal: $\dot{m}_{\text{Supply}} = \dot{m}_{\text{Return}} =: \dot{m}$. To exploit the highest performance of the xenon purifier, we aim for a gas recirculation flow of at least 70 slpm in the purification loop and set a flow of $r = 100\,\text{slpm}$ as design goal for the calculation here. This corresponds to a mass flow rate of roughly $\dot{m} = 0.01\,\text{kg/s}$. Thus, the available cooling power of 50 W, calculated in the previous section, sets an allowable recirculation heat leak of $\leq 0.5\,\text{W/slpm}$. Of course, this represents only an upper limit and we try to design a system with good performance at moderate size to account for future upgrades of the system that require additional cooling power. For comparison, in a test setup using $\sim 1.5\,\text{kg}$ of LXe a loss of 0.34 W/slpm has been achieved [367].

Configurations with a cascade of two thermally decoupled heat exchangers, one for the phase change and one for the remaining gas-gas exchange, have shown a higher efficiency over single heat exchangers in the cryogenics system of the demonstrator for XENON1T [368]. For this reason, we also split the process into a pure gas warming/cooling step and a gas warming/cooling plus phase change step, see Figure 7.4. For better performance, we consider the xenon flows to be in counter-current arrangement. As opposed to a co-current configuration, this allows for an almost constant temperature difference between the supply and the return line at any point, driving the heat exchange. It also enables us to actually achieve LXe temperature at the supply line outlet and to get close to

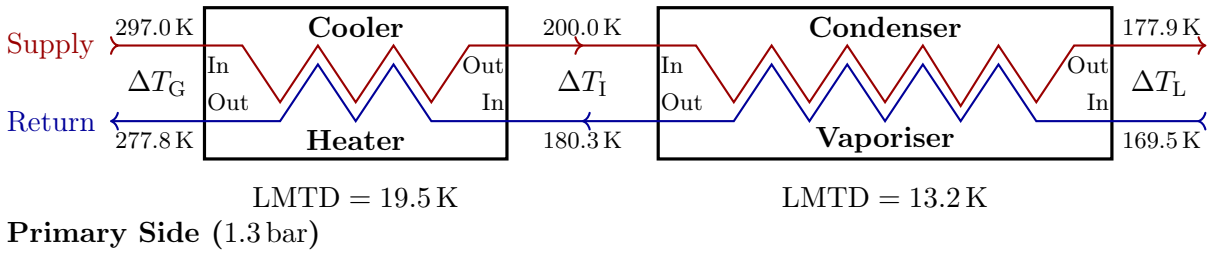

Figure 7.4: Schematic of the heat exchanger cascade in counter-current mode with the temperatures and pressures used in the design calculation.

room temperature at the return line outlet. These will even be equal to the return line and supply line inlet temperatures in the limit of perfect heat exchange.

Small in-line pressure drops over the heat exchangers will only have limited effect on the xenon properties. We thus assume in this design calculation constant pressures throughout the lines and define the desired temperatures at the inlets and outlets. This assumption is justified for large enough tubing and a high number of parallel channels or plates in the heat exchangers. However, over-sizing the number of parallel channels of heat exchangers reduces the pressure drop but also the heat transfer rate for which turbulent flow is required. We assume a pressure of 2.0 bar in the supply line which is the typical operating pressure of dual-phase xenon TPCs and also the design goal for Xenoscope. A typical temperature in the Xenoscope laboratory is 297.0 K which is the assumed temperature at the cooler inlet. We furthermore assume that the gas exits the cooler at 200.0 K before entering the condenser. At 2.0 bar, the boiling point of xenon is at 177.9 K which is the target condenser outlet temperature. As the specific heat capacity of xenon is temperature dependent, we use enthalpy differences ΔH also for cooling/heating processes without phase change. The heat loads for the two steps in the supply line are

$$\dot{Q}_{\mathrm{Cooler}} = \dot{m}\Delta H_{\mathrm{Cooler}} = 158.0\,\mathrm{W} \quad , \qquad \dot{Q}_{\mathrm{Condenser}} = \dot{m}\Delta H_{\mathrm{Condenser}} = 948.3\,\mathrm{W} \quad , \tag{7.5}$$

and, as expected, the exchange of latent heat during the phase transition dominates the heat load of the process. The sum of these heat loads is defined by the assumed typical inlet and outlet temperatures of the supply line at the typical cryostat pressure. However, the distribution of the heat loads on the cooler and condenser, respectively, is determined by the intermediate temperature on the supply line. We would like to remark that this intermediate temperature between the two heat exchangers is desirable as it well separates the phase transition from the gas-gas exchange. However, it was chosen randomly for this example and will, in a real application, be naturally set by the relative heat transfer capacity of the heat exchangers.

As we shall discuss also in the next section, the xenon in the return line inlet is sub-cooled by underpressure for which we assume 1.3 bar in this example calculation. This offset to the supply line outlet temperature drives the heat exchange and makes the phase change process efficient. We assume that the xenon enters at 169.5 K which is the boiling temperature of xenon at 1.3 bar. This choice already defines the efficiency of the heat exchanger system.

If heat is only exchanged between the xenon in the two lines and no heat is lost to the environment, we know that the rate of heat gained by the returning xenon is equal to the rate of heat lost by the supplied xenon. For thermally decoupled heat exchangers, this applies to each of them separately. We obtain, in the ideal loss-less case, for the enthalpy changes of the two sides of the heat exchangers

which are kept at constant pressures:

$$H\left(T^{\text{out}}_{\text{Heater}}\right) - H\left(T^{\text{in}}_{\text{Heater}}\right) = H\left(T^{\text{in}}_{\text{Cooler}}\right) - H\left(T^{\text{out}}_{\text{Cooler}}\right) \quad , \tag{7.6}$$

$$H\left(T^{\text{out}}_{\text{Vaporiser}}\right) - H\left(T^{\text{in}}_{\text{Vaporiser}}\right) = H\left(T^{\text{in}}_{\text{Condenser}}\right) - H\left(T^{\text{out}}_{\text{Condenser}}\right) \quad . \tag{7.7}$$

Hence, using the corresponding enthalpy values, we can determine the temperature at the exit of the vaporiser and the heater to be 180.3 K and 277.8 K, respectively. In summary, we deduced the remaining temperatures on the return line based on energy conservation. The example was fully defined by the temperatures and the pressure on the supply line, and the assumption that the xenon at the vaporiser inlet is at the boiling temperature at the respective pressure.

Based on the above, we have a temperature difference of $\Delta T_{\text{G}} = 19.2\,\text{K}$ between the gas inlet and outlet of the heat exchanger system. This determines the heat leak of the heat exchangers. We can derive a loss of

$$\frac{\dot{m}\Delta H_{\text{G}}}{r} = 0.28\,\text{W/slpm} \tag{7.8}$$

in this particular scenario which is within the requirement of $\leq 0.5\,\text{W/slpm}$ and even surpasses the heat exchanger system in Reference [367]. We can assign an efficiency to this process by relating this loss to the heat load of the heat exchange:

$$\varepsilon_{\text{Total}} \coloneqq 1 - \frac{\dot{m}\Delta H_{\text{G}}}{\dot{Q}_{\text{Cooler}} + \dot{Q}_{\text{Condenser}}} = 97.4\,\% \quad . \tag{7.9}$$

Note that we could have calculated the efficiency already with the temperature and pressure values on the liquid side. However, in a real application it is usually more practical to measure the temperatures and pressures on the gas side. We can define another measure of efficiency. Here, we follow the definitions and derivations in Reference [376]. Let us consider the ideal case of our model in which the outlet temperature of the supply fluid reaches the inlet temperature of the return fluid and vice versa. The maximum possible heat transfer rate in the two heat exchangers is therefore:

$$\dot{Q}^{\text{max}}_{\text{Cooler}} = \dot{m}\left(H(T^{\text{in}}_{\text{Cooler}}) - H(T^{\text{in}}_{\text{Heater}})\right) \quad , \tag{7.10}$$

$$\dot{Q}^{\text{max}}_{\text{Condenser}} = \dot{m}\left(H(T^{\text{in}}_{\text{Condenser}}) - H(T^{\text{in}}_{\text{Vaporiser}})\right) \quad . \tag{7.11}$$

The effectiveness of the heat exchangers, a dimensionless quantity with values between 0 and 1, is defined as the ratio of the actual heat transfer rates to the maximum possible ones, $\epsilon \coloneqq \frac{\dot{Q}^{\text{act}}}{\dot{Q}^{\text{max}}}$:

$$\epsilon_{\text{Cooler}} = \frac{H(T^{\text{in}}_{\text{Cooler}}) - H(T^{\text{out}}_{\text{Cooler}})}{H(T^{\text{in}}_{\text{Cooler}}) - H(T^{\text{in}}_{\text{Heater}})} = 84.8\,\% \quad , \tag{7.12}$$

$$\epsilon_{\text{Condenser}} = \frac{H(T^{\text{in}}_{\text{Condenser}}) - H(T^{\text{out}}_{\text{Condenser}})}{H(T^{\text{in}}_{\text{Condenser}}) - H(T^{\text{in}}_{\text{Vaporiser}})} = 97.1\,\% \quad . \tag{7.13}$$

Accordingly, we can calculate the overall effectiveness of the heat exchanger cascade to be

$$\epsilon_{\text{Total}} = \frac{H(T^{\text{in}}_{\text{Cooler}}) - H(T^{\text{out}}_{\text{Condenser}})}{H(T^{\text{in}}_{\text{Cooler}}) - H(T^{\text{in}}_{\text{Vaporiser}})} = \frac{H(T^{\text{out}}_{\text{Heater}}) - H(T^{\text{in}}_{\text{Vaporiser}})}{H(T^{\text{in}}_{\text{Cooler}}) - H(T^{\text{in}}_{\text{Vaporiser}})} = 97.5\,\% \quad . \tag{7.14}$$

This value is close to the efficiency calculated above in Equation 7.9 which can be shown to be a slightly different ratio of heat powers:

$$\varepsilon_{\text{Total}} = \frac{H(T^{\text{out}}_{\text{Heater}}) - H(T^{\text{out}}_{\text{Condenser}})}{H(T^{\text{in}}_{\text{Cooler}}) - H(T^{\text{out}}_{\text{Condenser}})} \quad . \tag{7.15}$$

However, the quantity effectiveness can also be interpreted as a measure of the efficiency of the heat exchange.

The described example is a good model of the thermodynamic situation expected in Xenoscope and thus defines our design goal. Next, we calculate the required heat exchanger design characteristics for both steps. First, we need to define the mean overall heat transfer coefficient k. It consists of the mean values of the heat transfer coefficients between the fluid and the heat transfer surface on both sides α_{Supply}, α_{Return}, of the thermal conductivity λ and the thickness d of the heat transfer surface, and of the fouling resistance R_f:

$$\frac{1}{k} \coloneqq \frac{1}{\alpha_{\text{Supply}}} + \frac{1}{\alpha_{\text{Return}}} + \frac{d}{\lambda} + R_f =: \frac{1}{k_{\text{C}}} + R_f \quad . \tag{7.16}$$

The fouling resistance accounts for surface degradation due to oxide or debris layers. These typically have a lower thermal conductivity than the transfer surface itself. With k_{C} we denote the clean mean overall heat transfer coefficient. One can then define the design margin as:

$$M \coloneqq \frac{k_{\text{C}} - k}{k} \quad . \tag{7.17}$$

LMTD Method

If we assume the mean overall heat transfer coefficient, the exchange surface and the specific heat capacities to be constant along the direction of heat exchange as well as constant with temperature and pressure, we can approximate the heat exchanger problem well by means of the log mean temperature difference (LMTD):

$$\text{LMTD}_{\text{Cooler}} \coloneqq \frac{\Delta T_{\text{G}} - \Delta T_{\text{I}}}{\ln \frac{\Delta T_{\text{G}}}{\Delta T_{\text{I}}}} \quad , \qquad \text{LMTD}_{\text{Condenser}} \coloneqq \frac{\Delta T_{\text{I}} - \Delta T_{\text{L}}}{\ln \frac{\Delta T_{\text{I}}}{\Delta T_{\text{L}}}} \quad . \tag{7.18}$$

We denote the temperature differences on the gas, intermediate and liquid side of the heat exchangers in order by $\Delta T_{\text{G}}, \Delta T_{\text{I}}, \Delta T_{\text{L}}$, cf. Figure 7.4. This approach is valid also for phase changes, i.e. for the case that the temperature of one of the fluids stays constant for at least parts of the process [377]. The LMTD is well-defined if the temperature differences on the two heat exchanger sides are not identical. If this is not the case, one defines the LMTD to be equal to the temperature difference of either of the two sides. The product of the mean overall heat transfer coefficients and the heat exchange areas of the two heat exchangers can then be calculated from

$$(k \cdot A)_{\text{Cooler}} = \frac{\dot{Q}_{\text{Cooler}}}{\text{LMTD}_{\text{Cooler}}} \quad , \qquad (k \cdot A)_{\text{Condenser}} = \frac{\dot{Q}_{\text{Condenser}}}{\text{LMTD}_{\text{Condenser}}} \quad . \tag{7.19}$$

From Equations 7.5, 7.18 and the latter equation, and the assumed temperatures at the inlets and outlets of the heat exchangers, we obtain $(k \cdot A)_{\text{Cooler}} = 8.1\,\text{W/K}$ and $(k \cdot A)_{\text{Condenser}} = 71.6\,\text{W/K}$, respectively.

Effectiveness-NTU Method

An alternative approach that is used when the available temperature information is insufficient to apply the LMTD method is based on the dimensionless size parameter number of transfer units (NTU) which is defined as:

$$\text{NTU} \coloneqq \frac{k \cdot A}{\dot{C}_{\text{min}}} \quad . \tag{7.20}$$

Here, we used the minimum heat capacity rate which is defined as:

$$\dot{C}_{\text{min}} \coloneqq \dot{m} \cdot \min\left(c_{p,\,\text{Supply}}, c_{p,\,\text{Return}}\right) \tag{7.21}$$

with c_p being the specific heat capacity of xenon at constant pressure. One can show the following relationship of NTU to the effectiveness of a counter-current heat exchanger [376]:

$$\epsilon = \frac{1 - e^{-\mathrm{NTU}(1-R)}}{1 - R \cdot e^{-\mathrm{NTU}(1-R)}} \quad , \tag{7.22}$$

where $R = \dot{C}_{\mathrm{min}}/\dot{C}_{\mathrm{max}}$ is the heat capacity rate ratio. The gas-gas exchange process in the cooler/heater is almost balanced with $R = 0.995$. Using its effectiveness calculated above, we obtain $\mathrm{NTU}_{\mathrm{Cooler}} = 5.5$. Applying the definition of NTU from Equation 7.20, we obtain $(k \cdot A)_{\mathrm{Cooler}} = 8.9\,\mathrm{W/K}$, close to the result of the LMTD method.

If a fluid undergoes a phase transition, we can assign an infinite heat capacity to it while latent heat is exchanged and the temperature of the fluid stays constant. Hence, $R = 0$ and the above equation is reduced to

$$\epsilon = 1 - e^{-\mathrm{NTU}} \quad . \tag{7.23}$$

However, unlike for the gas-gas exchange, we cannot use the definition of NTU for a pure phase change in order to obtain a result for $k \cdot A$, because it involves the minimum heat capacity rate $\dot{C}_{\mathrm{min}}$. Hence, splitting the heat exchange in the condenser in a pure gas-gas exchange and a pure phase transition process is not accessible with the $\epsilon - \mathrm{NTU}$ method. Although being a mixed process, it is dominated by the phase transition and we can still use the latter equation to estimate the NTU. Thus, we obtain for the condenser $\mathrm{NTU}_{\mathrm{Condenser}} = 3.5$. To perform the translation into $k \cdot A$, we use an averaged approach by means of the following heat capacities:

$$c_{p,\,\mathrm{Supply}} = \frac{H(T^{\mathrm{in}}_{\mathrm{Condenser}}) - H(T^{\mathrm{out}}_{\mathrm{Condenser}})}{T^{\mathrm{in}}_{\mathrm{Condenser}} - T^{\mathrm{out}}_{\mathrm{Condenser}}} = 4.4\,\mathrm{kJ/(kg \cdot K)} \quad , \tag{7.24}$$

$$c_{p,\,\mathrm{Return}} = \frac{H(T^{\mathrm{out}}_{\mathrm{Vaporiser}}) - H(T^{\mathrm{in}}_{\mathrm{Vaporiser}})}{T^{\mathrm{out}}_{\mathrm{Vaporiser}} - T^{\mathrm{in}}_{\mathrm{Vaporiser}}} = 9.0\,\mathrm{kJ/(kg \cdot K)} \quad . \tag{7.25}$$

These values include the discontinuous step of the enthalpy during phase transition. Using $\dot{C}_{\mathrm{min}} = \dot{m} c_{p,\,\mathrm{Supply}}$, we obtain from the NTU definition for the condenser $(k \cdot A)_{\mathrm{Condenser}} = 151.8\,\mathrm{W/K}$. Due to our rough approximation of the heat exchange process, this value is twice as high as calculated with the LMTD method. However, it still provides a good figure of merit. For completeness, we want to mention that, in the absence of phase change, both methods are connected by the relation

$$\mathrm{NTU}_{\mathrm{Cooler}} = \frac{T^{\mathrm{in}}_{\mathrm{Cooler}} - T^{\mathrm{out}}_{\mathrm{Cooler}}}{\mathrm{LMTD}_{\mathrm{Cooler}}} \tag{7.26}$$

for the case of the cooler.

7.3.3 Setup

A cascade of two brazed stainless-steel plate heat exchangers, made by Kelvion Holding GmbH [378], is connected to the cooling tower via a flexible umbilical section. The two heat exchangers, installed in series as seen in Figure 7.5, have respectively a heat exchange area of $4.602\,\mathrm{m}^2$ (Model GVH 500H-80) and $0.646\,\mathrm{m}^2$ (Model GVH 300H-40) and are operated in counter-current mode. The supply line is on the secondary side of the heat exchangers with 40 and 20 channels, respectively, while the return line is on the primary side with 39 and 19 channels. The primary channels are the inner channels, while the first and last channel is on the secondary side. For our application, the manufacturer quotes a mean overall heat transfer coefficient of $42\,\mathrm{W/(m^2 \cdot K)}$ for the primary and $36\,\mathrm{W/(m^2 \cdot K)}$ for the secondary side of the large and $21\,\mathrm{W/(m^2 \cdot K)}$ for the primary and $18\,\mathrm{W/(m^2 \cdot K)}$ for the secondary side of the small heat exchanger. Thus, on the supply line, the cooler provides $(k \cdot A)_{\mathrm{Cooler}} = 11.6\,\mathrm{W/K}$ while

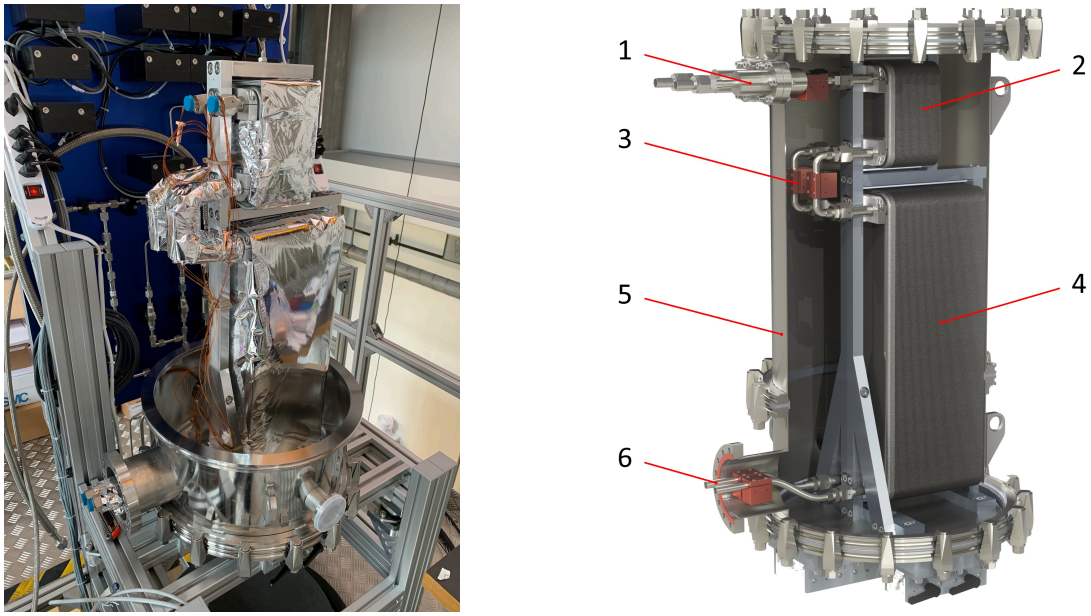

Figure 7.5: Heat exchanger cascade of Xenoscope in a ISO-K-400 vacuum chamber. **Left:** Photograph of the heat exchangers wrapped in MLI after installation. **Right:** Rendering. **Legend:** 1 – Gas inlet/outlet, 2 – Cooler/heater, 3 –Temperature sensors (6×), 4 – Condenser/vaporiser, 5 – Vacuum chamber, 6 –Liquid inlet/outlet.

the condenser provides $(k \cdot A)_{\text{Condenser}} = 165.7\,\text{W/K}$. In the view of the previous section where we derived with two methods required values of $8.1-8.9\,\text{W/K}$ and $71.6-151.8\,\text{W/K}$, respectively, we can conclude that the configuration is well-sized to reach the design goal. The experienced manufacturer performed more precise calculations as to the sizing of the heat exchanger models for our application than presented here. According to these, the configuration has a combined heat exchange power of $P_{\text{HE}} = P_{\text{Cooler}} + P_{\text{Condenser}} = 0.4\,\text{kW} + 1.1\,\text{kW} = 1.5\,\text{kW}$ for our use case. This allows for high recirculation rates through the purification loop with minimal heat loss in the cryostat. The mean overall heat transfer coefficients include small fouling resistances due to corrosion which are of course minimal if xenon is used as fluid. The respective design margins are 12.1 % for the small and 18.9 % for the large heat exchanger.

The heat exchangers are installed inside a ISO-K-400 vacuum vessel. To ease assembly and adapt to movements of the levelling assembly, the position of the vacuum chamber is adjustable both in height and distance, relative to the cooling tower. In addition, the entire heat exchanger cryostat rests on damping mounts from BIBUS AG [363] to reduce the transmission of possible vibrations onto the heat exchangers and the cooling tower, and the sensitive equipment inside. Large contact surfaces, bolts and washers inside the cryostat are vented to reduce virtual leakage. To minimise heat conduction over the inner holding structure, the heat exchangers are decoupled by plastic blocks at the attachment points on the fittings and on the back. To insulate against thermal radiation, the heat exchangers are enclosed in 20 layers of MLI of 12 µm thick polyester sheets, aluminised at 400 Å on both sides. The layers are perforated for use in vacuum with an open area of $0.05-0.1$ %. Each layer is separated by a layer of non-woven polyester spacer at $14-15\,\text{g/m}^2$. The MLI was produced by RUAG Space GmbH [379]. More details on the MLI can be found in Reference [15]. Before installation, both heat exchangers were flushed with deionised water and soap, rinsed and dried with ethanol. They were then baked out for over a week at temperatures up to 180 °C in order to efficiently remove liquids and outgassing vapours.

Recirculation through the purification loop is performed by removing xenon from the top of the liquid phase with an underpressure, relative to the cryostat pressure, created by the xenon compressor

in the return line. The reduced pressure reduces the boiling temperature of the liquid, induces a phase-change from liquid to gas and lowers the temperature of the latter by expansion. This creates a temperature gradient with the counter-flow in the supply line which is necessary for an efficient heat exchange process and crucial for phase changes that naturally happen at zero temperature difference [368]. The xenon is sent through the vacuum-insulated umbilical connection to the heat exchanger system. It passes through the larger vaporiser where, depending on the recirculation flow, some xenon accumulates in liquid form, and then through the smaller heater, which produces the remaining gas-gas heat exchange. Concurrently, on its way back from the purification loop in the supply line, the xenon is pre-cooled in the smaller heat exchanger and condensed in the larger one. As we shall see in Section 7.3.4, the condensation actually takes place inside the umbilical connection for the entire tested flow range. The purified xenon enters the cooling tower and is reintroduced at the very bottom of the inner vessel. Extraction from the top and re-introduction at the bottom induces a natural upward convection in the cryostat, ensuring that all the xenon is purified. For performance monitoring, a total of six PT100 resistance temperature detectors are installed in copper housings, in thermal contact with the heat exchanger connections, as shown in Figure 7.5, right.

7.3.4 Performance

Benchmarking Xenoscope during a 40 day commissioning run with 80.66 kg of xenon included the determination of the efficiency of the heat exchange and the evaluation of constant and flow-dependent heat leaks. For all the presented tests, we assume, like for the design calculation in Section 7.3.2, that the supply line close to the opening to the cryostat, and in particular throughout the heat exchangers, has the same constant pressure as the cryostat itself, and that all thermodynamical changes are isobaric. The underpressure in the return line cannot be measured directly with the present instrumentation, and no assumptions on its value are made unless stated explicitly. In particular, we do not use the enthalpy information of the liquid in the return line. However, pressure uncertainties on the gas side of the heat exchangers do not impact the results of the presented analysis much: The maximum (minimum) pressure of < 4 bar (> 0.1 bar) in the system is present directly after (before) the xenon compressor with a maximal difference to the cryostat pressure at high (low) flows, see Figure 7.6, left. This difference includes the flow-dependent pressure drop over the getter (flow-controller) on the supply (return) line and the connecting tubing. However, even if the pressure at the cooler inlet (heater outlet) would be equal to the post-pump (pre-pump) pressure, the gas enthalpy would only differ by 0.5 % in both cases [191]. Additionally, we assume that the cooling power is constant, and changes of the insulation vacuum as well as of the laboratory temperature are negligible. The cold head set-point was chosen to be 174.25 K and kept constant for all flows. This results in a flow-dependent cryostat pressure that directly influences the liquid temperature which is at its boiling point. For this particular temperature, the normal operating pressure of ~ 2 bar is obtained at 70 slpm. All measurements were taken in thermal equilibrium if not mentioned otherwise. To this end, the system was allowed to relax for 24 hours after flow changes such that all pressure and temperature parameters stabilised.

Thermal Equilibrium and Gas Enthalpy Change

In Figure 7.6, right, we show the temperature hierarchy of the inlets and outlets of the heat exchangers that follow the expectation. However, in particular at high flow rates, we observed a lower temperature at the condenser outlet than at the vaporiser inlet. This is attributed to the fact that the temperatures are measured on the connecting tubes close to the nozzles of the heat exchangers. Hence, the expansion of the outgoing gas after the temperature sensor would cool down the bottom of the large heat exchanger and in turn lead to a lower measured temperature on the supply line. We observed that the inlet of the cooler, as well as the condenser outlet and vaporiser inlet, became colder at lower

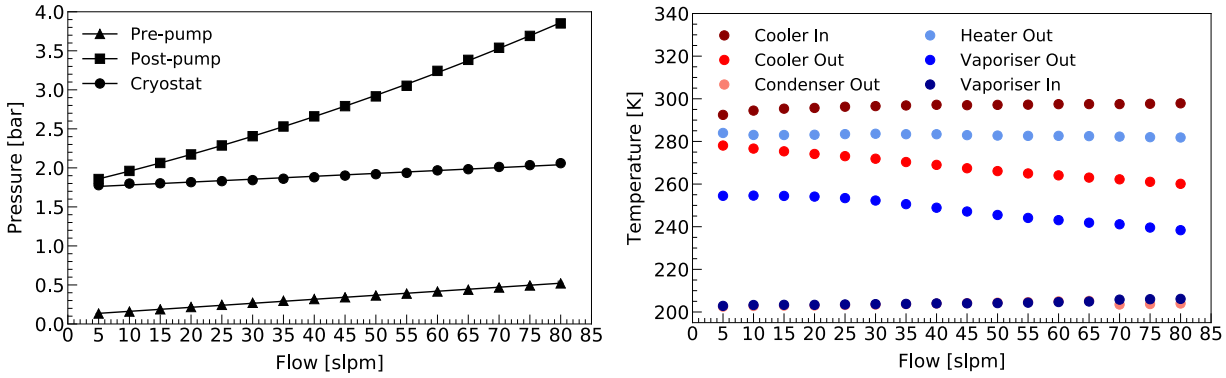

Figure 7.6: Data at 174.25 K cold head temperature set-point. The error bars are smaller than the markers. **Left:** Pressures at the xenon compressor and inside the cryostat for various flow rates. The fit function used for the post-pump pressure is a second order polynomial. **Right:** Temperature hierarchy of the heat exchanger inlets and outlets.

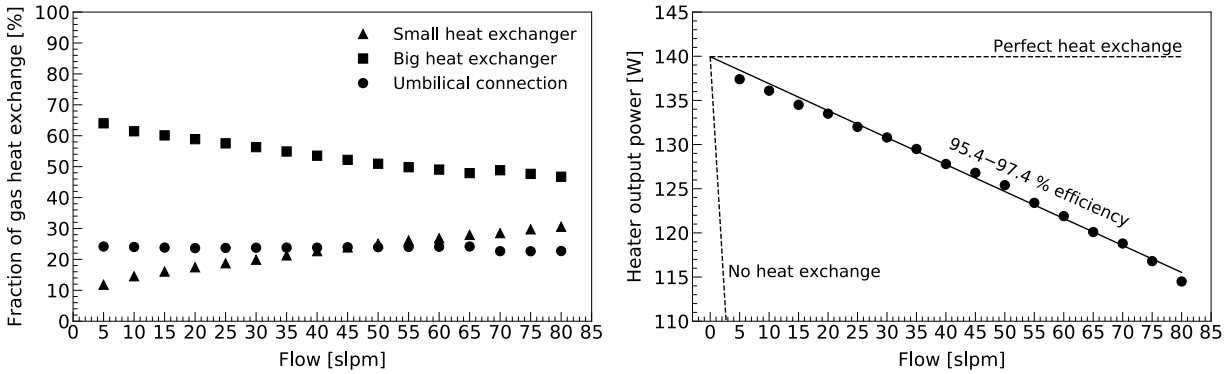

Figure 7.7: Data at 174.25 K cold head temperature set-point. The error bars are smaller than the markers. **Left:** Contribution of the heat exchangers to the gas cooling process. **Right:** Linear decrease of the heater output power with increasing flow rates.

flows. The first is due to the smaller heat input from the recirculation pump and the latter is due to the lower liquid temperature. Temperatures higher than the boiling point of xenon at the respective pressures suggest that the gas in the supply line does not condense inside the heat exchangers. The direct observation of LXe at the end of the supply line through a viewport points to a liquefaction in the umbilical connection, which we attribute to the physical contact of the tight MLI packing between the ingoing and outgoing hose. In fact, this increases the heat exchange efficiency. The contributions of the heat exchangers to the gas-gas exchange can be seen in Figure 7.7, left. Depending on the flow, this process only accounts for $\sim 20\,\%$ of the total isobaric enthalpy change as the majority is inherent to the phase change.

Heat Exchange Efficiency

The determination of the heat exchange efficiency is based on the idea outlined in Reference [368]. Assuming a constant cooling power at a certain cold head temperature set-point, the power output of the electrical heater on the cold head determines the actual required cooling power for steady state operation. Neglecting any constant and flow-dependent heat leaks that emerge when recirculating, a lower limit on the heat exchange efficiency can be calculated from:

$$\eta(r) = 1 - \frac{P(0) - P(r)}{\Delta H \cdot \rho \cdot r} \quad . \tag{7.27}$$

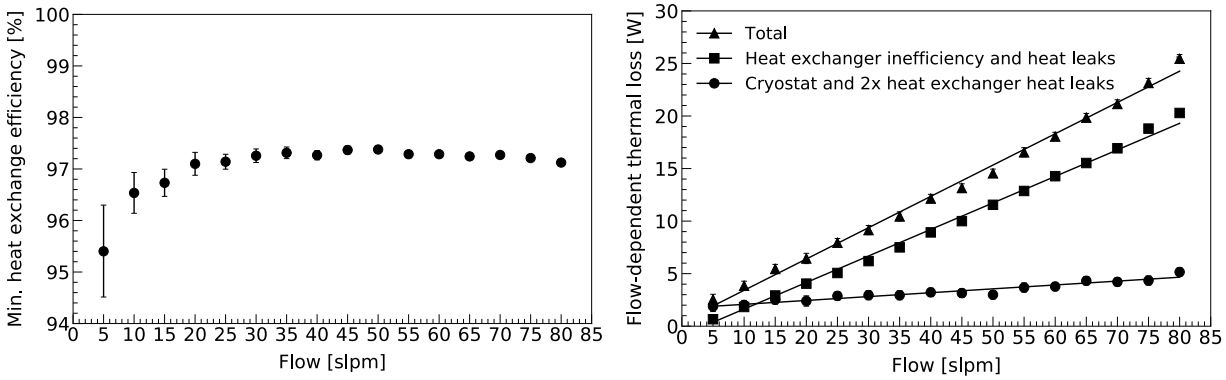

Figure 7.8: Data at 174.25 K cold head temperature set-point. The error bars are partially smaller than the markers. **Left:** Lower limit on the total heat exchange efficiency at various flow rates. **Right:** Flow-dependent thermal losses fitted with linear regressions.

Here, $P(0)$ and $P(r)$ [W] are the power outputs of the heater at zero and some recirculation rate r [slpm], respectively. The enthalpy change of the xenon from liquid at its boiling point to warm gas is denoted by ΔH [W · min/g] and the mass density of xenon under standard conditions by $\rho = 5.8982\,\mathrm{g/l}$. The enthalpy change was calculated individually for all flow rates for the isobaric process of cooling down from the respective cooler inlet temperature to the liquid temperature.

As expected, we obtain a linear heater output that decreases with flow, see Figure 7.7, right. From the linear regression we obtain a slope of $(0.305 \pm 0.007)\,\mathrm{W/slpm}$. This value is well within the requirements that we defined in Section 7.3.2, almost reaches the efficiency of the discussed ideally thermally isolated model, cf. Equation 7.8, and surpasses the efficiency obtained with the system described in Reference [367]. The fit yields furthermore a power-axis intercept at $(139.9 \pm 0.4)\,\mathrm{W}$ which represents the zero heater output in absence of constant recirculation-based heat leaks. In fact, the actual heater output power at zero recirculation flow is in the range $154 - 174\,\mathrm{W}$. This estimate originates from alternating low-flow and zero-flow measurements as, due to the lack of convection inside the cryostat, the system cannot be brought into a steady state below 2.5 bar without recirculation. In Figure 7.8, left, we show the lower limit on the heat exchange efficiency. It is constant at a mean value of $\bar{\eta} = 97.3\,\%$, in the range $20 - 80\,\mathrm{slpm}$. We find a lower efficiency of $\eta > 95.4\,\%$ in the range $5 - 15\,\mathrm{slpm}$. At very low flows of $\sim 1\,\mathrm{slpm}$, the heat exchangers warm up and the efficiency increases rapidly as the constant recirculation-based heat leak vanishes.

Thermal Leakage

To keep the system cold, a series of constant and flow-dependent heat leaks due to radiation, conduction and convection processes need to be compensated. The constant heat leak at zero flow is only due to losses at the cryostat and cold head and can be calculated from the heater output power if the cooling power of the PTR is known at the respective cold-head set-point. When recirculation is started, the umbilical and the heat exchangers are cooled down as well, even at very low flow. This represents another source of constant heat leak. It can be quantified from the offset of the power-axis intercept of the fit in Figure 7.7, right, and the actual measurement of the required zero-flow heater power. We obtain the estimate $14 - 34\,\mathrm{W}$ and conclude that the total constant heat leak is the sum of the constant heat leaks of the cryostat, the cold head, as well as the heat exchanger and the umbilical. The latter two only play a role when recirculating. In addition to the constant heat leaks, flow-dependent losses emerge when recirculating. One source of such a loss comes from the small inefficiency of the heat exchange. Moreover, flow-dependent temperature changes of the setup change the radiative heat input, the impact of heat conduction processes through holding structures and the

convection by a change of the quality of the insulation vacuum. The sum of all these losses as a function of the flow is obtained from the heater output measurement. The temperature difference of the cooler inlet and heater outlet allows us to calculate independently an efficiency from the enthalpy differences. To obtain the enthalpies on the heater outlet, we need to make an assumption on the pressure in the return line. The pressures will vary depending on the considered flow. However, we use the values at cryostat pressure for simplicity because, as mentioned above, they do not change much at slightly lower pressures. We note that, unlike our definition in Section 7.3.2 where we considered an ideally thermally isolated heat exchanger system, this efficiency is not equal to the efficiency of the heat exchange. This becomes obvious when considering the situation in which the cold outgoing gas from the return line would exchange its heat with a heat bath of the environment that provides the energy to heat up the gas, while the ingoing gas on the supply line enters the cryostat at room temperature. The temperature difference of gas inlet and outlet is zero, thus we could deduce a perfect heat exchange. For this reason, this method does not allow us to disentangle the heat exchange inefficiency and any other flow-dependent heat leaks from the heat exchanger and umbilical section. However, this measurement is not sensitive to flow-dependent heat leaks of the cryostat. Hence, the difference of the loss calculation of the heater power output and the gas inlet/outlet temperature measurement is equal to the flow-dependent heat leaks of the cryostat plus twice that of the heat exchanger, see Figure 7.8, right. We obtain a loss of 0.26 W/slpm from the sum of the inefficiency of the heat exchange and other flow-dependent losses on the heat exchangers and the umbilical, and can deduce that the latter are < 0.02 W/slpm. Furthermore, we can conclude that the sum of the cryostat, heat exchanger and umbilical losses are < 0.04 W/slpm.

7.4 Filtration and Safety Gas System

Figure 7.9 shows the P&ID of the entire system. Complementing the main gas handling and purification system, the heat exchanger unit features a secondary gas panel for the emergency recuperation line and particulate filters, see Figure 7.10. On the xenon extraction line, a 40 µm metal strainer element protects the purification loop from particulates. On the xenon supply line, a ceramic ultra-high purity filter removes particulates of 3 nm size with an efficiency of nearly 100 %. The former will create a pressure drop of 0.17 bar [380] and the latter of 0.4 bar [381] at 100 slpm air or nitrogen.

In case of an unexpected pressure increase anywhere in the gas system, the emergency line directs xenon released by pressure-relief valves to the gas storage and recovery system, where it is collected in an LN_2-cooled aluminium bottle, see Section 7.5.1. The pressure relief valves are located at strategic locations in the system: CV-01 protects the xenon compressor by relieving pressure from 4.0 bar absolute, CV-02 serves as the first pressure protection of the cryostat volume by releasing gas at pressures greater than 3.0 bar, CV-03 is located at the exit of the heat-exchanger system, limiting the pressure at the exit to 4.0 bar, CV-05 protects the getter system from pressures greater than 11.3 bar. The flow through all filters and check valves can be shut off by in-line manual valves or bypassed if needed. Finally, as a last resort, in case of an uncontrollable pressure rise above 8.0 bar absolute in the cryostat, CV-04 can vent the GXe to air. This pressure limit is the result of an engineering study which was performed by Helbling Technik AG [22]. The goal of this study was to ensure the structural integrity of the cryostat both under normal operating conditions at 2 bars and ~ 177 K, as well as in potential emergency situations, in the unlikely event of an uncontrollable increase in pressure. Finite element analysis (FEA) simulations of the cryostat and CF-flanges were performed to confirm their reliability against overload and leakage up to 8 bar at 170 K.

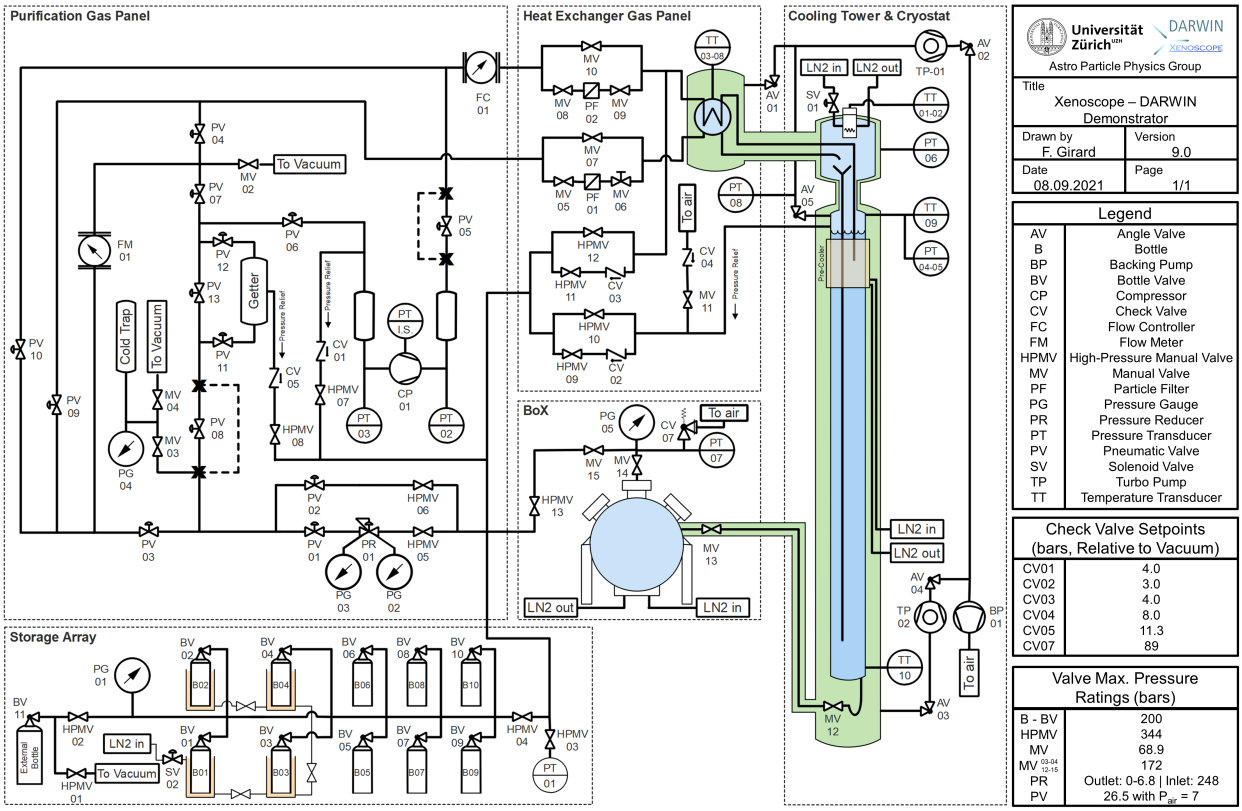

Figure 7.9: Piping and instrumentation diagram of Xenoscope. In the text we refer to the *heat exchanger gas panel* as *filtration and safety gas panel*.

7.5 Xenon Recovery and Storage Systems

For safe long-term storage of the xenon during maintenance, upgrade work and downtime, the gas handling system connects to dedicated recuperation systems. We distinguish a baseline system for the recuperation in the gas phase that is also used for automatic emergency recuperation, and a system that recuperates the xenon in the liquid phase to accelerate the recuperation procedure significantly. Both are designed, built and commissioned.

7.5.1 Gas Recovery System

As shown in Figures 7.9 and 7.11 a gas bottle storage array consisting of ten 40 l aluminium gas cylinders is connected to the gas handling system on the high-pressure side, allowing us to store a maximum of 470 kg of xenon. Four of the gas cylinders are suspended in tall, inter-connected open Dewar flasks from Cryofab, Inc. [382] (Model CF1248) that are 122 cm deep at full diameter. The Dewars feature custom-made bottom drains via which they are connected in series by means of vacuum insulated lines. Individual Dewars can be isolated from the others via vacuum-jacketed valves. Cane-shaped inlets and P-traps protect the valves from the accumulation of moisture. Depending on the xenon mass to be recuperated, a set number of Dewars is filled with LN_2. The xenon is then evaporated from the cryostat and recovered into the cold cylinders by means of cryogenic pumping. The four cold cylinders can hold the full xenon amount in liquid and solid phase. To reduce condensation and for safe operation of the bottle valves which are rated for $-20 - 60\,°C$, band heaters with a power of 1400 W each, located at the top of each bottle, keep the valve and the neck above the freezing temperature of water. For the initial cool-down of the four bottles to LN_2 temperature, the sublimation of 450 kg

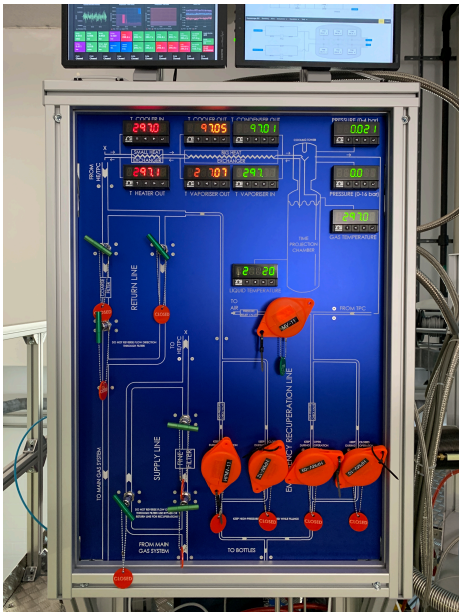

Figure 7.10: Photograph of the filtration and safety gas panel.

of xenon and the compensation of the radiative input onto the top of the bottles over the course of nine days, a total heat of $\sim 300\,\mathrm{MJ}$ has to be transferred. This period corresponds to the average gas recovery speed of $\sim 6\,\mathrm{slpm}$ that was reached during the commissioning phase for the recovery of $80.66\,\mathrm{kg}$ in $40\,\mathrm{h}$[1]. This heat corresponds to the vaporisation of $1500\,\mathrm{kg}$ LN_2 which well agrees with what can be extrapolated from the commissioning experience. However, the bottle heaters can be the dominant source of heat input depending on the LN_2 level in the Dewars and increase the LN_2 consumption significantly.

After recuperation, the xenon is equalised among all ten cylinders in gas phase during warm-up. The recuperation line features an analog pressure gauge with 250 bar full-range and a vacuum gauge with an admissible pressure of 10 bar which can be isolated by a valve. All components exposed to high-pressure are rated to 200 bar or higher. The first cylinder in the array is connected via the recuperation and emergency line to the check valves, cf. Section 7.4). As part of the passive safety system, this bottle is kept cold at any time during operation, resulting in a pressure of $10^{-2}-10^{-1}\,\mathrm{mbar}$ in the line. In the event of an automatic recuperation through the check valves, the vacuum gauge can be used to detect the increased pressure in the recuperation line.

A levelling system from KGW-Isotherm GmbH [383] controls the LN_2 level of the first Dewar. A total of six PT100 sensors are installed, four for two 2-point level controls at different heights and two for under- and overfill alarming. A bottle weighing system allows for the monitoring of the xenon inventory and indicates any xenon loss during run cycles. The suspended gas cylinders are supported by Mettler-Toledo Schweiz GmbH [384] (Model SLS510) 250 kg capacity load cells that feature an individual combined error of $\leq 45\,\mathrm{g}$. Two Soemer Messtechnik GmbH [385] (Model WK8 VA) junction boxes sum up the analog signals of five load cells each. The signals are then read out by two Mettler-Toledo (Model ACT350) terminals.

[1] The recovery speed highly depends on the heat input onto the inner vessel. In fact in a later run an average flow of $\sim 9\,\mathrm{slpm}$ was achieved for the recovery of 60 kg by heating the inner vessel with a hot air gun.

Figure 7.11: Gas xenon recovery and storage system of Xenoscope. Ten aluminium gas cylinders are suspended from load cells for mass determination, four of which are placed inside an inter-connected Dewar flask assembly. **Left:** Photograph with nine gas cylinders installed. **Right:** Rendering.

7.5.2 Liquid Recovery System – BoX

Purpose

Tests of multiple new technologies with Xenoscope inevitably involve frequent xenon filling and recuperation processes. A fast and safe recovery system with the potential for long-term storage is therefore essential. While the speed of gas recovery is limited by the heat input onto the inner vessel of the cryostat required to vaporise the LXe, transfer of xenon in liquid form is faster at lower LN_2 consumption. However, liquid transfer of xenon directly into the gas bottles is not possible due to their standardised valves that are not rated for cryogenic operation. For this reason, a separate LXe recovery system was designed and constructed. At its heart is a cryogenic pressure vessel into which LXe is drained by gravity [386] from the bottom of the cryostat, which we call BoX (Ball of Xenon). BoX can store up to 450 kg of xenon in both liquid and gas phase.

Setup

BoX is installed close to the cryostat, the liquid inlet below the bottom outlet of the cryostat, see Figure 7.12, right. A vacuum insulated 1/2 in cryogenic line connects the inlet of BoX on its side to the bottom of the cryostat. At its top, a warm 1/4 in gas line connects the outlet of BoX through the high-pressure side of the gas system, to the cold head of the cooling chamber. When fully filled with LXe, the hydrostatic pressure of the xenon column leads to an increased total pressure of ~ 3 bar at the bottom of the inner vessel of the cryostat at the nominal gas pressure of 2 bar. Located in the insulation vacuum and actuated by a rotary feedthrough, a cryogenic bellows sealed valve with secondary containment system and a spherical metal stem tip (Swagelok Company [387] model SS-8UW-V47-TF) which is rated up to 172 bar and down to $-200\,^{\circ}$C seals the inner vessel. The valve and the rotary feedthrough are connected via a telescopic Cardan shaft with two universal joints to account for offsets between the inner and outer bottom flange in all dimensions. The rotary feedthrough allows for the transmission of torques of up to 18 Nm. This is necessary for safe actuation of these valves that show an increased handle torque below $-40\,^{\circ}$C [388]. The valve is thermally decoupled

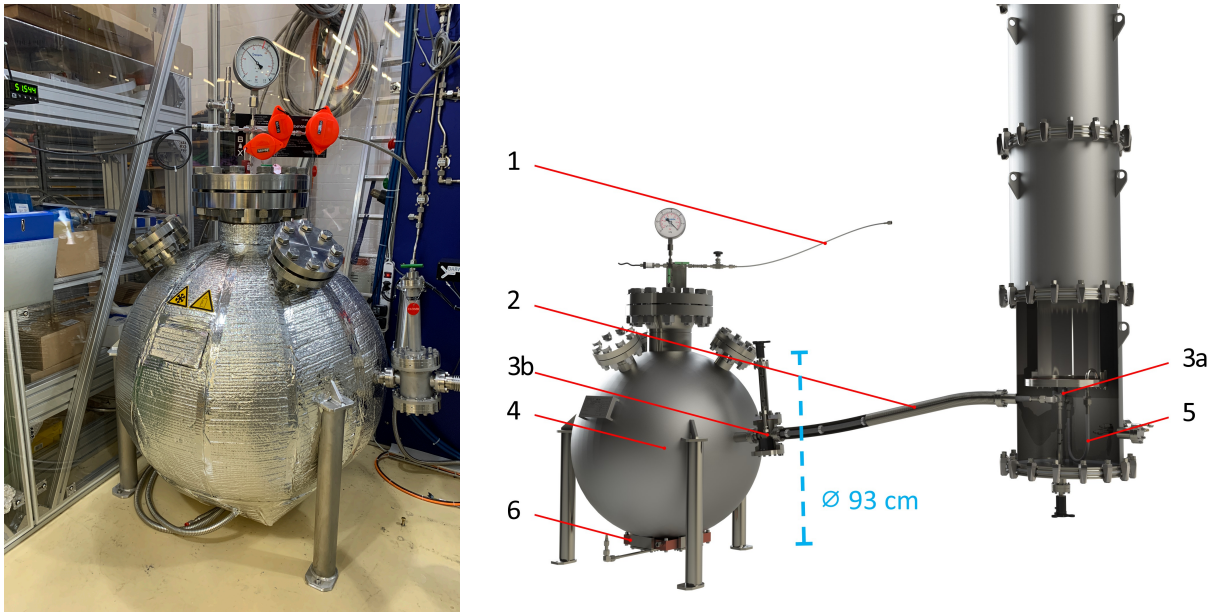

Figure 7.12: Liquid xenon recovery and storage system of Xenoscope. **Left:** Photograph of the pressure vessel BoX. The gas outlet with analog pressure gauge, pressure transducer and safety relief valve is on top of the central DN200 flange. The liquid inlet from the cryostat with the vacuum-jacketed valve is on the right. **Right:** Rendering of the pressure vessel BoX connected to the cryostat outlet via a vacuum insulated transfer line. **Legend:** 1 – Gas return line to the high-pressure side of the gas system, 2 – Vacuum-insulated liquid transfer line, 3a/b – Cryogenic valves, 4 – Spherical pressure vessel BoX, 5 – Cryostat drain with cane-shaped inlet and P-trap, 6 – LN_2 cooler. For better visualisation, the TPC and the HV feedthrough are hidden.

from the inner vessel with a plastic holder and from the rotary feedthrough with plastic sleeves. A P-trap and the fact that the bottom drain is located at the cryostat wall protect the detector volume from gas bubbles that are possibly created at the warmer, potentially gaseous, dead end. Depending on the amount of xenon filled in the detector, BoX will be empty or at a certain gas pressure during detector operation. Its liquid inlet is sealed by a second vacuum-jacketed cryogenic valve of the same type which is actuated and thermally decoupled in the same way. Its gas outlet features another valve of that kind in the 1/4 in version. Underneath BoX, a soldered LN_2 copper cooler with an internal spiral channel, see Figure 7.13, left, is mounted such that it is held and pressed against the surface by four welded brackets. For good thermal contact, a mixture of cryogenic Apiezon® N grease [389] and $0.5 - 1.0\,\mu m$ silver powder is applied in between the sphere's surface and the cooler, see Figure 7.13, right. BoX is single-walled and passively insulated with multiple layers of aluminised bubble wrap that features a reflective shield to prevent radiative heat absorption. The cooler region is additionally insulated by a milled foam part. During recuperation, we expect a need of $\sim 200\,W$ cooling power due to radiation, conduction and convection processes. This corresponds to an LN_2 consumption of $\sim 3.6\,kg/h$. At low or zero recirculation flows, the spare power of the PTR on the cryostat is sufficient to cover most of this demand.

The assembly is equipped with a proportional safety relief valve (CV-07) set to the maximum working pressure, see Appendix B for its dimensioning, and it is instrumented with an analog pressure gauge and a pressure transducer for pressure monitoring, see Figure 7.12, left.

Design

Based on our conceptual design, the manufacturer KASAG Swiss AG [390] provided the engineering for the final draft of the pressure vessel. To ensure its safety, KASAG Swiss AG performed calculations regarding the rules and standards AD 2000 [391] according to the European pressure equipment

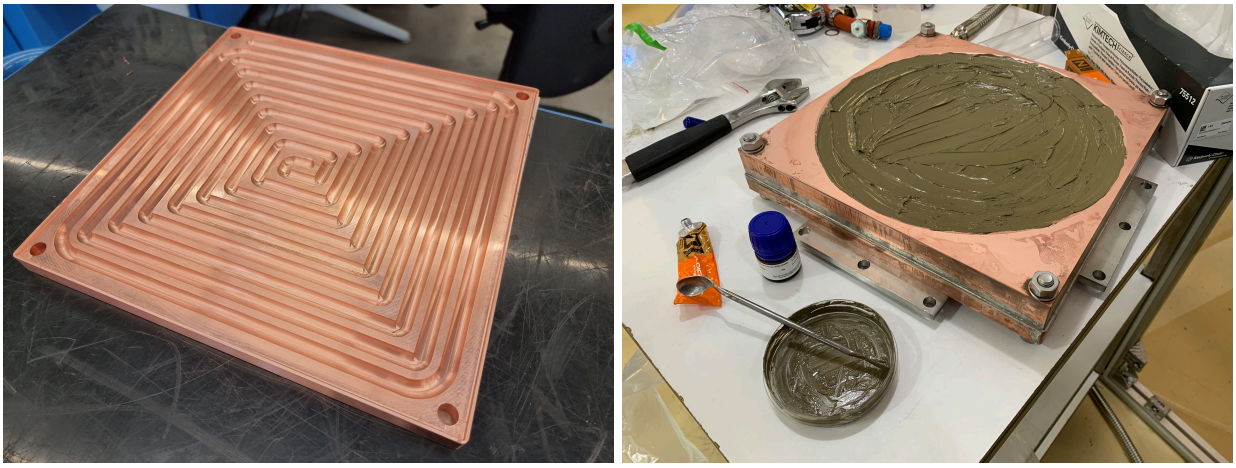

Figure 7.13: Liquid nitrogen copper cooler for BoX. **Left:** Photograph of one half-shell with the inside channels. **Right:** Photograph of the soldered copper cooler. On the heat transfer surface to BoX, a mixture of cryogenic Apiezon® N grease [389] and silver powder was applied.

directive PED 2014/68/EU [392]. The stainless steel pressure vessel was chosen to be spherical to minimise its mass and thus, its heat capacity, which is key for the cryogenic design to reduce the LN_2 consumption during the initial cool-down. In addition, a low mass reduces the cost of materials and facilitates handling during installation. The inner radius r, which directly influences the required wall thickness t for a given amount of xenon contained at an overpressure p, was optimised for mass based on:

$$m(r) = \mathrm{FOS} \cdot \frac{4}{3}\pi r^3 \left[\left(1 + \frac{p}{\sigma_{\mathrm{SS}}} \right)^{3/2} - 1 \right] \rho_{\mathrm{SS}} \quad , \tag{7.28}$$

where FOS denotes the required factor of safety on the yield strength σ_{SS} of the stainless steel, while ρ_{SS} is its density. The equation follows from the equilibrium of the tensile strength of the cross-section of a hollow sphere and the force from the inner overpressure acting onto the cross-section:

$$\sigma_{\mathrm{SS}} = \mathrm{FOS} \cdot \frac{r^2 p}{2rt + t^2} \quad . \tag{7.29}$$

Although we keep this calculation as general as possible, note that, the thin-shell theorem $\sigma_{\mathrm{SS}} \geq \frac{rp}{2t}$ would follow for $t \ll r$.

For a hollow sphere, $m(r)$ is constant for large r and divergent for small r. Unlike for ideal gases, $m(r)$ additionally features a minimum at moderate r for a Van der Waals gas. Using the Van der Waals constants of xenon (cf. Table 2.1, Chapter 2),

$$\begin{aligned} a &= \frac{27(RT_{\mathrm{crit}})^2}{64 p_{\mathrm{crit}}} = 0.42\,\mathrm{Pa\,m^6/mol^2} \quad , \\ b &= \frac{RT_{\mathrm{crit}}}{8 p_{\mathrm{crit}}} = 5.2 \times 10^{-5}\,\mathrm{m^3/mol} \quad , \end{aligned} \tag{7.30}$$

we obtain, for a capacity of 450 kg of xenon, the lowest mass at an inner radius of $r = 450\,\mathrm{mm}$ with $t = 10\,\mathrm{mm}$ at FOS = 1. For this we assumed a stainless steel with a yield strength of $\sigma_{\mathrm{SS}} = 200\,\mathrm{MPa}$ (0.2 % proof) [375]. However, the position of the minimum turns out to be rather insensitive to changes in the yield strength. Neglecting boundary effects and the connecting ports and flanges, the wall thickness from this simple analytical calculation was confirmed by FEA simulations with SolidWorks® [393]. Requiring a factor of safety of 1.5 on the yield strength, KASAG Swiss AG calculated a minimum wall thickness of 13.5 mm for stainless steel 1.4404/1.4435 based on AD 2000-Merkblatt B 1 [391]. The sphere consists of two half-spheres that were rolled from sheets with an

initial thickness of 18 mm. The half-spheres are welded together in such a way that the required minimum wall thickness is safely guaranteed. A measurement of the wall thickness confirmed that the sphere is at no point thinner than 15 mm. A radiographic examination with x-rays confirmed the high quality of the welds.

The vessel is designed for a maximum working pressure of 90 bar and for temperatures ranging from −196 °C to 50 °C. As the ultimate yield strength is at room temperature approximately twice as high as the yield strength where the elastic region ends, the pressure vessel will only rupture at roughly three times the maximum working pressure. Such high pressures can only be reached by overfilling or the exposure to external heat sources. However, note that the calculations were performed at the maximum operating temperature of 50 °C and the yield strength decreases at higher temperatures.

The inner surface, including the welds, is pickled and electropolished through the four service ports at the top to improve the inside cleanliness. Every wetted gasket, i.e. in contact with xenon, is entirely made of metal. Under vacuum and at $26.8 - 28.8\,°C$, the gaskets of the three DN80 and the single top DN200 service ports show a helium leak rate of $\mathcal{O}(10^{-8}\,\mathrm{mbar \cdot l/s})$. The manufacturer of the gaskets guaranties a maximum leakage of $\sim 10^{-4}\,\mathrm{mbar \cdot l/s}$ at low temperatures. The sphere is held by three welded legs bolted to the concrete floor. Since the maximum liquid level is located ~ 70 mm below the equator of the sphere, the legs are welded at the side, above the equator, to reduce heat conduction.

The pressure vessel assembly, i.e. the safety relevant minimal part of the liquid recuperation system, was certified by the Swiss Safety Center AG [19] to be conform with the PED 2014/68/EU [392].

Working Principle and Performance

For xenon recovery, BoX is pre-cooled, which also liquefies remnant xenon inside. This process consumes up to 200 kg LN_2. Before the recovery process is started, the pressure in BoX must be lower or equal to the pressure at the bottom of the inner vessel, i.e. $< 2 - 3$ bar. This is the expected pressure range from the sum of the cryostat gas pressure during normal operation and the hydrostatic pressure from the LXe column inside the cryostat. If a high remnant xenon amount is left in BoX, this process can be accelerated by transferring it to the gas recovery system. It is advantageous to reduce the pressure even further to vacuum. This accelerates the cooling of the transfer line at the beginning of the recovery process. When the valves on the liquid line between BoX and the inner vessel of the cryostat are opened, the pressure in BoX rises to the pressure present at the bottom of the cryostat and the connecting line starts cooling from LXe evaporation. By opening the valves on the gas return line, GXe is brought back to the cryostat, replacing the volume of the LXe flowing into BoX. The GXe flow is the sum of the LXe flow, by displacement, and the xenon which evaporates inside BoX. The speed of the recovery process can be controlled with the valves on the gas line or with the pressure regulator on the main gas panel. A check valve on the gas line was initially installed to avoid back-flow of gas in case of pressure fluctuations. However, its minimum relative opening pressure of 0.3 bar limited the speed of the recovery process in a first test as it created a pressure difference to the top of the cryostat. Since the flow during the recovery process was never observed to vanish, it could be removed. This increased the performance of the liquid recovery significantly. At the end of the recovery process, the remaining LXe and GXe in the system can be cryo-pumped into the gas bottles.

While isochorically warming up, see Figure 7.14, the LXe will change to gas. Above its critical pressure of 58.4 bar, xenon is in a supercritical state [191]. At a typical temperature of 296 K, the pressure in BoX is 66.5 bar when loaded with 450 kg of xenon. In its supercritical state, the pressure of xenon is highly temperature dependent. However, below 40 °C, the pressure will not exceed the working pressure of the vessel and hence, the set pressure of the safety relief valve, see the discussion in Appendix B.

The detector is filled with GXe through the pressure regulator on the main gas panel. Xenon

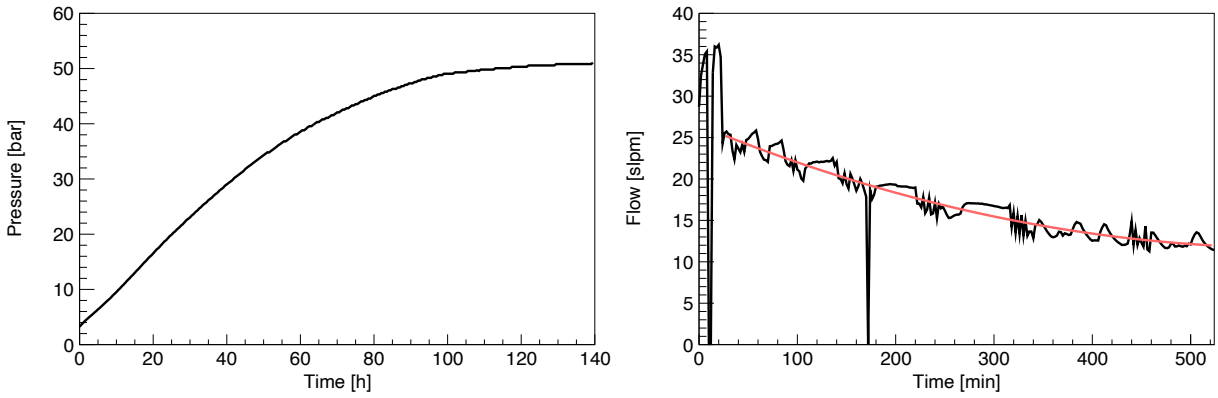

Figure 7.14: Left: Isochoric warming process of 167 kg in BoX after liquid recuperation. The pressure increase was linear while BoX contained a mixture of vapour and liquid, and changed its slope as soon as all liquid was evaporated. At this mass, the pressure stays subcritical. **Right:** Gas flow during liquid recuperation with second order polynomial fit function. The high flows at the beginning are due to the cooling of BoX. Flow anomalies down to zero flow are due to operator actions. The oscillations are due to the use of the pre-cooler. During most the recovery process, two paths to the cryostat were opened to reduce the pressure drop over the tubing due to friction. One path included the flowmeter for which we show the data, the other connection was opened on the high-pressure side of the gas system via HPMV 10. Thus, the actual flow was higher than shown.

condenses at the cold head cooled by the PTR, as it is the case when filling from the gas bottles.

In a test, the performance of the liquid recovery system was benchmarked. The cryostat was filled with 226 kg of xenon which corresponds to a LXe column of 155 cm above the cryostat drain and a hydrostatic pressure difference of 0.43 bar compared to the gas phase. Within a period of 8.7 h, a total of 167 kg were recuperated in liquid form which corresponds to an average transfer rate of 19.1 kg/h. Although not necessary to keep the system stable, the LN_2 pre-cooler on the inner cryostat vessel, which was developed for a faster filling of the cryostat with LXe, was used periodically to provide additional cooling, see Figure 7.14, right. This improved the recovery speed especially at the beginning when high quantities of xenon evaporate in BoX to cool it down. Note that this test was unplanned and necessary due to a failure of the xenon compressor. For this reason BoX and the liquid line could not be cooled down much prior to recuperation. The recovery process was stopped prematurely for the lack of a precise reading of the liquid level inside the cryostat. However, a mass of ~ 10 kg cannot be transferred in liquid form anyways, because they are located below the liquid drain, mostly inside a nipple which is reserved for a high-voltage feedthrough for later stages of the project. Because the recovery process is driven by the hydrostatic pressure created by the LXe column in the cryostat, the recovery was faster at the beginning, see Figure 7.14, right. The highest fully filled section of the inner vessel, which contains ~ 77 kg was emptied at a rate of 51.2 kg/h. The higher the LXe column is, the faster is the recovery speed. Torricelli's law predicts a linear flow decrease for a leaking vessel through a short open orifice. However, the speed of the outflow is reduced by the speed-dependent friction inside the tubing, and the evaporation inside BoX and the liquid transfer line which create back pressure. We obtained an improvement in speed, compared to the gas recovery process, of factor 16 at the beginning of the process for the first section of the inner vessel, and factor 6 on average (cf. Section 7.5.1).

7.6 Summary and Conclusion

In this chapter we have presented Xenoscope, the full-height DARWIN demonstrator which will house a 2.6 m TPC and involve $350 - 400$ kg xenon. We have provided a general overview of the facility,

discussed its objectives, of which the main one is the direct demonstration of an electron drift over 2.6 m in LXe, and have detailed on certain mechanical and cryogenic subsystems. Among these is the horizontal cryostat levelling mechanism which allows for an almost force-free fine-adjustment with a precision of $< 60\,\mu m/m$. Furthermore, we have discussed the heat budget of Xenoscope based on which we have defined the requirements for the heat exchanger system, leading to a design choice. A very efficient heat exchanger system is necessary for high recirculation flow rates through the purification loop. It was benchmarked in a commissioning run and showed a minimum mean efficiency of 97.3 % for a gas flow range of $20 - 80$ slpm. We have seen two independent xenon recovery and storage systems in this chapter, one that transfers the xenon as gas into gas cylinders by means of cryogenic pumping, and one that transfers the xenon as liquid into a pressure storage vessel named BoX. Both can hold the full xenon inventory at room temperature. We have detailed on the design and recovery performance of both systems.

Xenoscope will be used to demonstrate electron drift and to study optical properties of LXe at the DARWIN length scale, and to perform full-scale tests of systems relevant for DARWIN.

Chapter 8

Summary and Conclusion

Numerous astrophysical and cosmological observations provide strong evidence for an additional non-luminous matter component in the universe which is, by mass, more than five times as abundant as baryonic matter. These observations favour that such dark matter has a particle nature. However, at least the majority of dark matter must be made of new, BSM, particles. A well-motivated particle dark matter candidate is the WIMP which appears in several different BSM models. Due to its high mass number and a variety of other advantages, xenon is an ideal target for direct WIMP detection, i.e. the scattering of WIMPs with target nuclei. World-leading sensitivities to WIMP interactions can be achieved by deploying a tonne-scale xenon target in dual-phase TPCs. DARWIN is a proposed next-generation observatory with a dual-phase xenon TPC housing a 40 t active mass, with the ultimate goal to explore the WIMP parameter space down to the irreducible CEνNS neutrino background. With a 200 t × y exposure of a 30 t fiducial mass, DARWIN will reach a sensitivity of 2.5×10^{-49} cm^2 for 40 GeV/c^2 WIMPs. Besides its excellent sensitivity to WIMP interactions, DARWIN will be a unique platform to search for various other rare interactions. We outlined the reach in the search for neutrinoless double beta decay for which DARWIN will be able to obtain after 10 y run time a half-life sensitivity of $T^{0\nu}_{1/2} = 2.4 \times 10^{27}$ y, competitive to dedicated experiments. DARWIN will also provide a high-precision measurement of the low-energy *pp* and ^{7}Be solar neutrino flux and surpass the precision of the Borexino measurements with exposures of 1 t × y and 60 t × y, respectively, at a 30 t fiducial mass. The development of a detector as large and as sensitive as DARWIN necessitates a rich R&D programme in context of which this thesis was written.

In this thesis, we have presented an upgrade of Xurich II, the first dual-phase xenon TPC equipped with SiPMs in the top photosensor array. The detector was operated under stable conditions for more than one year and its performance was demonstrated with data from internal ^{37}Ar and ^{83m}Kr calibration sources. Based on the centre of gravity of ionisation signals detected by the SiPM top array, we have reconstructed the (x, y)-positions with a resolution of $\sim$ 1.5 mm within the fiducial radius. Furthermore, we have evaluated the *in situ* performance of the SiPMs in terms of gain, dark count rate, and internal and external crosstalk. In particular, we have presented a combinatorial approach to search for a DPE effect in SiPMs based on SE data and found no excess beyond the known internal crosstalk effect. The setup has demonstrated by a proof of concept that SiPMs are indeed a promising alternative to PMTs in small detectors. The scalability to much larger arrays, however, such as required by DARWIN is under investigation [15]. A major challenge, apart from reducing the dark count rate, which raises the energy threshold of the detector by a high accidental coincidence rate, is the readout and the signal pre-amplification. The main shortcoming of the described amplifier board for 16 channels is its heat dissipation of $\sim$ 3 W. To this end, the lowest allowable pre-amplification factor is to be evaluated and low-power cryogenic pre-amplifiers to be developed and tested. Readout schemes that merge the signal of several SiPMs into larger tiles can help to reduce the number of required pre-amplifiers [276, 284].

We have shown the production of gaseous ^{37}Ar sources filled in quartz glass ampules with activities of $19 - 22$ kBq each and presented the source introduction setup and procedure for Xurich II. The low energy threshold of the detector and its good energy resolution have allowed for an S1 and S2 analysis

of the 2.82 keV K-shell capture line and for an S2-only analysis of the 0.27 keV L-shell capture line of ^{37}Ar. An attempt to isolate the M-shell capture line at 17.5 eV, close to the excitation energy of LXe, by means of a time veto cut has been outlined. Moreover, we have briefly discussed the analysis of the 9.41 keV, 32.15 keV and the combined 41.56 keV energy lines of ^{83m}Kr. The later and the K-shell capture line of ^{37}Ar show a clear anti-correlation in charge versus light yield space. The light and charge yields have been compared with NEST v2.3.0 predictions.

Based on SE events and data from the mentioned low-keV internal calibration sources in Xurich II, we have measured the mean electronic excitation energy of LXe to be $W = 11.5\,^{+0.2}_{-0.3}\,(\text{syst.})\,\text{eV}$, with negligible statistical uncertainty. This value is in agreement with a measurement by the EXO-200 collaboration but contradicts the widely used value by E. Dahl of $(13.7 \pm 0.2)\,\text{eV}$. For this study, we have presented a careful treatment of the systematic uncertainties due to the hybrid photosensor configuration as well as the TPC, DAQ and data processing effects. We have additionally provided a comparison of our measurement to NEST and found that the discrepancy is mostly seen in the light channel. Such studies are important for the modelling of the response of LXe detectors and provide valuable input to NEST.

We designed, built and commissioned the full-scale vertical DARWIN demonstrator, Xenoscope, with the main objective of a first direct measurement of an electron drift over a distance of 2.6 m in LXe. The facility will also be a platform for testing several key technologies necessary to the realisation of the proposed DARWIN observatory. We have discussed in detail the design and working principle of the horizontal cryostat levelling system which was registered as a utility model at the German Patent and Trade Mark Office. The tripod levelling assembly allows for a maximum mass of 2100 kg and a levelling precision of $< 60\,\mu\text{m/m}$. Compared to common machine feet and bearings deploying leadscrews, it has several advantages. It allows for a load-independent, almost force-free levelling around the equilibrium point of the central springs in the levelling legs. This makes the use of precise fine thread screws possible to compensate for a potential tilting of the cryostat and reduces wear. The vibration coupling to the foundation is reduced by the use of springs that bear most of the load. The levelling assembly is successfully used for permanent bearing of the Xenoscope cryostat and regular levelling procedures. Furthermore, we have performed a design calculation for the heat exchanger system based on the cryogenic requirements set by facility and the purity goals of the project. We have outlined the inclusion of the heat exchangers in the system and characterised their performance in a commissioning run. The system showed a minimum mean efficiency of 97.3 % for a gas flow range of $20 - 80\,\text{slpm}$. We have also discussed the purpose and design of the filtration and safety gas system of Xenoscope. Two independent recovery and storage systems were designed and built: one gas bottle storage array for gas recovery via cryogenic pumping and one liquid recovery system with the pressure vessel BoX as its main component. In particular, we have discussed the design considerations for BoX. Both systems were successfully commissioned and show good performance during recuperation. A total of 80.66 kg was recuperated in gas form in less than two days at the end of the commissioning run. In a liquid recuperation test a xenon mass of 167 kg was recovered into BoX, with a maximum speed improvement of factor 16 compared to the gas recovery.

This doctoral project demonstrates the potential use of SiPMs in dual-phase xenon TPCs and contributes significantly to the understanding of LXe interactions at low-keV and sub-keV energies. Using SE events, it explores the low-energy frontier of these detectors by the measurement of the minimal interaction energy W needed to produce quanta in LXe. On the large-scale frontier, this project involves major developments and designs as to the realisation of Xenoscope, the vertical DARWIN demonstrator. In the upcoming years, Xenoscope will play a major role for the R&D for DARWIN, for the direct demonstration of the electron drift over the full DARWIN height and for the testing of subsystems for DARWIN. All these topics, novel photosensors, low-energy calibration techniques, understanding and modelling of interactions in LXe and the direct demonstration of the working principle at the full-scale are essential inputs for the development and the success of

the DARWIN observatory. DARWIN is considered as the ultimate evolution step of the dual-phase xenon TPC detectors for dark matter research for its reach down to the neutrino floor (fog). To reach even lower and to disentangle the CEνNS interactions from solar, atmospheric and supernova neutrinos from WIMPs [143, 394], new detector concepts should be considered. Directionality as well as annual and daily modulation of the expected dark matter signal and the neutrino background can be exploited [106,395,396]. Furthermore, the parallel use of different target nuclei can help to discriminate the neutrino background [142]. In any case, precise neutrino component flux measurements are essential to improve the discovery limit of dark matter experiments in the neutrino fog [142].

No matter if a signal is found above the neutrino fog or not, we have seen that dark matter detectors are ideal to perform exciting physics and allow for rare event discoveries, and the field stays as exciting and challenging as ever. With detectors like DARWIN, the astroparticle physics community can look forward to a bright and exciting future.

Appendix A

Calibration of the Xurich II TPC with a ^{83m}Kr Source

A common technique for the energy calibration of a xenon dual-phase TPC is to introduce ^{83m}Kr, a decay product of ^{83}Rb with $T_{1/2} = (86.2 \pm 0.1)$ d, into the system [258, 397–399]. This source with $T_{1/2} = (1.83 \pm 0.02)$ h offers a homogeneous distribution of events in the target volume with a line at 32.15 keV followed by a line at 9.41 keV with $T_{1/2} = (155.1 \pm 1.2)$ ns for the intermediate state [293] and was also used in Xurich II [23]. The data presented here was acquired between mid-January and early-February 2019. We used the anti-correlated light and charge yields obtained with this source in Chapters 5 and 6. Below, we summarise the data selection and quality cuts, the applied corrections as well as the obtained results.

A.1 Data Selection and Quality Cuts

The selection of split 32.15 keV and 9.41 keV ^{83m}Kr events is performed by exploiting the double-S1 and double-S2 signal topology as a result of the intermediate 9.41 keV level. That is, in the PMT channel, we require exactly two S1s with S2s and the S1s must contain less charge than their paired S2s. As mentioned in Chapter 4, Section 4.1, we remove events that triggered on an S2 signal to avoid a bias of events towards the upper half of the TPC due to the DAQ window. Furthermore, a cut on the delay time of the PMT signals is applied. We expect ^{83m}Kr events to have the same positive delay Δt between the two S1 signals and between the two S2 signals, see Figure A.1, left, and select $\pm 2\sigma$ around the centred mean in the $\Delta t_{S1} - \Delta t_{S2}$ histogram, see Figure A.1, right. As for ^{37}Ar, we use the fiducial volume cut developed in Chapter 4, Section 4.2.4, an AFT cut as well as an S2-width cut. In Figure A.2, left, we show the S2-width histogram of both lines. In Table A.1, we provide a summary of the event survival fraction after each cut. For ^{83m}Kr data, a fraction of 61.1 % of the recorded non-saturated events within the fiducial volume that generate at least two S1 and two S2 signals pass all data quality cuts.

Cut	**Abs. Survival Fraction** [%]	**Rel. Survival Fraction** [%]
Trigger on S2	99.8	99.8
S1 < S2	99.8	~ 100
Time delay	65.0	65.2
AFT	65.0	99.9
S2-width	61.1	94.0

Table A.1: Survival fraction of non-saturated events within the fiducial volume that generate at least two S1 and two S2 signals after each data selection and quality cut for the ^{83m}Kr analysis. We show the absolute survival fractions in order of the applied cuts and the relative survival fractions compared to the preceding cut.

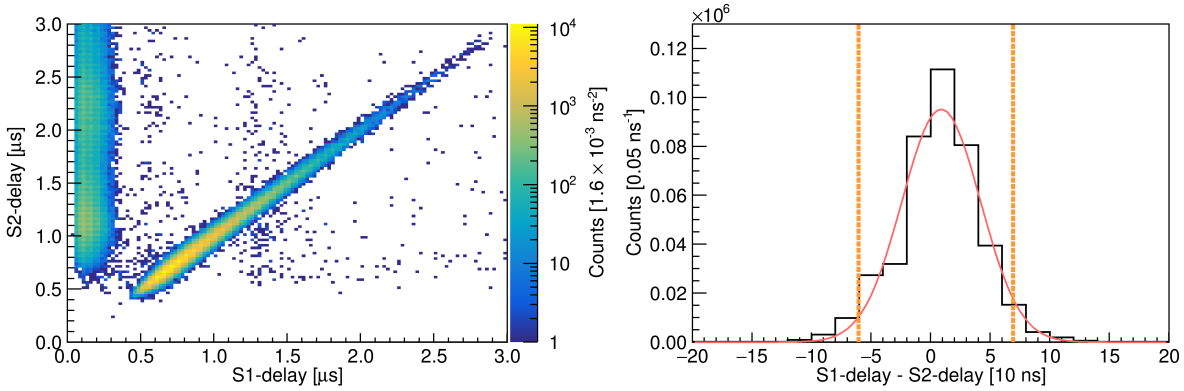

Figure A.1: Time delay cut for the split lines of the ^{83m}Kr population. **Left:** S1-delay versus S2-delay. The ^{83m}Kr population is expected to be located on a diagonal in that space. The population at constant low S1 signal contain non-split ^{83m}Kr and mispaired events. **Right:** Histogram of the difference of the S1- and S2-delays with Gaussian fit. We select the $\pm 2\sigma$ region around the mean within the dashed orange lines and observe a slight offset to the right.

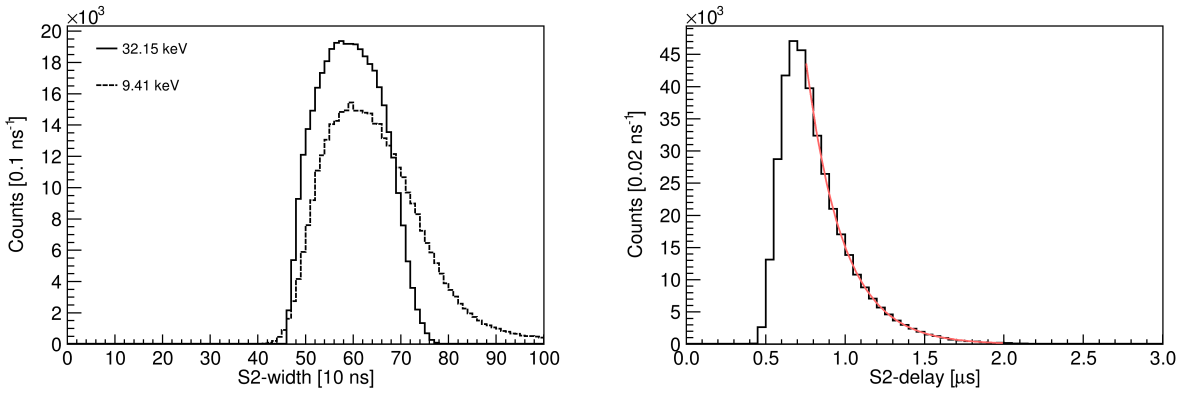

Figure A.2: ^{83m}Kr data at 968 V/cm drift field. **Left:** S2-width histogram of the 32.15 keV and 9.41 keV line. **Right:** S2-delay histogram.

The combined 41.56 keV line is obtained either by a standard single-S1 and single-S2 analysis, to select the events with peaks that were not split for their short delay time, or by purposely merging the two lines.

A.2 Corrections

We apply the same corrections on the ^{83m}Kr lines as described in Section 5.2.1, Chapter 5 for the K-shell line of ^{37}Ar. Due to the higher energy of the source, and thus the higher S1 signal seen by the top SiPMs, we can also correct the S1t signal with a 4th order polynomial showing qualitatively the opposite drift time dependency compared to the S1b signal (cf. Figure 5.8, right).

A.3 Results

Exponential fits of the S1- and S2-delay histograms such as shown in Figure A.2, right, yield on average (161 ± 5) ns for the half-life of the intermediate state, in agreement with the literature value stated above. This confirms that we indeed selected the ^{83m}Kr population.

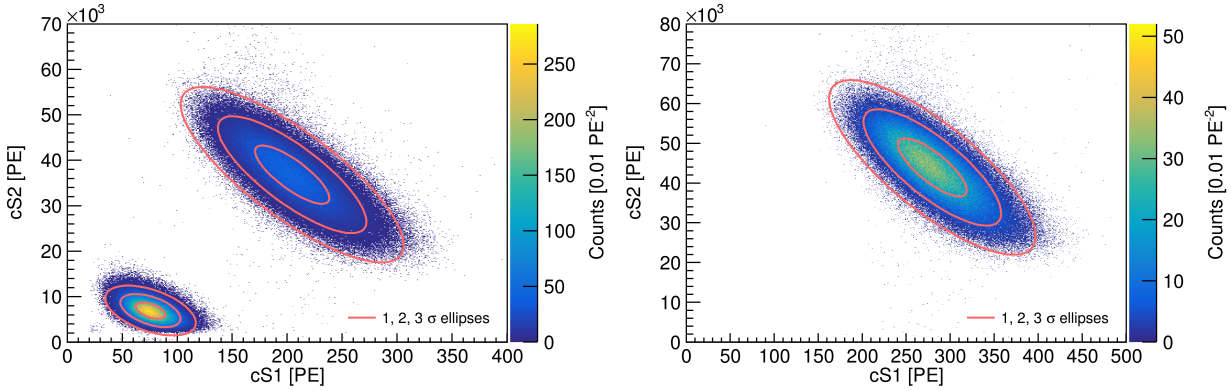

Figure A.3: ^{83m}Kr calibration lines in total S2- versus total S1-space. The anti-correlation is clearly visible. The data was acquired at a drift field of 968 V/cm. The ellipses show the 1, 2, 3 σ regions of the distribution. **Left:** Split 9.41 keV and 32.15 keV lines. **Right:** Merged 41.56 keV line.

Energy [keV]	**Light Yield** [PE/keV]	**Charge Yield** [PE/keV]
9.41	8.048 ± 0.003 (stat.) ± 0.121 (syst.)	737.6 ± 0.4 (stat.) ± 9.8 (syst.)
32.15	6.362 ± 0.002 (stat.) ± 0.096 (syst.)	1145.3 ± 0.4 (stat.) ± 13.6 (syst.)
41.56	6.732 ± 0.002 (stat.) ± 0.101 (syst.)	1056.5 ± 0.3 (stat.) ± 12.8 (syst.)

Table A.2: Light and charge yield values of the ^{83m}Kr lines. The systematic error includes the photosensor gain uncertainty. The values are not DPE/crosstalk corrected.

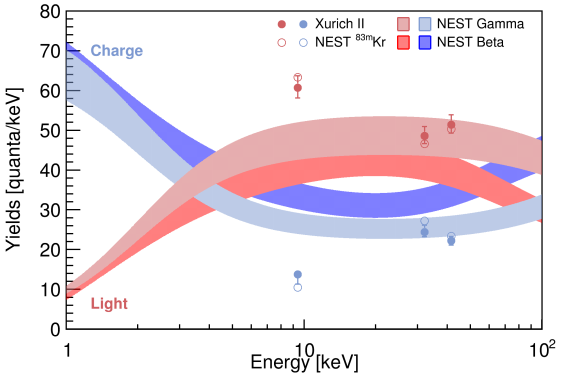

Figure A.4: Comparison of the obtained charge (blue) and light (red) yields at 484 V/cm from the ^{83m}Kr lines to the NEST v2.3.0 [344] gamma, beta and ^{83m}Kr models. The uncertainty bands reflect the typical ± 10 % intrinsic systematical uncertainty of NEST [345].

After applying the described corrections, we show in Figure A.3 the anti-correlated populations from the split and merged calibration lines of ^{83m}Kr in total S2- versus total S1-space. From the means of the ^{83m}Kr ellipses at 968 V/cm, we obtain the light and charge yield values shown in Table A.2. The uncertainties reflect the statistical errors on the mean of the yields and the systematic errors from the photosensor gain uncertainties. The discussion of the systematics, in particular the limitation of the ^{83m}Kr charge yield precision can be found in Section 6.3, Chapter 6.

In Figure A.4, we show the comparison of the light and charge yields of ^{83m}Kr at 484 V/cm to NEST v2.3.0 [344] predictions and find a similar agreement as in Figure 5.20, Chapter 5. The yield at 9.41 keV, however, matches better with the ^{83m}Kr model at this drift field than at 968 V/cm.

Appendix B

Dimensioning of the Pressure Relief Valve and Tubing for BoX

By law, the operation of a pressure vessel of the size of BoX requires a protection against exceeding of the maximal allowable working pressure. For this reason, a pressure relief valve, set to the maximal working pressure of 90 bar, was added for which we show here the design calculation. A pressure increase in the assembly can only be caused either by overfilling or by external heating. The former event would be due to a recuperation of a too large amount of LXe that warms up to room temperature and thus leads to an excess of the maximal allowed working pressure. This case requires the recuperation of 670 kg of xenon. Such a large amount exceeds the capacity of the inner vessel of the cryostat and the gas recuperation system by far. The pressure vessel BoX is designed for a maximum xenon load of $m_{\mathrm{Xe}} = 450\,\mathrm{kg}$ which leads to an internal pressure of 66.5 bar at a typical temperature of 296 K. The current xenon inventory is 347 kg and is internally well documented. Therefore, an eventuation of the case of overfilling is not possible under normal operation. An accidental event of external heating by a fire can on the other hand not be completely excluded. Below, we therefore investigate the event of external heating of a maximally filled vessel. All gas properties used here and subsequently are based on Reference [191].

B.1 Scenario

The pressure vessel is in an environment with non-flammable construction material and objects. It stands on a concrete floor and is surrounded by an aluminium structure. Only the acrylic glass cladding of the structure and possibly stored packaging material in the laboratory are flammable. Chemicals like ethanol and acetone are only used in small quantities and are stored at adequate distance to the vessel. However, nearby electrical installations and devices present a potential fire hazard. The PTR compressor, the xenon recirculation pump, the getter and the electrical cabinet are in close vicinity to BoX. These are located at typical distances of $1 - 2\,\mathrm{m}$. For this reason, we investigate a typical fire scenario in which, for simplicity, a spherical fire of a radius of $R_{\mathrm{fire}} = 0.5\,\mathrm{m}$ burns at a distance of $a = 2\,\mathrm{m}$ to the fire source. We assume a fire duration of $2\,\mathrm{h} = 7200\,\mathrm{s}$. However, this does not restrict the validity of our calculation, since, as we shall see later, the vessel would already be completely vented by that time. The temporal temperature evolution of the fire follows the temperature-time-curve according to DIN 4102-2 [400]:

$$T_{\mathrm{fire}}(t) = 296\,[\mathrm{K}] + 345\,[\mathrm{K}] \cdot \log_{10}(\frac{2}{15\,[\mathrm{s}]}t + 1) \quad . \tag{B.1}$$

The cross-section $A_0 = \pi r^2 = 0.68\,\mathrm{m}^2$ of the vessel with a mean outer radius $r = 0.465\,\mathrm{m}$ is, according to the Stefan-Boltzmann law, exposed to a black-body radiation power of

$$P(t) = \frac{R_{\mathrm{fire}}^2}{a^2}\sigma A_0 T_{\mathrm{fire}}^4(t) \quad , \tag{B.2}$$

where σ is the Stefan-Boltzmann constant. Since for a fire case radiation is the dominant heat transfer mechanism, over convection and conduction, we neglect these effects here. To describe a conservative situation and because we expect an overall warm environment in case of a fire, we neglect the emission of radiation from the vessel onto the environment as well. Furthermore, we assume that the reflective insulation of the vessel is ineffective or melted and that thus the vessel absorbes the radiation perfectly. Note that this is a very conservative approach as the metallised insulation foil is fireproof with a fire protection class M1 and is 97 % reflective against infrared radiation [401]. Thus, as long as the vessel is not in direct contact with the flames, we expect a large time delay in the warming process of the vessel.

B.2 Time Delay below the Set Pressure

First, we calculate the time delay in this scenario between the start of the fire at $t_1 = 0\,\mathrm{s}$ to the point in time t_2 when the set pressure of 90 bar of the safety relief valve is reached. This pressure corresponds to a vessel temperature of 314 K. For this thermal change of state to happen, the following heat has to be transferred by radiation onto the vessel:

$$Q^{1\to2} = c_{\mathrm{SS}} m_{\mathrm{SS}} \Delta T_{12} + m_{\mathrm{Xe}} \Delta H^{1\to2} = 5139\,\mathrm{kJ} \quad . \tag{B.3}$$

Here, we denote the specific heat capacity of the stainless steel 1.4404 by $c_{\mathrm{SS}} = 0.5\,\mathrm{kJ/(kg \cdot K)}$ and the mass of the spherical shell of the container with $m_{\mathrm{SS}} = 316\,\mathrm{kg}$. This assumes a mean wall thickness of 15 mm and a mass density of $8000\,\mathrm{kg/m^3}$ [375]. We further denote the temperature increase with $\Delta T_{12} = T_2 - T_1 = 18\,\mathrm{K}$ and the enthalpy change of the gas with $\Delta H^{1\to2} = 5.1\,\mathrm{kJ/kg}$. The container absorbs thermal energy over time:

$$\Delta E_{\mathrm{fire}} = \int_{t_1=0\,\mathrm{s}}^{t_2} P(t)\,\mathrm{d}t \quad . \tag{B.4}$$

With Equation B.2, we obtain $Q^{1\to2} = \Delta E_{\mathrm{fire}}^{1\to2}$ at $t_2 = 2020\,\mathrm{s}$ and $T_{\mathrm{fire}} = 1135\,\mathrm{K}$.

B.3 Gas Blowing above the Set Pressure

We calculate the amount of gas that needs to be released per time in order to keep the inner pressure in the vessel constant at 90 bar. To this end, we consider the density change of xenon with temperature for an isobaric process, see Figure B.1. Due to the different density derivatives, we distinguish two phases above 314 K:

Phase I
Temperature range: $314 - 350\,\mathrm{K}$
Mean enthalpy change: $\Delta H^{2\to3}/\Delta T_{23} = 0.73\,\mathrm{kJ/(kg \cdot K)}$
Mean xenon mass (75 %): 337.5 kg

Phase II
Temperature range: $> 350\,\mathrm{K}$
Mean enthalpy change: $\Delta H^{3\to4}/\Delta T_{23} = 0.21\,\mathrm{kJ/(kg \cdot K)}$
Mean xenon mass (25 %): 112.5 kg

To avoid a differential equation, we assume a constant amount of xenon within the phases.

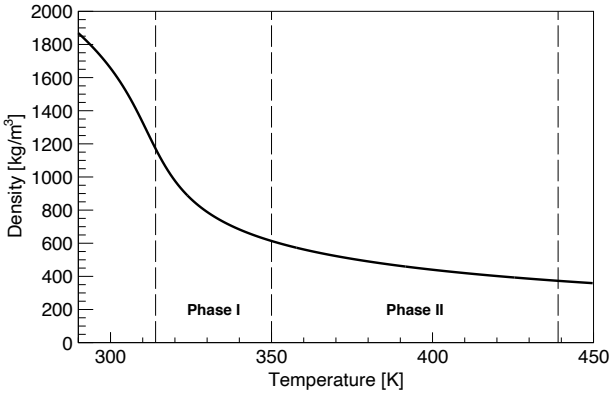

Figure B.1: Mass density of xenon on the 90 bar isobar [191]. We distinguish two phases after the set pressure of the pressure relief valve is reached: Phase I is the range of the fast density change between 314 K and 350 K, and Phase II is located above 350 K.

B.3.1 Phase I

Following Equation B.4, we find that the heat $Q^{2\to3}$, needed to increase the temperature of the vessel by $\Delta T_{23} = 36\,\mathrm{K}$ to 350 K, is transferred from the fire onto the vessel within the time window $[t_2, t_3] = [2020, 4830]\,\mathrm{s}$. Hence, in this phase, we deduce a mean temperature increase rate of the vessel of

$$\frac{\Delta T_{23}}{t_3 - t_2} = 0.013\,\mathrm{K/s} \quad . \tag{B.5}$$

To keep the inner pressure constant at the maximum allowable working pressure, the density of the contained xenon gas needs to decrease by $\Delta\rho_{23}/\Delta T_{23} = -15.8\,\mathrm{kg/(m^3 \cdot K)}$ by means of blowing to the outside. This corresponds to a rate of change of xenon mass of $\Delta m_{23}/\Delta T_{23} = -5.9\,\mathrm{kg/K}$ for a volume of $0.382\,\mathrm{m^3}$. The product with the temperature increase rate from Equation B.5 yields a required blowing rate of $\Delta m_{23}/(t_3 - t_2) = -0.077\,\mathrm{kg/s}$.

B.3.2 Phase II

According to our assumption, Phase II ends at $t_4 = 7200\,\mathrm{s}$. Analogously to the above calculations, we obtain, in this phase, a temperature rise of $\Delta T_{34} = 89\,\mathrm{K}$ by integration. Hence, the mean temperature increase rate of the vessel in this phase is

$$\frac{\Delta T_{34}}{t_4 - t_3} = 0.038\,\mathrm{K/s} \quad . \tag{B.6}$$

The required density change in this phase is $\Delta\rho_{34}/\Delta T_{34} = -1.06\,\mathrm{kg/(m^3 \cdot K)}$ which corresponds to a rate of change of mass of $\Delta m_{34}/\Delta T_{34} = -0.4\,\mathrm{kg/K}$. We obtain a required blowing rate of $\Delta m_{34}/(t_4 - t_3) = -0.015\,\mathrm{kg/s}$ which is, due to the lower dependence of the density on the temperature (cf. Figure B.1), smaller than the one in Phase I.

B.4 Mass Flow Through the Safety Relief Valve

The safety relief valve in the assembly has a certified discharge coefficient of $K_{\mathrm{dr}} = 0.035$ for gases and a seat diameter of 5 mm, which corresponds to a cross-section of $A = 2 \times 10^{-5}\,\mathrm{m^2}$ [402]. According to AD 2000-Merkblatt A 2 [391], the following formula is used to calculate the mass flow:

$$\dot{m} = K_{\mathrm{dr}} A \sqrt{\frac{p_{\mathrm{in}}}{\nu_{\mathrm{in}}}} \sqrt{2\frac{\kappa}{\kappa - 1}\left[\left(\frac{p_{\mathrm{out}}}{p_{\mathrm{in}}}\right)^{\frac{2}{\kappa}}_{\mathrm{crit.}} - \left(\frac{p_{\mathrm{out}}}{p_{\mathrm{in}}}\right)^{\frac{\kappa+1}{\kappa}}_{\mathrm{crit.}}\right]} \quad . \tag{B.7}$$

The maximum mass flow is required in Phase I. For this reason we utilise the thermodynamical properties of xenon at t_2. For a heat capacity ratio of $\kappa = C_p/C_V = 8.3$, a specific volume of $\nu_{\text{in}} = 8.5 \times 10^{-4}\,\text{m}^3/\text{kg}$ inside of the vessel, and a critical pressure ratio [403] of

$$\left(\frac{p_{\text{out}}}{p_{\text{in}}}\right)_{\text{crit.}} = \left(\frac{2}{\kappa+1}\right)^{\frac{\kappa}{\kappa-1}} = 0.17 \quad , \tag{B.8}$$

we obtain a mass flow of $0.078 - 0.082\,\text{kg/s}$ at an inner pressure of $90 - 99\,\text{bar}$. At this rate the vessel empties completely, or at least sufficiently for the safety relief valve to close again, within $\sim 5770\,\text{s}$ after the start of the fire. Thus, our assumption of a fire that lasts two hours was justified. The calculated mass flow corresponds to a norm volume flow of $50\,\text{m}^3/\text{h}$ and is conservative with regard to the measured air flow rates by the manufacturer above the set pressure of $\mathcal{O}(100\,\text{m}^3/\text{h})$ [402].

B.5 Upstream Mass Flow

It remains to be shown that the dimensions of the tubing, fittings and the valves do not restrict the calculated mass flow. First, we note that the inner diameter of all involved upstream parts is at least $d = 4.6\,\text{mm}$ [404–407]. The length of the gas path from the vessel to the outside is $l < 400\,\text{mm}$. Xenon is a real, compressible fluid and is in a supercritical state at 90 bar. Moreover, for large pressure differences between the inlet and the outlet of the tubing, we deal with large Reynolds numbers and thus, with turbulent flow. Hence, a calculation of the possible mass flow is not trivial. For the sake of simplicity, we show here, that the required mass flow can already be reached at small pressure differences and conclude that the tubing is not the bottleneck. To this end, we assume that the inlet pressure is $p_1 = 1\,\text{bar}$ only. At this pressure and at a temperature of 314 K, xenon has a viscosity of $\eta = 2.4 \times 10^{-5}\,\text{Pa}\cdot\text{s}$ and a mass density of $\rho_{\text{Xe}} = 5.05\,\text{kg/m}^3$. According to the Hagen-Poiseuille law, modified for compressible fluids, we obtain the mass flow at the outlet as a function of the outlet pressure p_2:

$$\dot{m} = \rho_{\text{Xe}} \frac{\pi (d/2)^4 (p_1 - p_2)}{8\eta l} \frac{p_1 + p_2}{2p_2} \quad . \tag{B.9}$$

Thus, the required mass flow of $0.082\,\text{kg/s}$ is reached at $\Delta p = p1 - p2 = 0.12\,\text{bar}$. This small pressure drop justifies the use of the mass density at 1 bar. The true mass flow through the piping is surely much higher due to the high mass density of the supercritical xenon of $1178\,\text{kg/m}^3$ and its low viscosity of $5.6 \times 10^{-5}\,\text{Pa}\cdot\text{s}$ at 90 bar.

We present another possible approach to estimate the mass flow. As the ratio of the inlet and outlet pressures is above critical, the maximum flow speed in the tubing is independent of the outlet pressure and equal to the speed of sound of $v_{\text{max}} = 170.99\,\text{m/s}$ in the medium at 90 bar. For turbulent flow in a tube, the mean flow speed is approximately $\bar{v} = 0.817 \cdot v_{\text{max}}$. Given the cross-section of the tubing and the density of the compressed xenon, we obtain a mass flow of $\dot{m} = 2.7\,\text{kg/s}$.

We also find that the upstream valve MV-14 (cf. Figure 7.9, Chapter 7) with a flow coefficient $C_{\text{F}} = 0.36\,\text{USG}/(\text{min}\cdot\text{psi})$ [404] does not restrict the mass flow. We apply the following empirical formula from the manufacturer [408] which is valid for small pressure drops $\Delta p < p_1/2$:

$$\dot{m} = \left[0.116\,\frac{\text{m}^3\cdot\text{min}\cdot\text{psi}}{\text{USG}\cdot\text{s}\cdot\text{bar}}\right] \rho_{\text{Xe}} \cdot C_{\text{F}} \cdot p_1 \left(1 - \frac{2\Delta p}{3p_1}\right) \sqrt{\frac{\Delta p}{p}\left(\frac{\rho_{\text{air}}}{\rho_{\text{Xe}}}\right)_{\text{norm.}} \frac{[K^{1/2}]}{T_1}} \quad . \tag{B.10}$$

At the maximum flow rate of $\dot{m} = 0.082\,\text{kg/s}$ through the safety relief valve, the pressure drop over MV-14 is $\Delta p = 1.8\,\text{bar}$. Given the short connection of the pressure vessel to the safety relief valve, this can be assumed to be the dominating contribution. However, it is still below the allowed maximum upstream pressure drop of 3 % on the set pressure of the safety relief valve, which is 2.7 bar, according

to AD 2000-Merkblatt A 2 [391]. The safety relief valve itself features an even higher flow coefficient of $C_{\mathrm{F}} = 0.49\,\mathrm{USG}/(\mathrm{min}\cdot\mathrm{psi})$ [402].

Downstream of the safety relief valve, an elbow deflects the blown gas to the back of the assembly to protect the user. Its inner diameter is 11.4 mm [406] and thus, no downstream flow restriction is expected.

B.6 Conclusion

In view of our calculations, we can conclude that the safety relief valve is able to blow off a higher mass flow than needed to keep the inner pressure at 90 bar for the considered fire scenario and that the maximum allowed inner pressure is not significantly exceeded. The safety relief valve reaches the calculated mass flow already at small excesses above the set pressure [402]. Hence, the allowable working pressure excess of 10 % according to AD 2000-Merkblatt A 403 [391] is left as safety margin for possible deviations and effects that were not considered here. Furthermore, we have shown that the tubing and the valves allow for the required mass flow. Note, that we did not consider an icing of the outlet of the safety relief valve caused by the rapid decompression of the blown gas. However, this is only likely to happen if the safety relief valve opens and closes repeatedly and is improbable in case of a fire and the use of a proportionally opening and closing relief valve. We did not consider here the case of overfilling due to the very well documented xenon inventory and the capacity limitations of the other subsystems. However, even if overfilled with LXe, the isochoric warming after a recuperation is a slow process of the order of several days (cf. Figure 7.14, left, Chapter 7) which is unlikely to exceed the capacity of the pressure relief valve in the absence of an external heat source.

List of Acronyms

$0\nu\beta\beta$	–	neutrinoless double beta decay
$2\nu\beta\beta$	–	two-neutrino double beta decay
ADC	–	Analog-to-Digital Converter
AFT	–	Area Fraction Top cut
ALP	–	Axion-Like Particle
APD	–	Avalanche PhotoDiode
BoX	–	Ball of Xenon
BSM	–	physics Beyond the Standard Model
CAD	–	Computer-Aided Design
CCD	–	Charge-Coupled Device
CDM	–	Cold Dark Matter
CE	–	Collection Efficiency
CEνNS	–	Coherent Elastic Neutrino-Nucleus Scattering
CL	–	Confidence Level
CMB	–	Cosmic Microwave Background
CNB	–	Cosmic Neutrino Background
CP	–	Charge conjugation Partity
DAQ	–	Data AcQuisition
DARWIN	–	DARk matter WImp search with liquid xenoN
DM	–	Dark Matter
DPE	–	Double Photoelectron Emission
ER	–	Electronic Recoil
FEA	–	Finite Element Analysis
FIMP	–	Feably Interacting Massive Particle
FV	–	Fiducial Volume (cut)
Geant4	–	Geometry and tracking 4
GXe	–	Gaseous Xenon
HE	–	Heat Exchanger
IR	–	InfraRed
LCE	–	Light collection Efficiency
LED	–	Light-Emitting Diode
LET	–	Linear Energy Transfer
LHC	–	Large hadron Collider
LKP	–	Lightest Kaluza-Klein Particle
LMTD	–	Log Mean Temperature Difference
LN_2	–	Liquid Nitrogen
LNGS	–	Laboratori Nazionali del Gran Sasso
LSP	–	Lightest Supersymmetric Particle
LTP	–	Lightest T-odd Particle
LXe	–	Liquid Xenon
LY	–	Light Yield
LZ	–	LUX-ZEPLIN

MACHO	–	Massive Astrophysical Compact Halo Object
Macro	–	Macroscopic (dark matter)
MC	–	Monte Carlo
MLI	–	Multi-Layer Insulation
MOG	–	MOdified Gravity
MOND	–	MOdified Newtonian Dynamics
MSSM	–	Minimal Supersymmetric Standard Model
NEST	–	Noble Element Simulation Technique
NIM	–	Nuclear Instrumentation Modul
NIST	–	National Institute of Standards and Technology
NR	–	Nuclear Recoil
NTU	–	Number of Transfer Units
P&ID	–	Piping and Instrumentation Diagram
PC	–	Personal Computer
PCB	–	Printed Circuit Board
PCI	–	Peripheral Component Interconnect
PED	–	Pressure Equipment Directive
PDE	–	Photon Detection Efficency
PE	–	PhotoElectron
PID	–	Proportional–Integral–Derivative
PMT	–	PhotoMultiplier Tube
PSD	–	Pulse-Shape Discrimination
PSI	–	Paul Scherrer Institute
PTFE	–	PolyTetraFluoroEthylene
PTR	–	Pulse Tube Refrigerator
QE	–	Quantum Efficiency
QY	–	charge (Q) Yield
R&D	–	Research and Development
RGA	–	Residual Gas Analyser
SBC	–	Scintillating Bubble Chamber
SD	–	Spin Dependent
SE	–	Single Electron
SI	–	Spin Independent
SINQ	–	Swiss Spallation Neutron Source
SiPM	–	Silicon PhotoMultiplier
slpm	–	standard litre per minute
SM	–	Standard Model of particle physics
SS	–	Stainless Steel
superWIMP	–	superWeakly Interacing Massive Particle
SUSY	–	SUperSYmmetry
TeVeS	–	Tensor–Vector–Scalar gravity
TPC	–	Time Projection Chamber
UED	–	Universal Extra Dimension
UZH	–	University of Zurich
VME	–	Versa Module Europa
VUV	–	Vacuum UltraViolet
WDM	–	Warm Dark Matter
WIMP	–	Weakly Interacting Massive Particle
ZLE	–	Zero Length Encoding

Bibliography

[1] XENON collaboration, E. Aprile et al., *Dark Matter Search Results from a One Ton-Year Exposure of XENON1T*, *Phys. Rev. Lett.* **121** (2018) 111302, [1805.12562].

[2] LUX collaboration, D. S. Akerib et al., *Results from a search for dark matter in the complete LUX exposure*, *Phys. Rev. Lett.* **118** (2017) 021303, [1608.07648].

[3] PandaX-II collaboration, Q. Wang et al., *Results of dark matter search using the full PandaX-II exposure*, *Chin. Phys. C* **44** (2020) 125001, [2007.15469].

[4] DarkSide collaboration, P. Agnes et al., *DarkSide-50 532-day Dark Matter Search with Low-Radioactivity Argon*, *Phys. Rev. D* **98** (2018) 102006, [1802.07198].

[5] XENON collaboration, E. Aprile et al., *Projected WIMP sensitivity of the XENONnT dark matter experiment*, *J. Cosmol. Astropart. Phys.* **11** (2020) 031, [2007.08796].

[6] B. J. Mount et al., *LUX-ZEPLIN (LZ) Technical Design Report*, 1703.09144.

[7] PandaX collaboration, H. Zhang et al., *Dark matter direct search sensitivity of the PandaX-4T experiment*, *Sci. China Phys. Mech. Astron.* **62** (2019) 31011, [1806.02229].

[8] DARWIN collaboration, J. Aalbers et al., *DARWIN: towards the ultimate dark matter detector*, *J. Cosmol. Astropart. Phys.* **11** (2016) 017, [1606.07001].

[9] DarkSide-20k collaboration, C. E. Aalseth et al., *DarkSide-20k: A 20 tonne two-phase LAr TPC for direct dark matter detection at LNGS*, *Eur. Phys. J. Plus* **133** (2018) 131, [1707.08145].

[10] E. M. Boulton et al., *Calibration of a two-phase xenon time projection chamber with a ^{37}Ar source*, *J. Instrum.* **12** (2017) P08004, [1705.08958].

[11] LUX collaboration, D. S. Akerib et al., *Improved Measurements of the β-Decay Response of Liquid Xenon with the LUX Detector*, *Phys. Rev. D* **100** (2019) 022002, [1903.12372].

[12] M. Alfonsi, "Injection and removal of the calibration isotope ^{37}Ar in the XENON1T detector." LIDINE 2019, Manchester, August, 2019.

[13] L. Baudis, Y. Biondi, C. Capelli, M. Galloway, S. Kazama, A. Kish, P. Pakarha, F. Piastra and J. Wulf, *A Dual-phase Xenon TPC for Scintillation and Ionisation Yield Measurements in Liquid Xenon*, *Eur. Phys. J.* **C78** (2018) 351, [1712.08607].

[14] J. Wulf, *Direct Dark Matter Search with XENON1T and Developments for Multi-Ton Liquid Xenon Detectors*. PhD thesis, University of Zurich, 2018.

[15] F. Girard, *Design and Construction of Xenoscope and Photosensor Charaterisation for the DARWIN Observatory (preliminary)*. PhD thesis, University of Zurich, to be published, 2022.

[16] DARWIN collaboration, F. Agostini et al., *Sensitivity of the DARWIN observatory to the neutrinoless double beta decay of ^{136}Xe*, *Eur. Phys. J. C* **80** (2020) 808, [2003.13407].

[17] C. Hils, *Studie von internen Kalibrationsmethoden für Flüssig-Xenon TPCs zur direkten Suche nach Dunkler Materie*, Diploma thesis, Johannes Gutenberg University Mainz, 2014.

[18] M. Szydagis, N. Barry, K. Kazkaz, J. Mock, D. Stolp, M. Sweany, M. Tripathi, S. Uvarov, N. Walsh and M. Woods, *NEST: A Comprehensive Model for Scintillation Yield in Liquid Xenon*, *J. Instrum.* **6** (2011) P10002, [1106.1613].

[19] Swiss Safety Center AG. [Online] Available: `https://www.safetycenter.ch/`, (accessed 2021, August 12).

[20] Suva. [Online] Available: `https://www.suva.ch/`, (accessed 2021, August 12).

[21] SVTI Schweizerischer Verein für technische Inspektionen. [Online] Available: `https://www.svti.ch/kesselinspektorat`, (accessed 2021, August 12).

[22] Helbling Technik AG. [Online] Available: `https://www.helbling.ch/`, (accessed 2021, May 26).

[23] S. Hochrein, *Calibration of the first dual-phase xenon time projection chamber with silicon photo-multiplier readout*, Bachelor's thesis, University of Zurich, 2019.

[24] F. Zwicky, *Die Rotverschiebung von extragalaktischen Nebeln*, *Helv. Phys. Acta* **6** (1933) 110–127.

[25] H. Poincaré, *La Voie lactée et la théorie des gaz*, *Bulletin de la Société astronomique de France* **20** (1906) 156–165.

[26] W. Thomson, Baron Kelvin, *Baltimore Lectures on Molecular Dynamics and the Wave Theory of Light*. Cambridge Library Collection - Physical Sciences. Cambridge University Press, 2010 (first published in 1904), 10.1017/CBO9780511694523.

[27] J. C. Kapteyn, *First Attempt at a Theory of the Arrangement and Motion of the Sidereal System*, *Astrophys. J.* **55** (May, 1922) 302.

[28] J. H. Oort, *The force exerted by the stellar system in the direction perpendicular to the galactic plane and some related problems*, *Bulletin of the Astronomical Institutes of the Netherlands* **6** (Aug., 1932) 249.

[29] Planck collaboration, N. Aghanim et al., *Planck 2018 results. VI. Cosmological parameters*, *Astron. Astrophys.* **641** (2020) A6, [1807.06209].

[30] V. C. Rubin and W. K. Ford, Jr., *Rotation of the Andromeda Nebula from a Spectroscopic Survey of Emission Regions*, *Astrophys. J.* **159** (1970) 379–403.

[31] K. C. Freeman, *On the disks of spiral and SO Galaxies*, *Astrophys. J.* **160** (1970) 811.

[32] V. C. Rubin, W. K. Ford, Jr. and N. Thonnard, *Extended rotation curves of high-luminosity spiral galaxies. IV. Systematic dynamical properties, Sa through Sc*, *Astrophys. J. Lett.* **225** (1978) L107–L111.

[33] V. C. Rubin, N. Thonnard and W. K. Ford, Jr., *Rotational properties of 21 SC galaxies with a large range of luminosities and radii, from NGC 4605 (R = 4 kpc) to UGC 2885 (R = 122 kpc)*, *Astrophys. J.* **238** (1980) 471.

[34] V. C. Rubin, W. K. Ford, Jr., N. Thonnard and D. Burstein, *Rotational properties of 23 SB galaxies*, *Astrophys. J.* **261** (1982) 439.

[35] V. C. Rubin, D. Burstein, W. K. Ford, Jr. and N. Thonnard, *Rotation velocities of 16 SA galaxies and a comparison of Sa, Sb, and SC rotation properties*, *Astrophys. J.* **289** (1985) 81.

[36] K. G. Begeman, A. H. Broeils and R. H. Sanders, *Extended rotation curves of spiral galaxies: dark haloes and modified dynamics*, *Mon. Not. Roy. Astron. Soc.* **249** (Apr., 1991) 523.

[37] Y. Sofue and V. Rubin, *Rotation curves of spiral galaxies*, *Ann. Rev. Astron. Astrophys.* **39** (2001) 137–174, [astro-ph/0010594].

[38] D. H. Rogstad and G. S. Shostak, *Gross Properties of Five Scd Galaxies as Determined from 21-centimeter Observations*, *Astrophys. J.* **176** (Sept., 1972) 315.

[39] M. S. Roberts, *The Rotation Curve of Galaxies*, in *Dynamics of the Solar Systems* (A. Hayli, ed.), vol. 69, p. 331, Jan., 1975.

[40] D. Clowe, A. Gonzalez and M. Markevitch, *Weak lensing mass reconstruction of the interacting cluster 1E0657-558: Direct evidence for the existence of dark matter*, *Astrophys. J.* **604** (2004) 596–603, [astro-ph/0312273].

[41] J. Merten et al., *Creation of cosmic structure in the complex galaxy cluster merger Abell 2744*, *Mon. Not. Roy. Astron. Soc.* **417** (2011) 333–347, [1103.2772].

[42] A. A. Penzias and R. W. Wilson, *A Measurement of excess antenna temperature at 4080 Mc/s*, *Astrophys. J.* **142** (1965) 419–421.

[43] D. J. Fixsen, *The Temperature of the Cosmic Microwave Background*, *Astrophys. J.* **707** (2009) 916–920, [0911.1955].

[44] Planck collaboration, N. Aghanim et al., *Planck 2018 results. I. Overview and the cosmological legacy of Planck*, *Astron. Astrophys.* **641** (2020) A1, [1807.06205].

[45] COBE collaboration, G. F. Smoot et al., *Structure in the COBE differential microwave radiometer first year maps*, *Astrophys. J. Lett.* **396** (1992) L1–L5.

[46] C. L. Bennett, A. Banday, K. M. Gorski, G. Hinshaw, P. Jackson, P. Keegstra, A. Kogut, G. F. Smoot, D. T. Wilkinson and E. L. Wright, *Four year COBE DMR cosmic microwave background observations: Maps and basic results*, *Astrophys. J. Lett.* **464** (1996) L1–L4, [astro-ph/9601067].

[47] WMAP collaboration, G. Hinshaw et al., *Nine-Year Wilkinson Microwave Anisotropy Probe (WMAP) Observations: Cosmological Parameter Results*, *Astrophys. J. Suppl.* **208** (2013) 19, [1212.5226].

[48] WMAP collaboration, C. L. Bennett et al., *Nine-Year Wilkinson Microwave Anisotropy Probe (WMAP) Observations: Final Maps and Results*, *Astrophys. J. Suppl.* **208** (2013) 20, [1212.5225].

[49] Planck collaboration, Y. Akrami et al., *Planck 2018 results. VII. Isotropy and Statistics of the CMB*, *Astron. Astrophys.* **641** (2020) A7, [1906.02552].

[50] K. Freese, *Review of Observational Evidence for Dark Matter in the Universe and in upcoming searches for Dark Stars*, *EAS Publ. Ser.* **36** (2009) 113–126, [0812.4005].

[51] E. W. Kolb and M. S. Turner, *The early universe*. Frontiers in physics. Westview Press, Boulder, CO, 1990, 10.1201/9780429492860.

[52] E. A. Baltz, *Dark matter candidates*, *eConf* **C040802** (2004) L002, [astro-ph/0412170].

[53] M. Davis, G. Efstathiou, C. S. Frenk and S. D. M. White, *The evolution of large-scale structure in a universe dominated by cold dark matter*, *Astrophys. J.* **292** (May, 1985) 371–394.

[54] M. Franx, G. Illingworth and T. de Zeeuw, *The Ordered Nature of Elliptical Galaxies: Implications for Their Intrinsic Angular Momenta and Shapes*, *Astrophys. J.* **383** (Dec., 1991) 112.

[55] S. Tulin, H.-B. Yu and K. M. Zurek, *Beyond Collisionless Dark Matter: Particle Physics Dynamics for Dark Matter Halo Structure*, *Phys. Rev. D* **87** (2013) 115007, [1302.3898].

[56] J. S. Bullock and M. Boylan-Kolchin, *Small-Scale Challenges to the ΛCDM Paradigm*, *Ann. Rev. Astron. Astrophys.* **55** (2017) 343–387, [1707.04256].

[57] M. R. Lovell, C. S. Frenk, V. R. Eke, A. Jenkins, L. Gao and T. Theuns, *The properties of warm dark matter haloes*, *Mon. Not. Roy. Astron. Soc.* **439** (2014) 300–317, [1308.1399].

[58] B. Audren, J. Lesgourgues, G. Mangano, P. D. Serpico and T. Tram, *Strongest model-independent bound on the lifetime of Dark Matter*, *J. Cosmol. Astropart. Phys.* **12** (2014) 028, [1407.2418].

[59] C. G. Lacey and J. P. Ostriker, *Massive black holes in galactic halos?*, *Astrophys. J.* **299** (Dec., 1985) 633–652.

[60] B. Moore, *An Upper Limit to the Mass of Black Holes in the Halo of the Galaxy*, *Astrophys. J. Lett.* **413** (Aug., 1993) L93, [astro-ph/9306004].

[61] H.-W. Rix and G. Lake, *Can the dark matter be 10^6 solar mass objects?*, *Astrophys. J. Lett.* **417** (1993) L1, [astro-ph/9308022].

[62] N. Afshordi, P. McDonald and D. N. Spergel, *Primordial black holes as dark matter: The Power spectrum and evaporation of early structures*, *Astrophys. J. Lett.* **594** (2003) L71–L74, [astro-ph/0302035].

[63] MACHO collaboration, C. Alcock et al., *The MACHO project: Microlensing results from 5.7 years of LMC observations*, *Astrophys. J.* **542** (2000) 281–307, [astro-ph/0001272].

[64] EROS collaboration, C. Afonso et al., *Limits on galactic dark matter with 5 years of EROS SMC data*, *Astron. Astrophys.* **400** (2003) 951–956, [astro-ph/0212176].

[65] W. Hu, R. Barkana and A. Gruzinov, *Cold and fuzzy dark matter*, *Phys. Rev. Lett.* **85** (2000) 1158–1161, [astro-ph/0003365].

[66] S. Tremaine and J. E. Gunn, *Dynamical Role of Light Neutral Leptons in Cosmology*, *Phys. Rev. Lett.* **42** (1979) 407–410.

[67] S. D. M. White, C. S. Frenk and M. Davis, *Clustering in a neutrino-dominated universe*, *Astrophys. J.* **274** (Nov., 1983) L1–L5.

[68] G. Bertone, D. Hooper and J. Silk, *Particle dark matter: Evidence, candidates and constraints*, *Phys. Rept.* **405** (2005) 279–390, [hep-ph/0404175].

[69] J. L. Feng et al., *Planning the Future of U.S. Particle Physics (Snowmass 2013): Chapter 4: Cosmic Frontier*, in *Community Summer Study 2013: Snowmass on the Mississippi*, Jan., 2014. 1401.6085.

[70] G. Jungman, M. Kamionkowski and K. Griest, *Supersymmetric dark matter*, *Phys. Rept.* **267** (1996) 195–373, [hep-ph/9506380].

[71] L. Roszkowski, E. M. Sessolo and S. Trojanowski, *WIMP dark matter candidates and searches—current status and future prospects*, *Rept. Prog. Phys.* **81** (2018) 066201, [1707.06277].

[72] G. Steigman, B. Dasgupta and J. F. Beacom, *Precise Relic WIMP Abundance and its Impact on Searches for Dark Matter Annihilation*, *Phys. Rev. D* **86** (2012) 023506, [1204.3622].

[73] H. Baer, K.-Y. Choi, J. E. Kim and L. Roszkowski, *Dark matter production in the early Universe: beyond the thermal WIMP paradigm*, *Phys. Rept.* **555** (2015) 1–60, [1407.0017].

[74] J. L. Feng and J. Kumar, *The WIMPless Miracle: Dark-Matter Particles without Weak-Scale Masses or Weak Interactions*, *Phys. Rev. Lett.* **101** (2008) 231301, [0803.4196].

[75] L. J. Hall, K. Jedamzik, J. March-Russell and S. M. West, *Freeze-In Production of FIMP Dark Matter*, *J. High Energy Phys.* **03** (2010) 080, [0911.1120].

[76] J. L. Feng, A. Rajaraman and F. Takayama, *Superweakly interacting massive particles*, *Phys. Rev. Lett.* **91** (2003) 011302, [hep-ph/0302215].

[77] B. W. Lee and S. Weinberg, *Cosmological Lower Bound on Heavy Neutrino Masses*, *Phys. Rev. Lett.* **39** (1977) 165–168.

[78] K. Griest and M. Kamionkowski, *Unitarity Limits on the Mass and Radius of Dark Matter Particles*, *Phys. Rev. Lett.* **64** (1990) 615.

[79] D. Hooper and S. Profumo, *Dark Matter and Collider Phenomenology of Universal Extra Dimensions*, *Phys. Rept.* **453** (2007) 29–115, [hep-ph/0701197].

[80] A. Birkedal, A. Noble, M. Perelstein and A. Spray, *Little Higgs dark matter*, *Phys. Rev. D* **74** (2006) 035002, [hep-ph/0603077].

[81] L. Visinelli and P. Gondolo, *Dark Matter Axions Revisited*, *Phys. Rev. D* **80** (2009) 035024, [0903.4377].

[82] R. D. Peccei and H. R. Quinn, *CP Conservation in the Presence of Instantons*, *Phys. Rev. Lett.* **38** (1977) 1440–1443.

[83] F. Wilczek, *Problem of Strong P and T Invariance in the Presence of Instantons*, *Phys. Rev. Lett.* **40** (1978) 279–282.

[84] S. Weinberg, *A New Light Boson?*, *Phys. Rev. Lett.* **40** (1978) 223–226.

[85] S. Dodelson and L. M. Widrow, *Sterile-neutrinos as dark matter*, *Phys. Rev. Lett.* **72** (1994) 17–20, [hep-ph/9303287].

[86] M. Fabbrichesi, E. Gabrielli and G. Lanfranchi, *The Dark Photon*, 2005.01515.

[87] E. W. Kolb, D. J. H. Chung and A. Riotto, *WIMPzillas!*, *AIP Conf. Proc.* **484** (1999) 91–105, [hep-ph/9810361].

[88] A. Kusenko and M. E. Shaposhnikov, *Supersymmetric Q-balls as dark matter*, *Phys. Lett. B* **418** (1998) 46–54, [hep-ph/9709492].

[89] L. Bergstrom, *Dark Matter Candidates*, *New J. Phys.* **11** (2009) 105006, [0903.4849].

[90] J. Silk et al., *Particle Dark Matter: Observations, Models and Searches*. Cambridge Univ. Press, Cambridge, 2010, 10.1017/CBO9780511770739.

[91] D. M. Jacobs, G. D. Starkman and B. W. Lynn, *Macro Dark Matter*, *Mon. Not. Roy. Astron. Soc.* **450** (2015) 3418–3430, [1410.2236].

[92] EROS-2 collaboration, P. Tisserand et al., *Limits on the Macho Content of the Galactic Halo from the EROS-2 Survey of the Magellanic Clouds*, *Astron. Astrophys.* **469** (2007) 387–404, [astro-ph/0607207].

[93] M. R. S. Hawkins, *A new look at microlensing limits on dark matter in the Galactic halo*, *Astron. Astrophys.* **575** (2015) A107, [1503.01935].

[94] M. Milgrom, *A Modification of the Newtonian dynamics as a possible alternative to the hidden mass hypothesis*, *Astrophys. J.* **270** (1983) 365–370.

[95] J. D. Bekenstein, *Relativistic gravitation theory for the MOND paradigm*, *Phys. Rev. D* **70** (2004) 083509, [astro-ph/0403694].

[96] S. Boran, S. Desai, E. O. Kahya and R. P. Woodard, *GW170817 Falsifies Dark Matter Emulators*, *Phys. Rev. D* **97** (2018) 041501, [1710.06168].

[97] P. van Dokkum et al., *A galaxy lacking dark matter*, *Nature* **555** (2018) 629–632, [1803.10237].

[98] F. Kahlhoefer, *Review of LHC Dark Matter Searches*, *Int. J. Mod. Phys. A* **32** (2017) 1730006, [1702.02430].

[99] Fermi-LAT collaboration, M. Ackermann et al., *Searching for Dark Matter Annihilation from Milky Way Dwarf Spheroidal Galaxies with Six Years of Fermi Large Area Telescope Data*, *Phys. Rev. Lett.* **115** (2015) 231301, [1503.02641].

[100] H.E.S.S. collaboration, H. Abdallah et al., *Search for dark matter annihilations towards the inner Galactic halo from 10 years of observations with H.E.S.S.*, *Phys. Rev. Lett.* **117** (2016) 111301, [1607.08142].

[101] CTA Consortium collaboration, M. Doro et al., *Probing Dark Matter and Fundamental Physics with the Cherenkov Telescope Array*, 2106.03582.

[102] IceCube collaboration, M. G. Aartsen et al., *Search for Neutrinos from Dark Matter Self-Annihilations in the center of the Milky Way with 3 years of IceCube/DeepCore*, *Eur. Phys. J. C* **77** (2017) 627, [1705.08103].

[103] J. Conrad and O. Reimer, *Indirect dark matter searches in gamma and cosmic rays*, *Nature Phys.* **13** (2017) 224–231, [1705.11165].

[104] A. M. Green, *Astrophysical uncertainties on the local dark matter distribution and direct detection experiments*, *J. Phys. G* **44** (2017) 084001, [1703.10102].

[105] J. I. Read, *The Local Dark Matter Density*, *J. Phys. G* **41** (2014) 063101, [1404.1938].

[106] P. Grothaus, M. Fairbairn and J. Monroe, *Directional Dark Matter Detection Beyond the Neutrino Bound*, *Phys. Rev. D* **90** (2014) 055018, [1406.5047].

[107] C. McCabe, *The Earth's velocity for direct detection experiments*, *J. Cosmol. Astropart. Phys.* **02** (2014) 027, [1312.1355].

[108] G. Gelmini and P. Gondolo, *WIMP annual modulation with opposite phase in Late-Infall halo models*, *Phys. Rev. D* **64** (2001) 023504, [hep-ph/0012315].

[109] T. Marrodán Undagoitia and L. Rauch, *Dark matter direct-detection experiments*, *J. Phys. G* **43** (2016) 013001, [1509.08767].

[110] A. L. Fitzpatrick, W. Haxton, E. Katz, N. Lubbers and Y. Xu, *Model Independent Direct Detection Analyses*, 1211.2818.

[111] N. Anand, A. L. Fitzpatrick and W. C. Haxton, *Weakly interacting massive particle-nucleus elastic scattering response*, *Phys. Rev. C* **89** (2014) 065501, [1308.6288].

[112] A. L. Fitzpatrick, W. Haxton, E. Katz, N. Lubbers and Y. Xu, *The Effective Field Theory of Dark Matter Direct Detection*, *J. Cosmol. Astropart. Phys.* **02** (2013) 004, [1203.3542].

[113] XENON collaboration, E. Aprile et al., *Effective field theory search for high-energy nuclear recoils using the XENON100 dark matter detector*, *Phys. Rev. D* **96** (2017) 042004, [1705.02614].

[114] R. H. Helm, *Inelastic and Elastic Scattering of 187-Mev Electrons from Selected Even-Even Nuclei*, *Phys. Rev.* **104** (1956) 1466–1475.

[115] J. D. Lewin and P. F. Smith, *Review of mathematics, numerical factors, and corrections for dark matter experiments based on elastic nuclear recoil*, *Astropart. Phys.* **6** (1996) 87–112.

[116] M. W. Goodman and E. Witten, *Detectability of Certain Dark Matter Candidates*, *Phys. Rev. D* **31** (1985) 3059.

[117] A. K. Drukier, K. Freese and D. N. Spergel, *Detecting Cold Dark Matter Candidates*, *Phys. Rev. D* **33** (1986) 3495–3508.

[118] G. Angloher et al., *Limits on WIMP dark matter using sapphire cryogenic detectors*, *Astropart. Phys.* **18** (2002) 43–55.

[119] CRESST collaboration, M. Bravin et al., *The CRESST dark matter search*, *Astropart. Phys.* **12** (1999) 107–114, [hep-ex/9904005].

[120] PICO collaboration, C. Amole et al., *Data-Driven Modeling of Electron Recoil Nucleation in PICO C_3F_8 Bubble Chambers*, *Phys. Rev. D* **100** (2019) 082006, [1905.12522].

[121] PICO collaboration, C. Amole et al., *Dark matter search results from the PICO-60 CF_3I bubble chamber*, *Phys. Rev. D* **93** (2016) 052014, [1510.07754].

[122] PICO collaboration, C. Amole et al., *Dark Matter Search Results from the Complete Exposure of the PICO-60 C_3F_8 Bubble Chamber*, *Phys. Rev. D* **100** (2019) 022001, [1902.04031].

[123] PICO collaboration, C. Amole et al., *Improved dark matter search results from PICO-2L Run 2*, *Phys. Rev. D* **93** (2016) 061101, [1601.03729].

[124] M. Bressler, P. Campion, V. S. Cushman, A. Morrese, J. M. Wagner, S. Zerbo, R. Neilson, M. Crisler and C. E. Dahl, *A buffer-free concept bubble chamber for PICO dark matter searches*, *J. Instrum.* **14** (2019) P08019, [1905.07367].

[125] P. Klos, J. Menéndez, D. Gazit and A. Schwenk, *Large-scale nuclear structure calculations for spin-dependent WIMP scattering with chiral effective field theory currents*, *Phys. Rev. D* **88** (2013) 083516, [1304.7684].

[126] E. Behnke et al., *Final Results of the PICASSO Dark Matter Search Experiment*, *Astropart. Phys.* **90** (2017) 85–92, [1611.01499].

[127] PICASSO collaboration, M. Barnabe-Heider et al., *Improved spin dependent limits from the PICASSO dark matter search experiment*, *Phys. Lett. B* **624** (2005) 186–194, [hep-ex/0502028].

[128] SuperCDMS collaboration, R. Agnese et al., *Search for Low-Mass Dark Matter with CDMSlite Using a Profile Likelihood Fit*, *Phys. Rev. D* **99** (2019) 062001, [1808.09098].

[129] CDMS-II collaboration, Z. Ahmed et al., *Dark Matter Search Results from the CDMS II Experiment*, *Science* **327** (2010) 1619–1621, [0912.3592].

[130] CDEX collaboration, L. T. Yang et al., *Limits on light WIMPs with a 1 kg-scale germanium detector at 160 eVee physics threshold at the China Jinping Underground Laboratory*, *Chin. Phys. C* **42** (2018) 023002, [1710.06650].

[131] CDEX collaboration, H. Jiang et al., *Limits on Light Weakly Interacting Massive Particles from the First 102.8 kg × day Data of the CDEX-10 Experiment*, *Phys. Rev. Lett.* **120** (2018) 241301, [1802.09016].

[132] EDELWEISS collaboration, V. Sanglard et al., *Final results of the EDELWEISS-I dark matter search with cryogenic heat-and-ionization Ge detectors*, *Phys. Rev. D* **71** (2005) 122002, [astro-ph/0503265].

[133] EDELWEISS collaboration, E. Armengaud et al., *Final results of the EDELWEISS-II WIMP search using a 4-kg array of cryogenic germanium detectors with interleaved electrodes*, *Phys. Lett. B* **702** (2011) 329–335, [1103.4070].

[134] EDELWEISS collaboration, L. Hehn et al., *Improved EDELWEISS-III sensitivity for low-mass WIMPs using a profile likelihood approach*, *Eur. Phys. J. C* **76** (2016) 548, [1607.03367].

[135] CRESST collaboration, A. H. Abdelhameed et al., *First results from the CRESST-III low-mass dark matter program*, *Phys. Rev. D* **100** (2019) 102002, [1904.00498].

[136] CRESST collaboration, G. Angloher et al., *Results on light dark matter particles with a low-threshold CRESST-II detector*, *Eur. Phys. J. C* **76** (2016) 25, [1509.01515].

[137] COSINUS collaboration, G. Angloher et al., *Results from the first cryogenic NaI detector for the COSINUS project*, *J. Instrum.* **12** (2017) P11007, [1705.11028].

[138] SBC, CEνNS Theory Group at IF-UNAM collaboration, L. J. Flores et al., *Physics reach of a low threshold scintillating argon bubble chamber in coherent elastic neutrino-nucleus scattering reactor experiments*, *Phys. Rev. D* **103** (2021) L091301, [2101.08785].

[139] SBC collaboration, P. Giampa, *The Scintillating Bubble Chamber (SBC) Experiment for Dark Matter and Reactor CEvNS*, *PoS* **ICHEP2020** (2021) 632.

[140] D. Baxter et al., *First Demonstration of a Scintillating Xenon Bubble Chamber for Detecting Dark Matter and Coherent Elastic Neutrino-Nucleus Scattering*, *Phys. Rev. Lett.* **118** (2017) 231301, [1702.08861].

[141] C. Levy, S. Fallon, J. Genovesi, D. Khaitan, K. Klimov, J. Mock and M. Szydagis, *Xenon Bubble Chambers for Direct Dark Matter Detection*, *J. Instrum.* **11** (2016) C03003, [1601.05131].

[142] J. Billard, L. Strigari and E. Figueroa-Feliciano, *Implication of neutrino backgrounds on the reach of next generation dark matter direct detection experiments*, *Phys. Rev. D* **89** (2014) 023524, [1307.5458].

[143] C. A. J. O'Hare, *New Definition of the Neutrino Floor for Direct Dark Matter Searches*, *Phys. Rev. Lett.* **127** (2021) 251802, [2109.03116].

[144] Dark Matter Limit Plotter v.5.16 by T. Saab and E. Figueroa. [Online] Available: https://supercdms.slac.stanford.edu/dark-matter-limit-plotter, (accessed 2021, November 9).

[145] DAMIC collaboration, A. Aguilar-Arevalo et al., *Results on low-mass weakly interacting massive particles from a 11 kg-day target exposure of DAMIC at SNOLAB*, *Phys. Rev. Lett.* **125** (2020) 241803, [2007.15622].

[146] CoGeNT collaboration, C. E. Aalseth et al., *CoGeNT: A Search for Low-Mass Dark Matter using p-type Point Contact Germanium Detectors*, *Phys. Rev. D* **88** (2013) 012002, [1208.5737].

[147] SENSEI collaboration, L. Barak et al., *SENSEI: Direct-Detection Results on sub-GeV Dark Matter from a New Skipper-CCD*, *Phys. Rev. Lett.* **125** (2020) 171802, [2004.11378].

[148] NEWS-G collaboration, Q. Arnaud et al., *First results from the NEWS-G direct dark matter search experiment at the LSM*, *Astropart. Phys.* **97** (2018) 54–62, [1706.04934].

[149] DRIFT collaboration, J. B. R. Battat et al., *Improved Sensitivity of the DRIFT-IId Directional Dark Matter Experiment using Machine Learning*, 2103.06702.

[150] R. Bernabei et al., *First Model Independent Results from DAMA/LIBRA-Phase2*, *Universe* **4** (2018) 116.

[151] COSINE-100 collaboration, G. Adhikari et al., *Search for a Dark Matter-Induced Annual Modulation Signal in NaI(Tl) with the COSINE-100 Experiment*, *Phys. Rev. Lett.* **123** (2019) 031302, [1903.10098].

[152] J. Amaré et al., *First Results on Dark Matter Annual Modulation from the ANAIS-112 Experiment*, *Phys. Rev. Lett.* **123** (2019) 031301, [1903.03973].

[153] KIMS collaboration, K. W. Kim et al., *Limits on Interactions between Weakly Interacting Massive Particles and Nucleons Obtained with NaI(Tl) crystal Detectors*, *J. High Energy Phys.* **03** (2019) 194, [1806.06499].

[154] DEAP collaboration, R. Ajaj et al., *Search for dark matter with a 231-day exposure of liquid argon using DEAP-3600 at SNOLAB*, *Phys. Rev. D* **100** (2019) 022004, [1902.04048].

[155] XMASS collaboration, K. Abe et al., *A direct dark matter search in XMASS-I*, *Phys. Lett. B* **789** (2019) 45–53, [1804.02180].

[156] UK Dark Matter collaboration, G. J. Alner et al., *First limits on nuclear recoil events from the ZEPLIN I galactic dark matter detector*, *Astropart. Phys.* **23** (2005) 444–462.

[157] XENON collaboration, J. Angle et al., *First Results from the XENON10 Dark Matter Experiment at the Gran Sasso National Laboratory*, *Phys. Rev. Lett.* **100** (2008) 021303, [0706.0039].

[158] XENON100 collaboration, E. Aprile et al., *XENON100 Dark Matter Results from a Combination of 477 Live Days*, *Phys. Rev. D* **94** (2016) 122001, [1609.06154].

[159] ZEPLIN collaboration, G. J. Alner et al., *First limits on WIMP nuclear recoil signals in ZEPLIN-II: A two phase xenon detector for dark matter detection*, *Astropart. Phys.* **28** (2007) 287–302, [astro-ph/0701858].

[160] V. N. Lebedenko et al., *Result from the First Science Run of the ZEPLIN-III Dark Matter Search Experiment*, *Phys. Rev. D* **80** (2009) 052010, [0812.1150].

[161] LUX-ZEPLIN collaboration, D. S. Akerib et al., *Projected WIMP sensitivity of the LUX-ZEPLIN dark matter experiment*, *Phys. Rev. D* **101** (2020) 052002, [1802.06039].

[162] PandaX collaboration, M. Xiao et al., *First dark matter search results from the PandaX-I experiment*, *Sci. China Phys. Mech. Astron.* **57** (2014) 2024–2030, [1408.5114].

[163] PandaX-4T collaboration, Y. Meng et al., *Dark Matter Search Results from the PandaX-4T Commissioning Run*, *Phys. Rev. Lett.* **127** (2021) 261802, [2107.13438].

[164] P. Benetti et al., *First results from a Dark Matter search with liquid Argon at 87 K in the Gran Sasso Underground Laboratory*, *Astropart. Phys.* **28** (2008) 495–507, [astro-ph/0701286].

[165] ArDM collaboration, J. Calvo et al., *Commissioning of the ArDM experiment at the Canfranc underground laboratory: first steps towards a tonne-scale liquid argon time projection chamber for Dark Matter searches*, *J. Cosmol. Astropart. Phys.* **03** (2017) 003, [1612.06375].

[166] E. Aprile, H. Contreras, L. W. Goetzke, A. J. Melgarejo Fernandez, M. Messina, J. Naganoma, G. Plante, A. Rizzo, P. Shagin and R. Wall, *Measurements of proportional scintillation and electron multiplication in liquid xenon using thin wires*, *J. Instrum.* **9** (2014) P11012, [1408.6206].

[167] EXO-200 collaboration, G. Anton et al., *Search for Neutrinoless Double-β Decay with the Complete EXO-200 Dataset*, *Phys. Rev. Lett.* **123** (2019) 161802, [1906.02723].

[168] nEXO collaboration, S. A. Kharusi et al., *nEXO Pre-Conceptual Design Report*, 1805.11142.

[169] MicroBooNE collaboration, R. Acciarri et al., *Design and Construction of the MicroBooNE Detector*, *J. Instrum.* **12** (2017) P02017, [1612.05824].

[170] nEXO collaboration, J. B. Albert et al., *Sensitivity and Discovery Potential of nEXO to Neutrinoless Double Beta Decay*, *Phys. Rev. C* **97** (2018) 065503, [1710.05075].

[171] NEXT collaboration, J. Martín-Albo et al., *Sensitivity of NEXT-100 to Neutrinoless Double Beta Decay*, *J. High Energy Phys.* **05** (2016) 159, [1511.09246].

[172] NEXT collaboration, C. Adams et al., *Sensitivity of a tonne-scale NEXT detector for neutrinoless double beta decay searches*, *J. High Energy Phys.* **2021** (2021) 164, [2005.06467].

[173] XENON collaboration, E. Aprile et al., *Observation of two-neutrino double electron capture in ^{124}Xe with XENON1T*, *Nature* **568** (2019) 532–535, [1904.11002].

[174] LUX collaboration, D. S. Akerib et al., *Search for two neutrino double electron capture of ^{124}Xe and ^{126}Xe in the full exposure of the LUX detector*, *J. Phys. G* **47** (2020) 105105, [1912.02742].

[175] DARWIN collaboration, J. Aalbers et al., *Solar neutrino detection sensitivity in DARWIN via electron scattering*, *Eur. Phys. J. C* **80** (2020) 1133, [2006.03114].

[176] XENON collaboration, E. Aprile et al., *Excess electronic recoil events in XENON1T*, *Phys. Rev. D* **102** (2020) 072004, [2006.09721].

[177] LUX collaboration, D. S. Akerib et al., *First Searches for Axions and Axionlike Particles with the LUX Experiment*, *Phys. Rev. Lett.* **118** (2017) 261301, [1704.02297].

[178] LZ collaboration, D. S. Akerib et al., *Projected sensitivities of the LUX-ZEPLIN (LZ) experiment to new physics via low-energy electron recoils*, 2102.11740.

[179] PandaX collaboration, X. Cui et al., *Dark Matter Results From 54-Ton-Day Exposure of PandaX-II Experiment*, *Phys. Rev. Lett.* **119** (2017) 181302, [1708.06917].

[180] E. Aprile and T. Doke, *Liquid Xenon Detectors for Particle Physics and Astrophysics*, *Rev. Mod. Phys.* **82** (2010) 2053–2097, [0910.4956].

[181] W. Ramsay and M. Travers, *On the extraction from air of the companions of argon, and neon*, *Note to the Meeting of the British Association for the Advancement of Science* (1898) 828.

[182] The Nobel Prize in Chemistry 1904. NobelPrize.org. Nobel Prize Outreach AB 2021. [Online] Available: https://www.nobelprize.org/prizes/chemistry/1904/summary/, (accessed 2021, September 25).

[183] R. B. Firestone, *Table of Isotopes*, vol. 1. John Wiley & Sons, Inc., 8th ed., 1999.

[184] J. Menendez, D. Gazit and A. Schwenk, *Spin-dependent WIMP scattering off nuclei*, *Phys. Rev. D* **86** (2012) 103511, [1208.1094].

[185] D. R. Tovey, R. J. Gaitskell, P. Gondolo, Y. A. Ramachers and L. Roszkowski, *A New model independent method for extracting spin dependent (cross-section) limits from dark matter searches*, *Phys. Lett. B* **488** (2000) 17–26, [hep-ph/0005041].

[186] Particle Data Group collaboration, P. A. Zyla et al., *Review of Particle Physics*, *Prog. Theor. Exp. Phys.* **2020** (2020) 083C01.

[187] Particle Data Group collaboration, K. A. Olive et al., *Review of Particle Physics*, *Chin. Phys. C* **38** (2014) 090001.

[188] M. J. Berger, J. H. Hubbell, S. Seltzer, J. Chang, J. S. Coursey, R. Sukumar, D. S. Zucker and K. Olsen, "XCOM: Photon Cross Sections Database (version 1.5)." [Online] Available: http://physics.nist.gov/xcom, (accessed 2021, October 1), National Institute of Standards and Technology, Gaithersburg, MD, Nov., 2010.

[189] M. J. Berger, J. S. Coursey, M. A. Zucker and J. Chang, "ESTAR, PSTAR, and ASTAR: Computer Programs for Calculating Stopping-Power and Range Tables for Electrons, Protons, and Helium Ions (version 2.0.1)." [Online] Available: http://physics.nist.gov/Star, (accessed 2021, October 1), National Institute of Standards and Technology, Gaithersburg, MD, July, 2017.

[190] Air Liquide. [Online] Available: https://encyclopedia.airliquide.com/xenon, (accessed 2021, September 27).

[191] P. J. Linstrom and W. G. Mallard, eds., *NIST Chemistry WebBook, NIST Standard Reference Database Number 69*, vol. 20899. National Institute of Standards and Technology, Gaithersburg MD, 20899, retrieved December 10, 2020, https://doi.org/10.18434/T4D303.

[192] XENON100 collaboration, E. Aprile et al., *Online ^{222}Rn removal by cryogenic distillation in the XENON100 experiment*, *Eur. Phys. J. C* **77** (2017) 358, [1702.06942].

[193] XENON collaboration, E. Aprile et al., *Removing krypton from xenon by cryogenic distillation to the ppq level*, *Eur. Phys. J. C* **77** (2017) 275, [1612.04284].

[194] X. Cui et al., *Design and commissioning of the PandaX-4T cryogenic distillation system for krypton and radon removal*, *J. Instrum.* **16** (2021) P07046, [2012.02436].

[195] J. Jortner, L. Meyer, S. A. Rice and E. G. Wilson, *Localized Excitations in Condensed Ne, Ar, Kr, and Xe*, *J. Chem. Phys.* **42** (1965) 4250.

[196] K. Fujii, Y. Endo, Y. Torigoe, S. Nakamura, T. Haruyama, K. Kasami, S. Mihara, K. Saito, S. Sasaki and H. Tawara, *High-accuracy measurement of the emission spectrum of liquid xenon in the vacuum ultraviolet region*, *Nucl. Instrum. Methods Phys. Res. A* **795** (2015) 293–297.

[197] B. Lenardo, K. Kazkaz, A. Manalaysay, J. Mock, M. Szydagis and M. Tripathi, *A Global Analysis of Light and Charge Yields in Liquid Xenon*, *IEEE Trans. Nucl. Sci.* **62** (2015) 3387–3396, [1412.4417].

[198] V. N. Solovov, V. Chepel, M. I. Lopes and A. Hitachi, *Measurement of the refractive index and attenuation length of liquid xenon for its scintillation light*, *Nucl. Instrum. Meth. A* **516** (2004) 462–474, [physics/0307044].

[199] G. Carugno, *Infrared emission in gaseous media induced by ionizing particles and by drifting electrons*, *Nucl. Instrum. Meth. A* **419** (1998) 617–620.

[200] G. Bressi, G. Carugno, E. Conti, D. Iannuzzi and A. T. Meneguzzo, *Infrared scintillation in liquid Ar and Xe*, *Nucl. Instrum. Meth. A* **440** (2000) 254–257.

[201] S. Belogurov, G. Bressi, G. Carugno, E. Conti, D. Iannuzzi and A. T. Meneguzzo, *Infrared scintillation in gases, liquids and crystals*, *IEEE Transactions on Nuclear Science* **47** (2000) 1791–1797.

[202] A. F. Borghesani, G. Bressi, G. Carugno, E. Conti and D. Iannuzzi, *Infrared fluorescence of Xe_2 molecules in electron/proton beam excited pure Xe gas and in an Ar/Xe gas mixture*, *The Journal of Chemical Physics* **115** (2001) 6042–6050.

[203] A. F. Borghesani, G. Carugno and I. Mogentale, *Infrared emission spectrum and potentials of 0_u^+ and 0_g^+ states of Xe_2 excimers produced by electron impact*, *Journal of Physics B: Atomic, Molecular and Optical Physics* **40** (Nov., 2007) 4551–4560.

[204] G. Bressi, G. Carugno, E. Conti, C. Del Noce and D. Iannuzzi, *Infrared scintillation: A comparison between gaseous and liquid xenon*, *Nucl. Instrum. Meth. A* **461** (2001) 378–380.

[205] S. Belogurov, G. Bressi, G. Carugno, E. Conti, D. Iannuzzi and A. T. Meneguzzo, *Measurement of the light yield of infrared scintillation in xenon gas*, *Nucl. Instrum. Meth. A* **452** (2000) 167–169.

[206] A. F. Borghesani and G. Carugno, *Infrared luminescence of Xe_2 excimers produced by electron impact in dense gas*, in *2008 IEEE International Conference on Dielectric Liquids*, pp. 1–4, 2008. DOI.

[207] A. F. Borghesani and G. Carugno, *Density-induced modifications of the IR emission spectrum of Xe_2 excimers in dense gas*, *IEEE Transactions on Dielectrics and Electrical Insulation* **16** (2009) 1543–1551.

[208] J. Meija, T. B. Coplen, M. Berglund, W. A. Brand, P. D. Bièvre, M. Gröning, N. E. Holden, J. Irrgeher, R. D. Loss, T. Walczyk et al., *Atomic weights of the elements 2013 (IUPAC Technical Report)*, *Pure Appl. Chem.* **88** (2016) 265–291.

[209] EXO-200 collaboration, J. B. Albert et al., *Improved measurement of the $2\nu\beta\beta$ half-life of ^{136}Xe with the EXO-200 detector*, *Phys. Rev. C* **89** (2014) 015502, [1306.6106].

[210] N. Ishida, M. Chen, T. Doke, K. Hasuike, A. Hitachi, M. Gaudreau, M. Kase, Y. Kawada, J. Kikuchi, T. Komiyama et al., *Attenuation length measurements of scintillation light in liquid rare gases and their mixtures using an improved reflection suppresser*, *Nucl. Instrum. Methods Phys. Res. A* **384** (1997) 380–386.

[211] B. N. V. Edwards et al., *Extraction efficiency of drifting electrons in a two-phase xenon time projection chamber*, *J. Instrum.* **13** (2018) P01005, [1710.11032].

[212] DarkSide collaboration, P. Agnes et al., *Low-Mass Dark Matter Search with the DarkSide-50 Experiment*, *Phys. Rev. Lett.* **121** (2018) 081307, [1802.06994].

[213] DarkSide-20k collaboration, P. Agnes et al., *Separating ^{39}Ar from ^{40}Ar by cryogenic distillation with Aria for dark-matter searches*, *Eur. Phys. J. C* **81** (2021) 359, [2101.08686].

[214] C. G. Wahl, E. P. Bernard, W. H. Lippincott, J. A. Nikkel, Y. Shin and D. N. McKinsey, *Pulse-shape discrimination and energy resolution of a liquid-argon scintillator with xenon doping*, *J. Instrum.* **9** (2014) P06013, [1403.0525].

[215] D. Akimov, V. Belov, A. Konovalov, A. Kumpan, O. Razuvaeva, D. Rudik and G. Simakov, *Fast component re-emission in Xe-doped liquid argon*, *J. Instrum.* **14** (2019) P09022, [1906.00836].

[216] C. Galbiati, X. Li, J. Luo, D. R. Marlow, H. Wang and Y. Wang, *Pulse shape study of the fast scintillation light emitted from xenon-doped liquid argon using silicon photomultipliers*, *J. Instrum.* **16** (2021) P02015, [2009.06238].

[217] A. Neumeier, T. Dandl, T. Heindl, A. Himpsl, L. Oberauer, W. Potzel, S. Roth, S. Schönert, J. Wieser and A. Ulrich, *Intense Vacuum-Ultraviolet and Infrared Scintillation of Liquid Ar-Xe Mixtures*, *EPL* **109** (2015) 12001, [1511.07723].

[218] P. Peiffer, T. Pollmann, S. Schonert, A. Smolnikov and S. Vasiliev, *Pulse shape analysis of scintillation signals from pure and xenon-doped liquid argon for radioactive background identification*, *J. Instrum.* **3** (2008) P08007.

[219] N. McFadden, S. R. Elliott, M. Gold, D. E. Fields, K. Rielage, R. Massarczyk and R. Gibbons, *Large-scale, precision xenon doping of liquid argon*, *Nucl. Instrum. Meth. A* **1011** (2021) 165575, [2006.09780].

[220] D. N. McKinsey and J. M. Doyle, *Liquid helium and liquid neon: Sensitive, low background scintillation media for the detection of low-energy neutrinos*, *J. Low Temp. Phys.* **118** (2000) 153–165, [astro-ph/9907314].

[221] D. N. McKinsey, C. R. Brome, J. S. Butterworth, S. N. Dzhosyuk, R. Golub, K. Habicht, P. R. Huffman, C. E. H. Mattoni, L. Yang and J. M. Doyle, *Detecting ionizing radiation in liquid helium using wavelength shifting light collection*, *Nucl. Instrum. Methods Phys. Res. A* **516** (2004) 475–485.

[222] B. Monreal, L. de Viveiros and W. Luszczak, *Sub-Penning gas mixtures: new possibilities for ton- to kiloton-scale time projection chambers*, 1512.04926.

[223] V. Chepel and H. Araujo, *Liquid noble gas detectors for low energy particle physics*, *J. Instrum.* **8** (2013) R04001, [1207.2292].

[224] R. E. Packard, F. Reif and C. M. Surko, *Ultraviolet Emission Spectra of Electron-Excited Solid and Liquid Neon*, *Phys. Rev. Lett.* **25** (Nov., 1970) 1435–1439.

[225] C. M. Surko, R. E. Packard, G. J. Dick and F. Reif, *Spectroscopic Study of the Luminescence of Liquid Helium in the Vacuum Ultraviolet*, *Phys. Rev. Lett.* **24** (Mar., 1970) 657–659.

[226] M. Stockton, J. W. Keto and W. A. Fitzsimmons, *Ultraviolet Emission Spectrum of Electron-Bombarded Superfluid Helium*, *Phys. Rev. A* **5** (Jan., 1972) 372–380.

[227] D. N. McKinsey and K. J. Coakley, *Neutrino detection with CLEAN*, *Astropart. Phys.* **22** (2005) 355–368, [astro-ph/0402007].

[228] S. A. Hertel, A. Biekert, J. Lin, V. Velan and D. N. McKinsey, *Direct detection of sub-GeV dark matter using a superfluid ^{4}He target*, *Phys. Rev. D* **100** (2019) 092007, [1810.06283].

[229] J. T. White, J. Gao, G. Salinas and H. Wang, *SIGN: A gaseous-neon-based underground physics detector*, *Nucl. Phys. B Proc. Suppl.* **173** (2007) 144–147.

[230] MINICLEAN collaboration, K. Rielage et al., *Update on the MiniCLEAN Dark Matter Experiment*, *Phys. Procedia* **61** (2015) 144–152, [1403.4842].

[231] J. Liao, Y. Gao, Z. Liang, Z. Peng, L. Zhang and L. Zhang, *A low-mass dark matter project, ALETHEIA: A Liquid hElium Time projection cHambEr In dArk matter*, 2103.02161.

[232] S. Kubota, M. Hishida and J. Raun, *Evidence for a triplet state of the self-trapped exciton states in liquid argon, krypton and xenon*, *J. Phys. C: Solid State Phys.* **11** (June, 1978) 2645–2651.

[233] LUX collaboration, D. S. Akerib et al., *Liquid xenon scintillation measurements and pulse shape discrimination in the LUX dark matter detector*, *Phys. Rev. D* **97** (2018) 112002, [1802.06162].

[234] A. Hitachi, T. Takahashi, N. Funayama, K. Masuda, J. Kikuchi and T. Doke, *Effect of ionization density on the time dependence of luminescence from liquid argon and xenon*, *Phys. Rev. B* **27** (1983) 5279–5285.

[235] W. H. Lippincott, K. J. Coakley, D. Gastler, A. Hime, E. Kearns, D. N. McKinsey, J. A. Nikkel and L. C. Stonehill, *Scintillation time dependence and pulse shape discrimination in liquid argon*, *Phys. Rev. C* **78** (2008) 035801, [0801.1531].

[236] F. Jörg, D. Cichon, G. Eurin, L. Hötzsch, T. Undagoitia Marrodán and N. Rupp, *Characterization of alpha and beta interactions in liquid xenon*, *Eur. Phys. J. C* **82** (2022) 361, [2109.13735].

[237] W. F. Schmidt, O. Hilt, E. Illenberger and A. G. Khrapak, *The mobility of positive and negative ions in liquid xenon*, *Radiat. Phys. Chem.* **74** (2005) 152–159.

[238] O. Hilt and W. F. Schmidt, *Positive hole mobility in liquid xenon*, *Chem. Phys.* **183** (1994) 147–153.

[239] T. Doke, A. Hitachi, J. Kikuchi, K. Masuda, H. Okada and E. Shibamura, *Absolute Scintillation Yields in Liquid Argon and Xenon for Various Particles*, *Jap. J. Appl. Phys.* **41** (2002) 1538–1545.

[240] EXO-200 collaboration, E. Conti et al., *Correlated fluctuations between luminescence and ionization in liquid xenon*, *Phys. Rev. B* **68** (2003) 054201, [hep-ex/0303008].

[241] M. Ibe, W. Nakano, Y. Shoji and K. Suzuki, *Migdal Effect in Dark Matter Direct Detection Experiments*, *J. High Energy Phys.* **03** (2018) 194, [1707.07258].

[242] XENON collaboration, E. Aprile et al., *Search for Light Dark Matter Interactions Enhanced by the Migdal Effect or Bremsstrahlung in XENON1T*, *Phys. Rev. Lett.* **123** (2019) 241803, [1907.12771].

[243] C. E. Dahl, *The physics of background discrimination in liquid xenon, and first results from Xenon10 in the hunt for WIMP dark matter*. PhD thesis, Princeton U., 2009.

[244] J. Lindhard, V. Nielsen, M. Scharff and P. V. Thomsen, *Integral Equations Governing Radiation Effects. (Notes On Atomic Collisions, III)*, *Kgl. Danske Videnskab., Selskab. Mat. Fys. Medd.* **33** (Jan., 1963) .

[245] P. Sorensen and C. E. Dahl, *Nuclear recoil energy scale in liquid xenon with application to the direct detection of dark matter*, *Phys. Rev. D* **83** (2011) 063501, [1101.6080].

[246] A. Hitachi, T. Doke and A. Mozumder, *Luminescence quenching in liquid argon under charged-particle impact: Relative scintillation yield at different linear energy transfers*, *Phys. Rev. B* **46** (1992) 11463.

[247] A. Hitachi, *Properties of liquid xenon scintillation for dark matter searches*, *Astropart. Phys.* **24** (2005) 247–256.

[248] F. Neves, A. Lindote, A. Morozov, V. Solovov, C. Silva, P. Bras, J. P. Rodrigues and M. I. Lopes, *Measurement of the absolute reflectance of polytetrafluoroethylene (PTFE) immersed in liquid xenon*, *J. Instrum.* **12** (2017) P01017, [1612.07965].

[249] S. Kravitz, G. D. Orebi Gann, R. J. Smith, L. Hagaman, E. P. Bernard, D. N. McKinsey, L. Rudd, L. Tvrznikova and M. Sakai, *Measurements of Angle-Resolved Reflectivity of PTFE in Liquid Xenon with IBEX*, *Eur. Phys. J. C* **80** (2020) 262, [1909.08730].

[250] XENON collaboration, E. Aprile et al., *XENON1T Dark Matter Data Analysis: Signal Reconstruction, Calibration and Event Selection*, *Phys. Rev. D* **100** (2019) 052014, [1906.04717].

[251] L. Baudis, Y. Biondi, M. Galloway, F. Girard, S. Hochrein, S. Reichard, P. Sanchez-Lucas, K. Thieme and J. Wulf, *The first dual-phase xenon TPC equipped with silicon photomultipliers and characterisation with ^{37}Ar*, *Eur. Phys. J. C* **80** (2020) 477, [2003.01731].

[252] EXO-200 collaboration, J. B. Albert et al., *Measurement of the Drift Velocity and Transverse Diffusion of Electrons in Liquid Xenon with the EXO-200 Detector*, *Phys. Rev. C* **95** (2017) 025502, [1609.04467].

[253] G. Mohlabeng, K. Kong, J. Li, A. Para and J. Yoo, *Dark Matter Directionality Revisited with a High Pressure Xenon Gas Detector*, *J. High Energy Phys.* **07** (2015) 092, [1503.03937].

[254] LUX collaboration, D. S. Akerib et al., *3D Modeling of Electric Fields in the LUX Detector*, *J. Instrum.* **12** (2017) P11022, [1709.00095].

[255] J. Xu, S. Pereverzev, B. Lenardo, J. Kingston, D. Naim, A. Bernstein, K. Kazkaz and M. Tripathi, *Electron extraction efficiency study for dual-phase xenon dark matter experiments*, *Phys. Rev. D* **99** (2019) 103024, [1904.02885].

[256] XENON Dark Matter Project. [Online] Available: http://www.xenon1t.org/, (accessed 2021, November 16).

[257] K. Thieme, *DARWIN – a next-generation liquid xenon observatory for dark matter and neutrino physics*, in *Proceedings of 37th International Cosmic Ray Conference — PoS(ICRC2021)*, vol. 395, p. 548, 2021. DOI.

[258] XENON collaboration, E. Aprile et al., *The XENON1T Dark Matter Experiment*, *Eur. Phys. J. C* **77** (2017) 881, [1708.07051].

[259] L. Baudis et al., *Performance of the Hamamatsu R11410 Photomultiplier Tube in cryogenic Xenon Environments*, *J. Instrum.* **8** (2013) P04026, [1303.0226].

[260] LUX collaboration, D. S. Akerib et al., *The Large Underground Xenon (LUX) Experiment*, *Nucl. Instrum. Meth.* **A704** (2013) 111, [1211.3788].

[261] PandaX collaboration, X. Cao et al., *PandaX: A Liquid Xenon Dark Matter Experiment at CJPL*, *Sci. China Phys. Mech. Astron.* **57** (2014) 1476–1494, [1405.2882].

[262] S. Li et al., *Performance of Photosensors in the PandaX-I Experiment*, *J. Instrum.* **11** (2016) T02005, [1511.06223].

[263] V. C. Antochi et al., *Improved quality tests of R11410-21 photomultiplier tubes for the XENONnT experiment*, *J. Instrum.* **16** (2021) P08033, [2104.15051].

[264] XENON collaboration, E. Aprile et al., *Lowering the radioactivity of the photomultiplier tubes for the XENON1T dark matter experiment*, *Eur. Phys. J.* **C75** (2015) 546, [1503.07698].

[265] D. S. Akerib et al., *An Ultra-Low Background PMT for Liquid Xenon Detectors*, *Nucl. Instrum. Meth. A* **703** (2013) 1–6, [1205.2272].

[266] M. Schumann et al., *Dark matter sensitivity of multi-ton liquid xenon detectors*, *J. Cosmol. Astropart. Phys.* **1510** (2015) 016, [1506.08309].

[267] XENON collaboration, E. Aprile et al., *Removing krypton from xenon by cryogenic distillation to the ppq level*, *Eur. Phys. J.* **C77** (2017) 275, [1612.04284].

[268] L. Baudis et al., *Neutrino physics with multi-ton scale liquid xenon detectors*, *J. Cosmol. Astropart. Phys.* **01** (2014) 044, [1309.7024].

[269] BOREXINO collaboration, M. Agostini et al., *Comprehensive measurement of pp-chain solar neutrinos*, *Nature* **562** (2018) 505–510.

[270] A. de Gouvêa, E. McGinness, I. Martinez-Soler and Y. F. Perez-Gonzalez, *pp Solar Neutrinos at DARWIN*, 2111.02421.

[271] K. Goldhagen, M. Maltoni, S. E. Reichard and T. Schwetz, *Testing sterile neutrino mixing with present and future solar neutrino data*, *Eur. Phys. J. C* **82** (2022) 116, [2109.14898].

[272] R. F. Lang, C. McCabe, S. Reichard, M. Selvi and I. Tamborra, *Supernova neutrino physics with xenon dark matter detectors: A timely perspective*, *Phys. Rev. D* **94** (2016) 103009, [1606.09243].

[273] A. M. Suliga, J. F. Beacom and I. Tamborra, *Towards probing the diffuse supernova neutrino background in all flavors*, *Phys. Rev. D* **105** (2022) 043008, [2112.09168].

[274] J. Aalbers et al., *A Next-Generation Liquid Xenon Observatory for Dark Matter and Neutrino Physics*, 2203.02309.

[275] L. Baudis, M. Galloway, A. Kish, C. Marentini and J. Wulf, *Characterisation of Silicon Photomultipliers for Liquid Xenon Detectors*, *J. Instrum.* **13** (2018) P10022, [1808.06827].

[276] F. Arneodo, M. L. Benabderrahmane, G. Bruno, V. Conicella, A. Di Giovanni, O. Fawwaz, M. Messina, A. Candela and G. Franchi, *Cryogenic readout for multiple VUV4 Multi-Pixel Photon Counters in liquid xenon*, *Nucl. Instrum. Meth. A* **893** (2018) 117–123, [1707.08004].

[277] K. Ozaki, S. Kazama, M. Yamashita, Y. Itow and S. Moriyama, *Characterization of New Silicon Photomultipliers with Low Dark Noise at Low Temperature*, *J. Instrum.* **16** (2021) P03014, [2007.13537].

[278] M. Keller, "CMOS based SPAD Arrays for light detection in rare event search experiments." LIDINE 2021, online, September, 2021.

[279] D. Ferenc, A. Chang and M. S. Ferenc, *The Novel ABALONE Photosensor Technology: 4-Year Long Tests of Vacuum Integrity, Internal Pumping and Afterpulsing*, 1703.04546.

[280] G. Barbarino et al., *A new generation photodetector for astroparticle physics: the VSiPMT*, *Astropart. Phys.* **67** (2015) 18–25, [1407.2805].

[281] F. C. T. Barbato and G. Barbarino, *Understanding VSiPMT: a comparison with other large area hybrid photodetectors*, 2004.12627.

[282] E. Erdal, L. Arazi, A. Breskin, S. Shchemelinin, A. Roy, A. Tesi, D. Vartsky and S. Bressler, *Bubble-assisted Liquid Hole Multipliers in LXe and LAr: towards "local dual-phase TPCs"*, *J. Instrum.* **15** (2020) C04002, [1912.10698].

[283] DARWIN collaboration, L. Althueser et al., *GPU-based optical simulation of the DARWIN detector*, 2203.14354.

[284] L. Baudis, Y. Biondi, M. Galloway, F. Girard, A. Manfredini, N. McFadden, R. Peres, P. Sanchez-Lucas and K. Thieme, *Design and construction of Xenoscope – a full-scale vertical demonstrator for the DARWIN observatory*, *J. Instrum.* **16** (2021) P08052, [2105.13829].

[285] F. Kuger, J. Dierle, H. Fischer, M. Schumann and F. Toschi, *Prospects of charge signal analyses in liquid xenon TPCs with proportional scintillation in the liquid phase*, *JINST* **17** (2022) P03027, [2112.11844].

[286] K. Sato, M. Yamashita, K. Ichimura, Y. Itow, S. Kazama, S. Moriyama, K. Ozaki, T. Suzuki and R. Yamazaki, *Development of a dual-phase xenon TPC with a quartz chamber for direct dark matter searches*, *Prog. Theor. Exp. Phys.* **2020** (2020) 113H02, [1910.13831].

[287] S. Bruenner, D. Cichon, S. Lindemann, T. Marrodán Undagoitia and H. Simgen, *Radon depletion in xenon boil-off gas*, *Eur. Phys. J. C* **77** (2017) 143, [1611.03737].

[288] S. Bruenner, D. Cichon, G. Eurin, P. Herrero Gómez, F. Jörg, T. Marrodán Undagoitia, H. Simgen and N. Rupp, *Radon daughter removal from PTFE surfaces and its application in liquid xenon detectors*, *Eur. Phys. J. C* **81** (2021) 343, [2009.08828].

[289] M. Murra, *Intrinsic background reduction by cryogenic distillation for the XENON1T dark matter experiment*. PhD thesis, University of Münster, 2019.

[290] S. A. Brünner, *Mitigation of ^{222}Rn induced background in the XENON1T dark matter experiment*. PhD thesis, Ruprecht Karl University of Heidelberg, 2017. 10.11588/heidok.00023261.

[291] N. M. R. E. Rupp, *Radon Induced Background in the XENON1T Dark Matter Search Experiment and Studies on Xenon Purity in the HeXe System*. PhD thesis, Ruprecht Karl University of Heidelberg, 2020. 10.11588/heidok.00029342.

[292] V. I. Barsanov et al., *Artificial neutrino source based on the Ar-37 isotope*, *Phys. Atom. Nucl.* **70** (2007) 300–310.

[293] E. A. McCutchan, *Nuclear Data Sheets for A = 83*, *Nuclear Data Sheets* **125** (2015) 201 – 394.

[294] Texas Instruments Incorporated. [Online] Available: https://www.ti.com/, (accessed 2021, December 17).

[295] CAEN S.p.A. [Online] Available: https://www.caen.it/, (accessed 2021, December 17).

[296] CAEN S.p.A., Via Vetraia, 11, 55049 Viareggia (LU), Italy, *User Manual UM3248, V1724/VX1724, 8 Channels 14 bit 100 MS/s Digitizer*, 32 ed., Apr., 2017.

[297] F. Piastra, *Materials Radioassay for the XENON1T Dark Matter Experiment, and Development of a Time Projection Chamber for the Study of Low-energy Nuclear Recoils in Liquid Xenon*. PhD thesis, University of Zurich, 2017. 10.5167/uzh-142441.

[298] R. Brun and F. Rademakers, *ROOT - An Object Oriented Data Analysis Framework, Proceedings AIHENP'96 Workshop, Lausanne, Sep. 1996*, *Nucl. Inst. & Meth. in Phys. Res. A* **389** (1997) 81–86. See also "ROOT" [software], Release v6.14/00, 19/06/2018, https://doi.org/10.5281/zenodo.1292566.

[299] B. F. Aull, A. H. Loomis, D. J. Young, R. M. Heinrichs, B. J. Felton, P. J. Daniels and D. J. Landers, *Geiger-mode avalanche photodiodes for three-dimensional imaging*, *Linc. Lab. J.* **13** (2002) 335–349.

[300] R. Saldanha, L. Grandi, Y. Guardincerri and T. Wester, *Model Independent Approach to the Single Photoelectron Calibration of Photomultiplier Tubes*, *Nucl. Instrum. Meth. A* **863** (2017) 35–46, [1602.03150].

[301] A. Bondar, A. Buzulutskov, A. Dolgov, V. Nosov, L. Shekhtman and A. Sokolov, *Characterization of photo-multiplier tubes for the Cryogenic Avalanche Detector*, *J. Instrum.* **10** (2015) P10010, [1509.02724].

[302] C. Marentini, *Characterization of Novel VUV-Silicon Photomultipliers and their Application in Xenon-Based Dual-Phase TPCs*, Master's thesis, University of Zurich, 2018.

[303] J. B. McLaughlin et al., *Characterisation of SiPM Photon Emission in the Dark*, *Sensors* **21** (2021) 5947, [2107.13753].

[304] C. H. Faham, V. M. Gehman, A. Currie, A. Dobi, P. Sorensen and R. J. Gaitskell, *Measurements of wavelength-dependent double photoelectron emission from single photons in VUV-sensitive photomultiplier tubes*, *J. Instrum.* **10** (2015) P09010, [1506.08748].

[305] B. López Paredes, H. M. Araújo, F. Froborg, N. Marangou, I. Olcina, T. J. Sumner, R. Taylor, A. Tomás and A. Vacheret, *Response of photomultiplier tubes to xenon scintillation light*, *Astropart. Phys.* **102** (2018) 56–66, [1801.01597].

[306] LUX collaboration, D. S. Akerib et al., *Extending light WIMP searches to single scintillation photons in LUX*, *Phys. Rev. D* **101** (2020) 042001, [1907.06272].

[307] GEANT4 collaboration, S. Agostinelli et al., *Geant4–a simulation toolkit*, *Nucl. Instrum. Meth. A* **506** (2003) 250–303.

[308] LZ collaboration, D. S. Akerib et al., *LUX-ZEPLIN (LZ) Conceptual Design Report*, 1509.02910.

[309] R. Kitamura, L. Pilon and M. Jonasz, *Optical constants of silica glass from extreme ultraviolet to far infrared at near room temperature*, *Appl. Opt.* **46** (Nov., 2007) 8118–8133.

[310] XMASS collaboration, K. Abe et al., *A measurement of the scintillation decay time constant of nuclear recoils in liquid xenon with the XMASS-I detector*, *J. Instrum.* **13** (2018) P12032, [1809.05988].

[311] H. H. Li, *Refractive index of silicon and germanium and its wavelength and temperature derivatives*, *J. Phys. Chem. Ref. Data* **9** (1980) 561–658.

[312] D. F. Edwards, *Silicon (Si) Revisited (1.4–6.0 eV)*, in *Handbook of Optical Constants of Solids* (E. D. Palik, ed.), pp. 531–536. Academic Press, Burlington, 1997. DOI.

[313] nEXO collaboration, P. Nakarmi et al., *Reflectivity and PDE of VUV4 Hamamatsu SiPMs in Liquid Xenon*, *J. Instrum.* **15** (2020) P01019, [1910.06438].

[314] nEXO collaboration, M. Wagenpfeil et al., *Reflectivity of VUV-sensitive silicon photomultipliers in liquid Xenon*, *J. Instrum.* **16** (2021) P08002, [2104.07997].

[315] M. A. Green, *Self-consistent optical parameters of intrinsic silicon at 300 K including temperature coefficients*, *Sol. Energy Mater. Sol. Cells* **92** (2008) 1305–1310.

[316] C. Schinke, P. Christian Peest, J. Schmidt, R. Brendel, K. Bothe, M. R. Vogt, I. Kröger, S. Winter, A. Schirmacher, S. Lim et al., *Uncertainty analysis for the coefficient of band-to-band absorption of crystalline silicon*, *AIP Adv.* **5** (2015) 067168.

[317] J. Cameron, J. Chen, B. Singh and N. Nica, *Nuclear Data Sheets for A = 37*, *Nuclear Data Sheets* **113** (2012) 365 – 514.

[318] D. Y. Akimov et al., *Experimental study of ionization yield of liquid xenon for electron recoils in the energy range 2.8–80 keV*, *J. Instrum.* **9** (2014) P11014, [1408.1823].

[319] S. Sangiorgio et al., *First demonstration of a sub-keV electron recoil energy threshold in a liquid argon ionization chamber*, *Nucl. Instrum. Meth. A* **728** (2013) 69–72, [1301.4290].

[320] D. Wenz, *Improving the calibration of MainzTPC using the isotope ^{37}Ar*, Master's thesis, Johannes Gutenberg University Mainz, 2018.

[321] DarkSide collaboration, P. Agnes et al., *Calibration of the liquid argon ionization response to low energy electronic and nuclear recoils with DarkSide-50*, *Phys. Rev. D* **104** (2021) 082005, [2107.08087].

[322] LUX collaboration, D. S. Akerib et al., *Improved Limits on Scattering of Weakly Interacting Massive Particles from Reanalysis of 2013 LUX Data*, *Phys. Rev. Lett.* **116** (2016) 161301, [1512.03506].

[323] LUX-ZEPLIN collaboration, J. Aalbers et al., *Cosmogenic production of ^{37}Ar in the context of the LUX-ZEPLIN experiment*, *Phys. Rev. D* **105** (2022) 082004, [2201.02858].

[324] XENON1T collaboration, E. Aprile et al., *Application and modeling of an online distillation method to reduce krypton and argon in XENON1T*, 2112.12231.

[325] Pfeiffer Vacuum GmbH. [Online] Available: https://www.pfeiffer-vacuum.com/en/, (accessed 2021, December 17).

[326] V. O. Altemose, *Helium Diffusion through Glass*, *J. Appl. Phys.* **32** (July, 1961) 1309–1316.

[327] J. Chen, *Nuclear Data Sheets for A = 39*, *Nuclear Data Sheets* **149** (2018) 1 – 251.

[328] C. D. Nesaraja and E. A. McCutchan, *Nuclear Data Sheets for A = 41*, *Nuclear Data Sheets* **133** (2016) 1 – 220.

[329] B. Singh and J. Chen, *Nuclear Data Sheets for A = 43*, *Nuclear Data Sheets* **126** (2015) 1 – 150.

[330] B. Singh and J. A. Cameron, *Nuclear Data Sheets for A = 42*, *Nuclear Data Sheets* **92** (2001) 1 – 146.

[331] P. Sorensen, *Anisotropic diffusion of electrons in liquid xenon with application to improving the sensitivity of direct dark matter searches*, *Nucl. Instrum. Meth. A* **635** (2011) 41–43, [1102.2865].

[332] M. Szydagis et al., *A Review of Basic Energy Reconstruction Techniques in Liquid Xenon and Argon Detectors for Dark Matter and Neutrino Physics Using NEST*, *Instruments* **5** (2021) 13, [2102.10209].

[333] LUX collaboration, D. S. Akerib et al., *Discrimination of electronic recoils from nuclear recoils in two-phase xenon time projection chambers*, *Phys. Rev. D* **102** (2020) 112002, [2004.06304].

[334] L. W. Goetzke, E. Aprile, M. Anthony, G. Plante and M. Weber, *Measurement of light and charge yield of low-energy electronic recoils in liquid xenon*, *Phys. Rev. D* **96** (2017) 103007, [1611.10322].

[335] E. Bodnia et al., *The electric field dependence of single electron emission in the PIXeY two-phase xenon detector*, *J. Instrum.* **16** (2021) P12015, [2101.03686].

[336] XENON100 collaboration, E. Aprile et al., *Observation and applications of single-electron charge signals in the XENON100 experiment*, *J. Phys. G* **41** (2014) 035201, [1311.1088].

[337] LUX collaboration, D. S. Akerib et al., *Investigation of background electron emission in the LUX detector*, *Phys. Rev. D* **102** (2020) 092004, [2004.07791].

[338] B. Edwards et al., *Measurement of single electron emission in two-phase xenon*, *Astropart. Phys.* **30** (2008) 54–57, [0708.0768].

[339] ZEPLIN-III collaboration, E. Santos et al., *Single electron emission in two-phase xenon with application to the detection of coherent neutrino-nucleus scattering*, *J. High Energy Phys.* **12** (2011) 115, [1110.3056].

[340] D. Y. Akimov et al., *Observation of delayed electron emission in a two-phase liquid xenon detector*, *J. Instrum.* **11** (2016) C03007.

[341] A. Kopec, A. L. Baxter, M. Clark, R. F. Lang, S. Li, J. Qin and R. Singh, *Correlated single- and few-electron backgrounds milliseconds after interactions in dual-phase liquid xenon time projection chambers*, *J. Instrum.* **16** (2021) P07014, [2103.05077].

[342] XENON collaboration, E. Aprile et al., *Emission of Single and Few Electrons in XENON1T and Limits on Light Dark Matter*, 2112.12116.

[343] XENON collaboration, E. Aprile et al., *Energy resolution and linearity of XENON1T in the MeV energy range*, *Eur. Phys. J. C* **80** (2020) 785, [2003.03825].

[344] M. Szydagis, J. Balajthy, G. Block, J. Brodsky, J. Cutter, S. Farrell, J. Huang, E. Kozlova, B. Lenardo, A. Manalaysay et al., *Noble Element Simulation Technique (v2.3.0)*, Nov., 2021. 10.5281/zenodo.5676553.

[345] M. Szydagis, C. Levy, G. M. Blockinger, A. Kamaha, N. Parveen and G. R. C. Rischbieter, *Investigating the XENON1T low-energy electronic recoil excess using NEST*, *Phys. Rev. D* **103** (2021) 012002, [2007.00528].

[346] EXO-200 collaboration, G. Anton et al., *Measurement of the scintillation and ionization response of liquid xenon at MeV energies in the EXO-200 experiment*, *Phys. Rev. C* **101** (2020) 065501, [1908.04128].

[347] L. Baudis, P. Sanchez-Lucas and K. Thieme, *A measurement of the mean electronic excitation energy of liquid xenon*, *Eur. Phys. J. C* **81** (2021) 1060, [2109.07151].

[348] E. M. Gushchin, A. A. Kruglov, V. V. Litskevich, A. N. Lebedev, I. M. Obodovskiĭ and S. V. Somov, *Electron emission from condensed noble gases*, *Sov. J. Exp. Theor. Phys.* **49** (May, 1979) 856.

[349] E. Aprile, K. L. Giboni, P. Majewski, K. Ni and M. Yamashita, *Proportional light in a dual-phase xenon chamber*, *IEEE Trans. Nucl. Sci.* **51** (2004) 1986–1990.

[350] S. Aiello, D. Lo Presti, E. Leonora, N. Randazzo, G. V. Russo and R. Leanza, *Aging characterization on large area photo-multipliers*, *Nucl. Instrum. Meth. A* **725** (2013) 151–154.

[351] Hamamatsu Photonics. [Online] Available: https://hamamatsu.su/files/uploads/pdf/3_mppc/s13370_vuv4-mppc_b_(1).pdf, (accessed 2021, July 18).

[352] G. Gallina et al., *Characterization of the Hamamatsu VUV4 MPPCs for nEXO*, *Nucl. Instrum. Meth. A* **940** (2019) 371–379, [1903.03663].

[353] L. Arazi, A. E. C. Coimbra, R. Itay, H. Landsman, L. Levinson, M. L. Rappaport, D. Vartsky and A. Breskin, *First observation of liquid-xenon proportional electroluminescence in THGEM holes*, *J. Instrum.* **8** (2013) C12004, [1310.4074].

[354] J. Schrott, M. Sakai, S. Naugle, G. O. Gann, S. Kravitz, D. McKinsey and R. Smith, *Measurement of the angular distribution of wavelength-shifted light emitted by TPB*, *J. Instrum.* **16** (2021) P12013, [2108.08239].

[355] L. Baudis, H. Dujmovic, C. Geis, A. James, A. Kish, A. Manalaysay, T. Marrodán Undagoitia and M. Schumann, *Response of liquid xenon to Compton electrons down to 1.5 keV*, *Phys. Rev. D* **87** (2013) 115015, [1303.6891].

[356] T. Shutt, C. E. Dahl, J. Kwong, A. Bolozdynya and P. Brusov, *Performance and Fundamental Processes at Low Energy in a Two-Phase Liquid Xenon Dark Matter Detector*, *Nucl. Instrum. Meth. A* **579** (2007) 451–453, [astro-ph/0608137].

[357] NEST Collaboration: Calculator. [Online] Available: https://nest.physics.ucdavis.edu/download/calculator, (accessed 2021, October 18).

[358] U. Fano, *Ionization Yield of Radiations. II. The Fluctuations of the Number of Ions*, *Phys. Rev.* **72** (1947) 26–29.

[359] T. Doke, A. Hitachi, S. Kubota, A. Nakamoto and T. Takahashi, *Estimation of Fano factors in liquid argon, krypton, xenon and xenon-doped liquid argon*, *Nucl. Instrum. Meth.* **134** (1976) 353–357.

[360] S. J. C. do Carmo, F. I. G. M. Borges, F. L. R. Vinagre and C. A. N. Conde, *Experimental Study of the w-Values and Fano Factors of Gaseous Xenon and Ar-Xe Mixtures for X-Rays*, *IEEE Trans. Nucl. Sci.* **55** (2008) 2637–2642.

[361] J. Seguinot, T. Ypsilantis and J. Tischhauser, *Liquid xenon scintillation: Photon yield and Fano factor measurements*, *Nucl. Instrum. Meth. A* **354** (1995) 280–287.

[362] Y. Biondi, *Sensitivity of DARWIN to Rare Events and the Purity Monitor for Xenoscope*. PhD thesis, University of Zurich, to be published, 2022.

[363] BIBUS AG. [Online] Available: https://www.bibus.ch/, (accessed 2021, December 9).

[364] BIBUS AG. [Online] Available: https://www.bibus.ch/fileadmin/editors/countries/bagch/4_Mechatronik/ace/Downloads/ACE_ACEolator-Vibration-ENG.pdf, (accessed 2021, December 9).

[365] Egli Federnfabrik AG. [Online] Available: https://www.eglifedern.ch/, (accessed 2021, December 9).

[366] G. Plante, E. Aprile, J. Howlett and Y. Zhang, *Liquid-phase purification for multi-tonne xenon detectors*, 2205.07336.

[367] K. L. Giboni et al., *Xenon Recirculation-Purification with a Heat Exchanger*, *J. Instrum.* **6** (2011) P03002, [1103.0986].

[368] E. Aprile et al., *Performance of a cryogenic system prototype for the XENON1T Detector*, *J. Instrum.* **7** (2012) P10001, [1208.2001].

[369] D. S. Akerib et al., *The LUX Prototype Detector: Heat Exchanger Development*, *Nucl. Instrum. Meth. A* **709** (2013) 29–36, [1207.3665].

[370] ULVAC Technologies Inc. Iwatani. [Online] Available: https://www.ulvac-cryo.com/products-en/refrigerator-en/cryocoolers/?lang=en, (accessed 2021, July 19).

[371] D. Singh, A. Pandey, M. K. Singh, L. Singh and V. Singh, *Heat radiation reduction in cryostats with multilayer insulation technique*, *J. Instrum.* **15** (2020) P07032, [2002.09586].

[372] B. Baudouy, *Heat Transfer and Cooling Techniques at Low Temperature*, in *CERN Accelerator School: Course on Superconductivity for Accelerators*, pp. 329–352, 2014. 1501.07153. DOI.

[373] P. M. Sutheesh and A. Chollackal, *Thermal performance of multilayer insulation: A review*, *IOP Conference Series: Materials Science and Engineering* **396** (Aug., 2018) 012061.

[374] D. Singh, M. K. Singh, A. Chaubey, A. K. Ganguly and V. Singh, *Improvement in the performance of multilayer insulation technique and impact in the rare physics search experiments*, 2107.09053.

[375] DIN EN 10088-3, *Nichtrostende Stähle - Teil 3: Technische Lieferbedingungen für Halbzeug, Stäbe, Walzdraht, gezogenen Draht, Profile und Blankstahlerzeugnisse aus korrosionsbeständigen Stählen für allgemeine Verwendung*, *Beuth Verlag GmbH* (Dec., 2014) .

[376] S. P. Venkateshan, *Heat Transfer*. Springer International Publishing, 3rd ed., 2021, 10.1007/978-3-030-58338-5.

[377] P. von Böckh and T. Wetzel, *Heat Transfer, Basics and Practice*. Springer-Verlag Berlin Heidelberg, 2012, 10.1007/978-3-642-19183-1.

[378] Kelvion Holding GmbH. [Online] Available: https://www.kelvion.com/, (accessed 2021, July 19).

[379] RUAG Space GmbH. [Online] Available: https://www.ruag.com/en, (accessed 2021, July 19).

[380] Swagelok Company. [Online] Available: https://www.swagelok.com/downloads/webcatalogs/en/ms-01-92.pdf, (accessed 2021, December 10).

[381] Swagelok Company. [Online] Available: https://www.swagelok.com/downloads/webcatalogs/en/ms-02-156.pdf, (accessed 2021 December 10).

[382] Cryofab Inc. [Online] Available: https://www.cryofab.com/, (accessed 2021, July 19).

[383] KGW-Isotherm. [Online] Available: https://kgw-isotherm.com/, (accessed 2021, July 19).

[384] Mettler-Toledo. [Online] Available: https://www.mt.com/ch/en/home.html, (accessed 2021, July 19).

[385] Soemer Messtechnik GmbH. [Online] Available: https://www.soemer.de/, (accessed 2021, July 19).

[386] L. Virone et al., *Gravity assisted recovery of liquid xenon at large mass flow rates*, *Nucl. Instrum. Meth. A* **893** (2018) 10–14.

[387] Swagelok Company. [Online] Available: https://www.swagelok.com/, (accessed 2021, July 6).

[388] Swagelok Company. [Online] Available: https://www.swagelok.com/downloads/webcatalogs/EN/MS-01-38.PDF, (accessed 2021, December 11).

[389] Apiezon by M&I Materials Ltd. [Online] Available: https://www.apiezon.com/, (accessed 2021, August 9).

[390] KASAG Swiss AG. [Online] Available: https://www.kasag.com/, (accessed 2021, May 27).

[391] Verband der TÜV e.V., ed., *AD 2000*. Beuth Verlag GmbH, 12 ed., 2020.

[392] Official Journal of the European Union. [Online] Available: http://data.europa.eu/eli/dir/2014/68/oj, (accessed 2021, July 6).

[393] SolidWorks by Dassault Systèmes SolidWorks Corporation. [Online] Available: https://www.solidworks.com/, (accessed 2021, August 9).

[394] C. A. J. O'Hare, *Can we overcome the neutrino floor at high masses?*, *Phys. Rev. D* **102** (2020) 063024, [2002.07499].

[395] SCENE collaboration, H. Cao et al., *Measurement of Scintillation and Ionization Yield and Scintillation Pulse Shape from Nuclear Recoils in Liquid Argon*, *Phys. Rev. D* **91** (2015) 092007, [1406.4825].

[396] M. Cadeddu et al., *Directional dark matter detection sensitivity of a two-phase liquid argon detector*, *J. Cosmol. Astropart. Phys.* **01** (2019) 014, [1704.03741].

[397] A. Manalaysay et al., *Spatially uniform calibration of a liquid xenon detector at low energies using ^{83m}Kr*, *Rev. Sci. Instrum.* **81** (2010) 073303, [0908.0616].

[398] LUX collaboration, D. S. Akerib et al., *^{83m}Kr calibration of the 2013 LUX dark matter search*, *Phys. Rev. D* **96** (2017) 112009, [1708.02566].

[399] V. Hannen et al., *Limits on the release of Rb isotopes from a zeolite based ^{83m}Kr calibration source for the XENON project*, *J. Instrum.* **6** (2011) P10013, [1109.4270].

[400] DIN 4102-2, *Brandverhalten von Baustoffen und Bauteilen; Bauteile, Begriffe, Anforderungen und Prüfungen*, *Beuth Verlag GmbH* (Sept., 1977) .

[401] riThermo-foil DPA. [Online] Available: http://www.jeanfrei.ch/pdfs/riThermo-foil%20DBA%20Beschrieb.pdf, (accessed 2021, April 30).

[402] Swagelok Company, *Proportional Safety Relief Valves, PRV Series*. [Online] Available: https://www.swagelok.com/downloads/webcatalogs/en/MS-02-432.pdf, (accessed 2021, May 1).

[403] M. Hellemans, *The Safety Relief Valve Handbook*. Elsevier Ltd., Imprint: Butterworth-Heinemann, 1st ed., 2009.

[404] Swagelok Company, *Bellows-Sealed Valves, U Series*. [Online] Available: https://www.swagelok.com/downloads/webcatalogs/en/MS-01-38.pdf, (accessed 2021, May 1).

[405] Swagelok Company, *VCR® Metal Gasket Face Seal Fittings*. [Online] Available: https://www.swagelok.de/downloads/webcatalogs/en/MS-01-24.pdf, (accessed 2021, May 2).

[406] Swagelok Company, *Pipe Fittings*. [Online] Available: https://www.swagelok.com/downloads/webcatalogs/en/MS-01-147.pdf, (accessed 2021, May 2).

[407] Swagelok Company, *Stainless Steel Seamless Tubing and Tube Support Systems*. [Online] Available: https://www.swagelok.com/downloads/webcatalogs/en/MS-01-181.PDF, (accessed 2021, May 1).

[408] Swagelok Company, *Valve Sizing, Technical Bulletin*. [Online] Available: https://www.swagelok.com/downloads/webcatalogs/en/ms-06-84.pdf, (accessed 2021, May 1).